UNIVERSITÀ DEGLI STUDI DI MILANO

Scuola di dottorato in Agricoltura, ambiente e bioenergia

Dipartimento di Scienze Agrarie e Ambientali – Produzione, territorio, agroenergia

Corso di dottorato in Agricoltura, ambiente e bionergia, XXIX ciclo

HYDROLOGICAL MODELLING FOR THE PREVENTION AND THE MANAGEMENT OF WATER SHORTAGE IN AGRICULTURE

AGR/08

Tesi di dottorato di:

Anna Borghi

Tutor: Prof. Arianna Facchi

Coordinatore del dottorato: Prof. Daniele Bassi

A.A. 2016

… the last rains came gently, and they did not cut the scar red earth. The plows crossed and recrossed the rivulet marks. The last rains lifted the corn quickly and scattered weed colonies and grass along the sides of the roads so that the gray country and the dark red country began to disappear under a green cover.

John Steinbeck, *The grapes of wrath*

ACKNOWLEDGEMENTS

First of all, I would like to thank my supervisor, Prof. Arianna Facchi, for giving me the opportunity to undertake the Ph.D. program. I am particularly grateful for her encouragement and enlightenment on my research during my Ph.D. career, as well as for her guidance on my technical skills in communicating and presenting the work.

I am grateful to Giovanni Giupponi, Fausto Gaini and Riccardo Marengoni of the Media Pianura Bergamasca Irrigation District for providing the information required for the study. Sincere thanks are also due to Dante Fasolini of ERSAF Lombardia for the support and the useful discussions.

I am also grateful to Dr. Francesco Vuolo from the University of Natural Resources and Life Sciences, for hosting me in his excellent research group during my visiting period in Austria, for supervising my work and for providing the “phenolox” dataset for the research area.

I would thank all my colleagues, in particular Dr. Michele “Letstryagain” Rienzner for always being available to discuss any doubt and results, and for being a light in the darkness of statistical analysis, Fabio “Gino” Olivotti and Stefano “Pino” Roverato for providing updated datasets for the irrigation district and derivations and for GIS suggestions. I would also like to thank all the friends with whom I have shared the journey, in particular Prof. Paola Morando, Dr. Yu Li, Martina Corti, Gerald Lindner, Hannah Wenng and Luca Zappa.

Finally, I would like to thank all my friends and colleagues “of the world out there”, in particular Annalisa Geronimi, Ivan Cataldo and Simone Bernasconi, for not blaming me for my madness and for being still here, waiting for me going back working with them.

ABSTRACT

In recent decades, frequent and severe droughts have occurred in several countries of the world under nearly all climatic regimes. Since the middle 20th century, drought areas have globally increased, and, more specifically, in southern and central Europe. Drought risk is expected to increase in the near future as a result of the climate change, leading to a decline in precipitation and an increase in air temperatures, and consequently in evapotranspiration rates in several regions, including southern Europe and the Mediterranean region.

Droughts can significantly affect the agricultural sector since they provoke losses in crop yields and livestock production, increased insect infestations, plant diseases and wind erosion. Moreover, low rainfall during the growing season may affect irrigated agriculture over subsequent years, as a result of low levels of water in reservoirs and groundwater aquifers.

In Europe, the monitoring and assessment of drought is entrusted to the European Drought Observatory (EDO), that applies a multi-indicator approach, based on earth observations (EOs) and hydrological modelling data. EDO indicators are computed considering rainfed agriculture, predominant in middle and northern Europe, and are produced on a $5 \ km$ grid. In southern Europe, however, the implementation of drought-coping measures (irrigation) can partially or completely alleviate the impacts of potentially severe droughts. Therefore, for these conditions, specific water scarcity indicators explicitly considering irrigation among the water inputs to agro-ecosystems need to be developed and adopted to inform and support stakeholders and decision makers of irrigated regions.

In this context, the main objective of the Ph.D. thesis is the presentation of the Transpirative Deficit Index (TDI), a newly developed indicator for the monitoring and the management of Water Scarcity and Drought phenomena based on the use of hydrological modelling, applied at a spatial scale of interest for end-users ($250 \ m$ grid) and suited for the assessment of water scarcity and drought in Italy as well as in other southern European countries. In particular, TDI was developed as a new module integrated into the spatially distributed hydrological model IdrAgra, and in the Ph.D. research it was tested over the Irrigation District of Media Pianura Bergamasca (IDMPB), considering a simulation period of 22 years (1993-2014) and subdividing the territory by means of a grid with cells of $250 \ m \times 250 \ m$.

As a first step in the thesis, $D\text{-}TDI$ was described as an agricultural drought index focusing on overcoming the limitation of other approaches, not taking into account with sufficient detail land cover and soil properties. The $D\text{-}TDI$ is based on the calculation of the spatially distributed actual transpiration deficit, to determine the level of drought experienced by crops within the single model cells; thus, it can provide a much more accurate measure of agricultural drought at the irrigation district scale than the one that could be achieved through meteorological drought indices such as SPI or $SPEI$. The auto-correlation analysis of $D\text{-}TDI$ showed to be positive with a persistence of 30 days for the two more widespread crops in the study area, maize and permanent grass. The analysis demonstrated also that soils characterized by a high available water content can more easily compensate dry spells. Finally, a positive significant correlation between $D\text{-}TDI$ and SPI was

observed for maize, with a persistence of 40 days, while no correlation was observed for permanent grass, probably related to cutting cycles, that could mask the relation between storage capacity and short-time variability of the meteorological conditions.

Successively, a methodology to compute crop yield using moderate spatial and temporal resolution Earth Observation (Landsat) data was set. In particular, the developed procedure, based on the integration of the Available Photosynthetically Active Radiation over the growing season, showed that statistical inventories and satellite data can be integrated to produce annual spatially distributed estimates of cropland productivity, while site-specific observational field data can be used to validate the relationship between $APAR$ and productivity for specific crops (i.e. maize in this Ph.D. research). A phenological parameter extraction algorithm was developed to derive key phenology stages for the maize crop. However, the results presented in the study showed two main weaknesses: (1) cloud cover and noise in the original Landsat dataset were not appropriately removed by the Whittaker algorithm, and (2) SOS (Start of Season) and EOS (End of Season) extracted from satellite data were underestimated for a discrete numbers of fields with respect to observed ground-truths, probably as a consequence of the method adopted for setting the thresholds. A crop specific light use efficiency (ε_b^*) was estimated as the ratio between the average maize yield over the study period taken from Regional Statistic Inventory (Regional Authority and ISTAT), and the average $APAR$ value calculated for the maize pixels over the same spatial extension and time period. The ε_b^* estimated value fell within the range of the coefficients calibrated with other satellite-based algorithms.

Finally, TDI was applied as a water scarcity index ($WS\text{-}TDI$), thus including water availability for irrigation within the inputs of the IdrAgra model. The behaviour of $D\text{-}TDI$ and $WS\text{-}TDI$ was compared over the same area, analysing their spatialized trend in response to varying meteorological conditions, and in particular considering drought events and dry spells. The two indices proved to be suitable to monitor agricultural drought and water scarcity over a territory, and helped in identifying drought and/or water scarcity prone sub-districts, as a function of crop, soil type and water availability. Both $D\text{-}TDI$ and $WS\text{-}TDI$ could therefore be used as operational indicators to produce periodic maps that could help farmers and irrigation district managers in coping with agricultural drought and water scarcity and, eventually, in setting up proper adaptation measures. In particular, in case of availability of real time meteorological data and water discharges at the main surface water diversions, the indicators may be adopted by an authority responsible for the monitoring of the state of agriculture (ERSAF or ARPA in the Lombardy region) to promptly inform (through newsletters or a web site) stakeholders on the agricultural drought/dry spells and water scarcity/shortages phenomena evolution. Additionally, the indicators may be adopted in climate change studies, allowing to visualize the evolution of drought and water scarcity phenomena over the territory, as a consequence of changes in meteorological forcing and in the availability of water by irrigation sources. Finally, they could be used as useful tools to support planning decisions on water resources allocation or action plans to reduce water consumptions in specific portions of the territory (e.g. conversion of irrigation methods, introduction of different crop species, etc.), also in view of an adaptation to the climate change. $WS\text{-}TDI$ maps over a pilot study area were statistically compared with the maize yield maps derived from EO data (Landsat dataset): an ensemble correlation analysis proved a positive correlation between the two variables.

CONTENTS

ACRONYMS

AC	Auto-correlation
APAR	Absorbed Photosynthetically Active Radiation
ARPA	Agenzia Regionale per la Protezione dell'Ambiente (Regional Authority for the Environmental Protection in Lombardy)
AVHRR	Advanced Very High Resolution Radiometer
AWC	Available Water Content
BOKU	Universität für BOdenKUltur Wien (University of Natural Resources and Life Sciences)
CAP	Community Agricultural Policy
CC	Cross-correlation
CCB	Carbon Content in Biomass
CDI	Combined Drought Indicator
CDR	(Landsat) Climate Data Record
CUE	Carbon Use Efficiency
D	Drought
DiSAA	Dipartimento di Scienze Agrarie e Ambientali (Department of Agricultural and Environmental Sciences)
DOY	Day Of Year
DTx	Deficit Traspirativo integrato (integrated Transpirative Deficit)
(D)-TD	(Drought) – Transpirative Deficit
D-TDI	Transpirative Deficit Index applied as a Drought index
EDO	European Drought Observatory
EO	Earth Observation
EOS	End of Season
EPIC	Environmental Policy Integrated Climate (model)
ERSAF	Ente Regionale per i Servizi all'Agricoltura e alle Foreste (Lombardy Region Agriculture and Forest Service)
ETDI	EvapoTranspiration Deficit Index

ET0	Reference crop EvapoTranspiration
FAO	Food and Agriculture Organization of the United Nations
fAPAR	fraction of Absorbed Photosynthetically Active Radiation
GIS	Geographic Information System
GPP	Gross Primary Production
HI	Harvest Index
ID	IDentifier
IDMPB	Irrigation District of Media Pianura Bergamasca
IDW	Inverse Distance Weighted (method)
IPCC	International Panel on Climate Change
ISTAT	Istituto nazionale di STATistica (Italian National Institute of Statistics)
IVFL	Institut für Vermessung, Fernerkundung und Landinformation (Institute of Surveying, Remote Sensing and Land Information)
JRC	Joint Research Centre
K-S	Kolgomorov-Smirnov (test)
LUE	Light Use Efficiency
MAC-D	Multiple Abrupt Changes in the mean value of Daily temperature series (method)
MC	Moisture Content
MODIS	MOderate Resolution Imaging Spectroradiometer
MOS	Maximum of Season
NaN	Not a Number
NDVI	Normalized Difference Vegetation Index
NDWI	Normalized Difference Water Index
PAR	Photosynthetically Activer Radiation
PDSI	Palmer Drought Severity Index
PEM	Production Efficiency Model
pF	Water potential
PTF	Pedo-Transfer Function

PWM	Probability Weighted Moment
RDI	Reconnaissance Drought Index
RS	Root to Shoot ratio
SC-PDSI	Self-Calibrating Palmer Drought Severity Index
SIARL	Sistema Informativo Agricolo Regione Lombardia (Agricultural Information System of the Lombardy Region)
SMDI	Soil Moisture Deficit Index
SOS	Start of Season
SPEI	Standardized Precipitation Evapotranspiration Index
SPI	Standardized Precipitation Index
SVI	Standardized Vegetation Index
SWDI	Soil Water Deficit Index
TDI	Transpirative Deficit Index
TDx	Integrated transpirative Deficit
VCI	Vegetation Condition Index
VI	Vegetation Index
WS	Water Scarcity
WS&D	Water Scarcity and Drought
(WS)-TD	(Water Scarcity) – Transpirative Deficit
WS-TDI	Transpirative Deficit Index applied as a Water Scarcity index

NOTATIONS

ACn	Lag-n Auto-correlation coefficient (adimensional)
$APAR_d$	Daily Absorbed Photosynthetically Active Radiation ($MJ \cdot m^{-2} \cdot d^{-1}$)
$APAR_y$	Absorbed Photosynthetically Active Radiation cumulated over the growing season ($MJ \cdot m^{-2}$)
AWC_T	Available Water Content of the Transpirative Layer ($m^3 \cdot m^{-3}$)
CCn	Lag-n Cross-correlation coefficient (adimensional)
D	Deficit, i.e. the difference between precipitation and reference evapotranspiration (mm)
D-$TDIn$	(Drought) – Transpirative Deficit Index over the accumulation period n (adimensional)
E	Evaporation rate $(mm \cdot d^{-1})$
ET_0	Reference crop evapotranspiration $(mm \cdot d^{-1})$
$fAPAR$	fraction of the Absorbed Photosynthetically Active Radiation (adimensional)
GPP_{inv}	Inventory based Gross Primary Production ($g \cdot m^{-2}$)
I	Canopy interception $(mm \cdot d^{-1})$
K_{cb}	Crop-related basal coefficient (adimensional)
K_e	Evaporative coefficient (adimensional)
K_s	Water stress coefficient (adimensional)
n	Accumulation period (d)
x^*	Calibrated parameter x
$\hat{x}$	Estimated parameter x
P	Rainfall rate $(mm \cdot d^{-1})$
PAR	Photosynthetically Active Radiation ($MJ \cdot m^{-2} \cdot d^{-1}$)
Q_e	Percolation from the evaporative to the transpirative layer $(mm \cdot d^{-1})$
Q_i	Irrigation supply $(mm \cdot d^{-1})$
Q_p	Ponding $(mm \cdot d^{-1})$
Q_s	Percolation from the transpirative layer to the deeper subsoil or capillary rise rate $(mm \cdot d^{-1})$

Q_u	Runoff $(mm \cdot d^{-1})$
RAW	Readily Available Water $(mm \cdot d^{-1})$
$SPEIn$	Standardized Precipitation Evapotranspiration Index over the accumulation period n (adimensional)
$SPIn$	Standardized Precipitation Index over the accumulation period n (adimensional)
t	Time step (d)
T	Transpiration rate $(mm \cdot d^{-1})$
T_a	Actual transpiration (mm)
T_p	Potential transpiration (mm)
TAW	Total Available Water $(mm \cdot d^{-1})$
TDn	Integrated transpirative deficit over an accumulation period of n days (mm)
V_E	Water content of the evaporative layer per unit surface area of the cell (mm)
V_T	Water content of the transpirative layer per unit surface area of the cell (mm)
$WS\text{-}TDIn$	(Water Scarcity) – Transpirative Deficit Index over the accumulation period n (adimensional)
Z_r	Root zone depth (m)
$\wedge$	Logical AND
$\vee$	Logical OR
α	Shape parameter (adimensional)
β	Scale parameter (adimensional)
γ	Origin parameter (adimensional)
$\Gamma(x)$	Gamma function
ε_b	Light use efficiency $(gC \cdot MJ^{-1})$
θ	Actual soil water content in the profile (adimensional)
θ_{FC}	Soil water content at field capacity (adimensional)
θ_{WP}	Soil water content at wilting point (adimensional)
μ	Mean
σ	Standard deviation

1 INTRODUCTION

1.1 MOTIVATION

In recent decades, frequent and severe droughts have occurred in several countries of the world under nearly all climatic regimes (European Environment Agency 2010; International Panel on Climate Change 2012; Mishra & Singh 2010; Rossi & Cancelliere 2013). Dai (2011) showed that, since the middle 20th century, drought areas have globally increased. Although for some European countries trends are generally less clear, in southern and central Europe an increase in dryness has been consistently observed since the 1950s (Dai 2011; Sheffield & Wood 2008).

Droughts can significantly affect the agricultural sector since they provoke losses in crop yields and livestock production, increased insect infestations, plant diseases and wind erosion. Longer term impacts include losses of productive assets (e.g. machinery, buildings) and decline in land value, which can reduce productivity and may require significant resources for recovery (Blinda et al. 2007; Organisation for Econonomic Cooperation and Development 2016). Moreover, low rainfall during the growing season may affect irrigated agriculture over subsequent years, as a result of low levels of water in reservoirs and groundwater aquifers (European Environment Agency 2010).

The overall economic impacts of water scarcity and drought events between 1976 and 2006 were estimated at € 100 billion in the European Union, but the annual average impact doubled between the first and the second half of the considered period (Collins et al. 2009). In the agricultural sector, the 2003 heat wave and associated droughts resulted in major regional crop shortfalls (Hov et al. 2013), with economic losses estimated at € 13 billion (Blinda et al. 2007). A drop in crop yield of 36% was estimated in the Po valley for maize, where extremely high temperatures prevailed (Ciais et al. 2005).

Drought risk is expected to increase in the near future as a result of the climate change, leading to a decline in precipitation and an increase in air temperatures, and consequently in evapotranspiration rates, in several regions, including southern Europe and the Mediterranean region (Dai 2011; Giorgi & Lionello 2008; International Panel on Climate Change 2012).

In Europe, the monitoring and assessment of drought is entrusted to the European Drought Observatory (EDO), that applies a multi-indicator approach (de Jager & Vogt 2015), based on earth observations (EOs) and hydrological modelling data. EDO indicators are computed considering rainfed agriculture, predominant in middle and northern Europe, and are produced on a $5\ km$ grid. In southern Europe, however, the implementation of drought-coping measures (irrigation) can partially or completely alleviate the impacts of potentially severe droughts. Therefore, for these conditions, specific water scarcity indicators explicitly considering irrigation among the water inputs to agro-ecosystems need to be developed and adopted to inform and support stakeholders and decision makers of irrigated regions.

In the Po River Plain, irrigated crops cover more than 70% of the agricultural land, massive amounts of water are diverted from rivers for irrigation, and surface irrigation methods are largely applied (Istituto Nazionale di Statistica 2014; Wriedt, van der Velde, et al. 2009). Nowadays, the region cannot be considered a water scarce basin, but irrigation water shortages have been occurring with increased frequency during the last two decades. Moreover, this area is included among European areas that by 2030 shall be affected by water scarcity (Strosser et al. 2012).

In this context, this Ph.D. thesis aims to develop an indicator for the management and the prevention of Water Scarcity and Drought (WS&D) phenomena based on the use of hydrological modelling, applied at a spatial scale of interest for end-users ($250\ m$ grid) and suited for the assessment of water scarcity and drought in Italy as well as in other southern European countries. Earth Observation data were moreover used in this work to validate the spatially distributed indicator estimates over a pilot study area within the Po River Plain.

1.2 OBJECTIVE AND ORGANIZATION OF THE DISSERTATION

The Ph.D. dissertation offers several contributions to WS&D assessment studies, in particular: (1) the development and the assessment of a new agricultural WS&D index, (2) an innovative method to estimate crop yield through the use of Landsat imagery, (3) a case-study application of the proposed approach over an extensive area within the Po River Plain, to assess its potential and its limits.

The manuscript is organized as follows:

Chapter 1 describes the state of the art of WS&D research, and states the objectives of the Ph.D.

Chapter 2 provides a comprehensive description of the Media Pianura Begamasca Irrigation District, study area for the index application, and of the available dataset. In the same chapter, the ground truth dataset used to validate the crop yield maps obtained from Landsat time series is detailed.

Chapter 3 illustrates the development of the Transpirative Deficit Index and its use for the monitoring of agricultural drought ($D\text{-}TDI$). In the same chapter, the hydrological model IdrAgra and its use to calculate the $D\text{-}TDI$ index over the Media Pianura Bergamasca Irrigation District is described. To better characterize the $D\text{-}TDI$, an auto-correlation analysis as well as a cross-correlation analysis against a well-known meteorological drought index, the Standardized Precipitation Index (SPI), is discussed. The work described in this chapter will be used to prepare a scientific paper to be submitted to *Natural Hazards*.

In chapter 4, a methodology to compute crop yield using moderate spatial and temporal resolution Earth Observation (Landsat) data is described. In particular, a complete temporal series of fAPAR (i.e. fraction of Absorbed Photosynthetically Active Radiation) derived by Landsat images, post-elaborated by the Institute of Surveying, Remote Sensing and Land Information (IVFL) of the University of Natural Resources and Life Sciences of Vienna (BOKU) with the objective to reconstruct usable data also in cloudy areas, is adopted for this study. The developed methodology is then applied to the Media Pianura Bergamasca Irrigation District, to calculate the yield of maize areas.

Obtained results are then validated against field observational yield data. The research activity described in the chapter will be organized in a paper for *International Journal of Remote Sensing*.

In chapter 5, the Transpirative Deficit Index is applied as a water scarcity index ($WS\text{-}TDI$) to a pilot study area within the Media Pianura Bergamasca Irrigation District. The main difference of $WS\text{-}TDI$ with respect to $D\text{-}TDI$ is the inclusion of irrigation within the water inputs in the simulation procedure. To do this, data about the temporal pattern of water diversions or abstractions from the different water sources, as well as about the irrigation water conveyance and distribution over the territory, have to be collected. $WS\text{-}TDI$ results are validated through a comparison with the maize yield maps derived from Earth Observation data, to evaluate the performance of the water scarcity index in the identification of areas where soil water deficit leads to yield reduction. The work presented in chapter 5 will be described in a paper for *Journal of Water Resources Planning and Management*.

Final remarks and suggestions on further developments of the research are provided in chapter 6.

1.3 DROUGHT AND WATER SCARCITY

The scientific community does not agree on univocal definitions for “water scarcity” and “drought” and, due to interconnections between the effects of these events, water managers, public and media use both terms often hazily (Mishra & Singh 2010).

With the Communication “Addressing the challenge of water scarcity and droughts”, the European Commission (2007) proposes a definition for different WS&D concepts, further elaborated in Schmidt et al. (2012) and Strosser et al. (2012), in which these phenomena are described in function of their causes and timescale (Table 1-1).

Table 1-1: Timescale and causes of water scarcity, drought and related concepts (Schmidt et al. 2012).

		Timescale		
		Short-term (days, weeks)	**Mid-term (months, seasons, years)**	**Long-term (decades)**
Causes	**Natural**	Dry spell	Drought	Aridity
	Man-made	Water shortage	Water scarcity	Desertification

In this framework, droughts are identified as natural and temporary phenomena, characterised by sustained and extensive occurrence of below-average water availability, caused by climate variability (European Environment Agency 2010; Heim 2002; Van Loon & Van Lanen 2013), and therefore can be observed in all climate regimes. The primary driver of drought is a precipitation shortage, that can result in a deficiency of the amount of water required for the functioning of natural ecosystems or human activities (Blinda et al. 2007).

The effects of a drought can be enhanced or reduced at any stage of the water cycle: high air temperatures and evapotranspiration rates may act in combination with lacking rainfall to exacerbate drought duration and severity, while during winter the low evapotranspiration rates can mitigate its effects. Drought severity and duration are also related to the precipitation timing (i.e. principal season of occurrence, delays in the start of the rainy season, occurrence of rains in relation to principal crop growth stages) and effectiveness (i.e. rainfall intensity and number of rainfall events). Moreover, drought effects can be compounded by anthropogenic activities, in particular water scarcity situations (Blinda et al. 2007; European Environment Agency 2010; Singleton 2012).

A related term is aridity, which is a long-term shortage of precipitation and moisture, based on the average climatic condition over a region (Blinda et al. 2007; European Environment Agency 2010; Van Loon & Van Lanen 2013).

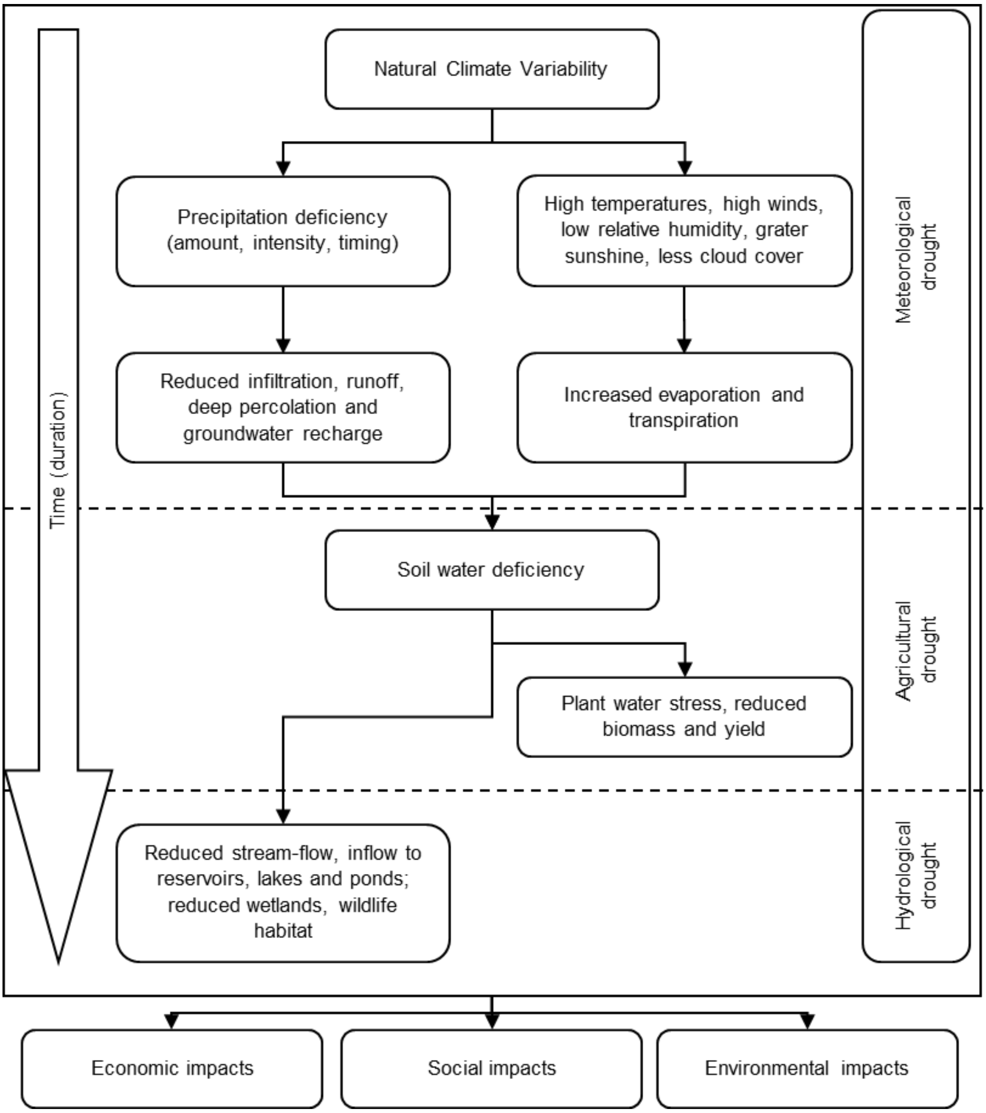

Figure 1-1: Sequence of drought occurrence and impacts for commonly accepted drought types (Source: http://drought.unl.edu/DroughtBasics/TypesofDrought.aspx)

On the other hand, water scarcity describes a situation of long-term water imbalance, where water abstraction exceeds the level of water resources availability. While these events usually emerge in areas of low water availability or rainfall, they can also occur in regions with high levels of water consumption, connected to high population density or to the use of significant volumes of water in agricultural or industrial activities (Blinda et al. 2007; European Commission 2007). Moreover, where water abstraction puts pressure on water resource, imbalance between demand and availability worsens during drought periods. Under these circumstances, a negative feedback can occur, particularly with agricultural water use, because the lack of rainfall drives greater abstraction in order to provide the water required for crops (European Environment Agency 2010).

While water stress is sometimes used as a synonym for water scarcity, water shortage is better defined as the water imbalance on a shorter time scale, i.e. less than a month. Desertification is the longer term equivalent of water scarcity, as it has anthropogenic causes (Van Loon & Van Lanen 2013).

Droughts are commonly classified according to the time interval of their occurrence and to their effect (Figure 1-1; European Environment Agency 2010; Mishra & Singh 2010).

Meteorological drought is defined by a precipitation deficiency, that lowers below a certain threshold, over a region and a predetermined time period. Both the chosen threshold and the duration period, that determine the drought initiation, may vary by location according to user needs or applications. Meteorological drought normally triggers other types of drought, that place greater emphasis on human or social aspects, focusing on the interaction between drought effects and human activities that depend on precipitation to provide adequate water supplies to meet societal and environmental demands (World Meteorological Organization 2006).

Agricultural drought usually refers to a period with declining soil moisture to support crop growth, leading to a consequent crop failure. Not always a direct relationship between precipitation or surface water resources and this type of drought can be observed, as the decline of soil moisture depends on several factors affecting meteorological and hydrological droughts along with differences between actual and potential evapotranspiration. The onset of an agricultural drought may therefore lag that of a meteorological drought, depending on the prior moisture status of the surface soil layers (Heim 2002; Mishra & Singh 2010).

Agricultural drought is more commonly observed in non-irrigated agricultural regions, because dryness in the root zone, which occurs at a critical time during the growing season, can severely reduce crop yields, even though deeper soil levels may be saturated (American Meteorological Society 2004). In irrigated areas, the implementation of drought-coping measures (irrigation) can partially or completely alleviate the impacts of agricultural drought, thus these areas are most likely to be affected later in time, when and if a hydrological drought develops (Smakhtin & Schipper 2008).

Hydrological drought is a period with inadequate surface and subsurface water resources (e.g. in natural bodies as streams, lakes or aquifers, but also artificial reservoirs) for established water uses of a given water resources management system (Mishra & Singh 2010). Like for agricultural drought, a direct relationship between precipitation amounts and status of surface and subsurface water supplies cannot be established, also because these hydrological system components are used for multiple and competing purposes (e.g. irrigation, transportation, power production, domestic water supply), complicating the sequence and quantification of impacts (Stahl 2001). The onset of a hydrological drought (i.e. decreased water levels in surface and subsurface components of the hydrological system) might be lagging behind the onset of the corresponding meteorological drought, and, as a consequence of water depletion from the reservoirs, their duration can differ, as considerable quantities of precipitation are required to restore river and lake levels back to their normal conditions (Blinda et al. 2007; World Meteorological Organization 2006).

Finally, **socio-economic drought** reflects the relationship between the supply and demand for an economic good (e.g. water, livestock forage, hydroelectric power) with elements of meteorological, hydrological, and agricultural drought. Socio-economic drought occurs therefore when the demand for an economic good exceeds supply as a result of a weather-related shortfall in water supply (Blinda et al. 2007; World Meteorological Organization 2006).

1.4 REVIEW OF INDICES USED IN AGRICULTURAL DROUGHT ASSESSMENT

The essential elements that distinguish droughts are their intensity, that refers to the degree of the precipitation shortfall or to the severity of impacts associated with the shortfall, their duration, and theirs spatial extent (Sivakumar et al. 2011). Therefore, a drought index helps assessing some of the effects of a drought and defining its parameters.

Common characteristics of drought indices are:

1) they are selected according to the problem being studied;
2) they are quantitative measures of drought conditions, that can be applied to long series, both in spatial and in temporal domains;
3) their time scale is appropriate for monitoring the considered effects. The most commonly used time scale is a year, useful to abstract information on the regional behaviour of drought, while monthly (or sub-monthly) timescale is more appropriate to monitor the effects of agricultural or hydrological droughts (Mishra & Singh 2010; Panu & Sharma 2002);
4) a long accurate past record of the index should be available or computable;
5) if the index is used in operational drought monitoring, it should be computed on a near-real-time basis (Heim 2002; Mishra & Singh 2010).

Niemeyer (2008) identified more than 80 drought indices that have been developed by several generations of researches during the 20th century in the domains of meteorology, hydrology, agricultural research and applications, remote sensing, and water resources management. A systematic review of drought indices has been recently published by World Meteorological Organization & Global Water Partnership (2016). Table 1-2 synthetizes the discussed indices and their characteristics.

Table 1-2: Comparison of commonly used drought indices (Main sources: Dai 2011; World Meteorological Organization & Global Water Partnership 2016).

Type	Index Name	Calculation	Strengths	Weaknesses	References
Meteorological drough indicest	Standardized Precipitation Index (SPI)	Fitting and transforming a long-term precipitation record into a normal distribution	Can be computed for different time scales Symmetric for both dry and wet spells Related to probability	Requires long-term precipitation data No consideration of evaporation (i.e. it does not allow the comparison of similar SPI with different temperature scenarios)	Edwards & McKee 1997; McKee et al. 1993; Guttman 1999
	Reconnaissance Drought Index (RDI)	Fitting and transforming a long-term record of precipitation over potential evapotranspiration into a normal distribution	Considers both precipitation and evapotranspiration Can be computed for different time scales Directly comparable to the FAO aridity index	Requires long-term meteorological data Sensitive to the method to calculate potential evapotranspiration	Asadi Zarch et al. 2015; Tsakiris & Vangelis 2005; Tsakiris et al. 2006
	Standardized Precipitation Evapotranspiration Index (SPEI)	Fitting and transforming a long-term deficit record into a normal distribution	Considers both water supply (precipitation) and demand (potential evapotranspiration) Can be computed for different time scales	Requires long-term meteorological data Sensitive to the method to calculate potential evapotranspiration	Beguería et al., 2014; Vicente-Serrano et al., 2010
Agricultural drought indices	Palmer Drought Severity Index (PDSI)	Departure of moisture balance from normal condition, based on a 2-layer bucket-type water balance model	Uses soil data and a total water balance methodology	Seasonal issues (i.e. does not handle snow or frozen soils) Has an inherent timescale of approximatively nine months May require re-normalization	Alley 1984; Heddinghaus & Sabol 1991; Palmer 1965
	Soil Water Deficit Index (SWDI)	Comparison between actual soil water content, θ_{FC} and θ_{WP}	Can be determined by direct measuring or EO Implicitly accounts for precipitation and irrigation inputs	Assumes that the lag between meteorological and agricultural drought represents the response time for impact occurrence	Martínez-Fernández et al. 2015; Martínez-Fernández et al. 2016
	Integrated transpirative Deficit (TDx)	Cumulate difference between potential and actual transpiration	Has been developed and tested in northern Italy Accounts for soil crop water balance	Sensitive to the assumptions of the hydrological model, its spatio-temporal resolution and its calibration Does not account for irrigation inputs	Marletto & Zinoni 2004; Marletto et al. 2005
	pF anomalies	z-score of water potential derived from a hydrological model	Accounts for fully hydrological balance	Sensitive to the assumptions of the hydrological model, its spatio-temporal resolution and its calibration Does not account for irrigation inputs	Laguardia & Niemeyer 2008; Sepulcre-Canto et al. 2012
	Vegetation Condition Index (VCI)	Linearly scale of NDVI derived from remote sensing	Identifies drought impact on vegetation	Limited by cloudiness Short period of records	Kogan 1995
	Standardized Vegetation Index (SVI)	z-score of VI derived from remote sensing	Identifies drought impact on vegetation	Limited by cloudiness Short period of records	Horion et al. 2012; Peters et al. 2002
Combined drought index	Combined Drought Indicator	Combination of indices (SPI, pF, fAPAR)	Characterizes agricultural drought cause-effect relationship Good spatial coverage and high resolution	May not represent conditions that may carry over from season to season (i.e. uses only a single SPI value) Hard to replicate outside Europe	de Jager & Vogt 2015; Horion et al. 2012; Sepulcre-Canto et al. 2012

1.4.1 METEOROLOGICAL DROUGHT INDICES

The first generation of drought indices relied essentially on meteorological variables that were observed at synoptic meteorological stations; accordingly, these indices were classified as meteorological drought indices (Niemeyer 2008). The most commonly used indices of this type are the Standardized Precipitation Index (SPI; McKee et al., 1993), the Reconnaissance Drought Index (RDI; Tsakiris and Vangelis, 2005), and the Standardized Precipitation Evapotranspiration Index (SPEI; Vicente-Serrano et al., 2010).

1.4.1.1 Standardized Precipitation Index

The **Standardized Precipitation Index (SPI)**, developed by McKee et al. (1993), has been defined as a key indicator for monitoring drought by the World Meteorological Organization (2012) and has been widely applied (e.g. de Jager & Vogt 2015; Hunt et al. 2014; Kingston et al. 2015; Mishra et al. 2015; Spinoni et al. 2015; Spinoni et al. 2016) as an operational and analysis tool (Heim 2002; Lloyd-Hughes & Saunders 2002). Its calculation relies on the assumptions that the variability in precipitation is much higher than that of other variables that also affect drought severity, and that the other variables are stationary (i.e. they have no temporal trend; Vicente-Serrano et al. 2014).

The computation of SPI is based on an equiprobability transformation of the probability of observed precipitation to the standard normal variable. SPI is therefore expressed in units of the number of standard deviations from the long-term mean of the standard distribution, with negative (positive) values denoting drier (wetter) conditions that “expected” for the timescale and location (Edwards & McKee 1997; McKee et al. 1993; Singleton 2012). It is a simple indicator, spatially invariant in its interpretation, and probabilistic, so it can be used in risk and decision analysis (Guttman 1999).

Theoretically, the SPI can be computed over different accumulation periods, as short as a 1-week (Mishra et al. 2015; Wu et al. 2007), but it is usually calculated from monthly precipitation observations, and is typically expressed as $SPIn$, where n is the number of months of accumulation. Different SPIs allow the estimation of different potential impacts, from short-term water supplies (i.e. soil moisture) to long-term water resources (i.e. groundwater supplies, streamflow, lake and reservoir levels). The exact relationship between accumulation period and impact depends on the natural environment (e.g. geology, soils) and the human interference (e.g. existence of irrigation schemes; Horion et al. 2012; Mishra & Singh 2010).

The calculation requires a long-term precipitation database, ideally covering a continuous period of at least 30 years (Edwards & McKee 1997; McKee et al. 1993). Secondly, the length of the precipitation record has a significant impact on the SPI, in particular when the fitting distribution derived from the available database is not reliable on the long-term (i.e. the fitting distributions are different; Singleton 2012; Wu et al. 2007). Moreover, according to the definition, the SPI values are normally distributed over the long-term precipitation record (McKee et al. 1993). This is not the case for dry climates where null precipitation is common for a particular season: in fact, in these conditions the calculated SPI values (i.e. particularly at short time scales or in dry season) may not be normally distributed because of the highly skewed underlying precipitation distribution (Singleton 2012; Wu et al. 2007).

1.4.1.2 Reconnaissance Drought Index

The **Reconnaissance Drought Index (RDI)** has been developed by Tsakiris and Vangelis (2005) for regional drought severity assessment in South-Eastern-Europe (Tsakiris, Pangalou, et al. 2007; Tsakiris, Loukas, et al. 2007; Vangelis et al. 2011); in recent years, its use spreaded in European and global drought studies (e.g. Asadi Zarch et al. 2015; Shokoohi & Morovati 2015; Spinoni et al. 2015; Spinoni et al. 2016; Vicente-Serrano et al. 2015).

This index is calculated as the ratio of the precipitation ($P,\ mm$) over the potential evapotranspiration ($ET_0,\ mm$):

$$\alpha = \frac{P}{ET_0} \tag{1.1}$$

over a certain accumulation period at a specific location (Tsakiris & Vangelis 2005). It can be considered as an extension of the SPI (Niemeyer 2008) that can be more effectively associated with hydrological and agricultural drought (Tsakiris & Vangelis 2005). Moreover, the annual value of the index, calculated over the hydrological year (i.e. from October to September for the Mediterranean region) corresponds to the FAO Aridity Index (i.e. the annual ratio between precipitation and potential evapotranspiration; United Nations Environment Programme 1992) of the area (Tsakiris, Pangalou, et al. 2007).

The index can then be normalized (RDI_n), as

$$RDI_n(k) = \frac{a_k}{\bar{a}_k} - 1 \tag{1.2}$$

where a_k (adimensional) is the value of the index for the month k and $\bar{a}_k$ is the corresponding average value (Tsakiris & Vangelis 2005). Assuming that the RDI is fitted by a lognormal distribution, a Standardized RDI (RDI_{st}) can be derived as:

$$RDI_{st}(k) = \frac{y_k - \bar{y}_k}{\hat{\sigma}_k} \tag{1.3}$$

where $y_k = \ln a_k$, $\bar{y}_k$ is its arithmetic mean and $\hat{\sigma}_k$ is its standard deviation (Tsakiris & Vangelis 2005; Tsakiris, Pangalou, et al. 2007).

1.4.1.3 Standardized Precipitation Evapotranspiration Index

The **Standardized Precipitation Evapotranspiration Index (SPEI)** compares the highest possible evapotranspiration (i.e. the evaporative demand of the atmosphere, represented by the reference evapotranspiration ET_0) with the current water availability (Vicente-Serrano et al. 2010). The index has been developed and used for global studies (Beguería et al. 2014; Dai 2011; Spinoni et al. 2015; Spinoni et al. 2016; Vicente-Serrano et al. 2010; Vicente-Serrano et al. 2015), as well as for regional assessments (Scaini et al. 2015; Törnros & Menzel 2014; Vicente-Serrano et al. 2014).

The procedure for calculating the SPEI is similar to that of the SPI; however, the SPEI uses as input the deficit or “climatic water balance” (i.e. the difference between precipitation and reference evapotranspiration), rather than precipitation alone (Vicente-Serrano et al. 2010; Beguería et al. 2014). The deficit can be calculated at various time scales, and the resulting values are fit to a log-logistic probability distribution to transform the original values to standardized units that are comparable in space and time and at different SPEI time scales (Beguería et al. 2014; Vicente-Serrano et al. 2010).

1.4.2 AGRICULTURAL DROUGHT INDICES

The Palmer Drought Severity Index (PDSI; Palmer 1965) was the first real agricultural index proposed in the literature; it accounted for soil moisture and actual evapotranspiration. More recently, the Soil Moisture Deficit Index (SMDI) and the Evapotranspiration Deficit Index (ETDI) were proposed by Narasimhan and Srinivasan (2005). Further developments in the field of agricultural drought indices are represented by the Integrated Transpirative Deficit Index (DTx, Marletto & Zinoni 2004; Marletto et al. 2005) and the Soil Water Deficit Index (SWDI, Sanchez et al. 2012).

Most agricultural drought indices are calculated through hydrological models, therefore their results are not only affected by data accuracy and reliability, but also by the assumptions embedded in the physical scheme conceptualization. In particular, the main limitations are connected to the soil water balance model formalization, its parametrization (e.g. soil characteristics, land use data, meteorological data, interpolation methods adopted), its spatial and temporal resolution (Van der Knijff & De Roo 2008; Van Der Knijff et al. 2010) and its calibration. In fact, models could produce in some case large approximation of the real soil moisture, that diverges from the real conditions (Horion et al. 2012).

1.4.2.1 Palmer Drought Severity Index

Palmer (1965) formulated the **Palmer Drought Severity Index (PDSI)**, using precipitation and temperature to estimate moisture supply and potential evapotraspirative demand within a two-layer soil model. The index is measured only from the begin of a dry (or wet) event, thus the PDSI cannot be used for real-time monitoring. For operational purposes, a real time version of PDSI, called modified PDSI, was introduced by Heddinghaus and Sabol (1991). In their version, the separate indices for dry and wet periods are combined by dynamically weighting their occurrence probabilities. Wells et al. (2004) introduced a Self-Calibrating PDSI (SC-PDSI) to account for precipitation variability between locations, to allow for more accurate comparisons between different climatic zones. This is achieved recursively calibrating two parameters that affect the range of the PDSI values and the sensitivity of the index at each location, the climatic characteristic K and the duration factors p and q.

The PDSI uses both precipitation and evaporative demand of the atmosphere as the main inputs for calculation, and is sensitive to variations in both terms. In fact, Hu and Willson (2000) assessed the effect of precipitation and temperature on the PDSI, and found that the index responded equally to changes of similar magnitude in each variable.

The index is calculated by carrying out a hydrological balance on a monthly basis for a long-term database (i.e. over 30 or more years), to obtain coefficients that are dependent upon the climate of the area being analysed. The data series are then reanalysed using the derived coefficients to determine the amount of moisture required for normal weather during each month, calculated as:

$$\hat{P} = \alpha_j PE + \beta_j PR + \gamma_j PRO - \delta_j PL \tag{1.4}$$

where PE (mm) is the potential evapotranspiration, PR (mm) is potential recharge, PRO (mm) is potential runoff, and PL (mm) is potential loss (i.e. the amount of soil moisture that can be lost by evapotranspiration during a zero precipitation period; Alley 1984). The coefficients are ratios of long-term mean quantities: α_j, evapotranspiration to potential evapotranspiration, β_j, recharge to potential recharge; γ_j, runoff to potential runoff; and δ_j, loss to potential loss. The monthly moisture anomaly, calculated as the difference between the observed precipitation in the month and $\hat{P}$, is then multiplied by a climate weighting factor K designed to account for variations in climate at different sites, and the product is the moisture anomaly index Z. The Palmer Drought Index PDSI for month t is then calculated as:

$$PDSI_t = p \cdot PDSI_{t-1} + q \cdot Z_t \tag{1.5}$$

where $p = 0.897$ and $q = 0.333$ are the duration factors, that were calibrated using the linear relationship of extreme droughts severity ($\sum Z_i$) against their duration (Palmer 1965; Wells et al. 2004).

The PDSI is in that way "standardized", facilitating the quantitative comparison of drought incidence at different locations and different times. However, the empirical relationships used to define the index (in particular K, the climate weighting factor) were determined by observations in the USA and are not applicable to other region, significantly limiting the general applicability of the scaling process (Heim 2002; Lloyd-Hughes & Saunders 2002). Guttman (1998) and Vicente-Serrano et al. (2010) showed that the spectral characteristics of the PDSI varied from site to site, and the PDSI represents water deficits at different time scales, depending on the region under consideration.

The PDSI is, by definition (equation 1.5), a first order autoregressive process; the inherent memory of the PDSI is however on the order of years, resulting from the nature of the water balance accounting approach upon which the index is based (Guttman 1998). Moreover, it is assumed that all precipitation is rain, thus PDSI values during winter months and at high elevation are questionable (Hayes et al. 1999; Mishra & Singh 2010).

Despite its limitations, the PDSI is still commonly used, especially in the USA (e.g. Choi et al. 2013; Rohli et al. 2016) but also for global assessments (e.g. Dai 2011; Trenberth et al. 2014).

1.4.2.2 Indices based on soil moisture deficit

In the last years, many different indices have been developed to assess agricultural drought, whether from soil moisture measurements (e.g. Martínez-Fernández et al., 2015) or from spatially distributed hydrologic models (e.g. Marletto et al. 2005; Narasimhan & Srinivasan 2005; Sepulcre-Canto et al. 2012). The authors have developed different approaches to remove soil and seasonal variability and to allow comparisons.

Martínez-Fernández et al. (2015) assume that the soil moisture deficit has to be compared to the total available soil water content to characterize an agricultural drought; the **Soil Water Deficit Index (SWDI)** is then defined as:

$$SWDI = \frac{\theta - \theta_{FC}}{\theta_{FC} - \theta_{WP}} \cdot 10 \tag{1.6}$$

where θ (adimensional) is the actual soil water content, and θ_{FC} and θ_{WP} are respectively the soil water content at field capacity and at wilting point. Positive values of SWDI mean that the soils have excess of water, while negative values indicate agricultural drought, and the wilting point is reached when $SWDI \leq -10$. Although the index was developed considering a monitoring network of *in situ* soil moisture content (Martínez-Fernández et al. 2015), it has recently been computed and validated by applying linear regression analysis of soil moisture series and EO data (Martínez-Fernández et al. 2016).

The **integrated transpirative deficit** ($\boldsymbol{TDx}$; Marletto & Zinoni 2004; Marletto et al. 2005) is calculated summing over an accumulation period of x days the transpirative deficit (i.e. the difference between potential and actual transpiration), and expressing the results as percentiles of the historical climatological record. The TDx is computed using a hydrological model, and its use was limited to the assessment of agricultural drought in the Emilia Romagna Region by simulating a reference crop (i.e. permanent grass), without considering irrigation inputs.

The European Drought Observatory (EDO; http://edo.jrc.ec.europa.eu) expresses the soil moisture content in term of water potential (pF) values (i.e. the logarithm of the capillary suction head, h, expressed in cm; Horion et al. 2012; Sepulcre-Canto et al. 2012). The soil suction provides an assessment of the plants difficulty to extract water from the soil matrix, and its evaluation, calculated by means of the Van Genuchten pedotransfer function, considers soil characteristics (i.e. it depends on the saturation and residual water content of the soil; Laguardia & Niemeyer 2008). The **anomalies of soil water content** are then calculated as a z-score:

$$pF_z = \frac{pF_t - \overline{pF}}{\sigma} \tag{1.7}$$

where pF_t is the mean of the logarithm of the water potential for the considered 10-days period t, and $\overline{pF}$ and σ are respectively the long-term mean and standard deviation for the same 10-days period over the available time series. By normalizing the soil moisture with the z-score, the results are expressed in standard deviation units, and can be compared directly to the SPI (Sepulcre-Canto et al. 2012).

The EDO updates the index every day over Europe, and distributes a projection of the anomalies for the consecutive week based on meteorology forecast (European Drought Observatory 2016).

1.4.2.3 Remote sensing vegetation indices

Remote sensing vegetation indices (VIs), based on the radiometric properties of the canopies, allow the detection of the impact of the drought on vegetation, with largest values attributable to healthy and dense vegetation (Heim 2002; F.N. Kogan 1995). However, they are primarily useful during the growing season, and their utility is limited during vegetation dormancy (Heim 2002).

The most used vegetation indices in drought monitoring are the **Normalized Difference Vegetation Index** (**NDVI**; Tucker 1979; Tucker & Choudhury 1987), defined as

$$NDVI = \frac{\rho_{NIR} - \rho_{RED}}{\rho_{NIR} + \rho_{RED}} \tag{1.8}$$

where ρ_{NIR} and ρ_{RED} are respectively the apparent reflectance in the near-infrared and in the red bands; the **Normalized Difference Water Index** (**NDWI**; Gao, 1996), that takes into account the apparent reflectances in the near-infrared and in the shortwave infrared:

$$NDWI = \frac{\rho_{NIR} - \rho_{SWIR}}{\rho_{NIR} + \rho_{SWIR}} \tag{1.9}$$

where ρ_{NIR} and ρ_{SWIR} are respectively the apparent reflectance in the near-infrared an the shortwave-infrared bands, and the **fraction of Absorbed Photosynthetically Active Radiation** (**fAPAR**, Gobron et al., 2004a, 2004b; Vanneuville et al., 2012), that is calculated by numerically inverting physically-based models describing the solar radiation transfer in plant canopies using the reflectance in the read and near-infrared bands:

$$fAPAR = \frac{l_{0,1} \cdot \rho_{R_{NIR}} - l_{0,2} \cdot \rho_{R_{RED}} - l_{0,3}}{\left(l_{0,4} - \rho_{R_{RED}}\right)^2 + \left(l_{0,5} - \rho_{R_{NIR}}\right)^2 + l_{0,6}} \tag{1.10}$$

where $\rho_{R_{NIR}}$ and $\rho_{R_{RED}}$ are respectively the rectified reflectance in the near-infrared and in the red bands and the $l_{0,m}$ are calibrated sensor-specific coefficients.

After the acquisition, the time-series of VIs data are always preprocessed to remove contamination (i.e. clouds). The obtained value can then be scaled into an index that varies between zero and 100, accounting for the interannual variability of every pixel:

$$VI_{scaled} = 100 \cdot \frac{VI - VI_{min}}{VI_{max} - VI_{min}} \tag{1.11}$$

where VI is the calculated vegetation index, and VI_{max} and VI_{min} are respectively the multi-year absolute maximum and minimum for the selected cell and time step (F.N. Kogan 1995). The derived index considers only the weather component (i.e. the short-term VI fluctuations), as this standardization removes the ecosystem component (i.e. the inter-annual changes; Kogan 1995b).

This approach has been applied by Kogan (1995a; 1995b) to the NDVI, and the scaled index derived from equation 1.11 is called **Vegetation Condition Index (VCI)**. Initially the index was calculated by using of Advanced Very High Resolution Radiometer (AVHRR) data (F.N. Kogan 1995; Felix N. Kogan 1995; Kogan 1997), but more recently in further studies it was computed using MOderate Resolution Imaging Spectroradiometer (MODIS; National Aeronautics and Space & Administration 2016), Landsat (United States Geological Survey 2016) and Copernicus (Copernicus 2016) data.

A second approach proposed in the literature implies the standardization of the vegetation index, that is therefore expressed as a z-score:

$$VI_z = \frac{VI_{ijk} - \overline{VI}_{ij}}{\sigma_{ij}} \tag{1.12}$$

where VI_z is the z-value for pixel i during time step j for year k, VI_{ijk} is the VI value for time step j for year k, and $\overline{VI}_{ij}$ and σ_{ij} are respectively the mean and the standard deviation for pixel i during time step j over the historical series (Horion et al. 2012; Peters et al. 2002). This method was applied to the NDVI, obtaining the **Standardized Vegetation Index** (**SVI**; Peters et al., 2002), to the NDWI (NDWI anomalies; Horion et al., 2012) and to the fAPAR (fAPAR anomalies; European Drought Observatory 2016; Horion et al. 2012).

1.4.3 THE COMBINED DROUGHT INDICATOR OF THE EUROPEAN DROUGHT OBSERVATORY

The European Drought Observatory (EDO; http://edo.jrc.ec.europa.eu) produces and publishes on its web-site five different drought monitoring products: the Standardized Precipitation Index (SPI), the soil moisture anomaly expressed as soil suction value (pF), the Normalized Difference Water Index anomaly, the fraction of Absorbed Photosynthetically Active Radiation anomaly and the **Combined Drought Indicator** (**CDI**; Horion et al., 2012).

The CDI was developed as an early warning system for agricultural drought, identifying three different indices that express every step of the cause-effect relationship between meteorological drought and agricultural impacts (Figure 1-2); this relationship assumes that a shortage of precipitation leads to a soil moisture deficit, that results in a reduction of vegetation production (Sepulcre-Canto et al. 2012).

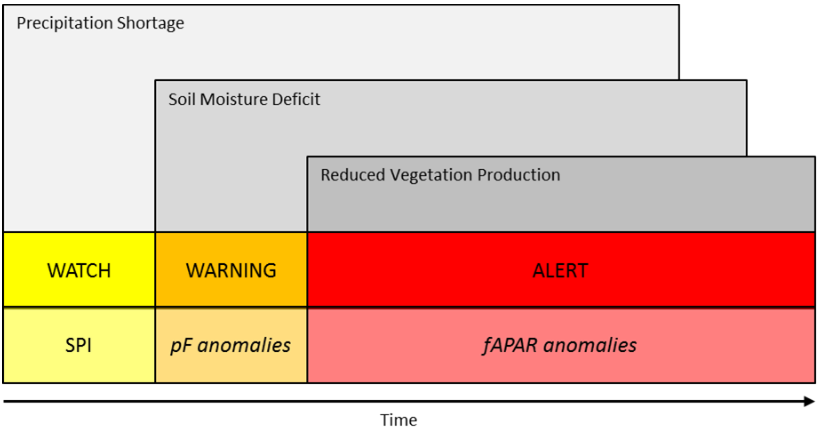

Figure 1-2: Representation of the stages of the idealized agricultural drought cause-effect relationship (modified after Sepulcre-Canto et al., 2012).

Table 1-3: Categories of the Combined Drought Indicator. The operator ∧ means that both conditions have to be satisfied, while the operator ∨ means that it is sufficient that one is true. Source: European Drought Observatory (2016); Sepulcre-Canto et al. (2012).

Category	Characteristics	Definition
Watch	Precipitation deficit	$\boldsymbol{SPI\text{-}3 < -1 \quad \vee SPI\text{-}1 < -2}$
Warning	Soil moisture deficit	$\boldsymbol{pF_z > 1 \quad \wedge (SPI\text{-}3 < -1 \quad \vee SPI\text{-}1 < -2)}$
Alert	Vegetation stress following precipitation deficit	$\boldsymbol{fAPAR_z < -1 \wedge (SPI\text{-}3 < -1 \quad \vee SPI\text{-}1 < -2)}$
	Vegetation stress following precipitation/soil moisture deficit	$\boldsymbol{fAPAR_z < -1 \wedge pF_z > 1 \wedge (SPI\text{-}3 < -1 \quad \vee SPI\text{-}1 < -2)}$

To characterize the different stages of the relationship, three different warning levels are selected (Table 1-3):

1. Watch, where precipitation is less than normal and there is an increased likelihood that there will be an agricultural drought: in this stage, the assessment relies on the $SPI1$ and on the $SPI3$ (i.e. SPI calculated over 1 and 3 months);
2. Warning, in which the precipitation deficit leads to a soil moisture deficit, increasing the possibility of effects on agricultural production: in this stage, also pF anomalies (pF_z) differ from the mean values by more than one standard deviation;
3. Alert, while vegetation shows signs of stress and drought has begun to affect agriculture: in this final stage, fAPAR anomalies ($fAPAR_z$) decrease below -1 (de Jager & Vogt 2015; Horion et al. 2012).

The EDO database covers the whole Europe, with datasets of indicators having different spatial resolution and time series length. In particular, the SPI was calculated from 1973 at the meteorological station sites, and was interpolated to a $0.25°$ squared grid starting from 1981, using 1981-2010 as a reference period to elaborate parameters distributions. Soil moisture data of the topsoil, expressed in terms of pF values and averaged over 10-days period, were calculated from 1990, with $5\ km$ spatial resolution. fAPAR and fAPAR anomalies maps are available from 2002 on $1\ km^2$ grid. Finally, CDI is computed every 10 days from 2012, with $1/24°$ spatial resolution (European Drought Observatory 2016).

1.5 DROUGHT AND WATER SCARCITY IN NORTHERN ITALY

The Mediterranean is widely considered as the most vulnerable European region to climate change (Giorgi & Lionello 2008; Spinoni et al. 2016) and water scarcity (e.g. Blinda et al. 2007; Spinoni et al. 2016). In this context, drought is considered to be one of the most relevant natural disasters (International Panel on Climate Change 2014), and it is generally forecasted that the situation will worsen in the coming decades, with southern Europe as a hotspot for drought (Forzieri et al. 2014; Sheffield & Wood 2008). Although many drought studies (e.g. Blinda et al. 2007; Hoerling et al. 2012; Lloyd-Hughes & Saunders 2002; Sheffield & Wood 2008; Spinoni et al. 2015; Spinoni et al. 2016; Törnros & Menzel 2014) focused on drought characterization over Europe or over the Mediterranean area, their spatial scale is mostly not sufficient to achieve detailed information over northern Italy.

Analysing the linear trend of meteorological variables on national scale over Europe for the last fifty years (i.e. 1951-2012), the European Commission's Joint Research Centre (JRC), in a recent study (Spinoni et al. 2016) observed a significant increase of the mean temperature of Italy ($+0.24\ °C \cdot decade^{-1}$), and a corresponding reduction in precipitation ($-5.1\ mm \cdot decade^{-1}$). By considering the derived meteorological drought indices, Spinoni et al. (2016) proved that these trends led in the recent past (i.e. 1981-2010) the south-western European countries to an increase in drought frequency ($+0.05\ \ events \cdot decade^{-1}$), severity ($+5.85\ score \cdot decade^{-1}$), duration ($+3.9\ \ month \cdot event^{-1} \cdot decade^{-1}$) and of the total areas under drought conditions ($+4.2\% \cdot decade^{-1}$). These findings confirmed that southern Europe faced, from the 1950s to 2010s, a drying tendency (Hoerling et al. 2012; Spinoni et al. 2014).

The International Panel on Climate Change (IPPC) scenarios (International Panel on Climate Change 2000), that describe greenhouse gases emissions on the basis of future socio-economic trends, are generally used to derive climate change projections and to estimate their impacts. Reviewing the available forecasts of meteorological variables over the Mediterranean region, derived from an ensemble of the IPCC scenarios, Giorgi and Lionello (2008) proved that the temperature and precipitation trends are very likely expected to continue. By 2071-2100 it is forecasted in the Alps region a temperature rise of $2.6 \div 5.0°C$ in winter and of $3.9 \div 8.4°C$ in summer, while precipitation will decrease ($-0.08 \div 1.16\, mm \cdot d^{-1}$ in winter, $-0.18 \div -1.81\, mm \cdot d^{-1}$ in summer; Giorgi & Lionello (2008).

Spinoni et al. (2016) forecasted the impacts on European droughts only using the A1b scenario (International Panel on Climate Change 2000), selected because it reflects the estimated global change of the recent past (i.e. 1981-2010). The A1b scenario is characterized by a future world of rapid economic growth, with a population peak in the 2050s, and the rapid introduction of more efficient technologies, balanced between all energy supply sources and end-use technologies (International Panel on Climate Change 2000). According to this study, drought events are estimated to be more frequent in the near (2041-2070) and in the far (2071-2100) future than in the recent past, in general in southern Europe, and in particular in the Mediterranean region. The main driver of this increase in drought frequency for the area is correlated to the rise in temperature, which in turns takes to an increase in potential evapotranspiration: Spinoni et al. (2016) highlight this aspect by comparing the $SPI12$ simulation results to the $SPEI12$, that focuses on the relationship between precipitation and evapotranspiration (Vicente-Serrano et al. 2010). In the prediction, the patterns of drought events severity and of their duration are found to be spatially related, since increases in drought severity are predicted to occur in the same areas that will be affected by longer drought spells (European Environment Agency 2008; Sillmann & Roeckner 2008; Spinoni et al. 2016). The areas affected by increased drought severity, in particular, seem to correspond to the areas with more consistent precipitation reduction in the near future, and with higher temperature increase in the far future (Spinoni et al. 2016).

To describe the cause-effect relationship between meteorological drought and its impact on agriculture and hydrology (Figure 1-1), it is necessary to focus on water availability and abstractions. Water is relatively abundant across Europe; in fact, total freshwater resource amounts to $2\ 270\ km^3 \cdot y^{-1}$, of which only 13% (around $288\ km^3 \cdot y^{-1}$) is currently abstracted. These figure suggest that, when considering the European scale, the water available is sufficient to meet demand (Collins et al. 2009). With abstractions of about $105\ km^3 \cdot y^{-1}$ (Blinda et al. 2007), agriculture accounts for about 37% of the total water abstraction in Europe, mostly used for irrigation; thus, agriculture is a key sector for future water management, in particular in areas where irrigation is used to compensate for drought impacts.

The global dataset related to “areas equipped for irrigation” (Figure 1-3a), elaborated by the Food and Agriculture Organization of the United Nations (Döll & Siebert 2002; Siebert et al. 2013), shows that the European irrigated agricultural land is broadly concentrated in southern Europe (i.e. southern Romania, northern Italy, Spain, Greece, Turkey). In 2010, the area equipped for irrigation in Italy was equal to $37\ 500\ km^2$ (i.e. 21% of total agricultural land; Collins et al. 2009; Istituto Nazionale di

Statistica 2010), and $24\ \ 200\ \ km^2$ (i.e. 64.5% of the area equipped for irrigation) were actually irrigated (Istituto Nazionale di Statistica 2010). The area equipped for irrigation is unequally distributed over the national territory, since more than 55% is located in the Po River basin (i.e. Lombardy, Emilia-Romagna, Piedmont and Veneto). In Lombardy, in particular, the irrigated agricultural land is equal to $5\ \ 800\ \ km^2$ (i.e. 83.9% of the area equipped for irrigation is actually irrigated; Istituto Nazionale di Statistica 2010; Istituto Nazionale di Statistica 2014).

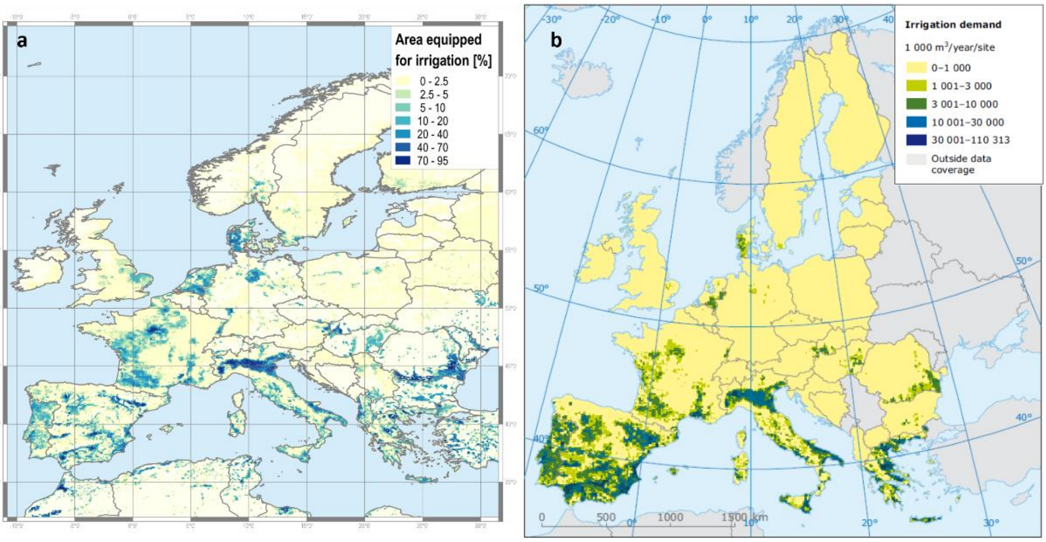

Figure 1-3: Irrigation intensity in Europe. a) Area equipped for irrigation in Europe, by 5' cell, derived from the Global Map of Irrigated Areas. Data source: Siebert et al. (2013). b) Average irrigation demand on a $10 \times 10\ \ km$ grid in the European Union and Switzerland ($1\ \ 000\ \ m^3 \cdot y^{-1} \cdot pixel^{-1}$) over the simulation period 1995-2002 Source: Wriedt, van der Velde, et al. (2009).

The JRC (Wriedt et al. 2009a; Wriedt et al. 2009b) estimated the average irrigation water demand in the European Union and Switzerland over the simulation period 1995-2002 (Figure 1-3b) by combining the information about the area equipped for irrigation with a spatially distributed implementation of the soil water and crop growth model EPIC (Environmental Policy Integrated Climate model; Bouraoui & Aloe 2007; Williams 1995). The algorithm not only considered net irrigation requirements, but also additional water abstraction needs to compensate for losses into the irrigation network, to prevent salinization and to take into account the water user efficiency of the different irrigation methods. In the Po River Plain the irrigation demand was estimated to fall between $1\ \ 000$ and $3\ \ 000\ \ m^3 \cdot y^{-1} \cdot ha^{-1}$. As a matter of fact, the national census of agriculture (Istituto Nazionale di Statistica 2010; Istituto Nazionale di Statistica 2014) reports that the actual abstraction rates are considerably higher with respect to this value. In Lombardy, abstractions are reported to be on average $8\ \ 000 m^3 \cdot ha^{-1}$, probably due to inefficiencies (water losses) of irrigation systems supplying crops with water (Collins et al. 2009; Istituto Nazionale di Statistica 2010; Istituto Nazionale di Statistica 2014), but also to approximation both in the JRC modelling formulation and parameters, and in the ISTAT estimation of abstraction volumes.

According to different studies (e.g. Milly et al. 2005; Dankers & Feyen 2008) investigating the trends in water availability derived from IPCC scenarios (International Panel on Climate Change 2000), annual river flows are projected to decrease in most European river basins, as well as their seasonal patterns are expected to change, with an increasing in winter and spring and a decreasing in summer and autumn river discharges. Although changes in average water availability in most European river basins would be relatively small by 2030 (Figure 1-4b), this is not the case for some basins in the Mediterranean region, which often already face water stress conditions. For these areas, the projection indicates a decrease in the annual water availability of 10% or more (Figure 1-4b) with respect to year 2000 (Figure 1-4a). These phenomena, accompanied by an increased water abstraction in irrigated areas caused by higher crop evapotranspiration rates, will change the frequency and intensity of agricultural droughts, particularly in southern and central Europe (Isoard & Henrichs 2005).

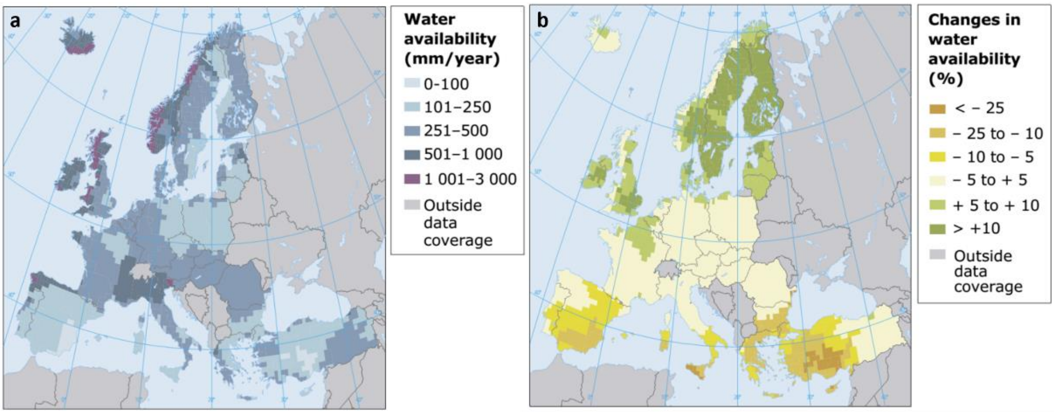

Figure 1-4: Average annual water availability in European river basins. a) 2000 water availability. b) Changes in average annual water availability by 2030 (Isoard & Henrichs 2005)**.**

2 STUDY SITE AND AVAILABLE DATA

2.1 STUDY AREA

The study area selected for the Ph.D. research activity is the Irrigation District of Media Pianura Bergamasca (IDMPB; Figure 2-1). It is located in the northern portion of the Po River basin (Bergamo Province, Lombardy). It covers an area of $209.48\ \ km^2$ and its elevation ranges from about $90\ \ m$ up to $300\ \ m\ \ a.s.l.$ Following the opinion of the Irrigation Consortium managing water within the IDMPB, the territory is characterized by water abundant as well as by water scarce sub-districts. One of the water scarce areas, located in the northern part of the IDMPB, extending for $63.95\ \ km^2$ and composed by 32 sub-districts (Figure 2-1 c), was selected for the assessment of the TDI when used as a water scarcity indicator (named “Pilot area” in Figure 2-1c).

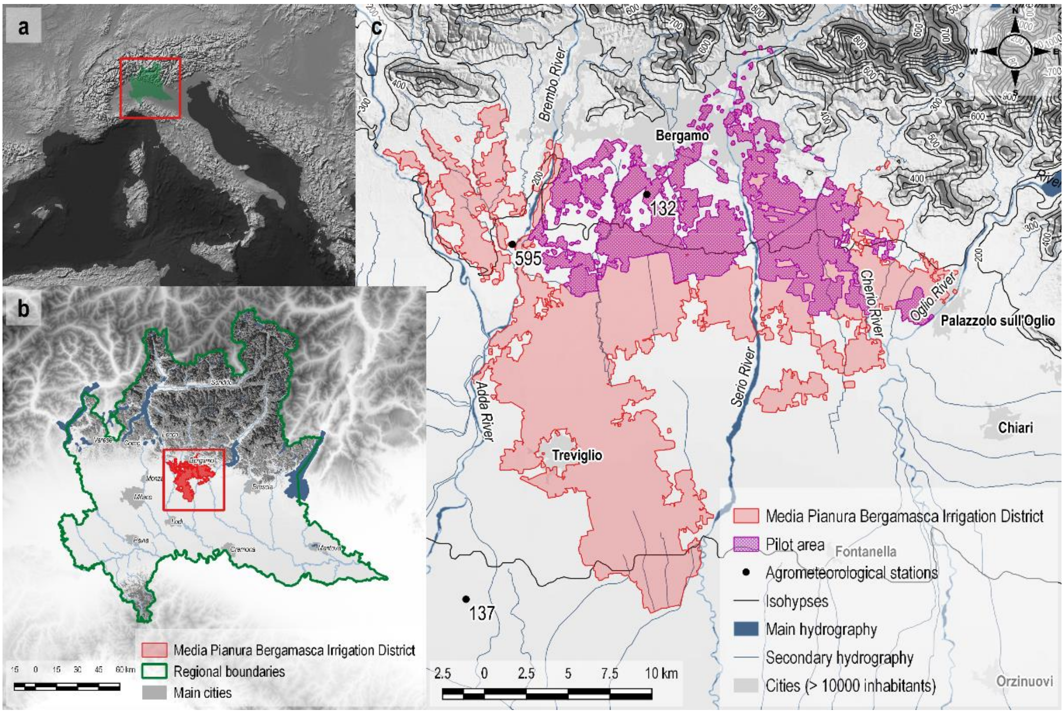

Figure 2-1: Overview of the Media Pianura Bergamasca Irrigation District (IDMPB): (a) Lombardy region (in green) location; (b) IDMPB location (in red) within the Lombardy region; (c) IDMPB (in red) and Pilot area (dotted area, in violet). Agro-meteorological stations are labelled by using their identification number.

2.2 AGRO-METEOROLOGICAL DATA

Agro-meteorological data for the Lombardy plain were obtained from the agro-meteorological stations managed by ARPA-Lombardia (Regional Authority for the Environmental Protection in Lombardy), after a selection based on the data series quality and aimed at achieving a homogeneous coverage of the Lombardy plain area (Rienzner 2009). In Figure 2-1 only the agro-meteorological stations located inside or very close to the IDMPB are reported.

For each agro-meteorological station, hourly data of precipitation, temperature, relative humidity, solar radiation and wind speed for the period 1993-2014 were collected. A quality control of raw data was performed on each series, considering the plausibility of each value (i.e. whether they were within acceptable range limits), the plausibility rate of change (i.e. the absence of unrealistic jumps or steady states in values), the internal consistency (i.e. based on the relation between two parameters) and the system consistency (i.e. based on the comparison with the nearest station). The checked data series were then homogenized by finding and adjusting non-climatic abrupt changes in the series (change-point detection and homogenization procedure, MAC-D method; Rienzner & Gandolfi 2013). Finally, the series were imputed transversally (i.e. using information of neighbouring stations) by a multiple linear regression (repeated for each season, best regressors set chosen with adjusted R^2).

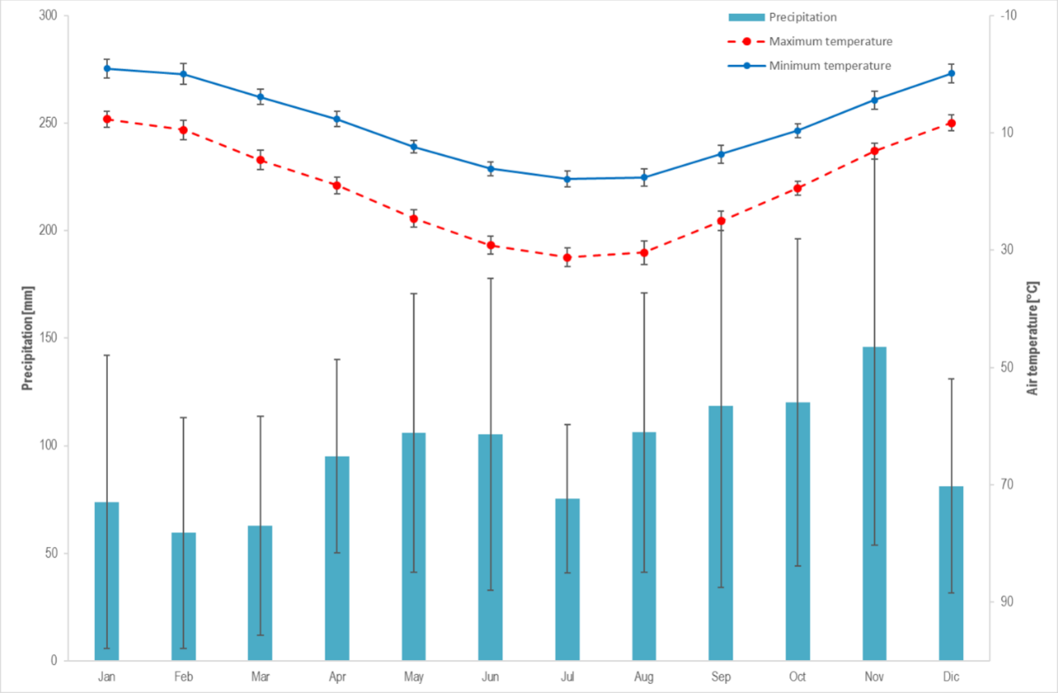

Figure 2-2: Averages and standard deviations of monthly values for the main climatic variables at the Stezzano agro-meteorological station (identification number 132) over 22 years, from 1993 to 2014. For rain monthly total amounts are reported, while for temperatures monthly averages are shown.

The spatial interpolation of the agro-meteorological data was based upon the inverse-square distance weighting (IDW), computed using the three nearest stations; thus the value of a generic meteorological variable z at a point was calculated as:

$$z_{x,y} = \frac{\sum_{i=1}^{3} z_i d_{x,j,i}^{-2}}{\sum_{i=1}^{3} d_{x,j,i}^{-2}} \tag{2.1}$$

where $z_{x,y}$ is the value of the variable at the point to be estimated (x, y), z_i is the value of the observed variable at the meteorological station i, and $d_{x,j,i}$ is the distance between (x, y) and i (Bartier & Keller 1996).

In Figure 2-2 the monthly mean temperature and precipitation for the period 1993-2014 at the Stezzano agro-meteorological station, which is the more representative for the study area, are reported. Annual mean temperature measured at this station is found to be $13.94 \pm 0.49°C$, with maxima in July ($24.52 \pm 1.46°C$) and minima in January ($3.34 \pm 1.38°C$). Annual mean precipitation is $1150.35 \pm 273.74 \quad mm$, with a maxima in autumn (November mean precipitation is $145.94 \pm 90.10\, mm$), and two minima, one in spring (February mean precipitation is $59.49 \pm 52.44\, mm$) and one in summer (July precipitation is $75.30 \pm 33.69 \quad mm$). As it can be inferred from these data, the precipitation has a marked variability from year to year.

2.3 LAND USE DATA

Land use data were provided every year from the Agricultural Information System of the Lombardy Region (SIARL, 2004-2014; ERSAF 2012; Lombardy Regional Authority 2016), that collects annual applications of farmers for the Community Agricultural Policy (CAP) contributions. In particular, data declared from farmers are linked to corresponding parcels within a digital cadastre map that can be visualized into a GIS. The resulting vectorial land use map is than rasterized using a $20 \quad m$ squared grid basis; the final raster is characterized by 21 land uses classes (Lombardy Regional Authority 2016). Figure 2-3 represents the portion of the regional land use map that convers IDMPB for the year 2014.

An analysis of the land use dataset (Table 2-1), that spans from 2004 to 2014, was conducted considering only the agricultural areas identified by the Irrigation District Consortium (i.e. urban areas where excluded), as shown in Figure 2-1. Maize is the dominant crop of the area, covering between 28% (in 2010) and 39% (in 2004) of the agricultural land. Forage crops (e.g. alfalfa, clover, permanent grass, meadow) cover between 27% (in 2011) and 35% (in 2009) of the total agricultural land, being the second land use class over the area in term of abundancy. The remaining crops are less significant, with other cereals (e.g. winter wheat, rye, barley, oat) covering $6 - 13\%$ of the area depending on the year.

In the irrigation district, both maize and forage crops are usually irrigated, while the other cereals, mainly winter crops, are never irrigated.

2.4 SOIL CHARACTERISTICS

According to the soil map $1:250 \quad 000$ of the Lombardy region (ERSAF 2008; Lombardy Regional Authority 2016), the study area can be divided into 23 cartographical units, that are described in terms of texture, hydrological group, drainage and permeability. Information about the soil profiles representative for each cartographic unit are also available (ERSAF 2008).

Table 2-1: IDMPB Land cover. Main agricultural crops coverage (ha) in the study area for the period 2004-2014. Data source: Lombardy Regional Authority (2016).

	Year										
	2004	2005	2006	2007	2008	2009	2010	2011	2012	2013	2014
Maize	439 882	398 923	355 727	378 194	390 356	366 166	331 988	359 599	375 870	367 435	374 334
Forage crops	311 263	308 475	331 883	407 749	379 048	427 984	327 786	321 594	331 433	337 031	344 368
Other cereals	111 856	111 144	102 697	135 240	155 003	136 777	102 803	73 305	87 617	99 178	88 139
Other agricultural land use	263 140	301 832	341 303	304 517	267 496	282 446	436 783	443 228	410 263	395 844	399 133

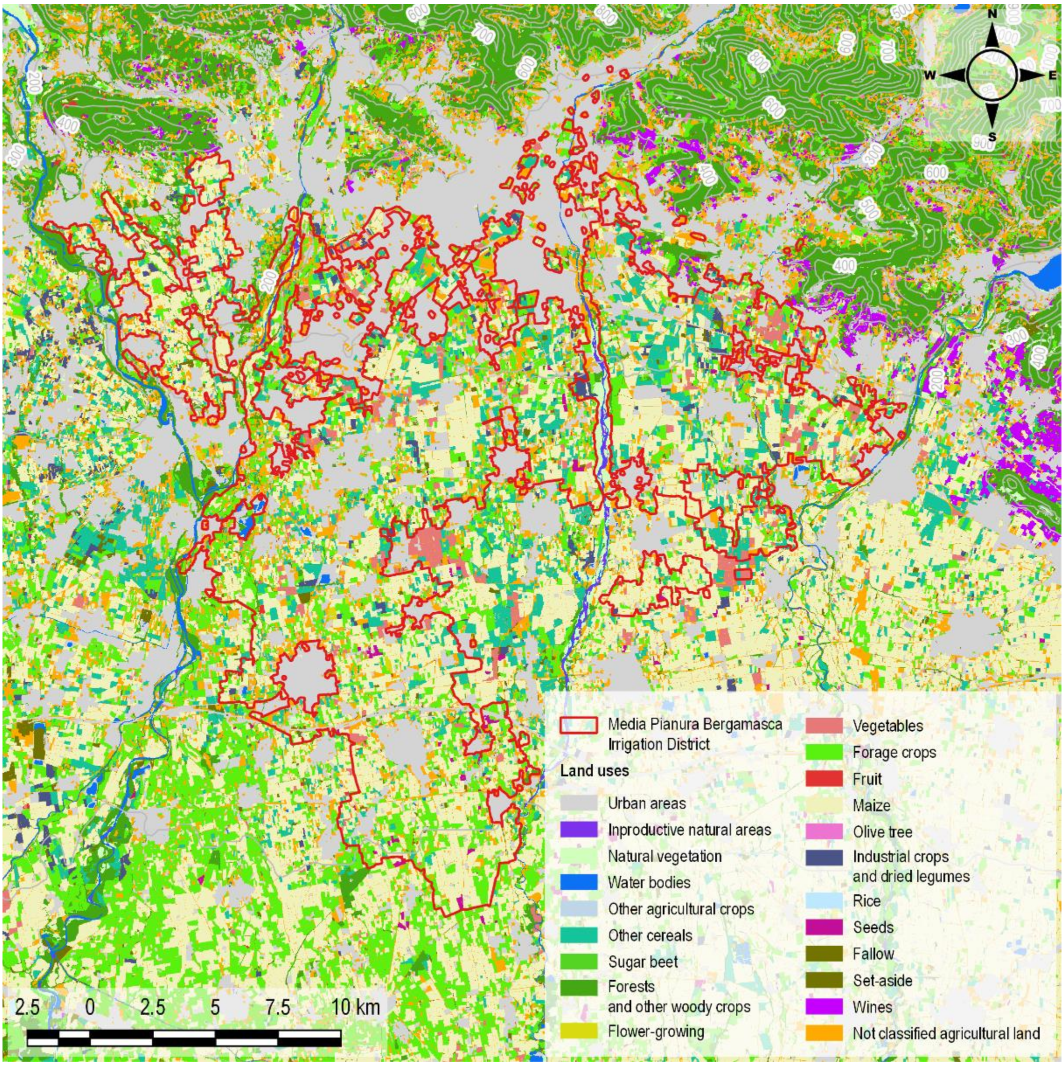

Figure 2-3: Land use classification over the Media Pianura Bergamasca Irrigation District for the year 2014 (modified after ERSAF 2012; Lombardy Regional Authority 2016).

Soil hydraulic parameters were derived from the physico-chemical description (% clay, % silt, % sand, % skeleton, % organic carbon) of the horizons of representative soil profiles by applying the Rawls & Brakensiek (1989) pedo-transfer functions (PTFs). In particular, soil hydraulic parameters obtained for the soil horizons of each reference soil profile through PTFs were depth-weighted to derive the soil hydraulic parameters used as inputs for the hydrological model IdrAgra (§ 3.3.3), one set for the evaporative layer (i.e. the first $0.15\ m$ of the soil profile) and one set for the transpirative layer (i.e. between $0.15\ m$ and $1\ m$; Gandolfi et al. 2006).

The study area is mainly characterized by sandy loam soils (Figure 2-4a), with coarser (i.e. loamy sand) soils over the more recent alluvial areas close to water bodies, and finer (i.e. loam) soils in the areas characterizing the fundamental level of the plain. This is reflected in all the hydraulic parameters characterizing the soils, for instance the available water content (AWC_T; Allen et al. 1998), which shows (Figure 2-4b) lower values (i.e. 0.045) near the Serio River banks, while reaches higher values (i.e. 0.165) in the areas south-west of Bergamo.

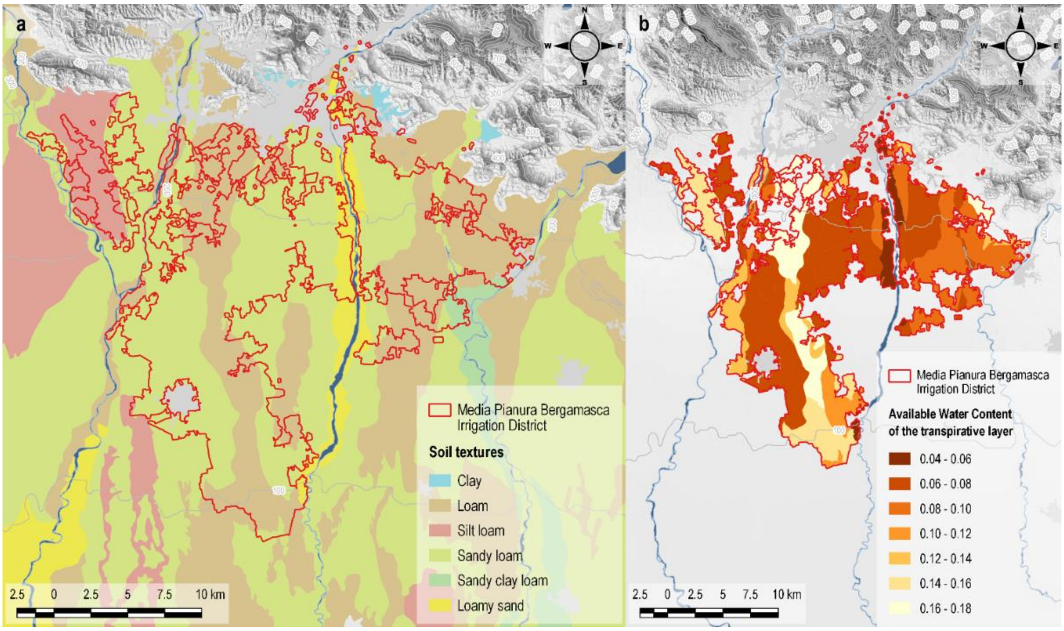

Figure 2-4: Soil map of the Media Pianura Bergamasca Irrigation District. (a) Soil texture classification. Sources: ERSAF (2008), Lombardy Regional Authority (2016). (b) Available Water Content, AWC_T ($m^3 m^{-3}$) (Allen et al. 1998) calculated for the transpirative layer (i.e. between $0.15\ m$ and $1\ m$) of the IdrAgra model (Facchi et al. 2004; Vassena et al. 2012; Gandolfi et al. 2014).

2.5 WATER AVAILABILITY FOR IRRIGATION FROM SURFACE SOURCES

The principal water courses within the study area are the Brembo, Cherio and Serio rivers. An extensive network of channels takes water from these main rivers, and provides it to the agricultural area.

From the middle of May to the middle of September water is diverted from rivers (about $10\, m^3 \cdot s^{-1}$ from the Brembo and Serio rivers, and $1\ m^3 \cdot s^{-1}$ from the Cherio river) at the diversion sites shown in Figure 2-5 (green squares). The diverted water is conveyed through 8 main (primary) canals and it is delivered to an extensive secondary network of around 740 canals. The last canals characterized by a continuous discharge (distribution canals) provide water to the single farms, on the basis of fixed turns (from 8 to 9 days on average over the district). The canals are mostly unlined and irrigation is mainly performed by gravitational methods with very low efficiency. Therefore, huge volumes of water infiltrate into the soil from agricultural fields and unlined channels, percolate through the unsaturated zone and recharge the phreatic aquifer. Moreover, the shallow water table feeds numerous springs and flowing wells in large areas which are located along a belt that develops where the topographic slope decreases, and the Adda and Oglio rivers bend eastwards, south to the Irrigation District (Vassena et al. 2012).

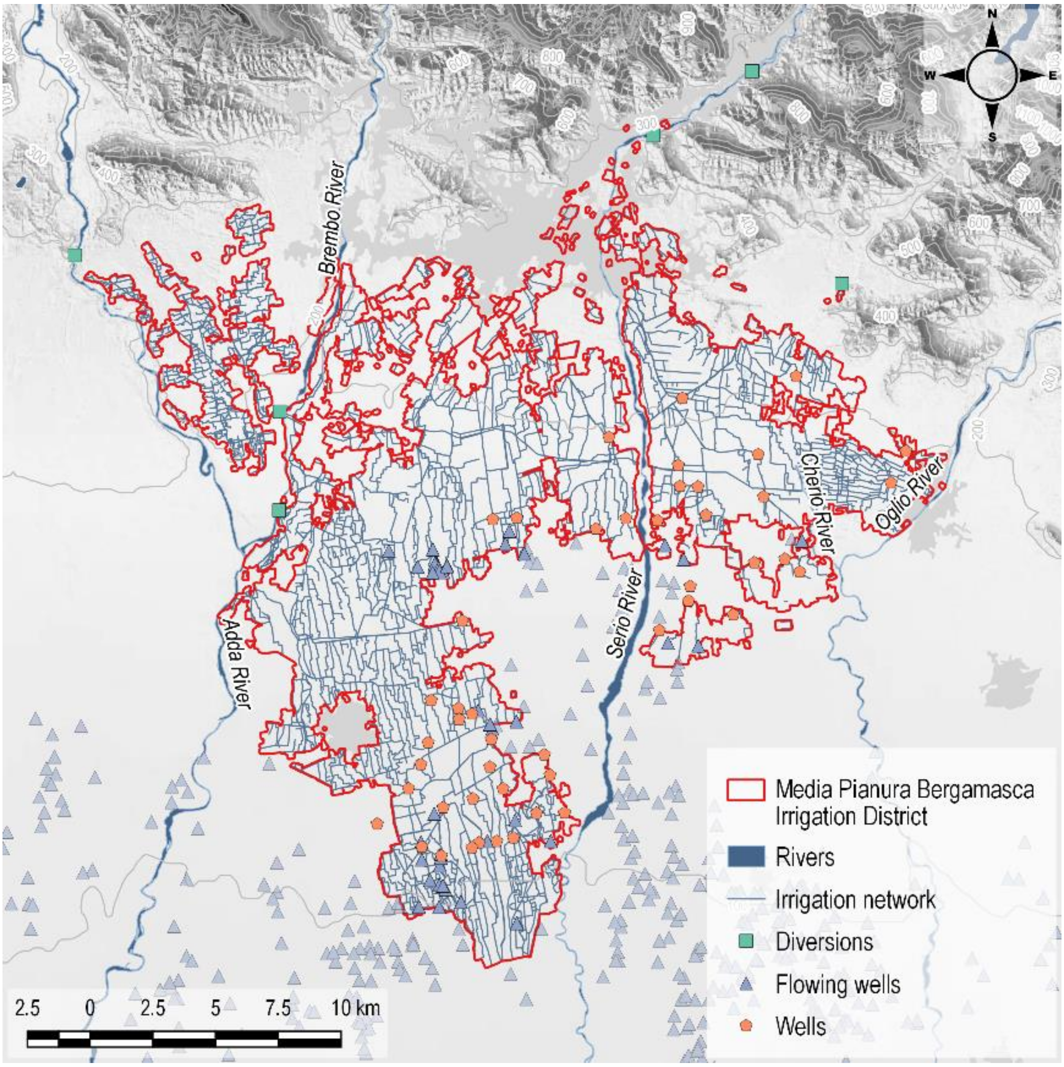

Figure 2-5: Irrigation network and diversions of the Media Pianura Bergamasca Irrigation District.

IDMPB is divided into 125 sub-districts. The sub-district is the last portion of the territory which is reached by a continuous (non–turned) irrigation water discharge. The Irrigation Consortium provided us with the information relative to the maximum irrigation discharges delivered to each sub-district. These maximum discharge values correspond to the conditions for which the river diversions can divert all the water in concession (i.e. this generally happens in the middle of the summer season, from early July to mid-August, in years in which there is good availability of water). Maximum irrigation discharges for the sub-districts are gross of conveyance and distribution losses, which are estimated by the Irrigation Consortium to be around 30% of the total amount diverted by rivers. From these values, the maximum specific irrigation supply rate for each sub-district was derived. On average, the pilot study area is provided with a supply rate of $1.10 \quad m^3 \cdot s^{-1} \cdot ha^{-1}$, one third lower than the average supply rate of the rest of the IDMPB ($1.72 \quad m^3 \cdot s^{-1} \cdot ha^{-1}$).

The daily series of diverted discharges from Brembo, Serio and Cherio rivers for the period 1995-2014, were obtained from the IDMPB Consortium. The raw data series showed some anomalies, mainly related to the use of $0 \quad m^3 \cdot s^{-1}$ as a no data flag, and to the unreliability of the discharge measurements in other periods. Moreover, some of the diversions were monitored only starting from the years 2000s. The raw data series were therefore validated, identifying the scheduled dry periods for channel maintenance as the periods when flows should be lower than a certain threshold, and removing the unrealistic jumps in the irrigation season (i.e. from mid May until the end of August). The pre-processed time series were then completed; in particular, if the number of the consecutive missing data was below a chosen threshold, they were filled by a linear regression; otherwise, the data series were imputed transversally (i.e. using information of neighbouring diversions) by a multiple linear regression (repeated for each season, best regressors set chose with adjusted R^2). Finally, to have a complete dataset starting from 1993, the missing discharge years were reconstructed by rescaling the median year on the frequency distribution observed in the time series.

2.6 LANDSAT SATELLITE DATA

An EO dataset, composed by NDVI and fAPAR time series from 2009 to 2014 was provided for the Ph.D. research activity by the Institute of Surveying, Remote Sensing and Land Information (IVFL) of the University of Natural Resources and Life Sciences of Vienna (BOKU). The dataset was obtained from the surface reflectance of Landsat Climate Data Record (CDR) data, using both Landsat 5 and Landsat 7 products. In particularly, Figure 2-6 represents the Landsat tiles from which BOKU dataset was provided and their spatial coverage.

The Landsat data were smoothed and gap-filled using a state-of-the-art Whittaker algorithm. The Whittaker smoother fits a noisy series, sampled at equal distances, basing on penalized least squares, while the series is automatically and smoothly interpolated at the positions where the raw data are missing. In successive iterations, all observed values that lie below the fitted curve are replaced by their fitted value. Thus, the Whittaker smoother down-weights negatively biased and unreliable observations, allowing a proper atmospheric noise and cloud removal and resulting in a more reliable time series (Atzberger & Eilers 2011a; Atzberger & Eilers 2011b; Shao et al. 2016). Due to these operations, a time series of 24 images per year, regularly spaced, both in the temporal (i.e. every 15 days) and in the spatial (i.e. $20\ m$) domain, was produced (Vuolo et al., in preparation).

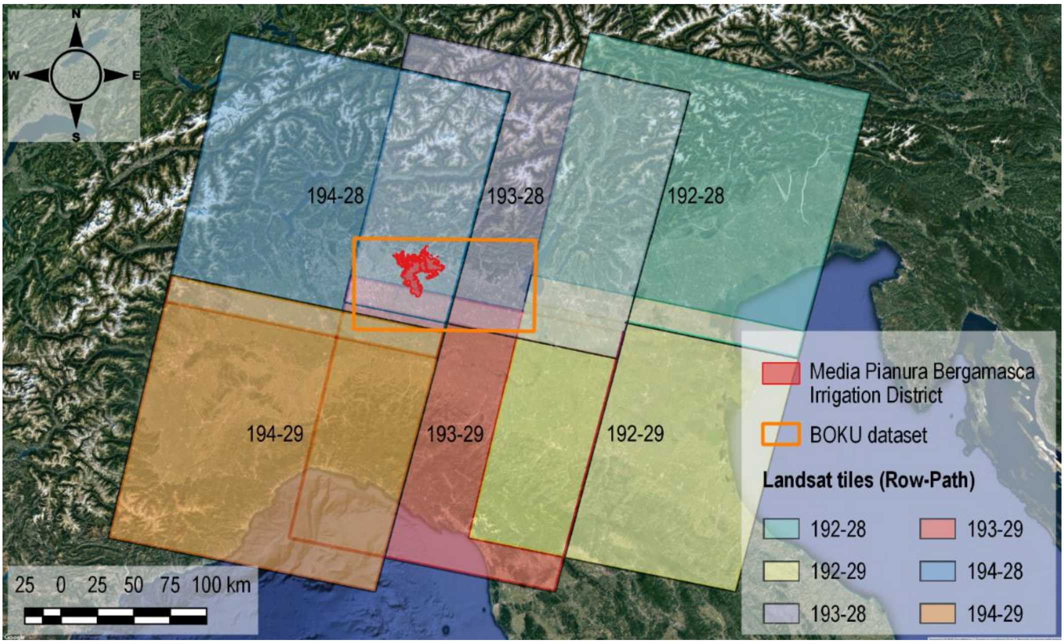

Figure 2-6: Landsat tiles from which the BOKU dataset for the Ph. D. research activity (orange box) was derived. Source: United States Geological Survey (2016). Base map © Google.

2.7 YIELD DATA

The extension of agricultural areas cultivated with different crops and their yield for the years 2009-2014 for all the Provinces of the Lombardy Region were taken from the regional statistical database (Lombardy Regional Authority & Istituto Nazionale di Statistica 2016). The data, aggregated on the Province scale, were analysed firstly by comparing those for the Bergamo Province to the others, to verify their reliability. As a matter of fact, some Provinces showed constant yearly yield per hectare for some crops. This was not the case for the Bergamo Province, where the grain maize yield oscillated between a minimum of $0.7\ kg \cdot m^{-2}$ in 2013 and a maximum of $1.4\ kg \cdot m^{-2}$ in 2008. These figures, that are roughly comparable with the data of the neighbouring Provinces of Brescia and Cremona, were therefore considered reliable.

2.8 VALIDATION AREAS

A groundtruth dataset was built through interviews conducted with six farmers whose fields were either located inside the IDMPB or in adjacent areas (Figure 2-7). The dataset was aimed to validate the results obtained from the EO analysis, with particular emphasis to the dates of the beginning and of the end of the growing season (i.e. emergence and harvest; Boschetti et al. 2009) and the overall productivity (Rembold et al. 2013; Xin et al. 2013; Xin et al. 2015), related to the harvested yield.

Information about the crop and the cultivar (or hybrid) grown in the period 2009-2014, sowing and harvesting dates, and harvested production were collected for each field. Unfortunately, not all the requested information was provided by all the farmers. The validation dataset for maize (i.e. the main crop, § 2.3) is constituted of 40 records (i.e. maize fields over the periods 2009-2014), with a minimum of 5 records in 2010 and a maximum of 8 in 2013.

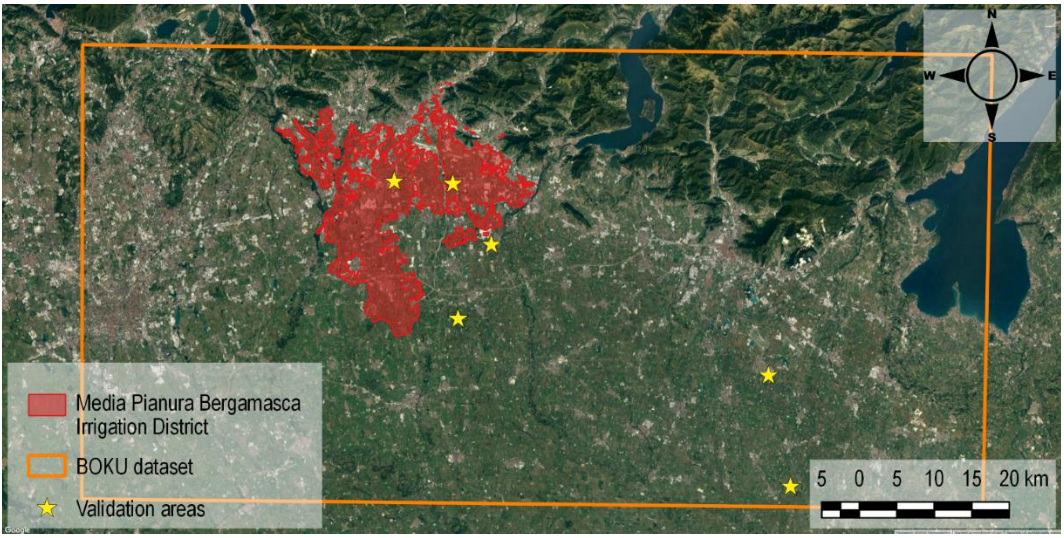

Figure 2-7: Location of the validation areas with respect to the IDMPB border, and to the BOKU dataset of EO data. Base map © Google.

3 DEVELOPMENT AND EVALUATION OF TRANSPIRATIVE DEFICIT INDEX ($\boldsymbol{D\text{-}TDI}$) FOR AGRICULTURAL DROUGHT MONITORING

3.1 ABSTRACT

Drought is a major cause of crop yield loss, both in rainfed and in irrigated agroecosystems. In past decades, many approaches have been developed to assess agricultural drought, usually based on a soil water shortage eventually dropping below a threshold limiting crop production. All these indices show weaknesses when the objective is to apply them for a real-time drought monitoring and management at the local scale, since they do not consider explicitly crop and soil properties at an adequate spatial resolution.

This chapter addresses the presentation and the description of a new agricultural drought index, the Transpirative Deficit Index ($D\text{-}TDI$), and the analysis of the result of its application over the Irrigation District of Media Pianura Bergamasca (IDMPB), which leads to the production of $D\text{-}TDI$ maps with a time step of 10 days and a spatial resolution of $250\ m$ for a time period of 22 years. The index, based on transforming the interannual distribution of the transpirative deficit to a standard normal distribution, is calculated using the IdrAgra hydrological model. The response of the $D\text{-}TDI$, taking into account two crops very different from each other and representative of the agriculture in the Padana Plain (i.e. maize and permanent grass), was compared with the Standardized Precipitation Index (SPI), and auto-correlation and cross-correlation analyses were conducted.

Results show that, since the $D\text{-}TDI$ relies both on climate and fine-resolution soil and land cover, it provides a more reliable measure of the evolution of agricultural drought over the irrigation district with respect to the one that could be achieved by using only meteorological drought indices such as SPI. In particular, the integration of the index over 10-day periods considering a mesh with cells of $250\ m$ allows to capture the response of the district to meteorological drought at a time and spatial-scales of interest for stakeholders. The $D\text{-}TDI$ shows a positive correlation to the SPI calculated over the previous month, with a higher persistence for silty-loamy or loamy soils, that, having a higher available water content, can provide a compensation to temporary reductions of water availability; a shorter persistence is shown for sandy soils.

The results of the study demonstrate that the adoption of $D\text{-}TDI$ can have a significant potential to shed light on the vulnerability of agricultural areas to dry spells and droughts. Additionally, the index may also be used for the spatially distributed monitoring of water shortage and water scarcity on irrigation districts, if information on the availability of water for irrigation in such areas could be available and used to implement the IdrAgra hydrological model. This would improve the ability of farmers and irrigation district managers to cope with drought events, allowing the development of adaptation measures.

3.2 INTRODUCTION

Water has always been the main limiting factor for crop production in many areas, in particular where rainfall is insufficient to meet crop water demand (Steduto et al. 2012). Therefore, drought is a major cause of crop losses and annual yield variations through the world, mainly in rainfed but also in irrigated agroecosystems (i.e. Blinda et al. 2007; International Panel on Climate Change 2014). According to its definition (§ 1.3), agricultural drought is identified by a soil water shortage (Mishra & Singh 2010) that eventually drops below a threshold limiting crop yields (Panu & Sharma 2002). As a consequence, soil moisture observation or estimation is a suitable approach for agricultural drought monitoring (Ochsner et al. 2013). However, plant water stress is more strongly related to the relative amount of plant-available water in the soil than to the absolute amount of soil moisture (Allen et al. 1998; Steduto et al. 2012).

In the past decades different approaches have been used for assessing agricultural drought (§ 1.4.2). In particular, the estimation of soil moisture, usually through hydrological model simulations, has been adopted by many authors (e.g. Marletto et al. 2005; Narasimhan & Srinivasan 2005; Van der Knijff & De Roo 2008). Another method, based on earth observation (EO) products, involves the selection of an appropriate vegetation index (VI) to evaluate the decrease in crop vitality and, therefore, in crop yields (e.g. Gao 1996; Kogan 1995a; Kogan 1995b; Scaini et al. 2014).

In both cases, many indices are not able to capture enough information for a feasible real-time drought management at a local scale (Mishra et al. 2015). In particular, many drought assessment methods have been proposed (also involving hydrological modelling based on long-term meteorological data series), but they typically do not consider site-specific crop properties (i.e. crop type, root and shoot development stages, length of the growing period) in the soil moisture simulation and thus in the drought index calculation (e.g. Marletto et al. 2005; Van der Knijff & De Roo 2008). As the transpirative component of the hydrological balance is related to the leaf area (Allen et al. 1998; Mishra et al. 2015), not considering crop properties with sufficient detail would bring to a misleading computation of the total water depleted by crops, and therefore of the agricultural drought index. This point is of particular importance in the development of an index suitable for the assessment of agricultural drought useful for irrigation district managers or farmers, who need accurate and high-resolution information to cope with this phenomenon. With respect to VIs retrieved by EO products, they have the limitation of not being implicitly able to discern between drought and other stress factors (e.g. pests, diseases); moreover, the interannual comparison of the index is possible only by assuming that the land cover does not change over long time periods, which normally is not true (European Drought Observatory 2016; World Meteorological Organization & Global Water Partnership 2016).

The aim of this chapter is to describe and evaluate the characteristics of a new agricultural drought index: the Transpirative Deficit Index ($D\text{-}TDI$). In the development of the index, attention was posed to overcome the weaknesses of other hydrological modelling approaches, by explicitly considering crop and soil properties, and allowing the calculation of the $D\text{-}TDI$ on a temporal and spatial resolution suitable for the drought assessment by stakeholders. In particular, the simulation mainframe devoted to the calculation of the index is illustrated. Secondly, the application of the index to the Irrigation District of Media Pianura Bergamasca (IDMPB) is described and discussed. For the application, a meteorological data series of 22 years (1993-2014) was considered, and values of the indicator cumulated over a 10-day time step were produced over a mesh with cells of $250\ m$. Finally, $D\text{-}TDI$ was compared with the Standardized Precipitation Index (SPI), and auto-correlation and cross-correlation analyses were carried out in order to analyse the index's response to meteorological forcing.

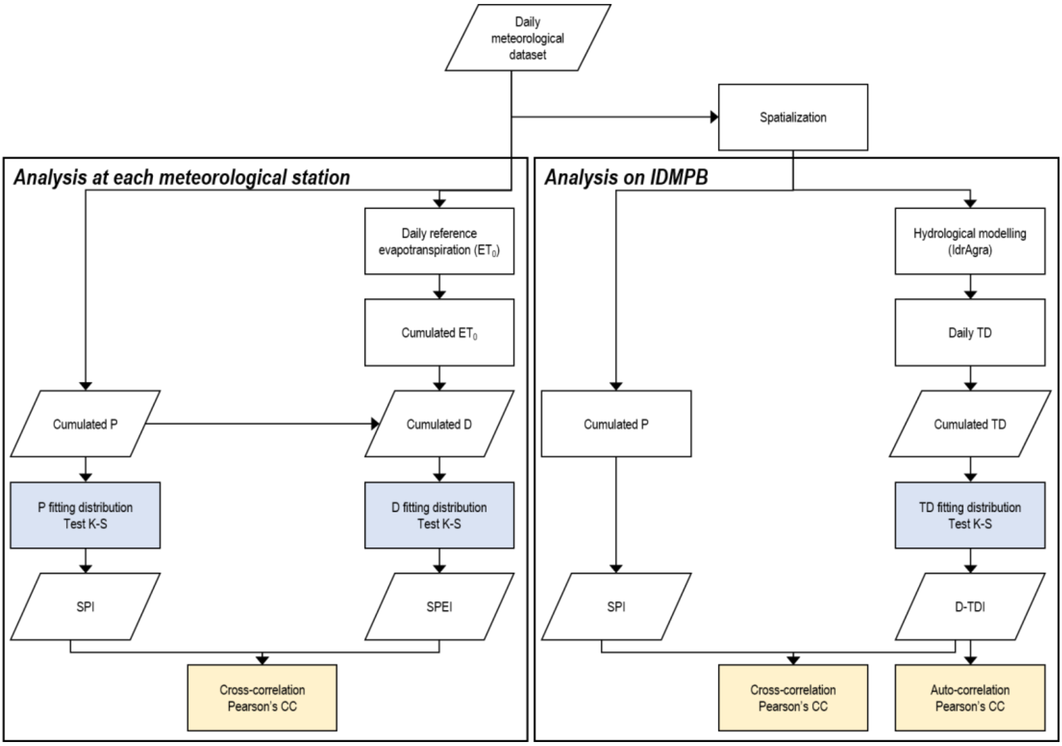

Figure 3-1: Flowchart of the methodology adopted in chapter 3. Rectangles represent the elaborations conducted, while parallelograms the data used or produced. IDMPB: Media Pianura Bergamasca Irrigation District, P: precipitation, D: deficit, ET0: Reference evapotranspiration, Test K-S: test Kolmogorov-Smirnov, CC: cross-correlation, SPI: Standardized Precipitation Index, SPEI: Standardized Precipitation Evapotranspiration Index, TD: (actual) transpirative deficit. D-TDI: Transpirative Deficit Index.

3.3 MATERIALS AND METHODS

The general workflow of this chapter is depicted in Figure 3-1 and briefly introduced hereafter. The meteorological dataset (22 years, from 1993 to 2014) was analysed using the Standardized Precipitation Index (SPI) and the Standardized Precipitation Evapotranspiration Index ($SPEI$), both calculated on the accumulation periods of 1, 3, 6, 9 and 12 months. The Kolmogorov-Smirnov (K-S) test was applied to choose the fitting distributions of precipitation and deficit data used to calculate all the considered indices (Lloyd-Hughes & Saunders 2002). A cross-correlation analysis of the results of the two indices was then performed to assess if using SPI could be sufficient to characterize the meteorological drought behaviour in the study area. Secondly, the IdrAgra hydrological model was set up considering all the needed input and parameters, and used to calculate the actual transpirative deficit (TD) on a daily time-step for each grid cell of the domain. After assessing the fitting distribution of the data series of TD cumulated over 10, 20 and 30 days, $D\text{-}TDI$ was derived on the same accumulation periods and an auto-correlation analysis of each derived $D\text{-}TDI$ series was performed. Finally, $D\text{-}TDI$ were compared to SPI series, calculated over the same accumulation periods (10, 20 and 30 days), and spatialized using the inverse distance weighted method (Bartier & Keller 1996; World Meteorological Organization 2012), through a cross-correlation analysis.

3.3.1 METEOROLOGICAL DROUGHT INDICES

To analyse the characteristics of meteorology (and thus the presence of meteorological dry-spells and droughts) in the study area, the following two indices were selected: the Standardized Precipitation Index (SPI, § 0; McKee et al. 1993), and the more recent Standardized Precipitation Transpiration Index ($SPEI$, § 1.4.1.3; Vicente-Serrano et al. 2010).

As previously stated (§ 0), the SPI is one of the most commonly used meteorological indices, and has been defined by the World Meteorological Organization as a key indicator for monitoring drought (Heim 2002; World Meteorological Organization 2012). The $SPEI$ was also considered in this analysis, since it allows to consider the effect of the temperature on drought (Vicente-Serrano et al. 2014; Vicente-Serrano et al. 2015).

The SPI ($SPEI$) is computed by summing precipitation (or deficit, defined as precipitation minus reference evapotranspiration ET_0) over an accumulation period, and fitting the accumulated values for the meteorological time series considered (i.e. 22 years, that means 22 values) to a parametric statistical distribution from which non-exceedence probabilities can be transformed to the standard normal distribution ($\mu = 0, \sigma = 1$; Beguería et al. 2014; Guttman 1999; McKee et al. 1993; Vicente-Serrano et al. 2010). Hence, the SPI ($SPEI$) value for each accumulation period of a specific year, represent the number of standard deviations from the long-term mean of the standard distribution (i.e. the mean precipitation or deficit; Kingston et al. 2015; Singleton 2012).

The fitting distribution for describing monthly precipitation – and to express SPI – is generally a gamma function, that has been proposed as a universal model (Guttman 1999). More recently, Lloyd-Hughes & Saunders (2002) assessed different models for describing monthly precipitation across Europe comparing the normal, the gamma and the log-normal distribution, confirming that the gamma provided the best fit of monthly precipitation, in particular for arid regions at short time scales.

The fitting distribution of the precipitation series, when expressed by a gamma, is:

$$g(P) = \frac{1}{\beta^{\alpha}\Gamma(\alpha)} P^{\alpha-1} e^{-\frac{P}{\beta}} \quad P > 0 \tag{3.1}$$

where α (adimensional) is the shape parameter, β (adimensional) is the scale parameter (both strictly positive), P (mm) is the cumlated precipitation amount and $\Gamma(\alpha) = \int_0^{\infty} y^{\alpha-1} e^{-y} \mathrm{d}y$ is the gamma function (Edwards & McKee 1997; Guttman 1999; McKee et al. 1993; Lloyd-Hughes & Saunders 2002).

The cumulative probability of an observed precipitation event is given by:

$$G(P) = \int_0^P g(P)\,dP = \frac{1}{\hat{\beta}^{\hat{\alpha}}\Gamma(\hat{\alpha})}\int_0^P P^{\hat{\alpha}} e^{-\frac{P}{\hat{\beta}}} dP \tag{3.2}$$

where $\hat{\alpha}$ and $\hat{\beta}$ are respectively the estimated shape and scale parameters, and P is the precipitation amount.

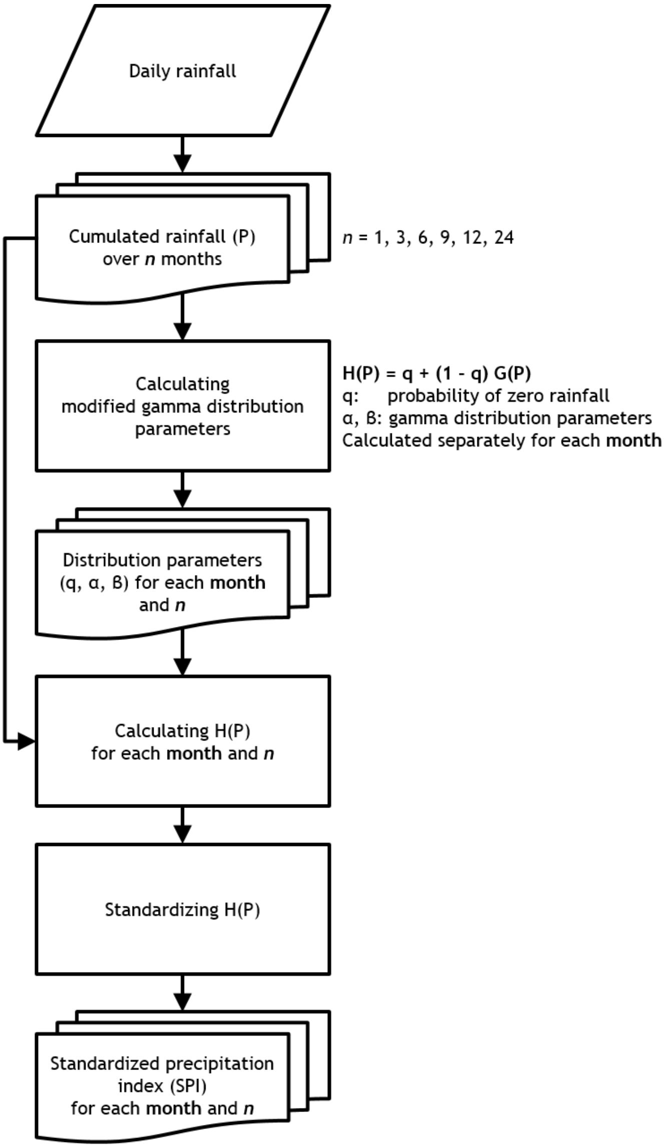

Figure 3-2: Flowchart describing the Standardized Precipitation Index (McKee et al. 1993) calculation.

If the series contains accumulation periods characterized by zero precipitation, the gamma distribution has to be modified to account for the probability of zero precipitation (Edwards & McKee 1997; McKee et al. 1993; World Meteorological Organization 2012), by:

$$H(P) = q + (1 - q)G(P) \tag{3.3}$$

where q is the probability of zero precipitation, estimated by the ratio $q = \frac{m}{n}$ (between the number of zeros in the precipitation time series, m, and the sample size, n), and $G(P)$ is the cumulative probability calculated by equation 3.2. Figure 3-2 represents the algorithm to compute the SPI.

To obtain reliable results, data series longer than 50 years are recommended, even if in many practical studies periods not longer than 20 years are frequently used (Guttman 1999; World Meteorological Organization 2012).

In this work, the α and β parameters of the gamma probability density function are estimated for each cell of the domain (i.e. a mesh with cells of $250\ m$ used to discretize the study area in unit volume), taking into account accumulation periods of 10, 20 and 30 days (i.e. calculating respectively the $SPI\text{-}10d$, $SPI\text{-}20d$ and $SPI\text{-}30d$) on every 10th day, and of 1, 3, 6, 9 and 12 months (i.e. $SPI1$, $SPI3$, $SPI6$, $SPI9$ and $SPI12$), for each month of the year, using maximum likelihood solutions (Thom 1996):

$$\begin{aligned} \hat{\alpha} &= \frac{1}{4A}\left(1 + \sqrt{1 + \frac{4A}{3}}\right) \\ \hat{\beta} &= \frac{\mu_P}{\hat{\alpha}} \end{aligned} \tag{3.4}$$

where here $\hat{\alpha}$ and $\hat{\beta}$ are the shape and scale parameters estimated for the SPI indices, μ_P is the average precipitation of all precipitation observations $P_1, P_2, \dots P_n$, and $A = \ln(\mu_P) - \frac{\sum \ln(P)}{n}$.

The fitting distribution for describing the cumulated deficit – thus the $SPEI$ – is the three-parameter log-logistic (Beguería et al. 2014):

$$f(D_n) = \frac{\beta}{\alpha}\left(\frac{D_n - \gamma}{\alpha}\right)^{\beta - 1}\left[1 + \left(\frac{D_n - \gamma}{\alpha}\right)^{\beta}\right]^{-2} \tag{3.5}$$

where $D_n = \sum_n (P - ET_0)_i$ is the deficit (mm), calculated as the difference between the precipitation P and the reference evapotranspiration ET_0, computed on a daily basis using the Penman-Monteith equation (see Annex I; Allen et al. 1998), for the accumulation period n, and α, β and γ are scale, shape and origin parameters, respectively, for D_n values in the range $(\gamma, +\infty)$ (Vicente-Serrano et al. 2010).

The parameters are obtained following Singh et al. (1993):

$$\begin{aligned} \hat{\beta} &= \frac{2w_1 - w_0}{6w_1 - w_0 - 6w_2} \\ \hat{\alpha} &= \frac{(w_0 - 2w_1)\hat{\beta}}{\Gamma(1 + 1/\hat{\beta})\Gamma(1 - 1/\hat{\beta})} \\ \hat{\gamma} &= w_0 - \hat{\alpha}\Gamma\left(1 + \frac{1}{\hat{\beta}}\right)\Gamma\left(1 - \frac{1}{\hat{\beta}}\right) \end{aligned} \tag{3.6}$$

where $\hat{\alpha}$, $\hat{\beta}$ and $\hat{\gamma}$ are the shape, scale and origin parameters estimated for the $SPEI$ indices, $\Gamma(x)$ is the gamma function of x and w_s are the probability weighted moments (PWMs) of order s.

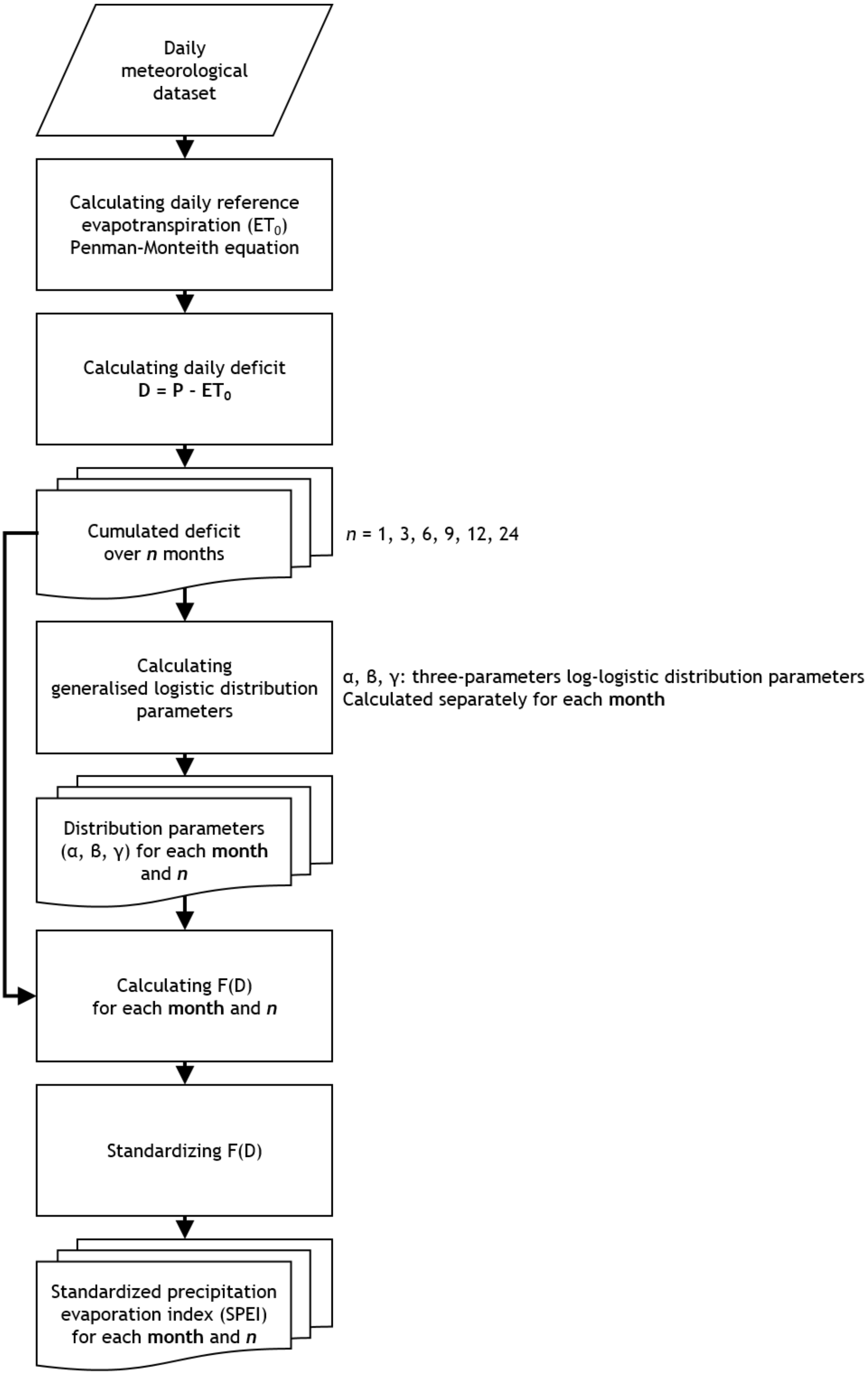

Figure 3-3: Flowchart describing the Standardized Precipitation Evapotranspiration Index (Vicente-Serrano et al. 2010) calculation.

In equation 3.6 the PWMs of order s are calculated as:

$$w_s = \frac{1}{N}\sum_{i=1}^{N}(1 - F_i)^s D_i \tag{3.7}$$

where $F_i = \frac{i-0.35}{N}$ is a frequency estimator calculated following the approach of Hosking (1990), i is the range of observations arranged in increasing order and N is the number of data points.

The log-logistic distribution as fitting distribution has been selected by Vicente-Serrano et al. (2010), because it shows a gradual decrease in the curve for low values, and more coherent probabilities for very low values of the deficit. Figure 3-3 represents the algorithm to compute the $SPEI$.

The cumulative probability $H(x)$ (respectilvely, $H(P)$ and $H(D)$ for the two indices) is finally transformed into the standard normal random variable (zero mean and unit variance), which gives the value of the SPI and the $SPEI$ (McKee et al. 1993; Edwards & McKee 1997; Vicente-Serrano et al. 2010). This is obtained by using the approximation of Abramowitz and Stegun (1964):

$$\mathrm{Z} = \begin{cases} -\left(\mathrm{t} - \frac{\mathrm{c_0+c_1t+c_2t^2}}{\mathrm{1+d_1t+d_2t^2+d_3t^3}}\right) & 0 < \mathrm{H(x)} \leq 0.5 \\ +\left(\mathrm{t} - \frac{\mathrm{c_0+c_1t+c_2t^2}}{\mathrm{1+d_1t+d_2t^2+d_3t^3}}\right) & 0.5 < \mathrm{H(x)} < 1 \end{cases} \tag{3.8}$$

where

$$\mathrm{t} = \begin{cases} \sqrt{\ln\left(\frac{1}{(\mathrm{H(x)})^2}\right)} & 0 < \mathrm{H(x)} \leq 0.5 \\ \sqrt{\ln\left(\frac{1}{(1.0-\mathrm{H(x)})^2}\right)} & 0.5 < \mathrm{H(x)} < 1 \end{cases} \tag{3.9}$$

$\mathrm{c_0} = 2.515517$, $\mathrm{c_1} = 0.802853$, $\mathrm{c_2} = 0.010328$, $\mathrm{d_1} = 1.432788$, $\mathrm{d_2} = 0.189269$ and $\mathrm{d_3} = 0.001308.$

Positive SPI (or $SPEI$) values indicate precipitation (or deficit) greater than the median, while negative values indicate precipitation (or deficit) lower than the median; the magnitude of departure from zero represents both drought intensity and a probability of occurrence (McKee et al. 1993; Hayes et al. 1999).

3.3.2 THE TRANSPIRATIVE DEFICIT INDEX AS AN AGRICULTURAL DROUGHT INDEX

The Transpirative Deficit Index has been developed in this study form the integrated transpirative deficit (TDn; § 1.4.2.2), proposed by the Emilia Romagna Region (Marletto & Zinoni 2004; Marletto et al. 2005). The TDn is an agricultural drought index, that in its original formulation takes into account not only the precipitation deficit, but also the effects of land use, soils, and climatic conditions that govern the crop transpiration (Niemeyer 2008). It is based on the transpiration deficit, computed daily by a water balance as the difference between potential and actual transpiration. The daily deficit is then cumulated over a period of n days (Marletto & Zinoni 2004; Marletto et al. 2005):

$$TDn_i = \sum_{i-n}^{i-1}(T_p - T_a) \tag{3.10}$$

where n is the accumulation period, T_p (mm) is the potential transpiration and T_a (mm) is the actual transpiration .

To develop the Transpirative Deficit Index (TDI), the distribution of TDn (i.e. the integrated transpirative deficit over an accumulation period of n days) was fitted with a fitting distribution, and successively transformed into the standard normal variable ($\mu = 0, \sigma = 1$); the TDI was defined as the non-exceedance probability referred to the outcoming cumulated distribution. This procedure allows the comparison of crop stress conditions both in the spatial and in the temporal domains. To allow direct comparison with other indicators (e.g. SPI, $SPEI$), the sign of the result has been inverted, thus positive (or negative) values indicate a higher (or lower) crop water stress with respect to the mean/median value.

In this chapter, the TDI is calculated by implementing the original equation by Marletto and Zinoni (2004) into the simulation model IdrAgra (§ 3.3.3), without considering irrigation inputs. Thus, in this study, the index is used to monitor agricultural dry-spells and droughts over the IDMPB territory: this is highlighted by the use of the acronym $D\text{-}TDI$ (i.e. Drought – Transpirative Deficit Index) in the following discussion.

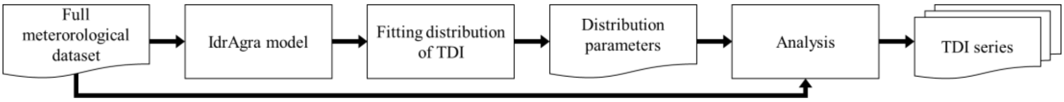

Figure 3-4: Flowchart of the data elaboration to compute $D\text{-}TDI$.

Figure 3-4 represents the flowchart of the computation and the analysis of the $D\text{-}TDI$ in the study case. Time series of $TD10$, $TD20$ and $TD30$ were calculated by applying IdrAgra to the simulation domain, and calculating, for each cell, the transpiration deficit (i.e. over 10, 20 and 30 days, respectively) every 10 days, over the entire simulation period (i.e. 1993-2014). Values for each 10-, 20-, and 30-days period were then fitted to the respective distributions, to obtain the parameters to derive TDI. Each TDn series was then expressed in the form of the respective TDI.

3.3.3 THE IDRAGRA MODEL AND THE TDn COMPUTATION

The simulation model IdrAgra (Facchi et al. 2004; Gandolfi et al. 2014; Vassena et al. 2012) is a distributed-parameter conceptual model developed by the Section of Agricultural Hydraulics of the Department of Agricultural and Environmental Sciences (DiSAA) of the University of Milano over 15 years, which allows the simulation of the irrigation water distribution in agricultural areas and the estimation of the hydrological balance on a daily basis (for a complete description of the model see Annex I). IdrAgra includes four main modules devoted to specific tasks (Figure 3-5): irrigation water sources, conveyance and distribution over the territory, crop phenological stages and soil-crop water balance. The model core is the soil-crop water balance module (Facchi et al. 2004; Galelli et al. 2010), which accounts for the spatial variability of soils, crops, meteorological and irrigation inputs by dividing the irrigation district with a regular mesh. Soil and crop characteristics, meteorological inputs, and irrigation supply are considered homogeneous within each cell of the mesh but may vary from cell to cell. Each cell identifies a soil volume which extends from the soil surface to the lower limit of the root zone.

The soil volume of each cell is subdivided into two layers: the top one (evaporative layer) represents the upper few centimetres of the soil, while the bottom one (transpirative layer) represents the root zone and has a time-varying depth Z_r. The two layers are modelled as non-linear reservoirs in cascade, where hydrological processes are represented as one-dimensional. The water percolating out of the bottom layer constitutes the recharge to the groundwater system (Facchi et al. 2004; Gandolfi et al. 2014; Vassena et al. 2012).

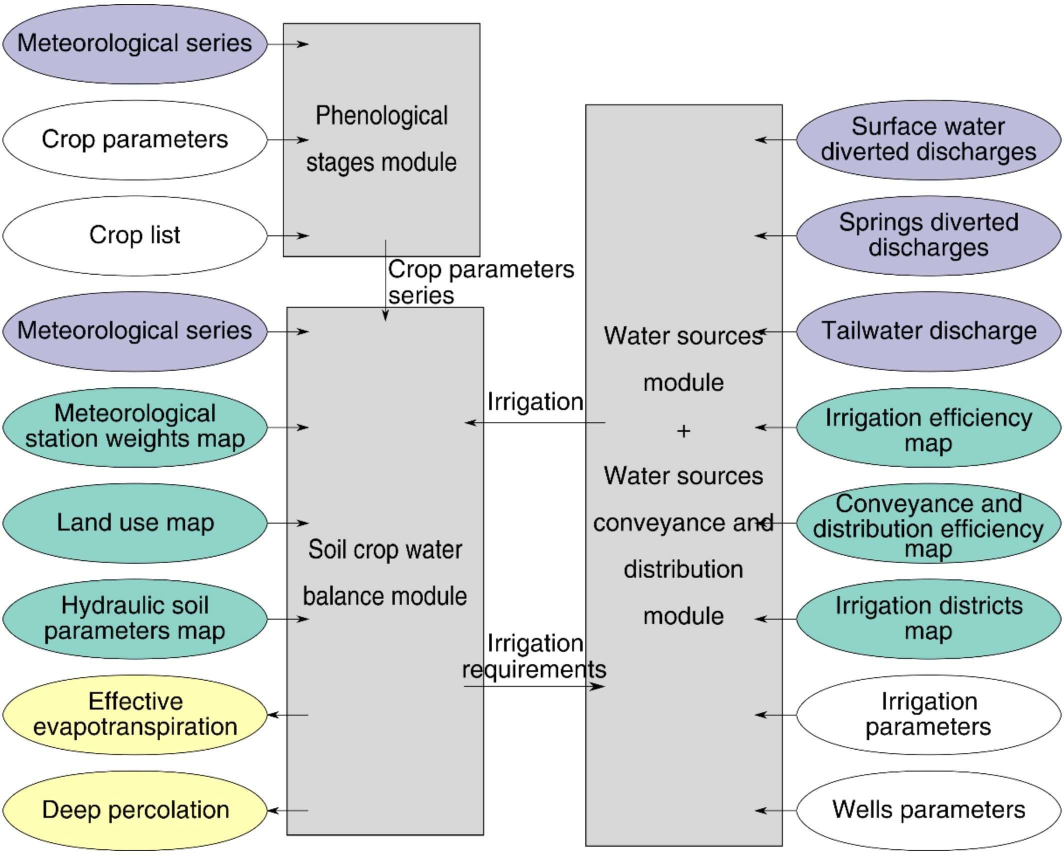

Figure 3-5: Flowchart of the IdrAgra simulation model: modules are reported in grey, parameters in whilte, punctual inputs in violet, spatial inputs in light blue, and outputs in yellow.

The dynamic of the water content in the evaporative layer of the cell is governed by the following balance equation:

$$\frac{\Delta V_E}{\Delta t} = \left[P - I + Q_i - Q_u - E - Q_e - \Delta Q_p\right]_t \tag{3.11}$$

where V_E (mm) is the water content of the evaporative layer of each cell, P $(mm \cdot d^{-1})$ is the rainfall rate, t (d) is the daily time step, I $(mm \cdot d^{-1})$ is the canopy interception, Q_i $(mm \cdot d^{-1})$ is the net inflow to the cell (irrigation supply), Q_u $(mm \cdot d^{-1})$ is the net runoff from the cell,

$E\ (mm \cdot d^{-1})$ is the evaporation rate, $Q_e\ (mm \cdot d^{-1})$ is the outflow to the transpirative layer and $\Delta Q_p\ (mm \cdot d^{-1})$ is the variation in the ponding water.

A similar equation holds for the water content dynamic in the transpirative layer:

$$\frac{\Delta V_{\mathrm{T}}}{\Delta t} = [Q_e - T \pm Q_s]_t \tag{3.12}$$

where $V_{\mathrm{T}}\ (mm)$ is the water content of the transpirative layer of each cell , $T\ (mm \cdot d^{-1})$ is the transpiration rate, $Q_e\ (mm \cdot d^{-1})$ is the inflow from the evaporative layer, $Q_s\ (mm \cdot d^{-1})$ is the water flux at the border of the root zone, directed downward to the deeper soil layers ($Q_s > 0$) or upward, being the capillary rise rate ($Q_s < 0$).

The canopy interception I in equation 3.11 is calculated following Von Hoyningen-Hüne (1983) and Braden (1985), as a function of the leaf area index, the cover fraction and the volume capacity per unit of foliage area, all varying according to the crop type and growing stage. The runoff rate Q_u is calculated by using the SCS-curve number method (USDA Soil Conservation Service 1972), modified to account for ponding, that acts as a linear function of the slope, while the remaining water infiltrates. The evaporative rate E and the transpirative rate T, in equations 3.11 and 3.12 respectively, are computed using the FAO-56 dual crop coefficient method (Allen et al. 1998). The reference crop evapotranspiration ET_0 is computed by applying the FAO-Penman-Monteith equation; the actual transpiration rate is then obtained by multiplying ET_0 by a basal coefficient K_{cb}, which accounts for the differences in ground cover, canopy properties and aerodynamic resistance from the reference crop, and by the water stress coefficient K_s, which introduces the effect of a limited soil water availability within the transpirative layer. The actual evaporation rate is determined by multiplying ET_0 by the evaporative coefficient K_e, depending, among other variables, on the soil water content in the evaporative layer through the water stress coefficient K_r. Coefficients K_{cb}, K_s and K_e are determined from crop and soil characteristics, meteorological data and soil water content within the respective soil layers through appropriate equations (Allen et al. 1998). Drainage discharges Q_e and Q_s are determined using a simplified scheme which considers a Darcian-type unit gradient gravity flow in the unsaturated soil. The relation between water content and unsaturated hydraulic conductivity is modelled using the Brooks and Corey (1964) equation. The capillary rise Q_s in equation 3.12 is calculated using the empirical approach described in Liu et al. (2006). The calculation of the input and output fluxes as well as the value of the final water content in the layers is performed with an implicit finite difference scheme, with a hourly numerical integration time step (Facchi et al. 2004; Gandolfi et al. 2014; Vassena et al. 2012). The “Phenological stages module” simulates crop parameters based on thermal time (growing degree-days method), which is the required daily accumulation of average air temperature above a base temperature and below a cutoff temperature to reach give growth stages (McMaster & Wilhelm 1997; Stöckle et al. 2003).

For the application presented in this chapter, IdrAgra was used as a model for the estimation of the crop water requirements over the study area; therefore the "Water sources module" and "Water conveyance and distribution module" (Figure 3-5) are note explained here. For details on these two modules refer to § 5.3.2 and to Annex I.

The main inputs and parameters required by the IdrAgra model to compute the crop water requirements by using the “Soil-crop water balance module” and the “Phenological stages module” are: soil map and soil hydraulic parameters, land use maps (one for each year of simulation) and crop biometric parameters, meteorological (rainfall, maximum and minimum air temperature, wind speed, maximum and minimum relative humidity, solar radiation) and groundwater level data series. In the case of the IdrAgra model used for the simulation of the complete irrigation system water balance (including "Water sources module" and "Water conveyance and distribution module"), information about the irrigation system (irrigation subdistricts map, irrigation sources data series, share of each irrigation source devoted to each subdistrict, conveyance efficiency) are moreover necessary.

In order to compute TDI (i.e. $D\text{-}TDI$) indices, IdrAgra model was modified with the addition of a specific procedure for the computation of TDn, that sums the daily transpirative deficit over the defined accumulation periods and fit them with the respective distributions to obtain the parameters to derive TDI (Figure 3-4). Finally, the corresponding maps are saved.

3.3.4 ASSESSMENT OF THE FITTING DISTRIBUTION

To assess which statistical distributions can better describe the data series of precipitation (P), deficit (D), TDn for the case study, the empirical cumulative probability distributions were tested with various theroretical cumulative distributions (gamma, log-logistic, Weibull, and Nakagami), by computing the Kolmogorov-Smirnov test statistic:

$$D_n = \max_n [F_n(x) - F(x)] \tag{3.13}$$

where $F_n(x)$ is the empirical cumulative probability (i.e. precipitation, deficit and TDn) and $F(x)$ is the theoretical cumulative probability distribution evaluated at x. Under the null hypothesis (i.e. data drawn from the theoretical distribution), D_n is compared with a critical value appropriate to the sample size and the assumed distribution. If D_n exceeds the critical value, the null hypothesis is rejected at the givel level of significance (Lloyd-Hughes & Saunders 2002).

3.3.5 CORRELATION ANALYSIS

The correlation analysis was adopted: (1) to compare SPI and $SPEI$ at diverse time steps, in order to assess if using SPI could be sufficient to characterize the meteorological drought behaviour in the study area, (2) to study the characteristics and the memory of $D\text{-}TDI$, as well as to assess its intra- and inter-annual variability, and (3) to assess the response of the agricultural drought – thus the information provided by $D\text{-}TDI$ – to meteorological drought – thus of SPI – over different temporal steps.

Pearson’s cross-correlation coefficient (D_{CC}) is defined as the degree of linear relationship between time series:

$$D_{CC(s)} = \frac{\sum_{t=0}^{N-1}[(f_t^p - \bar{f}^p)\cdot(f_{t-s}^q - \bar{f}^q)]}{\sqrt{\sum_{t=0}^{N-1}(f_t^p - \bar{f}^p)^2}\cdot\sqrt{\sum_{t=0}^{N-1}(f_{t-s}^q - \bar{f}^q)^2}} \tag{3.14}$$

where f_t^p and f_t^q are the time series values at moment t, $\bar{f}^p$ and $\bar{f}^q$ are the means of the corresponding series, s is the lag (time shift) between the time series, and N is the length of the time series (Warren Liao 2005). If $D_{CC(s)}$ is computed for $s = 0$, it estimates the standard Pearson's correlation coefficient (i.e. without any time shift).

When $D_{CC(s)}$ is calculated for one time series, i.e. when $f^p(t) = f^q(t)$, it measures the auto-correlation (Meek et al. 1999).

D_{CC} is 1 in case of an increasing deterministic linear relationship and -1 in case of a decreasing linear relationship. In equation 3.14, the index considered in the cross-correlation is f_t^p.

In inter-annual analysis, annual fluctuations of Transpirative Deficit Index were removed by applying the following formula:

$$f_t^* = \frac{f_t - \mu_f}{\sigma_f} \tag{3.15}$$

where f_t is the time series value at moment t, μ_f and σ_f are the mean and variance of the time series within the year including t, and f_t^* is the annual adjusted time series value.

3.3.6 STUDY AREA

In chapter 2 the Irrigation District of the Media Pianura Bergamasca (IDMPB), study area for the Ph.D. project, and the available data collection and pre-processing were described. This chapter is focused on the assessment of the information provided by the newly proposed $D\text{-}TDI$, also with respect to the SPI. For the correlation analysis, only the two predominant crops of the area (i.e. maize and permanent grass; § 2.3) were taken into account; in particular, the two crops were considered in two different simulation exercises as uniformly distributed over the whole agricultural area. The other main inputs and parameters adopted in the simulations were the following: agro-meteorological data series at the agro-meteorological stations selected for the study area (§ 2.2; Figure 3-6) for the period 1993-2014: soil hydraulic parameters maps for the two soil layers (§ 2.4); and crop parameter data series built by using the IdrAgra crop phenological stages module (Annex I).

3.4 RESULTS

3.4.1 PRECIPITATION AND DEFICIT DISTRIBUTIONS AND TIME PATTERNS

For each agro-meteorological station, daily precipitation (P) and deficit (D) data were cumulated over the selected integration periods (1, 3, 6, 9 and 12 months) and the results were stratified by calendar month (e.g. the cumulated precipitation series calculated for the month of January from 1993 to 2014 were used to derive the fitting distributions to calculate January SPIs; Guttman 1999). The fitting distributions were then separately assessed for each month, and the maximum level of significance for each station was analysed. For both variables, candidate distributions were: 2-parameter gamma, log-logistic, Weibull and Nakagami.

According to the Kolmogorov-Smirnov test at the 5% level of significance ($\alpha < 0.05$), the 2-parameter gamma is the best fitting distribution for the precipitation series; only a precipitation series cumulated over 12 months failed the test ($\alpha \cong 0.06$), that is far within the 5% of false positives expected for multiple testing. For the deficit distributions, the log-logistic was found to fit the series best. Both the fitting distributions, when used to fit the data of our specific study area, show to provide good results, as affirmed by their authors (McKee et al. 1993; Vicente-Serrano et al. 2010); in particular, the fitting distribution of SPI corresponded to the universal model proposed by Guttman (1999), while the one of $SPEI$ was in accordance with the procedure described in Beguería et al. (2014) SPI and $SPEI$ series were then generated accordingly.

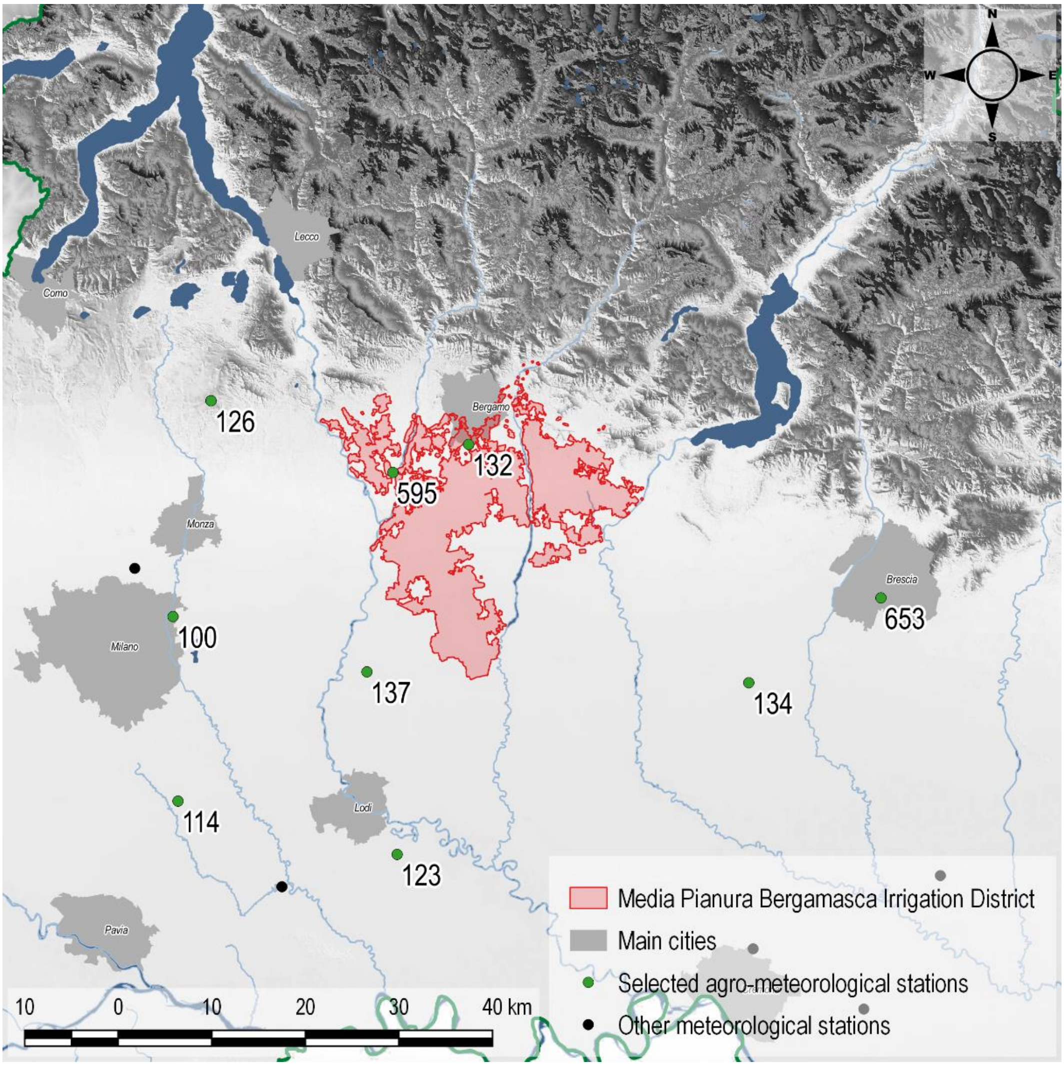

Figure 3-6: Agro-meteorological stations selected for the analysis.

Independently from the integration period, monthly values of SPI and $SPEI$ (the monthly average values for each station are shown in Figure 3-7) have a zero long-term mean (i.e. the mean calculated over the entire series), and show a slightly increasing trend. This does not match with the findings of Spinoni et al. (2016), that, by analysing the same indices, observed a drying tendency for southern Europe and in particularly for the entire Italy (§ 1.5).

Three periods with high SPI (and $SPEI$) – indicating thus moderate to severe wet events – can be identified. In particular, the first one occurred between the end of 1999 and the end of 2001, peaking during the winter 2000-2001 (the average $SPI12$ was 1.62 on March 2001). The second wet period lasted from mid-2008 until the end of 2011, with an interruption during the second half of 2009, characterized by a summer drought; also this event peaked during winter, with an average $SPI12$ of 1.60 in January 2011. The third event, still on-going at the end of 2014, run from the end of 2012, reaching $SPI12$ of 1.75 in November 2014. These periods were all characterized by almost high and stable SPI and $SPEI$ values considering integration periods from 6 months onward.

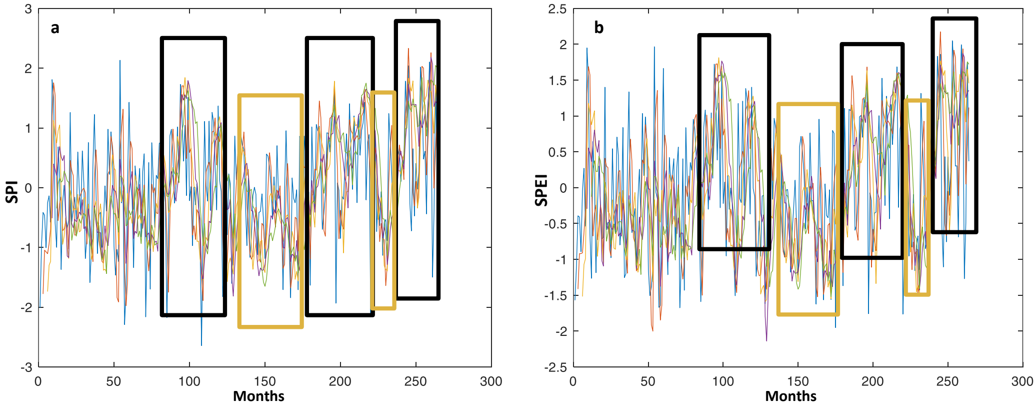

Figure 3-7: Monthly series of (a) SPI and (b) $SPEI$ computed as the mean of the values calculated at each agro-meteorological station: integration periods of 1, 3, 6, 9 and 12 months are respectively represented by the blue, red, yellow, violet and green lines. The considered time period is 1993-2014; months are indexed from January 1993. Black boxes identify periods characterized by positive values, gold boxes by negative values.

On the contrary, dry events in the data series of the study area were generally characterized by less stable trends, and the indices values tended to fluctuate reaching, or approaching, the near-normal values (i.e. $SPI \geq -0.99$; World Meteorological Organization 2012). Two moderately dry events can therefore be identified, the first one between mid- 2003 and mid-2008, with the lowest value of $SPI12$, -1.53 reached in April 2007, and the second one from the end of 2011 until the end of 2012, with $SPI12$ reaching -1.44 on average in March 2012.

3.4.2 CROSS-CORRELATION ANALYSIS OF SPI AND $SPEI$ SERIES

Cross-correlation between SPI and $SPEI$ for 1-, 3-, 6-, 9- and 12- months was calculated separately for each month of the year and each meteorological station in order to assess if using SPI could be sufficient to characterize the meteorological drought behaviour in the study area.

Results show that SPI and $SPEI$ are in a good accordance. The minimum lag-0 cross-correlation ($CC0$) observed between $SPI1$ and $SPEI1$ values (Table 3-1) is higher than 0.90 for all months and stations, with the exception of “Brescia – via Ziziola” station, that shows a lower value (0.80) in

July, caused by abnormally low values of deficit (thus, of $SPEI1$) in 2007. SPI and $SPEI$ on higher integration periods have higher $CC0$.

Table 3-1: Minimum over months of lag-0 cross-correlation coefficient ($CC0$) between $SPI1$ and $SPEI1$.

Meteorological station	***Station ID***	***Minimum $CC0$***
Milano - Lambrate	100	0.96
Landriano	114	0.93
Cavenago d'Adda	123	0.91
Casatenovo prato	126	0.93
Bergamo - Stezzano	132	0.94
Bargnano	134	0.94
Rivolta d'Adda	137	0.90
Filago - via Don Milani	595	0.92
Brescia - via Ziziola	653	0.80

Table 3-2: Minimum lag-0 cross-correlation coefficients ($CC0$) of the comparisons between $SPI1$ and $SPEI1$ for each pair of agro-meteorological stations, identified by the station identifiers (IDs). $CC0$ are calculated on a triangular matrix, and the other values are set to "Not a Number" (NaN).

Station ID ***Station ID***	***100***	***114***	***123***	***126***	***132***	***134***	***137***	***595***	***653***
100	NaN	0.687	0.543	0.717	0.349	0.544	0.713	0.375	0.514
114	NaN	NaN	0.772	0.418	0.381	0.535	0.746	0.412	0.416
123	NaN	NaN	NaN	0.309	0.312	0.470	0.596	0.349	0.380
126	NaN	NaN	NaN	NaN	0.569	0.589	0.513	0.504	0.600
132	NaN	NaN	NaN	NaN	NaN	0.549	0.457	0.461	0.615
134	NaN	NaN	NaN	NaN	NaN	NaN	0.541	0.478	0.527
137	NaN	NaN	NaN	NaN	NaN	NaN	NaN	0.560	0.413
595	NaN	NaN	NaN	NaN	NaN	NaN	NaN	NaN	0.497
653	NaN	NaN	NaN	NaN	NaN	NaN	NaN	NaN	NaN

When considering two different agro-meteorological stations in the correlation analysis of SPI and $SPEI$, results are expected to be greatly affected by the seasonal fluctuations affecting both indicators. In this case, the analysis was conducted separately on each of the 12 monthly series for each pair of meteorological stations and for each integration period (1-, 3-, 6-, 9- and 12- months). Table 3-2 shows the minimum $CC0$ values calculated between each pair of $SPI1$ or each pair of $SPEI1$ (i.e. the minimum value of the two comparisons is reported) and each couple of meteorological stations.

As expected, $CC0$ values are inversely related to the distance between the stations (Figure 3-6). In particular, low $CC0$ coefficients are registered when comparing SPI or $SPEI$ values computed in the southern part (ID 123) or, secondarily, in the western part (ID 114), with the corresponding indices calculated for the meteorological stations located in the northern part (ID126, 135, 595).

3.4.3 AUTO-CORRELATION ANALYSIS OF $\boldsymbol{D\text{-}TDI}$

An auto-correlation analysis was performed to study the characteristics and the memory of $D\text{-}TDI$, and its eventual relationship with soil hydraulic parameters and meteorological data. The analysis was performed by considering the time series of $D\text{-}TDI$s calculated every 10 days, over the whole meteorological year in the case of permanent grass, and over the time lapse between emergence and harvest dates for maize. To overcome problems related to a memory effect caused by overlapping data used in the indices calculation, the auto-correlation analysis was conducted every 20 days for the $D\text{-}TDI20$ and every 30 days for the $D\text{-}TDI30$. Results for the two crops are described below.

Maize

From the auto-correlogram of $D\text{-}TDI10$ (Figure 3-8a), it can be observed that the index is positively auto-correlated with a significance level of 0.05, with a persistence of 3 lags (i.e. 30 days). As a matter of fact, the transpirative deficit at a time step depends by the soil water available during the previous time steps, that are linked to the corresponding transpirative deficits. Lag-1 auto-correlation ($AC1$), in particular, is significative and positive for 84.32% of the cells. Positive auto-correlation persists around 30 days also for indices calculated over longer integration periods (Figure 3-8c, e).

The auto-correlogram of Figure 3-8b was computed after standardizing $D\text{-}TDI10$ series. In particular, annual fluctuations of the $D\text{-}TDI10$ were removed through the application of the equation 3.15 to each cell independently. Most of the cells (Figure 3-8b) showed negative auto-correlation, with a persistence of 6 lags (i.e. 60 days), demonstrating the positive auto-correlation found for maize is mostly due to the inter-annual behaviour of the index.

In fact, the $D\text{-}TDI10$ calculated for consecutive time steps within the same year are mostly consistently positive (or negative), in dependence on the dryness (or wetness) of the year. This behaviour is depicted in Figure 3-10a, representing the $D\text{-}TDI10$ series for a single cell, constructed by removing from each value the mean of the whole series (i.e. the long-term mean): the derived index tends to be mostly positive (or negative) during the same year. By comparing this series with the results of Figure 3-7, it can be inferred that the $D\text{-}TDI10$ response is consistent with the meteorological data; in fact, the derived index tends to be mostly positive (i.e. the $D\text{-}TDI10$s are higher than the long-term mean) in years characterized by positive SPIs (1995, 1997-2000, 2002, 2008, 2014), negative (i.e. the $D\text{-}TDI10$s are lower than the long-term mean) in years characterized by negative SPIs (1996, 2003, 2005-2007, 2012-2013). On the other hand, the oscillations within each year, that are depicted in Figure 3-10b by removing from each term the yearly mean, do not show a clear trend.

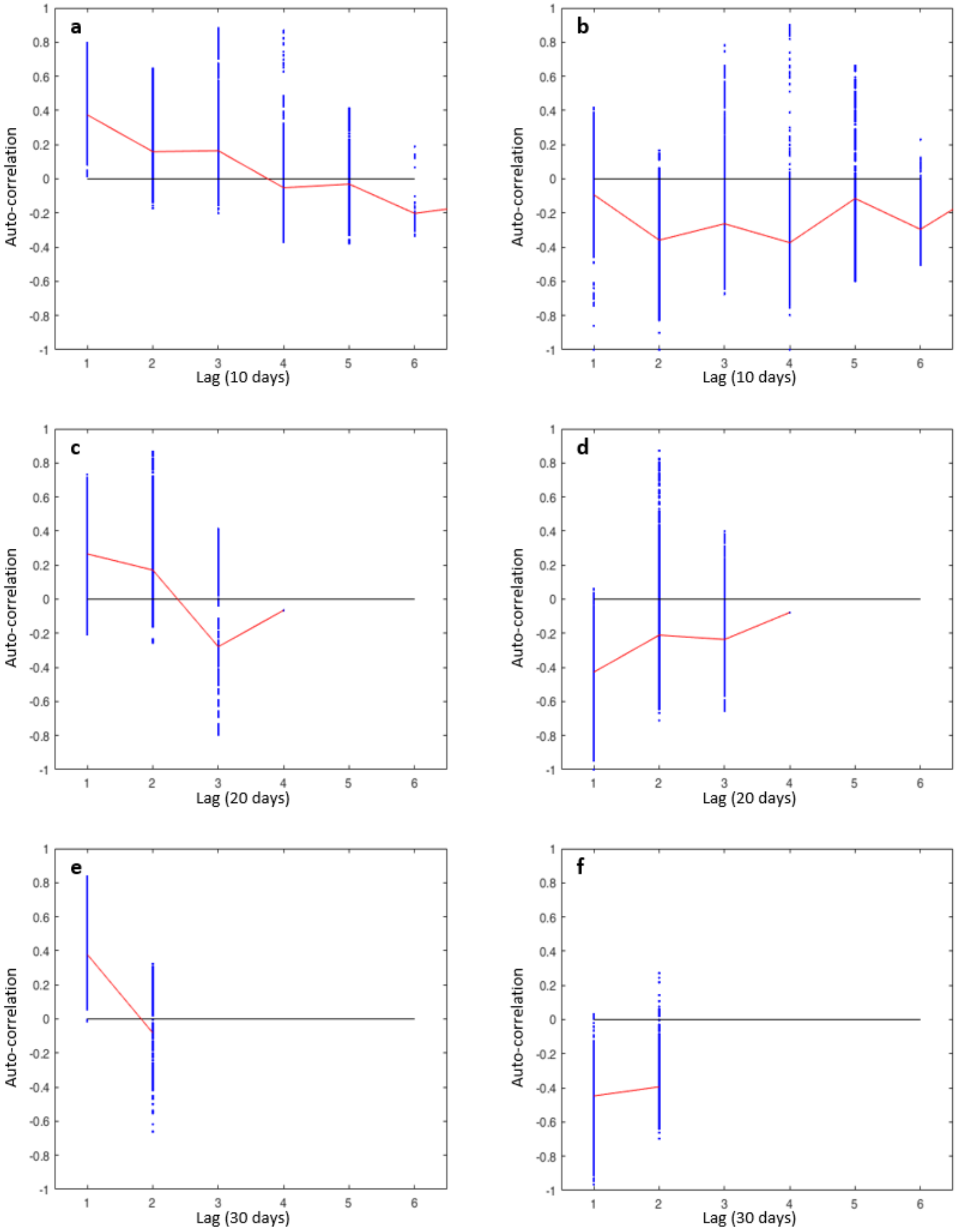

Figure 3-8: Auto-correlogram of $D\text{-}TDI$ for maize: auto-correlograms obtained analysing (a) original series and (b) standardized series of $D\text{-}TDI10$; (c) original series and (b) standardized series of $D\text{-}TDI20$; (e) original series and (f) standardized series of $D\text{-}TDI30$. In the diagrams, blue dots represent cell-values and red line is the mean.

Table 3-3: Maize growing period (from emergence to harvest) simulated with IdrAgra.

Year	1993	1994	1995	1996	1997	1998	1999	2000	2001	2002	2003	2004	2005	2006	2007	2008	2009	2010	2011	2012	2013	2014
Growing period	145	127	163	163	147	131	141	139	135	146	118	145	137	138	137	138	134	138	143	123	142	156
Emergence date	20 Apr	22 Apr	22 Apr	18 Apr	29 Apr	25 Apr	24 Apr	20 Apr	28 Apr	23 Apr	19 Apr	22 Apr	27 Apr	20 Apr	12 Apr	22 Apr	13 Apr	20 Apr	10 Apr	27 Apr	16 Apr	13 Apr
Emergence date (Julian)	111	113	113	110	120	116	115	112	119	114	110	114	118	111	103	114	104	111	101	119	107	104
Harvest date	12 Sep	27 Aug	02 Oct	28 Sep	23 Sep	03 Sep	12 Sep	06 Sep	10 Sep	16 Sep	15 Aug	14 Sep	11 Sep	05 Sep	27 Aug	07 Sep	25 Aug	05 Sep	31 Aug	28 Aug	05 Sep	16 Sep
Harvest date (Julian)	256	240	276	273	267	247	256	251	254	260	228	259	255	249	240	252	238	249	244	242	249	260

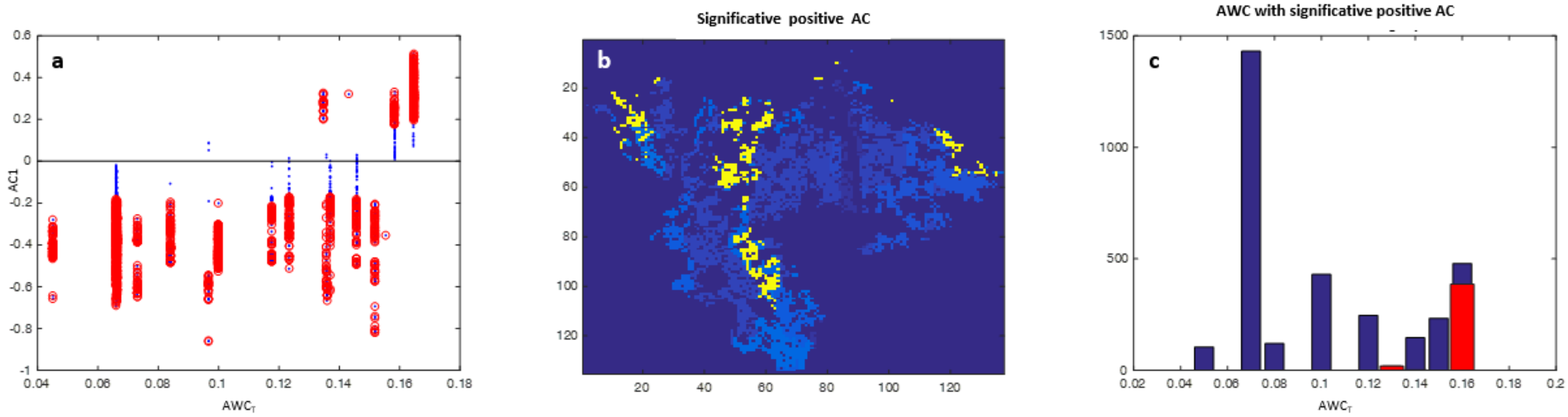

Figure 3-9: Lag-1 auto-correlation ($AC1$) of $D\text{-}TDI10$ for maize, using standardized series: (a) $AC1$ values as a function of available water content of the transpirative layer; red dots present significative auto-correlation ($p = 0.05$); (b) map representing the location of significative and positive values: in light blue is represented the IDMPB, in yellow the cells with significative and positive auto-correlation ($p = 0.05$); (c) histogram of the AWC_T: in blue are represented all the cells, in red the ones with significative and positive auto-correlation of the standardized values.

To analyse the relationship between soil types and the $D\text{-}TDI$, the lag-1 auto-correlation ($AC1$), using standardized series, was plotted against the available water content (AWC_T; Figure 3-9a). It should be noted that 6% of the cells (Figure 3-9), all characterized by high available water content ($AWC_T = 0.16$), show positive $AC1$ even after standardization ($AC1 = 0.2$; $p = 0.05$). This suggests that a large storage capacity of the soil can always compensate the short-time variability of the meteorological conditions.

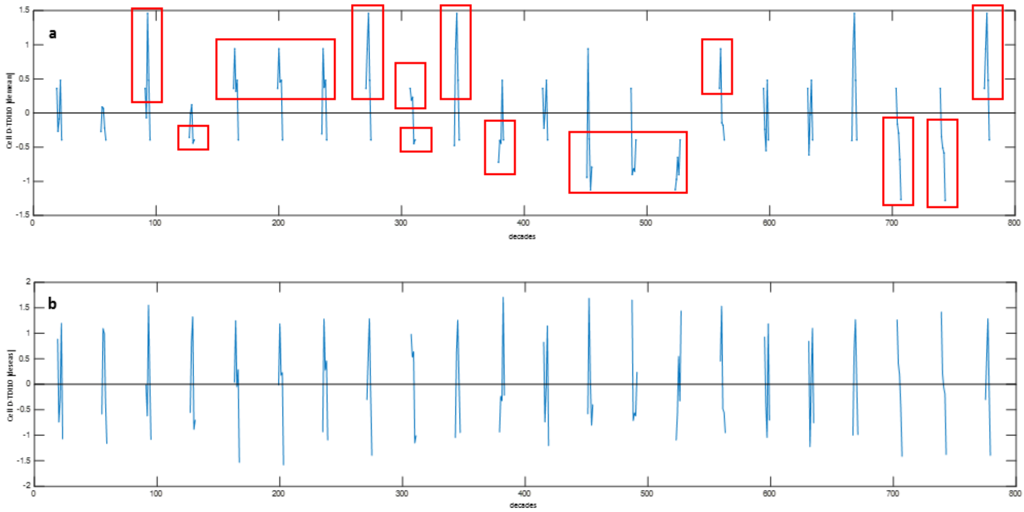

Figure 3-10: Example of the $D\text{-}TDI10$ series for a single cell. (a) Series obtained after removing from each term of the $D\text{-}TDI10$ series the mean of the whole series (i.e. the long-term mean); (b) series obtained after removing from each term the yearly mean.

$D\text{-}TDI20$ auto-correlation shows a similar pattern with respect to $D\text{-}TDI10$ and, also, a similar memory of the process (Figure 3-8c), presenting a significative auto-correlation at lag 1 and 2 (i.e. 40-50 days). The main difference is that no cell shows a positive significative auto-correlation at lag 1 when the inter-annual effect is removed (Figure 3-8d). The behaviour is the same also considering the $D\text{-}TDI30$ auto-correlation (Figure 3-8e, f). No information can be inferred for a time lapse longer than 60 days as, in the study area, the maize growing period simulated with IdrAgra (Table 3-3) is on average of 140 days and the daily transpirative deficit is negligible until mid-May.

Grass

The auto-correlation of $D\text{-}TDI10$ series for permanent grass (Figure 3-11a) is positive and significative for all the cells, with a linear decrease of the auto-correlation as a function of the lag. The persistence is generally equal to 3 lags (i.e. 30 days). Moreover, the auto-correlation is linearly correlated to the AWC of the transpirative layer.

The mean periodical seasonality was removed assuming that the grass $D\text{-}TDIn$ data can be represented by a periodical and sinusoidal signal, with peaks roughly corresponding to cutting cycles. Thus, each cell $D\text{-}TDIn$ series was independently fitted by a sinusoid, used to standardize the data. In particular, the mean μ_f and the standard deviation σ_f of equation 3.15 were calculated for each time step t over a moving window centred on the element f_t, and the f_t^* series was constructed.

In this case, the $AC1$ (Figure 3-11b) is positive $(0.20 - 0.30)$ and significative for most of the cells, whereas the analysed values are not correlated at higher lags. The $AC1$ and the AWC_T are independent, meaning that the linear relationship detected by analysing the original data series are mostly explained by the seasonality of the $D\text{-}TDI10$.

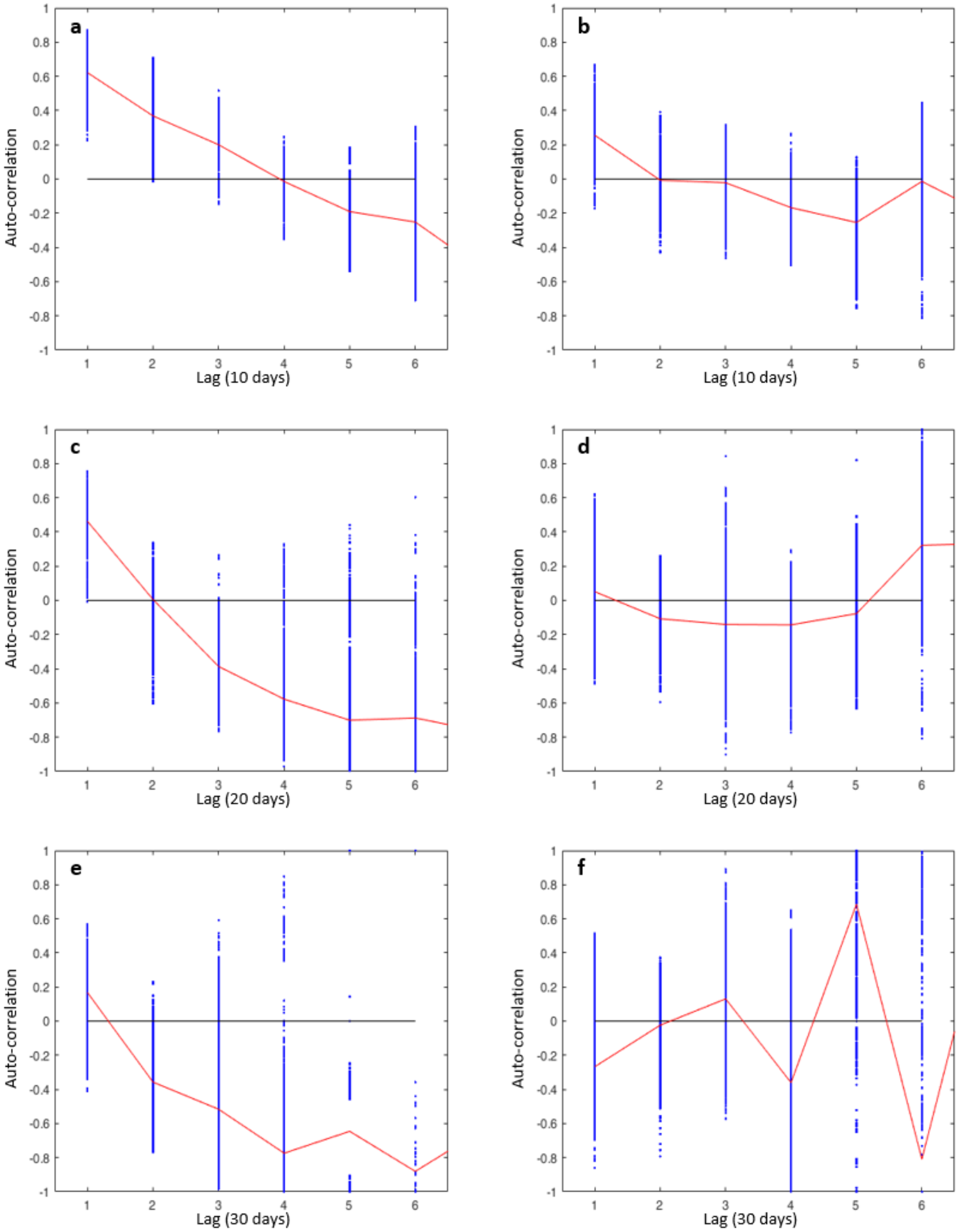

Figure 3-11: Auto-correlogram of $\boldsymbol{D\text{-}TDI}$ for permanent grass: auto-correlograms obtained analysing (a) original series and (b) standardized series, obtained by removing seasonal fluctuations, of $\boldsymbol{D\text{-}TDI10}$; (c) original series and (b) standardized

series of $D\text{-}TDI20$; (e) original series and (f) standardized series of $D\text{-}TDI30$. In the diagrams, blue dots represent cell-values and red line is the mean.

The auto-correlograms for $D\text{-}TDI20$ (Figure 3-11c, d) and $D\text{-}TDI30$ (Figure 3-11e, f) show the same trends. In particular, as highlighted for maize, the persistence of $D\text{-}TDI20$ (Figure 3-11c), generally equal to 1 lag (i.e. 20 days), is almost completely due to the seasonality (Figure 3-11d). On the contrary, when the seasonality is removed, $D\text{-}TDI30$ (Figure 3-11f) show a negative and significative $AC1$, probably related to grass cutting cycles, that have a periodicity of about 30 days.

In this case, the auto-correlation patterns at different lags did not seem directly related to the differences in available water content, probably due to the variations of the transpiration related to the cuts, that could mask the relation between storage capacity and short-time variability of the meteorological conditions.

3.4.4 CROSS-CORRELATION ANALYSIS OF $D\text{-}TDI$ AND SPI

Cross-correlation analysis between $D\text{-}TDI$ and SPI was performed to assess the response of the agricultural drought to meteorological drought. In this case, indices calculated over the same time period – 10 days – were compared (i.e. $D\text{-}TDI10$ versus $SPI\text{-}10d$, $D\text{-}TDI20$ versus $SPI\text{-}20d$, and $D\text{-}TDI30$ versus $SPI\text{-}30d$). Results in the case of maize and permanent grass crops are illustrated below.

Maize

$SPI\text{-}10d$ and $D\text{-}TDI10$ for maize original series (Figure 3-12a) are positively and significantly cross-correlated (in general, $CC0 < 0.3$) for the most of the cells within the simulation domain (81%), with a persistence of 4 lags (i.e. 40 days); the correlation is possibly due to causality (SPI influences $D\text{-}TDI$) and common influencing factors (e.g. absence of clouds produces less rain and higher evapotranspiration).

Cells with lower lag-0 cross correlation ($CC0$) have a moderately high available water content ($AWC_T = 0.15$), and are mainly located in two zones in the western part of the study area, characterized by silt loamy soils. As a general feature, $CC0$ decreases with increasing levels of available water content of the transpirative layer.

Cross-correlograms obtained by longer integration periods (Figure 3-12c, e) show similar features, but with a longer memory ($CC0$ on average of 80 and 150 days for 20 and 30 days integration periods respectively). Cells with higher AWC_T usually have $CC1$ and $CC2$ higher than $CC0$. Although part of this correlation persistence may be explained by the partial overlap between data used for the indices calculation (i.e. the series are composed by indices calculated over adjacent time periods of 10 days), these cells, as expected also by considering the positive $AC1$, show a response that is more related to the longer-term precipitation than to the last 10-day period; in fact, the increment in the CC at higher lags with respect to $CC0$ means that the system shows a delayed response of 1 to 2 10-day periods to SPI variations (and thus, precipitation patterns).

By removing the seasonal effect (Figure 3-12b, d, f), $CC0$ is often still positive for all the integration periods, but its value is reduced to a half, demonstrating that almost half of the $CC0$ was related to the annual meteorological conditions. In particular, the average persistence is reduced to a lag equal to the integration period of the considered indices (e.g. 10 days when considering $D\text{-}TDI10$ and $SPI\text{-}10d$, 30 days for the $D\text{-}TDI30$ and $SPI\text{-}30d$).

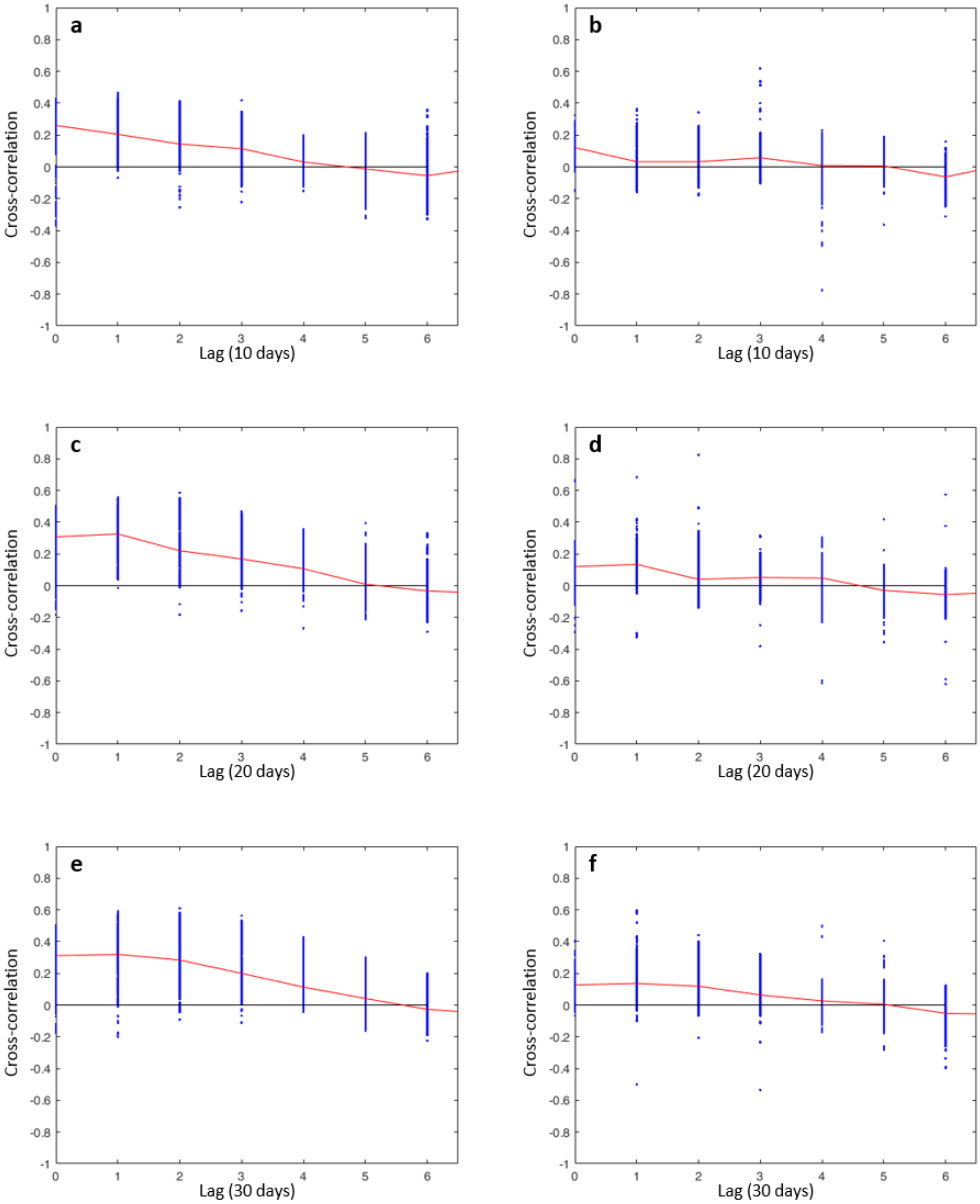

Figure 3-12: Cross-correlogram of $D\text{-}TDI$ vs SPI for maize: cross-correlograms obtained analysing (a) original series and (b) standardized series of $D\text{-}TDI10$ and $SPI\text{-}10d$; (c) original series and (b) standardized series for $D\text{-}TDI20$ and $SPI\text{-}20d$; (e) original series and (f) standardized series of $D\text{-}TDI30$ and $SPI\text{-}30d$. In the diagrams, blue dots represent cell-values and red line is the mean.

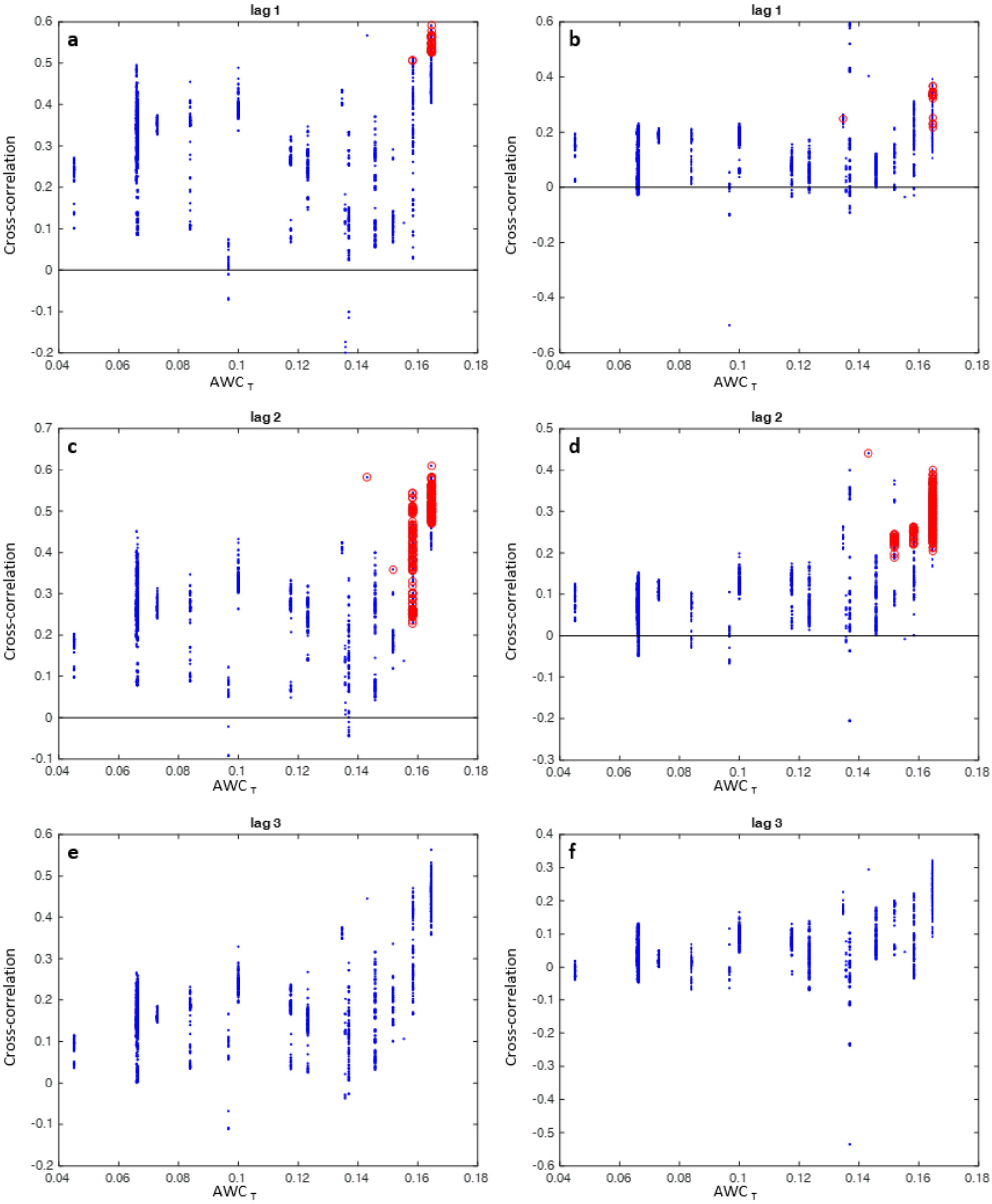

Figure 3-13: Cross-correlation values of $D\text{-}TDI30$ vs $SPI\text{-}30d$ for maize plotted against the available water content of the transpirative layer (AWC_T). On the left side, the original series and, on the right side, the standardized series: (a) and (b) lag-1 cross-correlation ($CC1$); (c) and (d) $CC2$; (e) and (f) $CC3$. In the diagrams, blue dots represent cell-values and the red circles show the cells that present a CC coefficient (e.g. $CC2$) significatively higher than the previous CC coefficients (e.g. $CC0$, $CC1$).

On the other hand, notwithstanding the integration period, the same relationship seems to exist between AWC_T and the cross-correlation of the deseasonalized series. With AWC_T lower than 0.11, $CC0$ is often both significantly greater than zero and than $CC1$ and $CC2$, showing a direct short-time effect of SPI on $D\text{-}TDI$. Whereas, with AWC_T higher than 0.155, the fraction of cells with significant $CC0$ is lower, while the number of cells showing $CC2$ significantly positive, and higher than their $CC0$, increases sharply.

A lower $CC0$ for soils with high AWC_T values could indicate that $D\text{-}TDI$ does not respond readily to the precipitation fluctuations when the soil water content can compensate for temporary reductions of water availability; this phenomenon should be linked to a memory effect in the $D\text{-}TDI$. On the contrary, when the yearly fluctuations were removed, the AC of the $D\text{-}TDI$ (§ 3.4.3) was relevant only for $AWC_T > 0.16$, while no significant auto-correlation was detected with lower AWC_T, that could have a significant memory of less than 10 days (i.e. a significative AC could be identified integrating the $D\text{-}TDI$ over shorter accumulation periods), and that could affect to some extent the CC for those soils. To analyse this aspect, the cross-correlation values of $D\text{-}TDI30$ and $SPI\text{-}30d$ at lag 1 to lag 3 have been plotted against the AWC_T (Figure 3-13). In both the series (i.e. the original series on the left side and the standardized series on the right side), for AWC_T higher than 0.155 (i.e. silt loamy and loamy soils), there is a number of cells that have $CC2$ higher than the respective $CC0$, suggesting for these soils a 20 days lag in the response. Although less pronounced, an analogous behaviour is detectable on lower integration periods.

Grass

Cross-correlograms of $D\text{-}TDI$ and SPI for permanent grass (Figure 3-14) are highly influenced by seasonal fluctuation of $D\text{-}DTI$, related to the multiple cuts of the fields, that influence their transpirative response as well as the soil water deficit, more than the precipitation pattern. $CC0$ (Figure 3-14a) is generally very low and not significative, with the exception of a number of cells characterized by lower AWC_T, which have a positive $CC0$. No correlation is detected at higher lags. By removing the seasonal fluctuations (Figure 3-14b), cross-correlation is substantially equal to 0 for all lags.

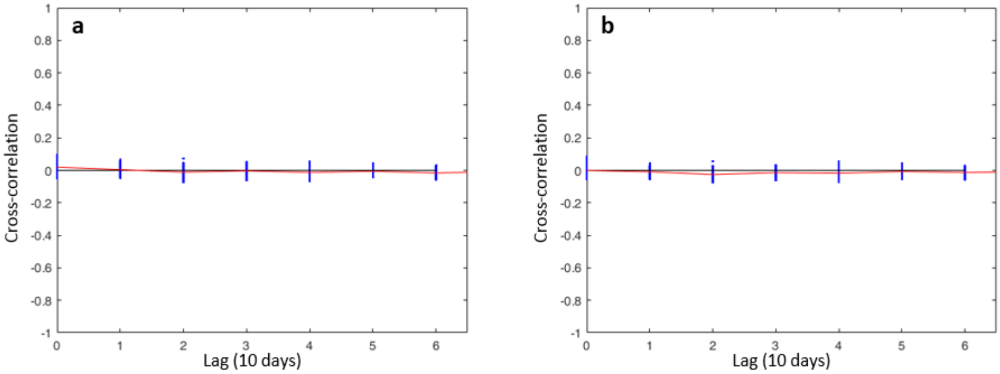

Figure 3-14: Cross-correlogram of $D\text{-}TDI$ vs SPI for permanent grass: cross-correlograms obtained analysing (a) original series and (b) standardized series of $D\text{-}TDI10$ and $SPI\text{-}10d$. In both diagrams, blue dots represent cell-values and red line is the mean.

3.5 DISCUSSION AND CONCLUSIONS

Monitoring agricultural drought is a difficult task because it depends both on meteorological forcing and on hydrological fluxes related to soil properties, crop type and stage of growth (Mishra & Singh 2010). Therefore, to improve our management of agricultural drought it is necessary to take into account these features on adequate spatial and temporal scales. In this study the Transpirative Deficit Index ($D\text{-}TDI$) has been described as an agricultural drought index focusing on overcoming the limitation of other approaches, not taking into account with sufficient detail land cover and crop properties. The $D\text{-}TDI$ responds to the actual transpirative deficit to determine the level of drought experienced by a crop. Because the $D\text{-}TDI$ relies both on climate and fine-resolution land cover and soil data, it can provide a much more accurate measure of drought at the irrigation district scale than what could be achieved through meteorological drought indices such as SPI or $SPEI$, and other rain-based agricultural drought indices.

The ability of $D\text{-}TDI$ to provide a spatial and temporal description of agricultural drought across the Media Pianura Bergamasca Irrigation District is explored in this chapter. The $D\text{-}TDI$ response was particularly studied taking into consideration two crops widespread in the study area: the former is maize, the most typical summer crop within the Po River plain, and the latter is permanent grass, an annual crop characterized by having 4-6 cuts during the summer period. A correlation analysis was adopted with three main objectives: (1) to compare SPI and $SPEI$ at different time steps, in order to assess whether the use of SPI could be sufficient to describe the meteorological drought behaviour in the study area, (2) to study the characteristics and the memory of $D\text{-}TDI$ as a function of soil and crop variability, and (3) to assess the response of the $D\text{-}TDI$, that provides information about agricultural drought, to SPI variations, that describe meteorological drought, over diverse temporal steps.

The cross-correlation analysis of SPI and $SPEI$ series demonstrates that the two selected meteorological indices are in a good accordance; thus, SPI is sufficient to characterize the meteorological drought pattern of the study area. The auto-correlation analysis of $D\text{-}TDI$ shows a positive auto-correlation with a persistence of 30 days, both considering maize and grass. As a matter of fact, the removal of annual fluctuations in the analysis demonstrates that the auto-correlation is related to the general meteorological pattern of a single year, that can be roughly classified as a “wet” or “dry” year. Moreover, the auto-correlation analysis suggests that soils characterized by high available water content can compensate for the short-time variability of precipitation pattern, at least for maize; whereas no clear signal was detected for grass. Finally, a positive significative correlation between $D\text{-}TDI$ and SPI was observed for maize, with a persistence of 40 days, while no relation between the indices was found for grass. Finally, soils with higher available water content can compensate for temporary reductions of water availability, while for soils with lower available water content a short-time effect of SPI on $D\text{-}TDI$ could be identified (i.e. they could have a significant memory of less than 10 days).

Modelling efforts utilizing the $D\text{-}TDI$ have significant potential to shed light on the vulnerability of agricultural areas to dry spells and drought. Future work using the $D\text{-}TDI$ as a tool to map drought prone areas could therefore improve the ability of farmers and irrigation district managers to cope with agricultural droughts and set up adaptation actions.

With respect to future developments of the study, further research should be conducted to verify the behaviour of $D\text{-}TDI$ when applied to other crops and soil types. As the $D\text{-}TDI$ was calculated in this study using an historical data record, it can be used as a planning tool. Anyway, the index has potential to be applied for real-time or provisional monitoring. In fact, the index can be calculated by incorporating real-time or provisional meteorological data, giving the opportunity to stakeholders to promptly cope with slight or severe agricultural droughts. Furthermore, the assimilation of time-dependent variables (e.g. crop growing stages and/or soil moisture derived from remote sensing) into the modelling framework might be helpful to improve the index accuracy.

4 ESTIMATING MAIZE YIELD USING LANDSAT IMAGERY IN NORTHERN ITALY

4.1 ABSTRACT

In many studies over the last thirty years, time series of remotely sensed vegetation indices have been used to estimate vegetation productivity over extended geographic areas, based on the fact that the biomass production depends on the amount of photosynthetically active solar radiation absorbed (APAR) by the vegetation, and on the vegetation light interception capacity. However, this approach have shown some obstacles when used in the modelling of crop yields. In particular, the maximum light use efficiency parameter showed to be scale- and sensor-specific (i.e. its value differs widely in studies conducted at different spatial scales and with different sensors) especially in the case of C_4 crops.

This chapter describes an algorithm developed to estimate maize yield starting from time series of Landsat data, and its application over the Irrigation District of Media Pianura Bergamasca. Within the method, the daily photosynthetically active radiation was computed from the spatially interpolated daily shortwave radiation registered at the meteorological stations, while the fraction of photosynthetically active radiation was derived from a Landsat fAPAR dataset, smoothed and gap-filled by the BOKU research group. Information about the phenological parameters were extracted from the same Landsat dataset, to define the integration limits over which the yearly APAR must be calculated. Year-specific maize masks, derived from yearly land use maps obtained by the Lombardy regional dataset, were used to filter the APAR maps. Mean maize yield annual data, derived from the National Statistical Inventory for the Bergamo province, were used to calibrate the light use efficiency parameter, and thus to calculate the maize grain production.

The algorithm results highlight the feasibility of estimating maize productivity from high resolution satellite time series and inventory data. In particular, the light use efficiency estimation fell within the range of those calculated from satellite-based algorithms in other studies. The study demonstrates that using a more accurate APAR estimation, obtained by removing the baseline fAPAR value within each pixel, would not lead to a better result in terms of productivity. Despite the promising results obtained in this study, further research, and particularly more site-specific crop phenology and yield data collected in extended field campaigns, is needed to better calibrate and validate the gross primary production estimates. In fact, with recalibrated light use efficiency values, the modelled annual productivity could match groundtruth data and the same approach could also be adopted for other crops.

4.2 INTRODUCTION

Time series of remotely sensed vegetation indices are valuable data sets to be used in studies that fall in various Earth science fields. In particular, they have been successfully used to map land cover, vegetation productivity and status, from the field level to extended geographic areas (Atzberger 2013; Pettorelli et al. 2005; Rembold et al. 2013).

The relationship between the spectral properties of crops and their biomass has been recognized since the first spectrometric field experiments, and the use of satellite imagery spectral data for this purpose was started in the early 1970s (Atzberger 2013; Rembold et al. 2013).Tucker & Sellers (1986) described the first attempt to obtain quantitative estimates of crop productivity. Encouraging results for North America were obtained by Running and Nemani (1988). Ever since then, different approaches to crop productivity estimation have been developed and adopted, ranging from simple regression equations to the use of remotely sensed data within simple and more complex crop growth models (Atzberger 2013; Rembold et al. 2013).

A group of widely employed approaches to estimate the terrestrial productivity and to monitor and forecast crop yields is based on Production Efficiency Models (PEMs; e.g. Field et al. 1995; Running et al. 2000). The underlying theory behind them is that the biomass production of a crop depends on the amount of photosynthetically active solar radiation (PAR) absorbed, as well as on the crop PAR interception capacity:

$$GPP_d = \varepsilon_b \cdot PAR \cdot fAPAR \tag{4.1}$$

where GPP_d $(g \cdot m^{-2} \cdot d^{-1})$ is the daily gross primary production, expressed as carbon uptake, $fAPAR$ (adimensional) is the fraction of incident PAR absorbed by the canopy, mainly dependent on the leaf area of the canopy (Monteith 1972), PAR $(MJ \cdot m^{-2} \cdot d^{-1})$ is the photosynthetically active radiation incident on the canopy, and ε_b $(g \cdot MJ^{-1})$ represents the maximum light use efficiency (LUE) when the environment (i.e. temperature and soil moisture) is not limiting for plant carbon uptake (Rembold et al. 2013; Running et al. 2000; Running & Zhao 2015; Xin et al. 2015). Provided that enough images are available, the seasonal integration of equation 4.1 gives the capability of estimating the biomass and, finally, the harvestable yield (Rembold et al. 2013; Xin et al. 2013; Xin et al. 2015).

This theoretical approach shows some main obstacles to the successful prediction of crop yields. In particular, the main problem lies in the determination of the core parameter in these models, the maximum light use efficiency ε_b, whose value differs widely in studies at different spatial scales (Chen et al. 2011; Xin et al. 2015). In fact, although the maximum light use efficiency is generally taken as a biome-specific physiological parameter describing the photosynthetic activity under optimal conditions (e.g. Garbulsky et al. 2010; Gilabert et al. 2015; Running & Zhao 2015), different studies (e.g. Bandaru et al. 2013; Singer et al. 2011; West et al. 2010; Xin et al. 2013) demonstrated that a constant value would be inappropriate to estimate yields for different crops, especially for C_4 plants (e.g. maize). In particular, typical ε_b for croplands in site-scale studies range from 2.40 to 4.24 $gC \cdot MJ^{-1}$ for C_4 crops, and from 1.41 to 1.96 $gC \cdot MJ^{-1}$ for C_3 (e.g. wheat, soybean, alfalfa) crops (e.g. Chen et al. 2011; Kalfas et al. 2011; Lobell et al. 2002), while in many large-scale studies ε_b is set between $0.604 - 1.08$ $gC \cdot MJ^{-1}$ (e.g. Lobell et al. 2002; Running & Zhao 2015).

To consider only a specific crop within the yield forecasting procedure, the ideal approach should be to consider year- and crop-specific subsets of pixels (i.e. image masks), to take into account only vegetation indices (VIs) information pertaining to the crop of interest for each year of analysis. However, identifying mono-cropped ("pure") pixels is not always feasible with low resolution (i.e. above $6.25\ ha \cdot pixel^{-1}$) imagery, as the recorded spectral radiances provide mostly mixed information from several surface types, lowering the reliability of the derived information products (Atzberger 2013; Rembold et al. 2013).

Furthermore, it is necessary to define appropriately the timespan over which the integration of results provided by equation 4.1 can be conducted. This can be done identifying the most significant phenological stages from the time series image dataset (i.e. emergence and harvest). Most of the phenology detection studies aimed to capture single seasonal crop growth cycles per year (e.g. Jamali et al. 2015; Sakamoto et al. 2005; Zeng et al. 2016). However, the phenological variability in agriculture, especially connected with winter crops interposed to summer crops, demonstrates the necessity of identifying more than one crop cycle per year (e.g. Li et al. 2014; Patel & Oza 2014). Finally, remote sensing of phenology has been largely applied using MODIS normalized difference vegetation index (NDVI) data with a spatial resolution of $250\ m$, which is often not sufficient to describe highly fragmented agricultural land surfaces.

This chapter describes an approach to estimate crop yield from low resolution time series of images (Landsat data). In particular, the method tries to overcome the obstacles illustrated above, with respect to the possibility to identify year- and crop-specific subsets of "pure" pixels over a large agricultural territory, to the definition of integration limits based on the detection of crop phenology, and to the calibration of the maximum light use efficiency parameter. Finally, an application of the algorithm to predict the maize crop yield over the period 2009-2013 within the Irrigation District of the Media Pianura Bergamasca (IDMPB) is illustrated and discussed.

4.3 MATERIALS AND METHODS

The general workflow of this chapter is briefly introduced hereafter and schematized in Figure 4-1 . The main assumption adopted in the procedure is similar to what considered to derive the crop productivity from MODIS data (Running & Zhao 2015). Basically, the procedure relies on the relationship between daily gross primary production (GPP) and photosynthetically active radiation intercepted by the crop (equation 4.1), integrated between the start of season (SOS) and the end of season (EOS), to obtain the carbon stored in the biomass at the end of the growing cycle.

The working steps, shown with different colour in Figure 4-1, are described below:

(1) The fAPAR dataset (Landsat fraction of Absorbed Photosynthetically Active Radiation smoothed and gap-filled by the BOKU research group) was initially used to extract the phenological parameters, using a newly developed algorithm that allows the identification of multiple crop cycles within the same year.

(2) The daily photosynthetically active radiation (PAR) series were computed for each pixel of the Landsat image starting from the daily shortwave radiation measured at the available agro-meteorological stations, spatially interpolated using the inverse distance weighted method (§ 2.2; Bartier & Keller 1996). The daily available photosynthetically active radiation (APAR)

series were then calculated using the Monteith (1972) equation. Information about SOS (start of season) and EOS (end of season), derived from the first step of the procedure (1), was then used to define the integration limits and calculate the yearly APAR for each pixel of the Landsat cover.

(3) Year-specific masks of Bergamo province, derived from yearly land use maps distributed by the Lombardy Regional Authority (ERSAF 2012; Lombardy Regional Authority 2016), were then used to filter the APAR maps in order to select only pixels characterized by maize. For each year, maize pixels were used to calculate the yearly average APAR value. As no reliable estimation of light use efficiency ε_b is available for Landsat data over the study area, its value for maize was calibrated against yield data, derived from the National Statistic Inventory (Lombardy Regional Authority & Istituto Nazionale di Statistica 2016), with an approach similar to Xin et al. (2015).

(4) Maize productivity maps were generated for the period 2009-2014, and pilot test areas (§ 2.8) were used to validate the algorithm results.

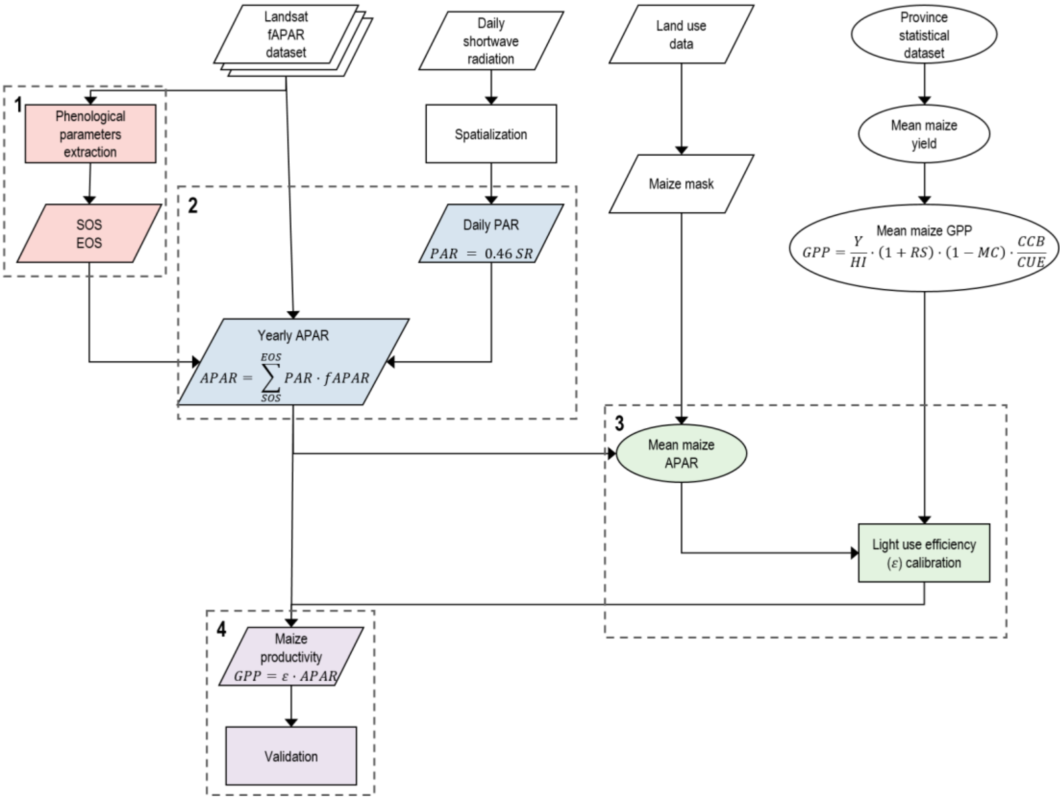

Figure 4-1: Flowchart of the methodology adopted in chapter 0. Rectangles represent elaborations, ovals synthetic point data, and parallelograms spatially distributed data. Working steps are represented by different colours. In the flowchart, the following notations are adopted: PAR Photosynthetically Active Radiation, APAR Absorbed Photosynthetically Active Radiation, fAPAR fraction of Absorbed Photosynthetically Active Radiation, SOS Start Of Season, EOS End Of Season, GPP Gross Primary Production, Y Yield, HI Harvest Index, RS Root to Shoot ratio, MC Moisture Content, CCB Carbon Content in Biomass, CUE Carbon Use Efficiency.

4.3.1 PHENOLOGICAL PARAMETERS EXTRACTION

An approach to extract phenological parameters was implemented for detecting uni- and bi-modal growing patterns. This approach can also handle growing seasons spanning over different years, since the vegetation index (VI) time-series is considered as a whole (i.e. not segmented by year before the analysis). The extraction, run separately for each pixel, consists of three steps:

(1) Using a moving window approach, the BOKU multi-temporal time series of VI was linearly interpolated and analysed to extract local maxima and minim for each pixel (Li et al. 2014). To select an appropriate time-span of analysis aimed to capture more than one growing season over the study area, many pixels time series were visually and automatically analysed with different moving window sizes. According to this test, a window size of nine images was selected, that, as VI data are provided every 15 days, corresponds in the ability to detect a potential minimum and/or maximum within 135 days.

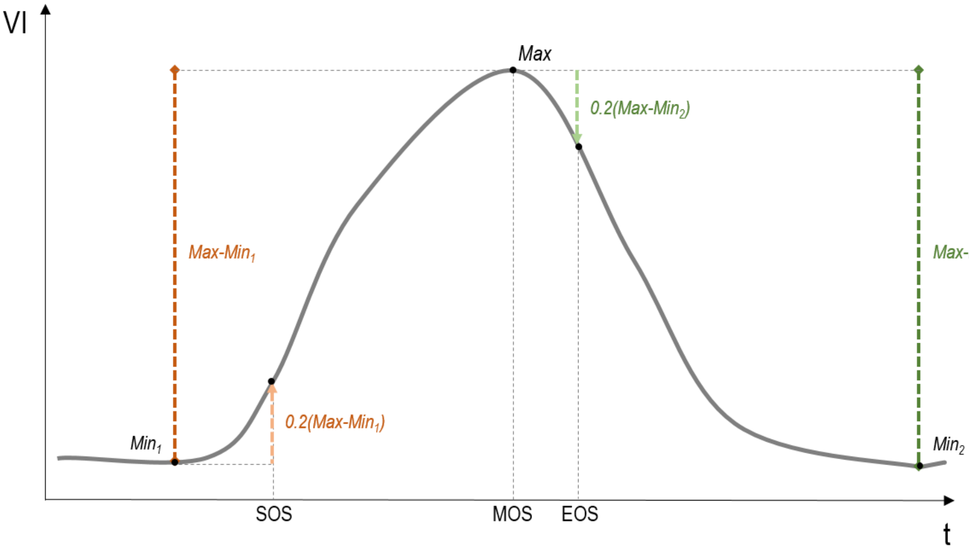

Figure 4-2: Selection of Start Of Season (SOS), Maximum Of Season (MOS), and End Of Season (EOS) dates. Max: maximum, Min$_1$: minimum before the maximum VI, Min$_2$: minimum after the maximum VI.

(2) The resulting values were automatically screened to identify the absolute maxima and minima for each crop cycle. Because pixels with sparse vegetation may also have peaks and troughs that are unrelated to vegetation development, spurious peaks were discarded if the corresponding VI values were less than the 20% of the distribution of the absolute maxima VI detected over the area. Moreover, the maximum was accepted if the amplitude between the considered maximum and the surrounding minima ($Max - Min_1$ and $Max - Min_2$ in Figure 4-2) was more than 0.2. Potential peaks and troughs were also checked to verify that only one trough was falling between peaks; where present, successive potential peaks with no intervening trough were merged (Li et al. 2014).

(3) Finally, the algorithm provided the timing of key phenological periods for each pixel (Figure 4-2). In particular, the maximum of season (MOS) was defined at the time when the highest VI value is reached during the growing season. Successively, the SOS was detected using a relative threshold (Atzberger et al. 2013; White et al. 2009), namely when VI reached the 20% of the amplitude ranging from the minimum VI value preceding the MOS, and the MOS VI value. Finally, EOS was defined at the time when VI decreased of the 20% with respect to the amplitude from MOS VI value and the minimum VI value following the MOS.

A linear regression analysis between the calculated dates for SOS and EOS and available sowing and harvesting dates was finally set for fields falling in the groundtruth database (§ 2.8) in order to verify the accuracy of the obtained metrics.

4.3.2 TOTAL $APAR$ (AVAILABLE PHOTOSYNTHETICALLY ACTIVE RADIATION) ESTIMATION

The daily $APAR$ was determined for each pixel of the Landsat cover using the Monteith (1972) equation:

$$APAR_d = PAR \cdot fAPAR \tag{4.2}$$

where $APAR_d$ ($MJ \cdot m^{-2} \cdot d^{-1}$) is the daily photosynthetically active radiation, PAR ($MJ \cdot m^{-2} \cdot d^{-1}$) is the photosynthetically active radiation incident on the canopy, estimated as 0.45 of total incident shortwave radiation (Heinsch et al. 2006; Running & Zhao 2015), and $fAPAR$ (adimensional) is the fraction of incident PAR absorbed by the canopy, obtained at a daily time step by computing, for each pixel, the linear interpolation between two successive images of the BOKU fAPAR dataset.

As applying a general cropland mask cannot account for the effects of variability between pixels, mainly derived from productivity differences related to different photosynthetic pathways (i.e. C_3 and C_4; Xin et al. 2015), the procedure filtered the $APAR_d$ maps on the basis of yearly specific maize mask, available in the land use database of the Lombardy Regional Authority.

Two different versions of the approach for the light use efficiency calculation were tested, both considering the computation of the integral of the crop cycle between the start of the growing period (SOS) and the beginning of the descending phase of the seasonal $fAPAR$ profile, identified as the EOS (Meroni et al. 2013; Rembold et al. 2013):

$$APAR_y = \sum_{SOS}^{EOS}(APAR_d) \tag{4.3}$$

where $APAR_y$ ($MJ \cdot m^{-2}$) is the photosynthetically active radiation over the growing season and $APAR_d$ ($MJ \cdot m^{-2} \cdot d^{-1}$) is the daily photosynthetically active radiation.

The main difference between the two approaches is that in the first one (Figure 4-3a) the integral was calculated after the removal of the baseline $fAPAR$ value, thus the equation 4.3 can be written as:

$$APAR_y = \sum_{SOS}^{EOS}[PAR \cdot (fAPAR_d - fAPAR_{min})] \tag{4.4}$$

where $APAR_y$ $(MJ \cdot m^{-2})$ is the photosynthetically active radiation over the growing season, PAR $(MJ \cdot m^{-2} \cdot d^{-1})$ is the photosynthetically active radiation incident on the canopy, $fAPAR_d$ (adimensional) is the fraction of incident PAR absorbed by the canopy for the day d, and $fAPAR_{min}$ (adimensional) is the minimum fraction of incident PAR absorbed by the canopy for the year y (Meroni et al. 2013).

In the second approach (Figure 4-3b), the baseline $fAPAR$ value was not removed, thus the equation 4.3 is written as:

$$APAR_y = \sum_{SOS}^{EOS}(PAR \cdot fAPAR_d) \tag{4.5}$$

following an approach similar to that applied for obtaining the MODIS product (Rembold et al. 2013; Running & Zhao 2015).

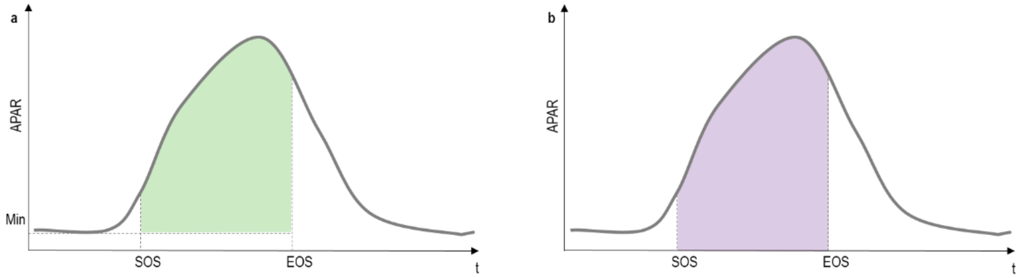

Figure 4-3: Two approaches tested for the computation of the yearly available photosynthetically active radiation (APAR): in (a) the integral is calculated cumulating the daily APAR exceeding the baseline fAPAR (Min) between the Start Of Season (SOS) and the End Of Season (EOS); in (b) the minimum fAPAR value is not removed.

4.3.3 PRODUCTIVITY CALIBRATION

To quantify the productivity, a regression model calibrated using inventory-based agricultural maize yield statistics was set (Lombardy Regional Authority & Istituto Nazionale di Statistica 2016; Rembold et al. 2013). The available crop yield statistics for the Lombardy region are aggregated at the province level. For this reason, the average yearly APAR values were extracted, considering only pixels selected by year-specific maize masks, over the same territorial extension, as the calibration of regression approaches need an appropriate crop mask (Rembold et al. 2013).

In particular, inventory based productivity GPP_{inv} $(g \cdot m^{-2})$ for maize was estimated using crop-specific factor for dry weight, harvest index, root to shoot ratio, and estimated harvest efficiency in conjunction with yield data:

$$GPP_{inv} = \frac{Y}{HI} \cdot (1 + RS) \cdot (1 - MC) \cdot \frac{CCB}{CUE} \tag{4.6}$$

where Y $(g \cdot m^{-2})$ is the dry crop yield; MC (adimensional) is the moisture content at harvest, HI (adimensional) is the harvest index, RS (adimensional) is the root to shoot ratio (i.e. the ratio of belowground biomass to aboveground biomass), CCB $(g \cdot g^{-1})$ is the carbon content in biomass (i.e. the percentage of dry biomass composed of carbon), and the CUE (adimensional) is the carbon use efficiency (i.e. the ratio of the net primary production to the gross primary production; Lobell et al. 2002; Xin et al. 2013). The carbon content in biomass is estimated to be $0.45 \quad g \cdot g^{-1}$ (Hicke et al. 2004; Xin et al. 2015), while the carbon use efficiency is 0.46 for all the crops (Bandaru et al. 2013; Choudhury 2000). The other parameters are crop-specific; values for maize, obtained from Lobell et al. (2002) and Xin et al. (2013), are reported in Table 4-1.

Table 4-1: Conversion factors used for the gross primary production estimate. Sources of data: (a)Xin et al. (2013), (b)Lobell et al. (2002).

Parameter	***Grain maize***	***Silage maize***
Root to shoot ratio (RS)	0.18(a)	0.18(a)
Harvest index (HI)	0.53(a)	1.00(b)
Moisture content (MC)	0.11(a)	0.65(b)

Theoretically, average inventory-based GPP (GPP_{inv}) at the province level for the maize crop, and average APAR calculated over the same territorial scale for maize can be used to compute the mean light use efficiency ε_b for this crop:

$$\varepsilon_b = \frac{GPP_{inv}}{APAR} \tag{4.7}$$

where GPP_{inv} is the yearly GPP reported in the inventory, and $APAR$ is the average APAR calculated over the same territorial scale referred to the yearly-specific masked area (Bandaru et al. 2013).

Having more than one pair $(GPP_{inv}, APAR)$, a linear regression with no intercept between GPP_{inv} and $APAR$ were therefore fitted to derive the optimal ε_b^* value by minimizing the squared errors (Sjöström et al. 2013; Xin et al. 2015). ε_b^* represents the mean ε_b value estimated for each pair of $(GPP_{inv}, APAR)$ of the analysed time series.

To estimate GPP for individual crop pixels, the calibrated light use efficiency value was assigned to maize pixels, thus:

$$GPP = \varepsilon_b^* \cdot APAR_y \tag{4.8}$$

where $APAR_y$ is the photosynthetically active radiation over the growing season for the selected pixel and ε_b^* is the calibrated light use efficiency for maize (Bandaru et al. 2013).

4.3.4 PRODUCTIVITY VALIDATION

The results were then validated by a linear regression analysis between groundtruth data and satellite estimations of yields, calculated from the GPP of each individual pixel as:

$$Y = GPP \cdot \frac{HI}{1+RS} \cdot \frac{1}{1-MC} \tag{4.9}$$

where Y $(g \cdot m^{-2})$ is the dry crop yield; MC (adimensional) is the moisture content at harvest, HI (adimensional) is the harvest index and RS (adimensional) is the root to shoot ratio. The maize crop-specific parameters are reported in Table 4-1 (Lobell et al. 2002; Xin et al. 2013).

4.3.5 STUDY AREA AND AVAILABLE DATA

In chapter 2 the study area of Media Pianura Bergamasca Irrigation District (IDMPB) and the available data collected and pre-processed were described. This section is focused on the estimation of the productivity of maize from the time-series fAPAR dataset provided by the Institute of Surveying, Remote Sensing and Land Information (IVFL) of the University of Natural Resources and Life Sciences of Vienna (BOKU) described in § 2.6. A second main input used to derive crop productivity was the incident short-wave radiation series at the available agro-meteorological stations located in the area, spatially interpolated using the inverse distance weighted method (§ 2.2; Bartier & Keller 1996). Year-specific masks of maize coverage over the Bergamo province were derived from the yearly land use data (§ 2.3) obtained from the Agricultural Information System of the Lombardy Region (ERSAF 2012; Lombardy Regional Authority 2016). Yield data aggregated at the province scale, derived from the Regional Statistical Inventory (§ 2.7; Lombardy Regional Authority & Istituto Nazionale di Statistica 2016), were used to calibrate the light use efficiency coefficient. The groundtruth dataset built through interviews with farmers (§ 2.8) was used to validate the results obtained from the earth observation analysis.

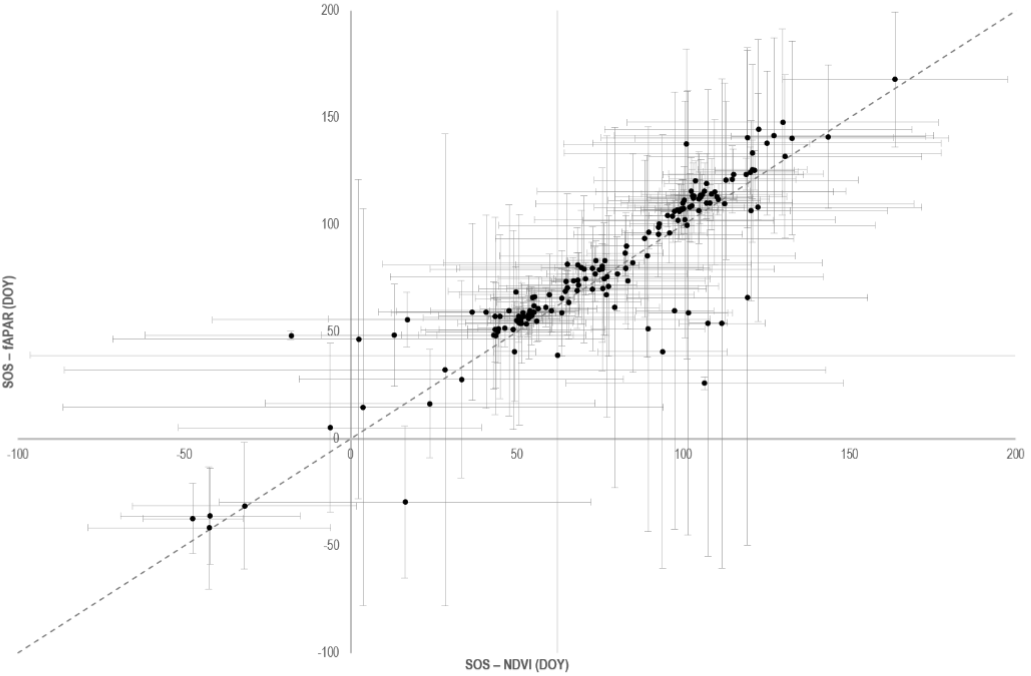

Figure 4-4: Landsat signal analysis for the detection of the Start Of Season (SOS). Comparison of the results obtained from NDVI versus fAPAR time-series: black circles represent polygon means, bars are standard deviations. DOY is Day Of Year.

4.4 RESULTS

4.4.1 EVALUATION OF PHENOLOGICAL PARAMETERS ESTIMATES

Two phenological metrics, SOS and EOS, were calculated over the time period 2009-2014 following the procedure illustrated in § 4.3.1. In order to verify the accuracy of the obtained metrics, SOS and EOS were extracted in correspondence to the fields included in the groundtruth database for the analysis of NDVI and fAPAR temporal profiles. A total of 40 groundtruth points were present in the validation dataset, considering the available fields over 6 years (2009-2014). SOS and EOS were compared with the timing of sowing and harvesting of maize fields within the groundtruth dataset by computing the regression coefficient between field and measured metrics, in order to verify the predictive capacity of the model.

The results obtained from fAPAR analysis are generally well correlated ($R^2 = 0.80$) to the NDVI results (Figure 4-4). In fact, most of the pairs of SOS and EOS detected from analysing the two VIs lay on the $1:1$ line. However, some of the pairs are in the 3rd quadrant; these values represent fields with the maxima in the first part of the considered year (e.g. 2012), which corresponding SOS was detected in the previous autumn (e.g. 2011). The few values in the 2nd and in the 4th quadrant derive from inconsistency between fAPAR and NDVI trends.

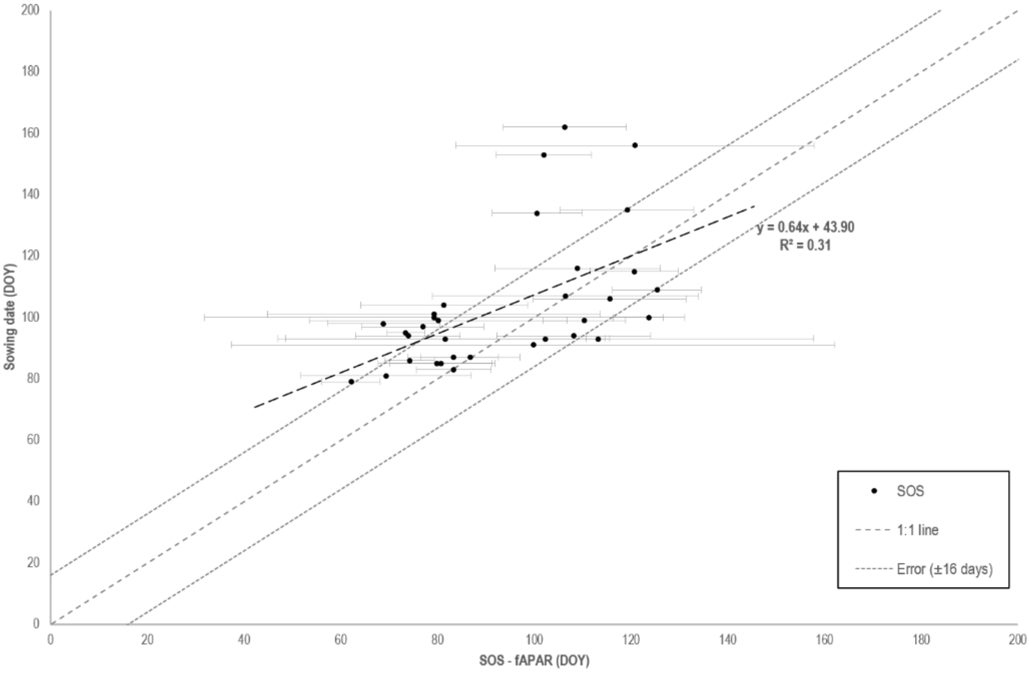

Figure 4-5: Landsat signal analysis for the detection of the Start Of Season (SOS) dates versus groundtruth sowing dates. Comparison of the results obtained in the groundtruth polygons: black circles represent polygon means, bars are standard deviations. DOY is Day Of Year.

As the analysis of the two Vegetation Index time series led to very similar results, for the present work the fAPAR time-series was selected, to have an internal coherency with the yield estimation procedure.

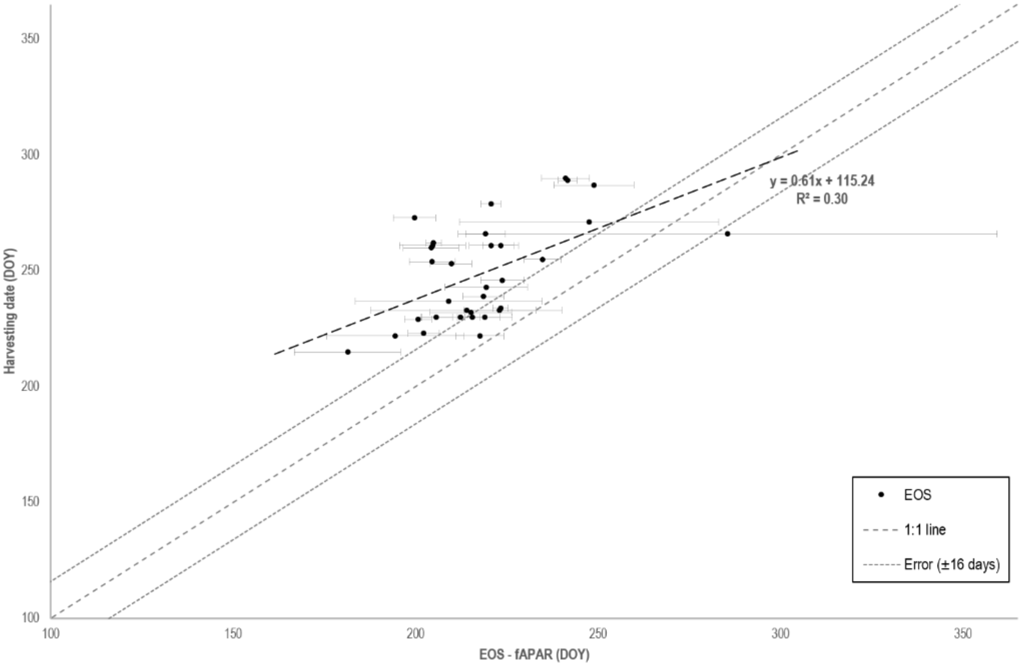

Figure 4-6: Landsat signal analysis for the detection of the End Of Season (EOS) dates versus harvesting dates. Comparison of the results obtained in the groundtruth polygons: black circles represent polygon means, bars are standard deviations. DOY is Day Of Year.

The temporal fAPAR results were then filtered, discarding situations presenting anomalous temporal profiles. In particular, minimum SOS was set on March 1st, and the difference between average EOS and average SOS over each polygon was set to be positive. In general, SOS dates are identified with respect to the groundtruth time of sowing, with an accuracy related to the year of analysis. From Figure 4-5 it can be seen that SOS dates are generally scattered, and satellite predictions are often anticipated with respect to the real time of sowing, in particular when the sowing occurs in May. The regression coefficient is $R^2 = 0.31$, and this value is mainly dependent on the smoothing and on the filtering ability to treat and analyse the fAPAR signal: the start of the season occurs at the beginning of the crop cycle when the green up effect is still very low and noise can influence the signal. The scattering of the signal was already identified by analysing EO products in Lombardy plain for many rice fields by Boschetti et al. (2009), who report an analogous regression coefficient ($R^2 = 0.38$) for emergence, after discarding pixels presenting anomalous temporal VI profiles.

The end of season detection (Figure 4-6) shows a tendency to the underestimation of the harvesting dates, and the R^2 of the interpolating line is similar to the one detected for SOS (0.30). This is because this phenological stage is not easily detectable on the basis of the fAPAR temporal signal: the EOS detected by the decrease of the fAPAR signal is mainly influenced by leaf senescence. However, the yellowing process is not always directly connected to the time of harvesting, since very often farmers take decisions about the harvesting date not only considering the crop maturity, but also based on other factors, such as the availability of a contractors for the harvesting operation.

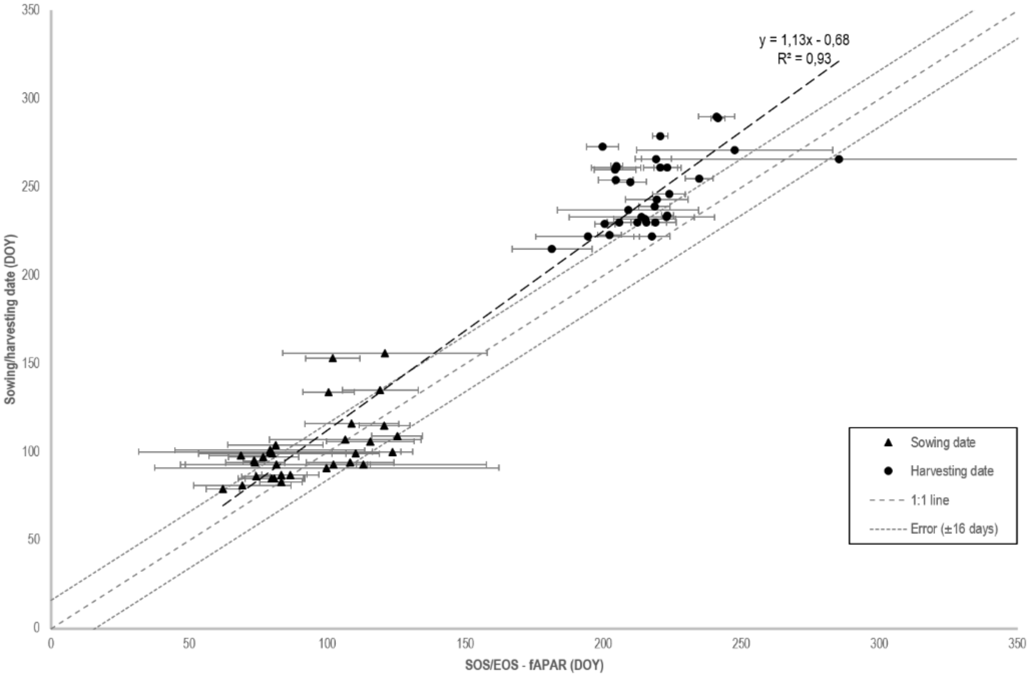

Figure 4-7: Landsat signal analysis for the detection of the Start Of Season (SOS) and End Of Season (EOS) versus sowing and harvesting date. Comparison of the results obtained in the groundtruth polygons: black points represent polygon means, bars are standard deviations. DOY, day of year.

In a successive analysis conducted considering together both phenological parameters (SOS and EOS), the agreement between the satellite derived and the groundtruth dates increases ($R^2 = 0.93$). The regression line presents a slope coefficient close to 1 (1.13), confirming that the majority of the data are close to the bisector of the first quadrant (Figure 4-7). Different estimates present an error greater than the fAPAR time step, probably related to difficulties in identifying the winter minima in the time series. In fact, cloud cover and noise in the original Landsat dataset are not always appropriately removed by the Whittaker algorithm; in the study area scenes with a low cloud cover (i.e. $\leq 20\%$) were only the 30% of the total, with good images in early-spring period scarcely represented in the dataset. Moreover, striping in the original Landsat data generate high variability within adjacent cells, as shown by the high standard deviations of both SOS and EOS.

The spatial distributions of SOS and EOS over the Media Pianura Bergamasca Irrigation District for the years of analysis (2009-2014) are respectively presented in Figure 4-10 and Figure 4-11, while Figure 4-8 shows the frequency distribution of SOS and EOS extracted from the two phenology metric maps.

SOS maps (Figure 4-10) showed an underestimation of the SOS date, particularly evident in 2012 (Figure 4-8a), when 97% of the maize area is estimated to be sown before the 16th March. When values lower than 16th March and higher than 16th June (i.e. the date range of maize sowing in the area) were removed, SOS maps showed a north-south spatial pattern; in particular, the areas characterized by a late date (mid-May to mid-June) are concentrated in the northern part of the area. However, the statistical significance of this pattern should be further analysed and validated by comparing the earth observation results to a more consistent number of groundtruths in the area; in fact, no groundtruth data are available to detect the north-south pattern. An analogous north-south spatial pattern is also detected in the EOS maps (Figure 4-11); moreover, years with early SOS generally showed anticipated EOS (i.e. 2009, 2010 and 2012).

A visual analysis conducted to verify the results within each field showed that pixels that belong to the same field generally present SOS and EOS in a reasonable range (i.e. within ± 16 days), as exemplified in Figure 4-9.

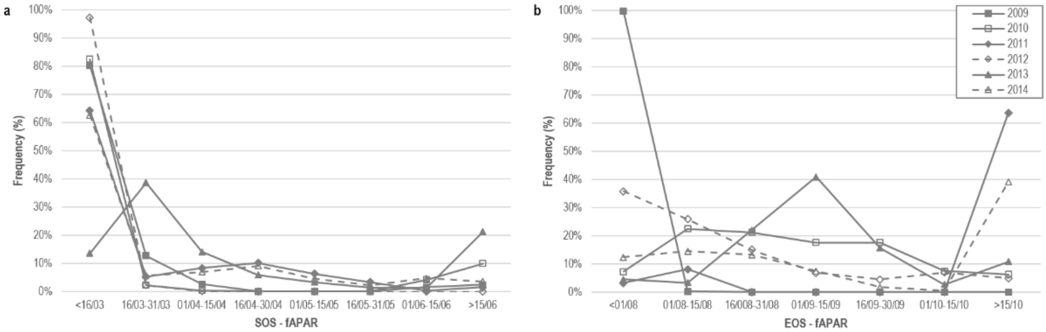

Figure 4-8: (a) Frequency distribution of Start Of Season (SOS), and (b) End Of Season (EOS) maps extracted from maize areas over the Media Pianura Bergamasca Irrigation District.

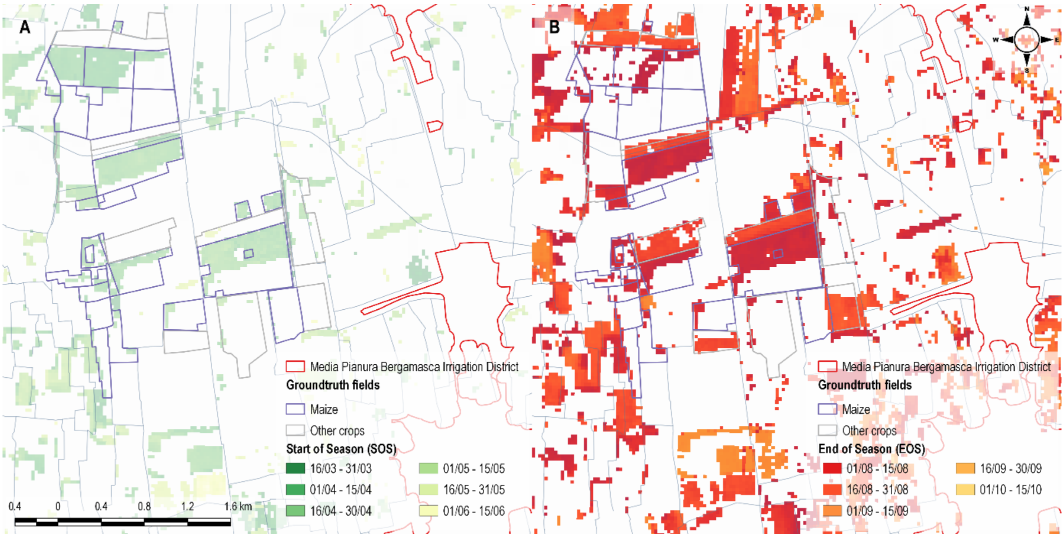

Figure 4-9: Zoom on (a) Start Of Season (SOS) and (b) End Of Season (EOS) maize maps for 2011 over a farm included within the groundtruth dataset. Maps were produced through the Landsat fAPAR data analysis, after the outliers removal.

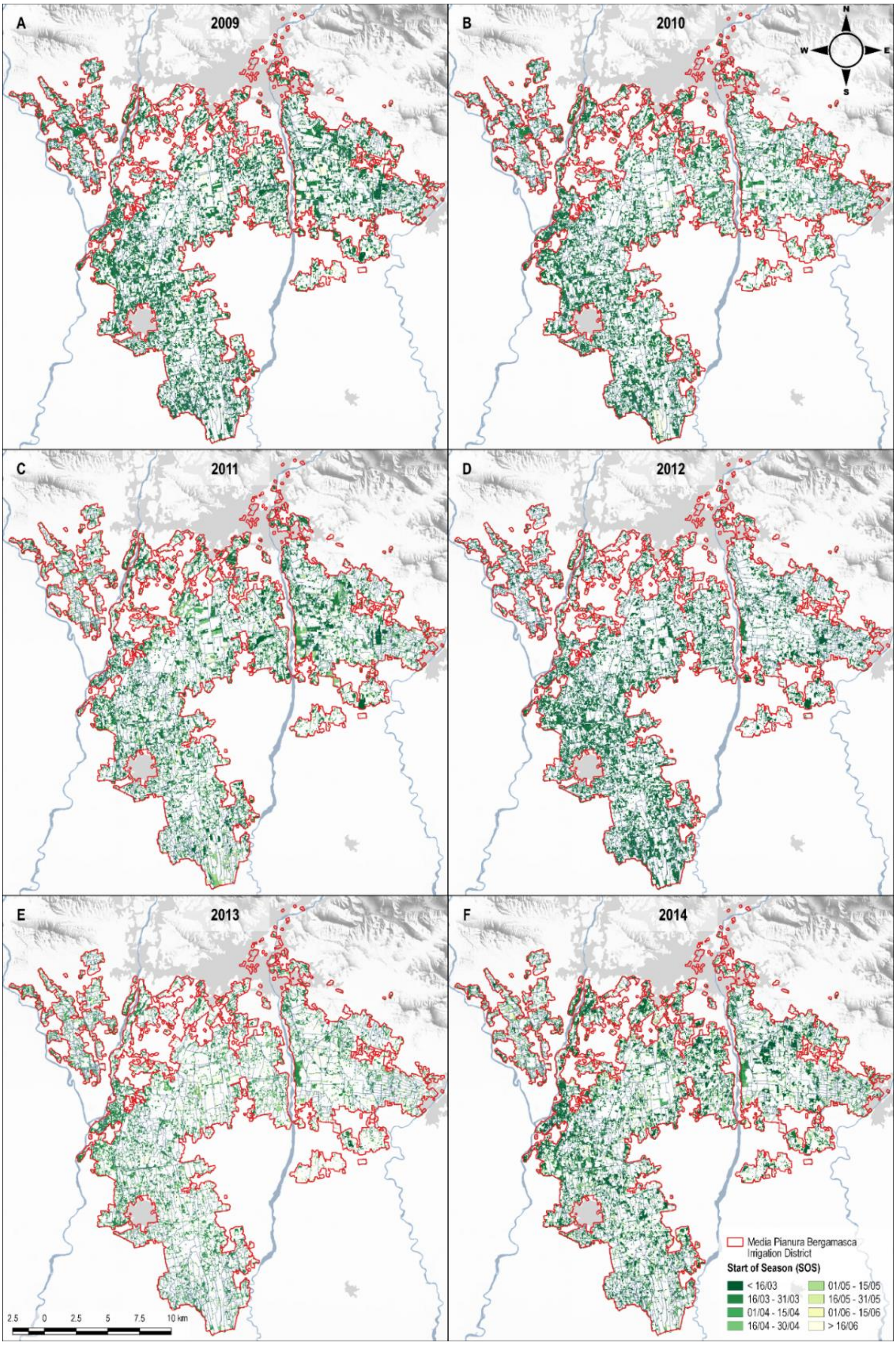

Figure 4-10: Start Of Season (SOS) maps over the Media Pianura Bergamasca Irrigation District, as produced from the Landsat fAPAR data analysis. Only maize pixels are represented.

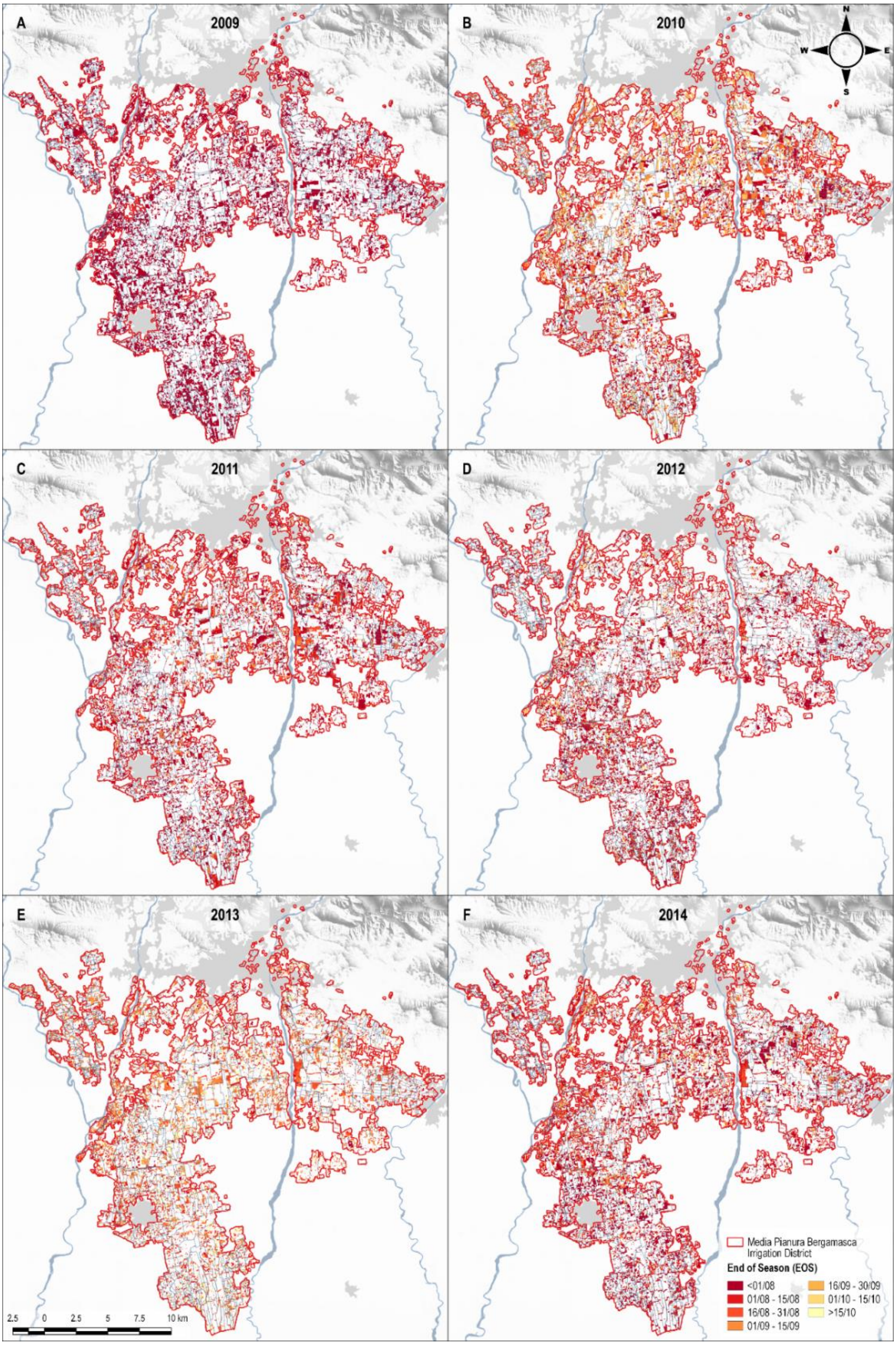

Figure 4-11: End of Season (EOS) maps over the Media Pianura Bergamasca Irrigation District as produced from the Landsat fAPAR data analysis. Only maize pixels are represented.

4.4.2 PRODUCTIVITY CALIBRATION

The maize grain yield over the Bergamo province territory (Lombardy Regional Authority & Istituto Nazionale di Statistica 2016) resulted in $113 \pm 23 \quad q \cdot ha^{-1}$. The average value is well within the yields registered for the other Lombardy provinces where maize is a dominant crop (e.g. $111 \pm 11 \quad q \cdot ha^{-1}$), while the higher variance is mainly due to an anomalous yield value in 2013, with a reported yield of $70 \quad q \cdot ha^{-1}$.

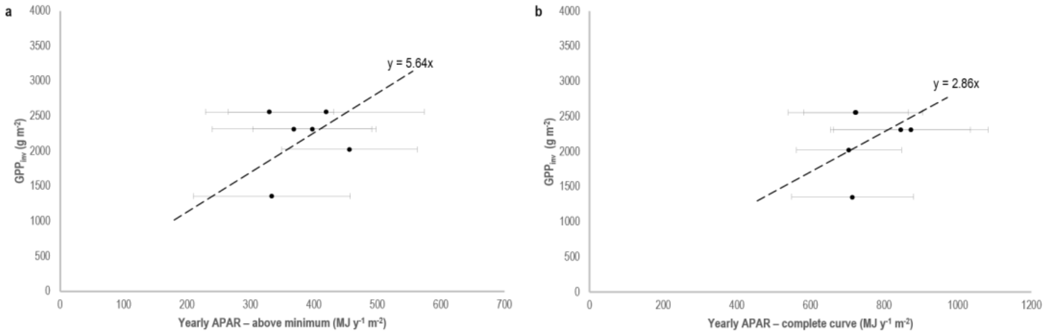

Figure 4-12: Calibration curves of maize maximum light use efficiency ε_b obtained by applying the approaches presented in § 4.3.2: in (a) yearly APAR is calculated by cumulating the daily APAR exceeding the baseline fAPAR level; in (b) the baseline fAPAR is not removed. Black points represent polygon means, bars the standard deviations.

Two different calibrated values of ε_b^* were obtained by a linear regression with no intercept of yearly maize $APAR$ averaged over the province territory and GPP_{inv} (Figure 4-12), as a function of the different approaches used. In particular, when the yearly APAR is calculated removing the baseline fAPAR level (Figure 4-12a), ε_b^* equals $5.64 \quad g \cdot MJ^{-1}$, while computing the yearly APAR without taking into account this baseline (Figure 4-12b) ε_b^* resulted to be $2.86 \quad g \cdot MJ^{-1}$.

The second value was within the range of the light use efficiency coefficients calibrated with similar methodology reported in the literature, that ranged between $0.89 - 3.35 \quad g \cdot MJ^{-1}$ (Bandaru et al. 2013; Xin et al. 2015). In particular, the value is similar to the one derived by Xin et al. (2013) for a regional scale analysis of maize grain production (i.e. equal to $2.23 \quad g \cdot MJ^{-1}$) when applying a fractional cropland mask using fAPAR data derived from MODIS, and in the range of the maize variability calculated by site-scale analysis (i.e. $2.44 - 3.94 \quad g \cdot MJ^{-1}$) in the same study.

The ε_b^* derived using both approaches were applied on the year-specific maize masks to derive grain maize yields over the study area.

4.4.3 PRODUCTIVITY VALIDATION

The methodology was validated against groundtruth grain yield production for medium to late maturity maize (FAO 600-700). This choice derived from two considerations: (1) early maturity maize was discarded because the phenological parameters estimation was not able in many cases to correctly detect SOS and EOS (§ 4.4.1); and (2) silage maize is harvested in different growing phases, depending on various meteorological, agronomic and economic reasons.

The estimated yield, averaged over the polygons bordering the fields of the groundtruth dataset, is plotted against the groundtruth yields in Figure 4-13. Both methods to derive ε_b^* showed to overestimate the actual yield, with a similar linear slope coefficient: 0.83 when the yield is estimated by cumulating the daily APAR exceeding the base daily fAPAR level (Figure 4-13a), and 0.81 when the baseline is not considered (Figure 4-13b). However, this second approach produced a smaller variability (i.e. lower standard deviations) around the polygon means. The overestimation, as already pointed out by precedent studies (Lobell et al. 2002; Xin et al. 2013), is probably due to the GPP contribution of vegetation other than crops when estimating the yield, while the removal of the baseline fAPAR level did not improved the estimation.

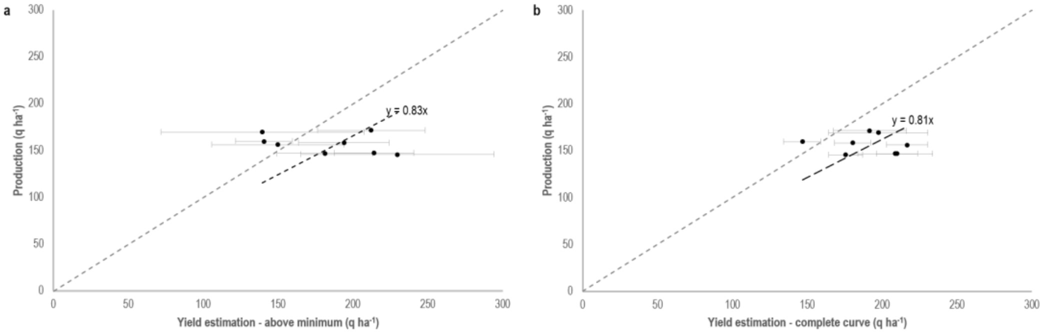

Figure 4-13: Grain maize yield estimation from Landsat analysis versus actual production. Comparison of the results obtained in the groundtruth polygons by applying the approaches presented in § 4.3.2: in (a) yearly APAR is calculated by cumulating the daily APAR exceeding the base daily fAPAR level; in (b) the minimum daily fAPAR level is not removed; black points represent polygon means, bars are standard deviations.

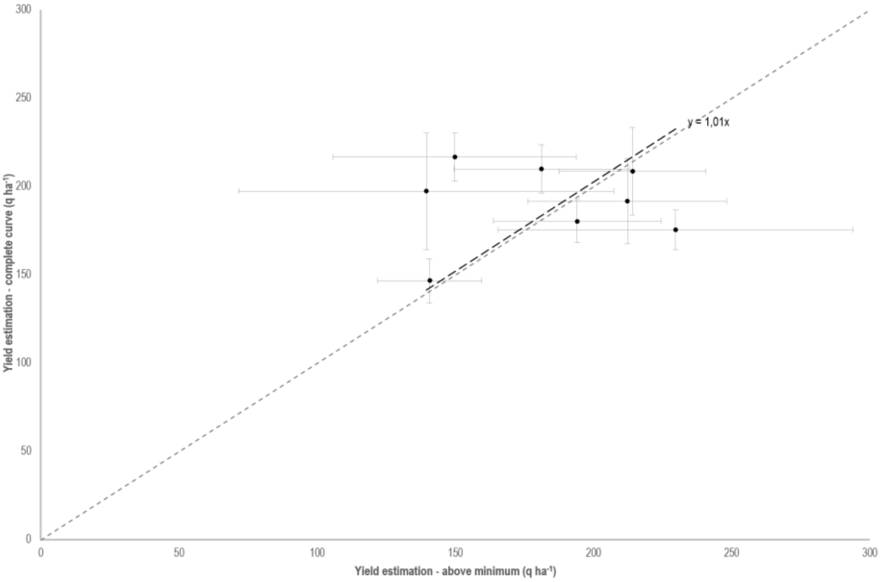

Figure 4-14: Grain maize yield estimation obtained from Landsat analysis. Comparison of the results for the groundtruth polygons by adopting the two approaches for the estimation of ε_b^*presented in § 4.3.2. On the x-axis the yearly APAR is calculated by cumulating the daily APAR exceeding the baseline fAPAR; on the y-axis the baseline fAPAR level is not removed. Black points represent polygon means, bars the standard deviations.

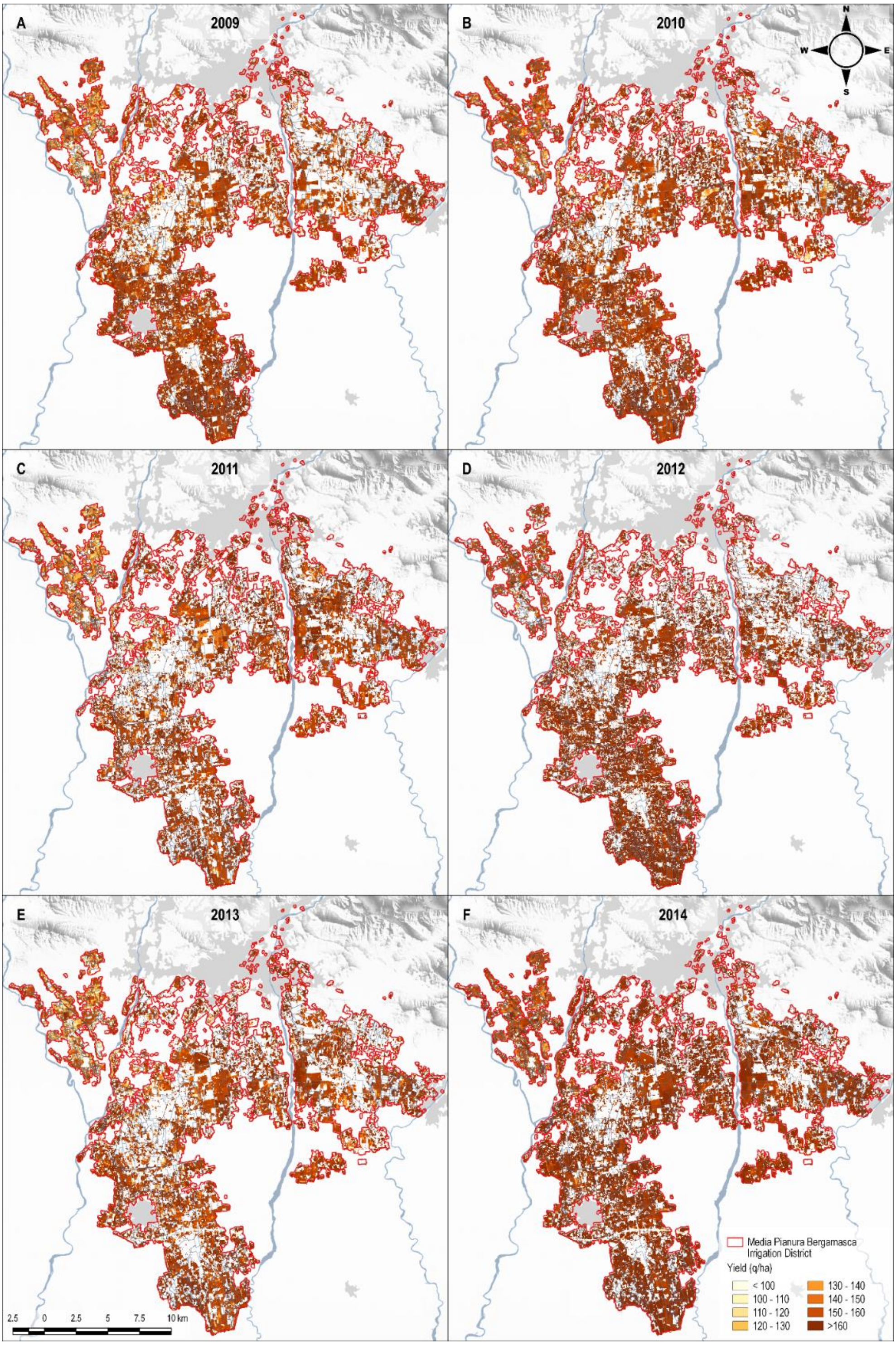

Figure 4-15: Yield estimation over the Media Pianura Bergamasca Irrigation District by means of the Landsat fAPAR data analysis; ε_b^* was calculated without removing the baseline fAPAR. Only maize pixels are represented.

A direct comparison of the yield estimations obtained in the groundtruth polygons by using the two proposed approaches is plotted in Figure 4-14, demonstrating that whatever is the choice for the estimation of ε_b^*, the result in terms of production would be analogous. As a matter of fact, the regression line presents a slope coefficient equal to 1.01, that does not deviate from the bisector of the first quadrant.

Yield spatial distribution over Media Pianura Bergamasca Irrigation District for the years of analysis (2009-2014) are presented in Figure 4-15. Although the result quality is also determined by the accuracy of the phenological parameters estimation, a clear inter-annual variability is detectable; in particular, 2009 yield was estimated as the lowest ($196.7 \pm 45.6 \quad q \cdot ha^{-1}$, Figure 4-15a), while 2012 ($249.1 \pm 60.2 \quad q \cdot ha^{-1}$, Figure 4-15d) and 2014 ($253.3 \pm 67.7 \quad q \cdot ha^{-1}$, Figure 4-15f) were the more productive years. Moreover, a definite spatial pattern is detectable, as the areas in the south of the IDMPB and near Serio River had higher yields.

4.5 DISCUSSION AND CONCLUSIONS

This chapter illustrates an algorithm developed to estimate the maize yield starting from time series of Landsat data, and its application over the Irrigation District of Media Pianura Bergamasca. Information about the phenological parameters of maize to define the integration limits over which the yearly $APAR$ must be calculated are extracted by the Landsat dataset. With respect the productivity estimation, the developed procedure shows that inventory and satellite data can be integrated to produce annual spatially distributed estimates of cropland productivity, while site-specific field data can be used to validate the relationship between $APAR$ and productivity (in the case of the present study, this was done for the maize crop).

The phenological parameter extraction algorithm highlights good potential in deriving key phenological stages for maize crop such as sowing-emergence and harvesting, respectively estimating SOS and EOS, from high resolution satellite time series of fAPAR (and NDVI). However, the results presented in this study show two main weaknesses. Firstly, cloud cover and noise in original Landsat data are not appropriately removed by the Whittaker algorithm, not allowing to correctly detect the winter minimum in the time series. As a matter of fact, in the study area scenes with a low cloud cover (i.e. $\leq 20\%$) were only the 30% of the total, with good images in early-spring period scarcely represented in the dataset. Given the quality of data from Landsat, better results in the application of the algorithm could be reached by using data from Sentinel, when they will be more easily and widely available. Dates extracted from satellite data for a discrete number of fields showed to be underestimated with respect to observed groundtruths. This could be partially due to the method adopted for setting the SOS and EOS thresholds and could be overcome by setting more appropriate thresholds (White et al. 2009) defined on the basis of data collected over more extensive field measurement campaigns. The major advantage of the satellite-based approach is the estimation of phenological parameters in a spatially distributed way; for the case study maps of phenological parameters derived from satellite data showed patterns that correspond to the fields geometry.

A crop-specific light use efficiency (ε_b^*) estimation method was applied within the calculation of the maize yield. In particular, ε_b^* was calculated as the slope of the linear regression between the average maize yield over the study area and the considered time period taken from Regional Statistic Inventory, and the average APAR value calculated for the maize pixels over the same spatial extension and time period. The ε_b^* estimated value fell within the range of the coefficients calibrated with other satellite-based algorithms. The study demonstrates that using a more accurate APAR estimation within the calculation of ε_b^*, obtained by removing the baseline fAPAR value within each pixel, does not lead to a better result in terms of productivity estimate. Inventory data were used as a determining factor in calibrating the light use efficiency, thus in estimating the productivity. While comparison with mean yields statistical inventory provides useful information, basing the calibration solely on this information is not sufficient for a reliable calibration of the model. In fact, yield inventories at the Province scale often lack in data accuracy and, due to their coarse spatial resolution, the sample size is too small to accurately calibrate the model. Shortwave radiation data from flux towers would be also useful for the calibration, but they are limited in space and time, and previous studies (e.g. Bradford et al. 2005; Lobell et al. 2002) reported large discrepancies between light use efficiency values retrieved by remote sensing models and fields measurements. Future research is needed to better calibrate and validate the gross primary production estimates on the basis of yield data collected in extended field campaigns, or using a combination of statistical inventory data and groundtruth yields. With accurate ε_b^* values, the modelled annual productivity could reach a better match with groundtruth data.

5 APPLICATION OF TRANSPIRATIVE DEFICIT INDEX (TDI) TO ASSESS WATER SCARCITY IN NORTHERN ITALY

5.1 ABSTRACT

The Mediterranean is widely considered the most vulnerable European region to water scarcity, a situation of long-term water imbalance, where water abstraction exceeds the level of resources availability. In particular, irrigated agriculture, accounting for a considerable share of water abstraction, is a key sector for water management, thus areas where irrigation is used to compensate for drought impacts are prone to water shortages or scarcity. The development and the adoption of indices able to monitor water deficits at a sub-basin scale are therefore critical to recognize, understand, and address drought and water scarcity risks and impacts for their management.

This chapter aims (1) to compare the behaviour of the Transpirative Deficit Index, both as an agricultural drought ($D\text{-}TDI$) and a water scarcity ($WS\text{-}TDI$) index, in two years, respectively characterized by abundant rainfall (2014) and drought conditions (2009), and (2) to evaluate the effects of water scarcity on productivity, by comparing an earth-observation product, the yearly cumulated Absorbed Photosynthetically Active Radiation ($APAR_y$) to the $WS\text{-}TDI$ maps through an ensemble correlation analysis. Both the activities were conducted on a pilot study area located in the Irrigation District of Media Pianura Bergamasca (IDMPB), characterized by a lower availability of surface water compared to others in the district. The two indices were cumulated over a 10-days period ($D\text{-}TDI$ and $WS\text{-}TDI$) and calculated over a 22 years time lapse (1993-2014).

The visual comparison between $D\text{-}TDI10$ and $WS\text{-}TDI10$ was conducted in a critical period for maize (mid-June to mid-July), and showed that some areas, characterized by loamy soils but also by low water availability for the two years (2009, 2014), were the most prone to agricultural drought, while less retentive soils quickly reacted to precipitation variations. The effects of dry spells were mitigated by irrigation, although in some areas water availability is still not sufficient. The ensemble correlation analysis between $WS\text{-}TDI10$ and productivity data for the two years demonstrated that a positive correlation exists between the two variables, therefore productivity maps obtained from EO data can be usefully adopted in the validation of water scarcity indicators, as the shortage of water in irrigated areas leads to a reduction in the production.

The results illustrated in this chapter demonstrates that $WS\text{-}TDI$ can be used as an operational indicator in the monitoring of water shortage and scarcity in irrigated areas, allowing the periodical production of maps that could help farmers and irrigation district managers in copying with water scarcity. In particular, in this study the $WS\text{-}TDI$ indicator was used for producing decadal maps over a 22 years historical database, allowing to identify areas more prone to water shortages. However, in case of availability of real time meteorological data and water discharges at the main surface water diversions, the indicator may be adopted by an authority responsible for the monitoring of the state of agriculture (ERSAF or ARPA in the Lombardy region) to promptly inform (through newsletters or a web site) stakeholders on the water scarcity and shortages phenomena evolution.

Additionally, the indicator may be also adopted in climate change studies, allowing to visualize the evolution of water scarcity phenomena over the territory, as a consequence of changes in meteorological forcing and in the availability of water by irrigation sources.

In fact, it could be used as a useful tool to support irrigation distribution management, irrigation application and management actions involving water resources allocations or action plans to reduce water consumption over specific portions of the territory.

5.2 INTRODUCTION

Water scarcity is a situation of long-term water imbalance, where abstraction exceeds the level of water resources availability. While these events are usually quite expected to take place in areas of low water availability, they can also occur in regions characterized by abundant water resources, in connection with high population densities and/or with the use of significant volumes of water for agricultural or industrial activities (Blinda et al. 2007; European Commission 2007). When the water imbalance occurs on a shorter time scale, i.e. less than a month, it is properly defined as water shortage (Schmidt et al. 2012; Strosser et al. 2012).

The Mediterranean is widely considered the most vulnerable European region to water scarcity (e.g. Blinda et al. 2007; Spinoni et al. 2016). Irrigated agriculture, accounting for a considerable share of water abstraction, is a key sector for water management (Blinda et al. 2007). Thus, areas where irrigation is used to compensate for drought impacts are prone to water shortages or scarcity.

Quantification of water shortages in regions that depend on surface water diversions to meet agricultural demand is a significant topic in water management (Hoekema & Ryu 2016). Thus, the development and the adoption of indices able to monitor water deficits at a sub-basin scale are critical to recognize, understand, and address drought and water scarcity risks and impacts for their management (Ryu et al. 2014).

Although agricultural drought and water scarcity indices could either be calculated through hydrological models (e.g. Palmer 1965; Narasimhan & Srinivasan 2005; Sepulcre-Canto et al. 2012), or derived from remote sensing products (e.g. Kogan 1995a; Peters et al. 2002; Horion et al. 2012), both approaches have some limitation. In particular, water scarcity analyses based on hydrological modelling have never been designed for application at the basin scale. As a matter of fact, available models do not take explicitly into account water diverted and distributed, limiting the application of hydrological modelling in deriving agricultural drought indices. On the other hand, indices based on earth observation (EO) implicitly consider the irrigation distribution, but their reliability is limited in territories where crop rotations include plants with very different crop water requirements, because they are usually based on the standardization of the adopted vegetation index (VI) over an historical data series for the same pixel (Felix N. Kogan 1995).

Since agricultural drought and water scarcity involve that a continuous and intense soil moisture stress leads to a significant crop yield reduction (Strosser et al. 2012), and yield can be estimated by means of EO approaches (Rembold et al. 2013; chapter 0 if this Ph.D. thesis), remote sensed information could be used to validate results achieved by hydrological models. Theoretically, a regression relationship can be set between drought and yield (Woli et al. 2014), but its interpretation can be misleading. In fact, the application of EO based models to derive yields can be very difficult under extreme drought conditions (i.e. whose impacts are not registered in the historical records of EO products), because the regression relationship varies largely due to inter-annual variations in climate, water availability and management practices (Xin et al. 2013).

This chapter describes the characteristics of the Transpirative Deficit Index used as a water scarcity indicator ($WS\text{-}TDI$), and its application to a pilot study area located in the Irrigation District of the Media Pianura Bergamasca (IDMPB). For the application, a meteorological data series of 22 years (1993-2014) was considered, and values of two indicators, the Transpirative Deficit Index used as an agricultural drought indicator ($D\text{-}TDI$) and as a water scarcity indicator ($WS\text{-}TDI$), cumulated over a 10-day time step, were produced over a mesh with cells of $250\ m$. In this analysis, in particular, a dry year (2009) and a year characterized by abundant rainfall (2014) were taken into account. Finally, $WS\text{-}TDI$ response was compared with an EO product, the Absorbed Photosynthetically Active Radiation cumulated over the growing season ($APAR_y$), that is directly proportional to the yield (as illustrated in chapter 0 of this Ph.D. Thesis).

5.3 MATERIALS AND METHODS

The first objective of this chapter is to evaluate and compare the behaviour of $D\text{-}TDI$ and $WS\text{-}TDI$ in two years, respectively characterized by abundant rainfall and drought conditions. The flowchart of this analysis is illustrated in Figure 5-1. The Standardized Precipitation Index (SPI), a well-known meteorological index, was calculated on two accumulation periods: on 6 months ($SPI6$), that represents an accumulation period adequate to assess the meteorological drought condition over a single growing season, and on 10 days ($SPI\text{-}10d$), useful to compare the results of TDI to varying meteorological conditions. From the analysis of the trend of $SPI6$, two years were selected: one characterized by drought, and a second by abundant rainfall. Therefore, the analysis was conducted by comparing TDI, calculated with the hydrological model IdrAgra, over an accumulation period of 10 days, with four different settings:

(1) In the first run of the model, $D\text{-}TDI10$ for the dry year was computed, comparing $(D)\text{-}TD$ of each 10-day period of the selected year with the respective fitting distribution of the complete time series (1993-2014). To obtain reliable statistics, the model was fed with the land use map of the dry year for each year of analysis (e.g. a maize pixel in the dry year was treated as maize in all the time series). In this case, no information about irrigation was provided to the model;
(2) $D\text{-}TDI10$ for the wet year was computed for the wet year in a similar way. In this case, the land use map of the wet year was used for the entire simulation period (1993-2014);
(3) $WS\text{-}TDI10$ for the dry year was calculated feeding the model with land use data of the dry year. Daily meteorological dataset and daily diversions for the complete simulation period (1993-2014) were provided to the IdrAgra model, that computed the $(WS)\text{-}TD$ taking into account irrigation availability and distribution for each year;
(4) Finally, $WS\text{-}TDI10$ for the wet year was computed, by considering the land use map of the wet year for the entire simulation period (1993-2014).

Results in terms of the four indices were then visually compared for three consecutive 10-day periods, appropriately selected to cover heading and flowering growing stages of the maize crop.

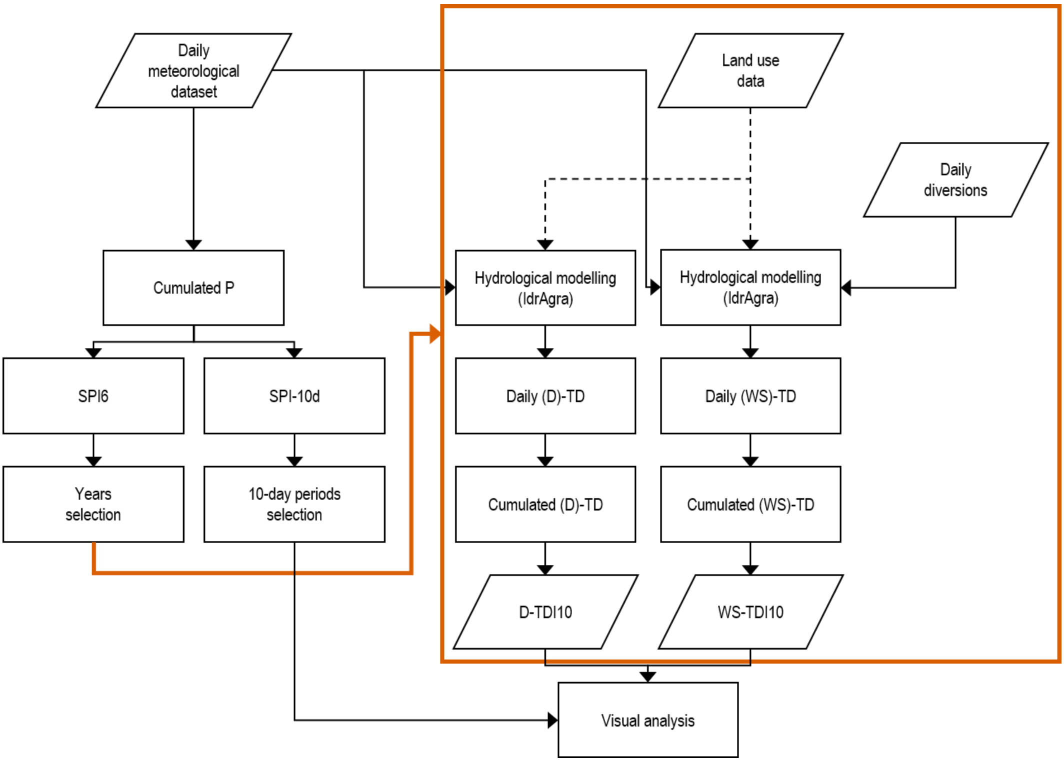

Figure 5-1: Flowchart of the methodology adopted to achieve the first objective in chapter 0. Rectangles represent elaborations, parallelograms data; dotted arrows represent input data that vary according to the year of analysis. P: Precipitation, SPI: Standardized Precipitation Index, (D)-TD: (Drought) – Transpirative Deficit, D-TDI: Drought – Transpirative Deficit Index, (WS)-TD: (Water Scarcity) – Transpirative Deficit, WS-TDI: Water Scarcity – Transpirative Deficit Index.

The second objective of this chapter, that is the evaluation of the effects of water scarcity on productivity, was performed by comparing the Absorbed Photosynthetically Active Radiation ($APAR_y$), a proxy of the maize productivity maps obtained in chapter 0, with the $WS\text{-}TDI$ results of this chapter. In particular (Figure 5-2), the $WS\text{-}TDI10$ series were generated for each year of the Landsat dataset (1999-2014), and maps were successively masked in order to consider only maize pixels. The $APAR_y$ maps were computed as described in chapter 0, cumulating between the Start Of Season (SOS) and the End Of Season (EOS) the Photosynthetically Active Radiation (PAR) – derived from the meteorological dataset – multiplied by the Landsat fAPAR product. Also the $APAR_y$ maps were then masked to analyse only maize pixels. Finally, cross-correlation and regression analyses were performed between $WS\text{-}TDI10$ and $APAR_y$.

5.3.1 THE STANDARDIZED PRECIPITATION INDEX

The Standardized Precipitation Index (SPI; McKee et al. 1993), one of the most commonly used meteorological drought indices, was used (1) to analyse the time series, in order to define the years on which focusing the subsequent elaborations, and (2) to further describe dry spells within the selected years. The calculation of the index, fully descripted in § 3.3.1, is briefly summarized in this paragraph.

SPI is computed by summing precipitation over an accumulation period, and fitting the accumulated values for the meteorological time series considered (i.e. 22 years between 1993 and 2014, that means 22 values) to a parametric statistical distribution from which non-exceedence probabilities can be transformed to the standard normal distribution ($\mu = 0, \sigma = 1$; McKee et al. 1993; Guttman 1999). Hence, the SPI value for each accumulation period of a specific year represents the number of standard deviations from the long-term mean of the standard distribution (i.e. the mean precipitation; Singleton 2012; Kingston et al. 2015).

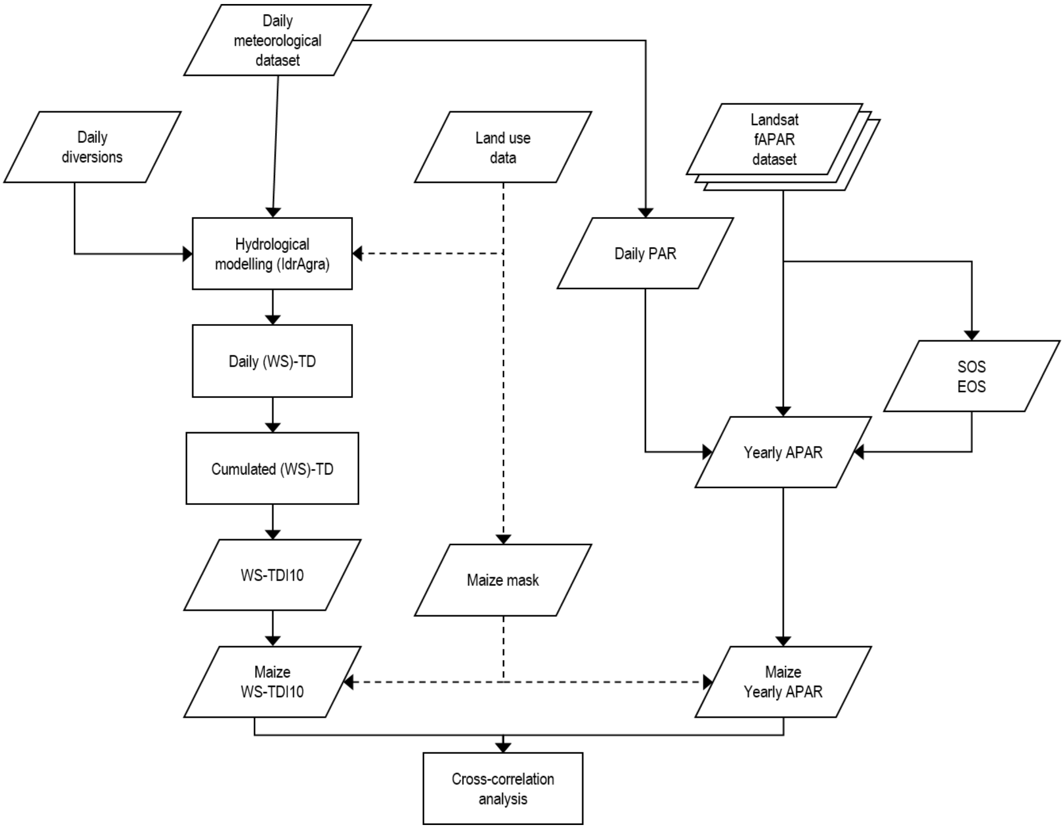

Figure 5-2: Flowchart of the methodology adopted in the second part of chapter 0. Rectangles represent elaborations, parallelograms data; dotted arrows represent input data that vary according to the year of analysis. (WS)-TD: (Water Scarcity) – Transpirative Deficit, WS-TDI: Water Scarcity – Transpirative Deficit Index, PAR: Photosynthetic Active Radiation, fAPAR: fraction of Absorbed Photosynthetic Active Radiation, APAR: Absorbed Photosynthetic Active Radiation, SOS: Start Of Season, EOS: End Of Season.

The fitting distribution for describing monthly precipitation – and to express SPI – is generally a gamma function, that was proposed as a universal model (Guttman 1999), modified to take into account for the probability of zero precipitation (McKee et al. 1993; Edwards & McKee 1997; World Meteorological Organization 2012), by the following equation:

$$H(P) = q + (1 - q)G(P) \tag{5.1}$$

where q is the probability of zero precipitation, estimated by the ratio $q = \frac{m}{n}$ (between the number of zeros in the precipitation time series, m, and the sample size, n), and $G(P)$ is the cumulative probability calculated by the gamma distribution. The modified gamma fitting distribution demostrated to fit adequatelly the time series for the study area (§ 3.4.1).

Finally, the cumulative probability $H(P)$ is transformed into the standard normal random variable (zero mean and unit variance), which gives the value of the SPI (McKee et al. 1993; Edwards & McKee 1997). Positive SPI values indicate precipitation greater than the mean, while negative values indicate precipitation lower than the median; the magnitude of departure from zero represents both drought intensity and a probability of occurrence (McKee et al. 1993; Hayes et al. 1999).

5.3.2 THE TRANSPIRATIVE DEFICIT INDEX AS AN AGRICULTURAL WATER SCARCITY INDEX

The Transpirative Deficit Index has been introduced in § 3.3.2 as an agricultural drought index ($D\text{-}TDI$). In fact, in its original formulation, it takes into account the effect of land use, soils, and climatic conditions that govern the crop transpiration, but it does not consider irrigation inputs.

The TDI is based on the transpiration deficit, computed daily by a water balance model as the difference between potential and actual transpiration. Cumulating the daily deficit over a period of n days, the integrated transpirative deficit (TDn) is obtained (Marletto & Zinoni 2004; Marletto et al. 2005) as:

$$TDn_i = \sum_{i-n}^{i-1} \left(T_p - T_a\right) \tag{5.2}$$

where n is the accumulation period, T_p (mm) is the potential transpiration and T_a (mm) is the actual transpiration.

The Transpirative Deficit Index (TDI) is then obtained by fitting the distribution of TDn with an appropriate distribution and transforming the results into the standard normal variable ($\mu = 0, \sigma = 1$). Thus, the TDI expresses the non-exceedance probability referred to its cumulated distribution. To allow direct comparison with other indicators, such as SPI, the sign of the result has been inverted, thus positive (negative) values indicate a higher (lower) crop water stress with respect to the average.

In this chapter, differently from the original formulation of the TDn (Marletto & Zinoni 2004; Marletto et al. 2005) and from what adopted for the chapter 3 elaborations, the computation of the daily deficit in each cell of the hydrological model IdrAgra was performed by taking into account explicitly the irrigation inputs (§§ 3.3.3 and 5.3.3). Thus, in this case the TDI is used as an agricultural water scarcity index, as highlighted by the use of the acronym $WS\text{-}TDI$ (i.e. Water scarcity – Transpirative Deficit Index) in the following discussion.

5.3.3 THE IDRAGRA MODEL: IRRIGATION SUPPLY

The simulation model IdrAgra (Facchi et al. 2004; Vassena et al. 2012; Gandolfi et al. 2014) is a distributed-parameter conceptual model which allows the simulation of the irrigation water distribution in agricultural areas and the estimation of the hydrological balance on a daily basis (for a complete description of the model see Annex I). IdrAgra includes four main modules devoted to specific tasks: irrigation water sources, conveyance and distribution over the territory, crop phenological stages and soil-crop water balance. The model core is the soil-crop water balance module (Facchi et al. 2004; Galelli et al. 2010), that was described in § 3.3.3 and that is briefly delineated hereinafter, while, in addition, this chapter focuses on the modelling of the irrigation supply, conducted through the use of the following two IdrAgra modules: (1) irrigation water sources and (2) irrigation conveyance and distribution.

As previously described, the soil volume referred to each cell that composes the regular mesh into which the irrigation district is divided, is subdivided into two layers: the evaporative layer, that represents the upper few centimetres of the soil (i.e. $10 \ cm$), and the transpirative layer, that represents the root zone and has a time-varying depth Z_r. The two layers are modelled as non-linear reservoirs in cascade, and hydrological processes are schematized as one-dimensional. The water percolating out of the bottom layer constitutes the recharge to the groundwater system (Facchi et al. 2004; Vassena et al. 2012; Gandolfi et al. 2014).

The dynamics of the water content in the evaporative layer of the cell is governed by the balance equation:

$$\frac{\Delta V_{\mathrm{E}}}{\Delta t} = \left[P - I + Q_i - Q_u - E - Q_e - \Delta Q_p\right]_t \tag{5.3}$$

where V_E (mm) is the water content of the evaporative layer of each cell, P $(mm \ \ d^{-1})$ is the rainfall rate, t (d) is the daily time step, I $(mm \ \ d^{-1})$ is the canopy interception, Q_i $(mm \ \ d^{-1})$ is the net inflow to the cell (irrigation supply), Q_u $(mm \ \ d^{-1})$ is the net runoff from the cell, E $(mm \ \ d^{-1})$ is the evaporation rate, Q_e $(mm \ \ d^{-1})$ is the outflow to the transpirative layer and ΔQ_p $(mm \ \ d^{-1})$ is the variation in the ponding water.

A similar equation holds for the dynamics of the water content in the transpirative layer:

$$\frac{\Delta V_{\mathrm{T}}}{\Delta t} = [Q_e - T \pm Q_s]_t \tag{5.4}$$

where V_{T} (mm) is the water content of the transpirative layer of each cell, T $(mm \ \ d^{-1})$ is the transpiration rate, Q_e $(mm \ \ d^{-1})$ is the inflow from the evaporative layer, Q_s $(mm \ \ d^{-1})$ is the outflow from the root zone to the deeper subsoil ($Q_s > 0$) or the capillary rise rate ($Q_s < 0$; Facchi et al. 2004; Vassena et al. 2012; Gandolfi et al. 2014).

The description of the water conveyance and distribution reflects the typical structure of the irrigation network in most districts of the Po River plain. The district is subdivided into a number of subdistricts, i.e. each single unit of the territory that receives continuous (non-turned) irrigation supply from one or more sources. During the irrigation season, water derived from the sources is conveyed to the subdistricts, and each of them receives a fixed share of the flow that is diverted from the sources supplying that specific subdistrict through the irrigation network. In practice, an incidence matrix is used to represent the links between the sources and the subdistricts, and two numerical values are associated with each active link: the fraction of the diverted discharge which is conveyed to the subdistrict and the conveyance efficiency (Galelli et al. 2010; Vassena et al. 2012).

Distribution within each subdistrict takes place with a mechanism that simulates the timetable of water allocation to the farms (Figure 5-3). In each day, (i) a fixed number of cells is explored to check if irrigation is required and (ii) a cell is actually irrigated only if the soil water content in the root zone, calculated by the soil volume balance model, is at risk of limiting crop growth:

$$V_{Tr} - (TAW - RAW) < \alpha_i RAW \tag{5.5}$$

where V_{Tr} $(mm \cdot d^{-1})$ is the water content, minus the residual water content, of the transpirative layer, TAW $(mm \cdot d^{-1})$ is the total available water in the root zone, RAW $(mm \cdot d^{-1})$ is the readily available water in the root zone, and α_i (adimensional) is the threshold coefficient for the activation of irrigation (Facchi et al. 2004; Galelli et al. 2010; Vassena et al. 2012).

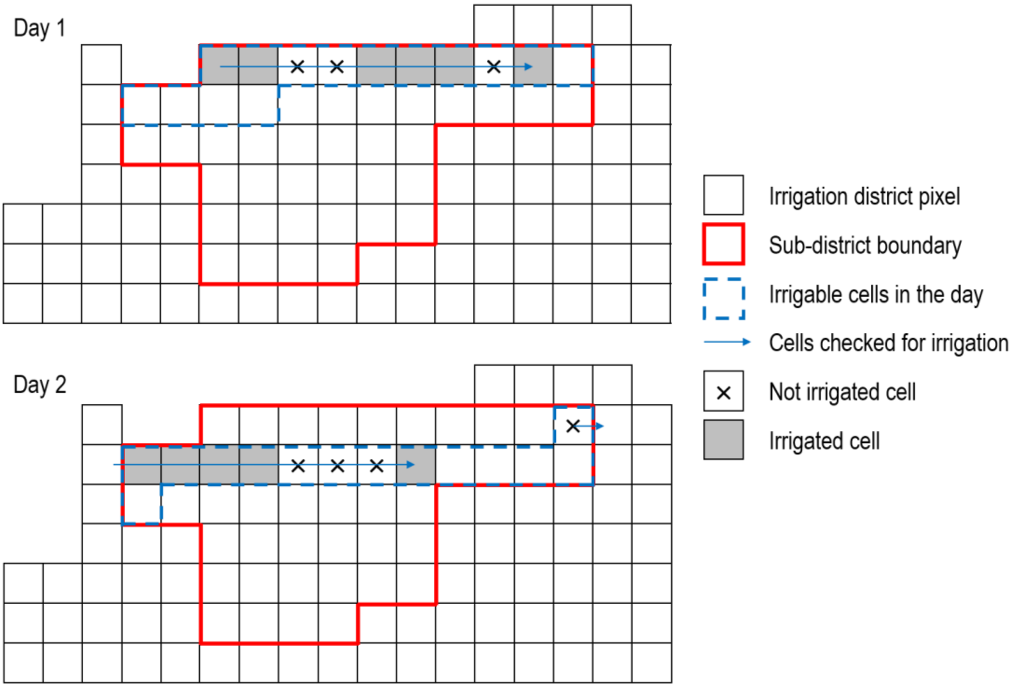

Figure 5-3: IdrAgra simulation of irrigation water distribution within a subdistrict in two consecutive days.

The main inputs and parameters required by the IdrAgra model to compute crop water requirements are: soil map and soil hydraulic parameters, land use maps and crop biometric parameters, meteorological data series (rainfall, maximum and minimum air temperature, wind speed, maximum and minimum relative humidity, solar radiation) and groundwater level data series. Moreover, information about the irrigation system (irrigation subdistricts map, irrigation sources data series, share of each irrigation source diverted to each subdistrict, conveyance efficiency) are necessary to account for the irrigation supply.

Figure 5-4 represents the flowchart of the computation and the analysis of the TDI in the study case (i.e. both $D\text{-}TDI$ and $WS\text{-}TDI$). For the analysis illustrated in the present chapter, time series of $TD10$ were calculated by applying IdrAgra to the simulation domain, and cumulating, for each cell and every 10 days, the 10-days transpiration deficit over the entire simulation period (i.e. 1993-2014).

The set of values of each 10-days period, grouped over the years, was then fitted to the respective distribution, to obtain the parameters to derive TDI. Each TDn series was then expressed in form of the respective TDI.

In particular, in order to avoid land use changes in the same pixel over the 22 year simulation period, the algorithm was run separately for each year of analysis, maintaining the actual land use of the specific year (e.g. 2012) as a fixed parameter for all the reference period (i.e. 1993-2014). Thus, the time series of $TD10$ spanning over the reference period (i.e. 1993-2014) were computed and the fitting distribution parameters were calculated for the year-specific (e.g. 2012) land use. Finally, the $TD10$ series of the selected year (e.g. 2012) were expressed as $WS\text{-}TDI$.

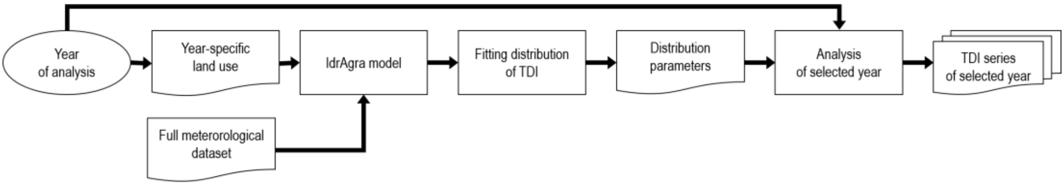

Figure 5-4: Flowchart of the data elaboration to compute TDI.

5.3.4 MAIZE YIELD PROXY ESTIMATION USING LANDSAT IMAGERY

The sum of the available photosynthetically active radiation over the growing period ($APAR_y$), a proxy of crop yield, was estimated for the study area using the methodology delineated in chapter 0 and briefly summarized hereinafter.

The employed approach is based on a Production Efficiency Model (PEM; e.g. Field et al. 1995; Running et al. 2000), that assume that the biomass production of a crop depends on the amount of photosynthetically active solar radiation (PAR) absorbed, as well as on the crop PAR interception capacity, following the equation:

$$GPP_d = \varepsilon_b \cdot PAR \cdot fAPAR \tag{5.6}$$

where GPP_d $(g \cdot m^{-2} \cdot d^{-1})$ is the daily gross primary production, expressed as carbon uptake, $fAPAR$ (adimensional) is the fraction of incident PAR absorbed by the canopy, mainly dependent on the leaf area of the canopy (Monteith 1972), PAR $(MJ \cdot m^{-2} \cdot d^{-1})$ is the photosynthetically active radiation incident on the canopy, and ε_b $(g \cdot MJ^{-1})$ represents the maximum light use efficiency (LUE) when the environment (i.e. temperature and soil moisture) is not limiting for plant carbon uptake (Rembold et al. 2013; Running et al. 2000; Running & Zhao 2015; Xin et al. 2015). The seasonal integration of equation 5.6 allows the estimation of the biomass and, finally, of the harvestable yield (Rembold et al. 2013; Xin et al. 2013; Xin et al. 2015).

The daily $APAR$ can be defined by the means of the Monteith (1972) equation:

$$APAR_d = PAR \cdot fAPAR \tag{5.7}$$

where $APAR_d$ $(MJ \cdot m^{-2} \cdot d^{-1})$ is the daily photosynthetically active radiation, PAR $(MJ \cdot m^{-2} \cdot d^{-1})$ is the photosynthetically active radiation incident on the canopy, estimated as

0.45 of total incident shortwave radiation (Heinsch et al. 2006; Running & Zhao 2015), and $fAPAR$ (adimensional) is the fraction of incident PAR absorbed by the canopy.

The $APAR_y$ is finally obtained by the sum of the $APAR_d$ between the start of the growing period (Start Of Season, SOS) and the beginning of the descending phase of the seasonal $fAPAR$ profile (End Of Season, EOS; Meroni et al. 2013; Rembold et al. 2013). The $APAR_y$ is thus directly proportional, through a crop-dependent proportionality coefficient ε_b, to the yield, and can therefore used as a proxy for crop productivity.

The daily PAR series were computed for each pixel of the Landsat cover from the daily shortwave radiation at the available agro-meteorological stations, spatially interpolated using the inverse distance weighting method (§ 2.2; Bartier & Keller 1996). The daily available photosynthetically active radiation (APAR) series were then calculated using the Monteith (1972) equation. Information about the growing season (start of season and end of season), extracted from the analysis of the Landsat cover as described in § 4.3.1, was used to define the integration limits for the calculation of the yearly APAR for each pixel of the Landsat cover.

5.3.5 CORRELATION ANALYSIS BETWEEN $WS\text{-}TDI10$ AND PRODUCTIVITY DATA

An auto-correlation analysis on the $WS\text{-}TDI10$ dataset, and an ensemble correlation analysis between the $WS\text{-}TDI10$ and yield data were conducted. The main objective of the first analysis was to verify whether the $WS\text{-}TDI10$ along the 10-day periods could be considered not correlated; this test was a necessary step to perform the ensemble analysis. The ensemble correlation analysis had the objective of evaluating whether the proposed water scarcity index could help in identifying areas associated with crop yield losses.

A preliminary regression analysis was conducted, for each year y, using all the $WS\text{-}TDI10$ dataset as independent variable, and the $APAR_y$ as dependent variable. Year-specific maize masks were applied to the $WS\text{-}TDI$ and $APAR_y$ datasets. In each regression, $WS\text{-}TDI10$ values for each cell were compared with the corresponding $APAR_y$ for assessing possible relationship between the indicator (computed for a specific year and 10-day period) with the proxy of the production of the same year. After computing the single correlation coefficients between $WS\text{-}TDI10$ over the year y and $APAR_y$, an ensemble correlation analysis was performed, i.e. an analysis performed on the result of a group of analysis, in this case on the correlation coefficients (Shu, 2016). $APAR_y$ dataset is randomly scattered along time, because the productivity of the year y is not related to the productivity of other years. If also $WS\text{-}TDI10$ data can be considered randomly scattered along time (and this could be demonstrated by the auto-correlation analysis), thus the hypothesis of the presence of an ensemble correlation based on the group of comparisons conducted ($WS\text{-}TDI10$ over the period that spans between the emergence and the harvest versus $APAR_y$) can be tested. The test was based on the following assumption: if two variables are not correlated, the sign of the regression coefficient is randomly positive or negative. So, under the null hypothesis (H_0) of the absence of an ensemble correlation, the probability of the regression coefficient to be negative is 0.5. With N completely random regressions, the number of negative regression coefficients would be than distributed as a binomial distribution with coefficients N (number of regressions) and p (probability of negative coefficient 0.5):

$$n \quad \sim binomial(N, p) \tag{5.8}$$

The probability under the null hypothesis of having a specified number of negative regressions n can thus be computed through the binomial cumulate probability function.

5.3.6 STUDY AREA AND AVAILABLE DATA

In chapter 2, the study area of the Media Pianura Bergamasca Irrigation District (IDMPB) and the available data collection and pre-processing were described. This chapter is focused on the calculation of $D\text{-}TDI$ (i.e. considering TDI as a drought index, without taking into account irrigation inputs), and $WS\text{-}TDI$ (i.e. considering TDI as a water scarcity index, providing irrigation inputs to the IdrAgra model) over the "Pilot study area" described in § 2.1 and represented in Figure 2-1. In particular, the following data were used: agro-meteorological data series of the agro-meteorological stations selected for the study area (§ 2.2 and Figure 3-6), land use maps derived from the Lombardy Regional Authority geographic information portal (§ 2.3), soil hydraulic parameters maps (§ 2.4). Moreover detailed information about the discharges diverted daily by the main rivers supplying water to the pilot study area, the channel network characteristics and the rules of allocation of water diverted by rivers to each irrigation subdistrict provided by the IDMBP (§ 2.5) were used. Crop parameter data series were built using the crop phenology module of IdrAgra (Annex I). Finally, the fAPAR dataset provided by the Institute of Surveying, Remote Sensing and Land Information (IVFL) of the University of Natural Resources and Life Sciences of Vienna (BOKU) and described in § 2.6 was used to estimate $APAR_y$.

5.4 RESULTS

5.4.1 METEOROLOGICAL DROUGHT TREND

The analysis of $SPI6$ (Figure 5-5) at the Stezzano agro-meteorological station for the study period (1993-2014) shows several maxima, often in the winter season, and three well defined minima, reaching values lower than -2 (i.e. extreme dry periods, according to McKee et al. (1993) classification), in 2003, between 2005 and 2007, and in 2009. The summer of 2009 is the third driest growing season over the data series, with a $SPI6$ reaching the value of -2.58 in August 2009. On the contrary, the spring-summer of 2014 shows to be the wetter season, with a $SPI6$ of 1.95 in June 2014, and the persistence of severely wetness until the end of the year ($SPI6$ of 1.5 in December 2014).

Table 5-1 shows the crop stage lengths for maize, the predominant crop in the study area, over the period 2009-2014, as computed by the "Phenological stages module" of IdrAgra. Maize in the study area normally emerges between April 11th and April 28th (11th to 12th 10-day period of the year), and is harvested between August 26th and September 17th (24th to 27th 10-day period). It should be noted that 2009 was characterized not only by a lack of rainfall, but also by high temperatures leading to a reduction of the growing period (maize was harvested at the end of August), while in 2014 the lower temperatures lengthened the growing period of maize until mid-September.

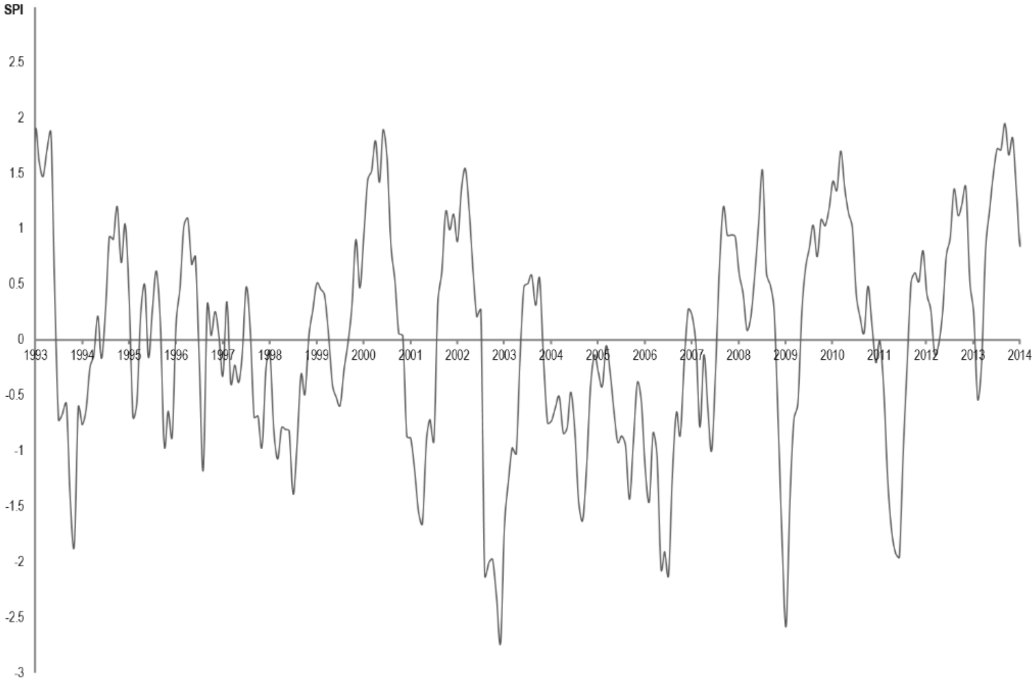

Figure 5-5: $SPI6$ series at the Stezzano agro-meteorological station, calculated for the period 1993-2014.

Table 5-1: Maize growing period simulated by IdrAgra for the years 2009-2014. Dates are expressed as Day of Year (DoY).

	2009	2010	2011	2012	2013	2014
Emergence	104	111	101	119	107	104
Stem elongation	135	141	132	145	132	138
Heading/Flowering	169	177	171	178	178	174
Ripening	218	221	222	222	222	228
Harvest	238	249	244	242	249	260
Cycle length	134	138	143	123	142	156

In the following, $D\text{-}TDI10$ and $WS\text{-}TDI10$ for the 10-day periods 18th to 20th (i.e. from June 20th to July 19th) in 2009 and 2014 are illustrated and discussed. This period for the two years was selected on the basis of $SPI\text{-}10d$ values and maize crop stages length. In fact, the chosen period is critical for maize, because it coincides with its heading and flowering. Furthermore, July to middle of August in many areas of the Padana Plain is the time lapse in which irrigation water supply may be more limited.

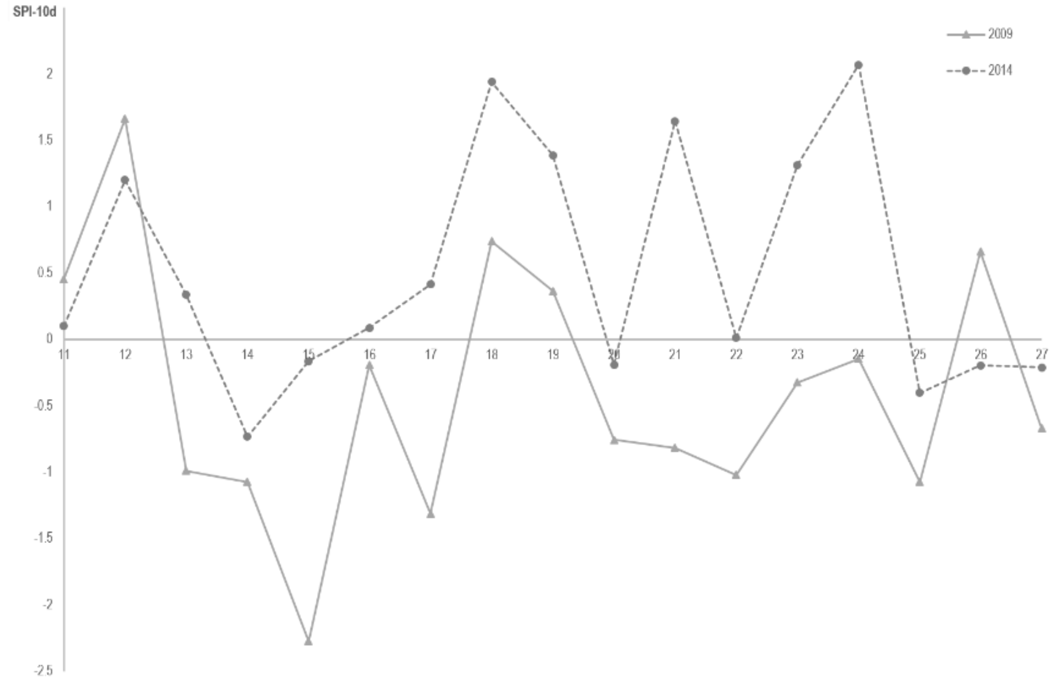

Figure 5-6: $\boldsymbol{SPI\text{-}10d}$ a series at the Stezzano agro-meteorological station, for years 2009 and 2014, calculated over the reference period 1993-2014.

5.4.2 AGRICULTURAL DROUGHT AND WATER SCARCITY TREND IN SELECTED YEARS

Both in 2009 and 2014, the second half of June (Figure 5-6) was characterized by a dry spell, more pronounced in 2014 ($SPI\text{-}10d$ of 1.94 in 18th 10-day period), and followed by rainfall at mid-July in both years.

From middle of June 2009 until middle of July 2009 (Figure 5-7a, b, c), the $D\text{-}TDI10$ increased from -1.03 ± 0.18 in the 18th 10-day period (Figure 5-7a) to -0.62 ± 0.46 in the 20th (Figure 5-7c). Loamy soils in the south-east of the pilot study area, characterized by a medium available water content (AWC) and cropped with maize, showed lower $D\text{-}TDI10$ in the three time steps. On the contrary, in a part of cells located in the central portion of the area, characterized by sandy-loamy soils and cropped with permanent grass, the $D\text{-}TDI10$ increased relevantly and became positive by the mid of July. This effect is explainable as sandy or sandy-loamy soils, having a lower AWC, reacted rapidly to changes in precipitation (§ 3.4.4).

In 2014, 18th 10-day period (Figure 5-8a) was characterized by the not-complete recovery of the system (-0.91 ± 0.44). This is particularly true for the medium-retentive cells of the south-eastern portion of the area, after the month of May, when a moderate dry spell occurred (Figure 5-6). Abundant precipitation in the considered month led to a complete recovery of the area (Figure 5-8b, c), with $D\text{-}TDI10$ values at the end of the period of 0.55 ± 0.71. As in 2009, sandy-loamy soils showed higher $D\text{-}TDI10$ values at the end of the period, confirming their quick response to $SPI\text{-}10d$ variations (i.e. within 10 days), while more retentive soils still present negative $D\text{-}TDI10$.

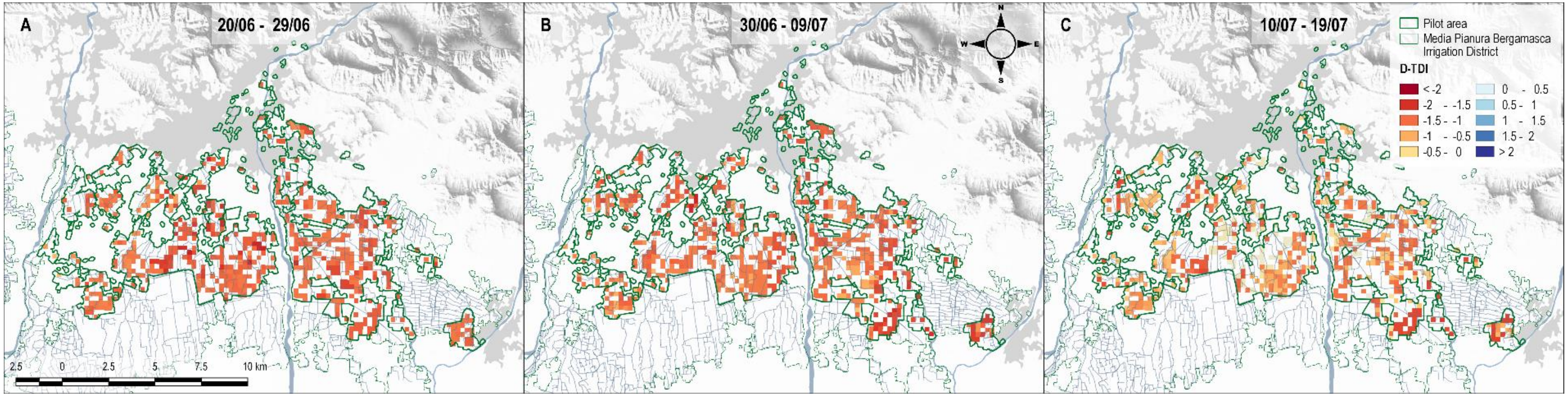

Figure 5-7: $D\text{-}TDI10$ over the pilot area, year 2009: (a) 18th 10-day period (June 20th– June 29th); (b) 19th 10-day period (June 30th– July 9th); (c) 20th 10-day period (July 10th– July 19th).

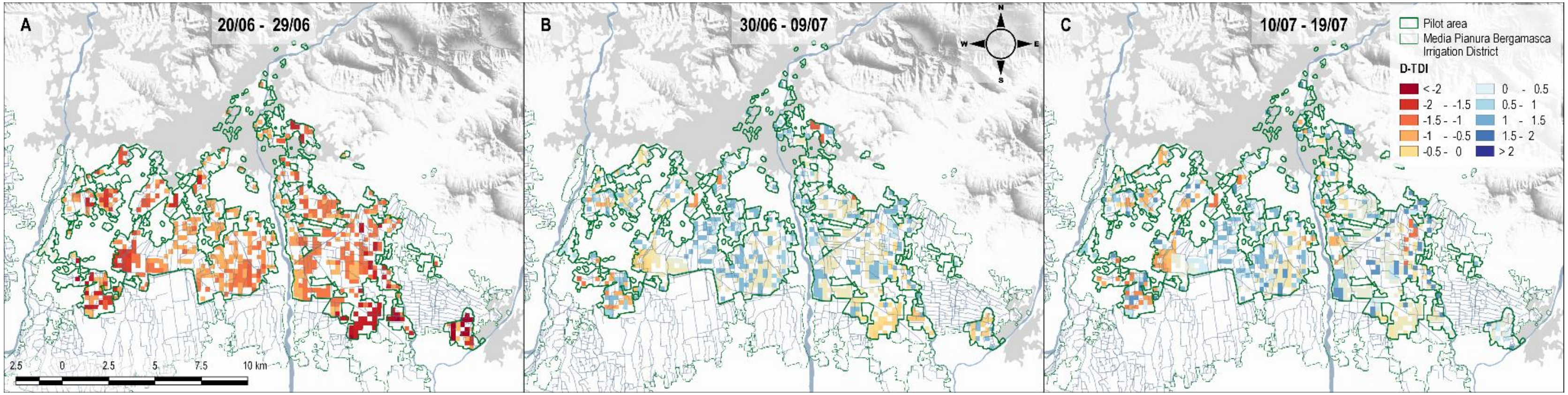

Figure 5-8: $D\text{-}TDI10$ over the pilot area, year 2014: (a) 18th 10-day period (June 20th– June 29th); (b) 19th 10-day period (June 30th– July 9th); (c) 20th 10-day period (July 10th– July 19th).

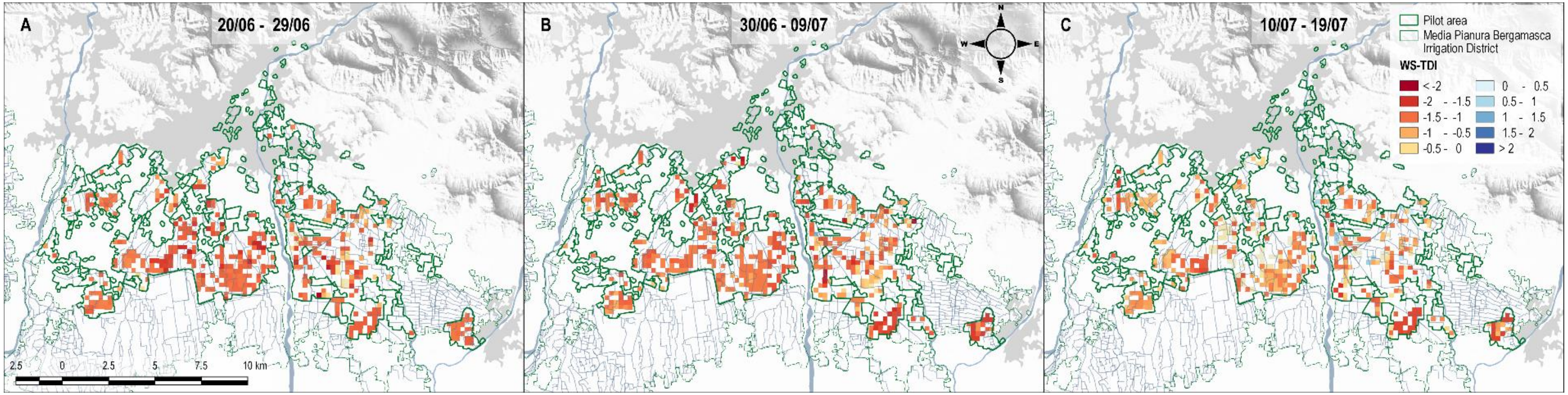

Figure 5-9: $\boldsymbol{WS\text{-}TDI10}$ **over the pilot area, year 2009: (a) 18th 10-day period (June 20th– June 29th); (b) 19th 10-day period (June 30th– July 9th); (c) 20th 10-day period (July 10th– July 19th).**

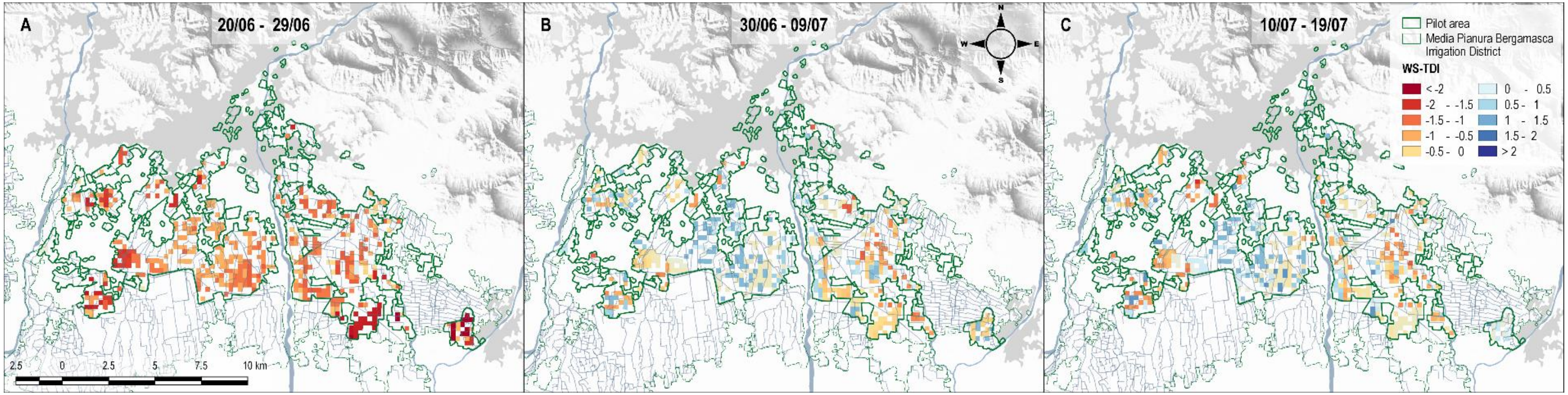

Figure 5-10: $\boldsymbol{WS\text{-}TDI10}$ **over the pilot area, year 2014: (a) 18th 10-day period (June 20th– June 29th); (b) 19th 10-day period (June 30th– July 9th); (c) 20th 10-day period (July 10th– July 19th).**

When taking into account $WS\text{-}TDI10$, it can be observed that the meteorological drought of 2009 is only slightly mitigated by the irrigation. In fact, the $WS\text{-}TDI10$ increased from -0.94 ± 0.35 computed between June 20th and June 29th (Figure 5-9a) and a similar value for the successive 10-day period (Figure 5-9b), to -0.55 ± 0.52 at the end of the considered time lapse (Figure 5-9c). Cells affected by agricultural water scarcity were fewer than when considering agricultural drought; this aspect is particularly visible in comparing Figure 5-9b and Figure 5-7b. In fact, the subdistricts on the left-side of the Serio River seemed to be characterized by a good water availability, that could help coping with drought, while on the right-side of the Serio River, and particularly in the south of the area, drought conditions are not mitigated by irrigation.

The effects of the dry spell of May-June 2014 were only slightly mitigated by irrigation; in fact, some areas, in particular the western and the south-eastern parts of the pilot test area (Figure 5-10a), showed very low $WS\text{-}DTI10$ in the 18th 10-day period, reaching -2, while the mean value was -0.86 ± 0.49. As in 2009, water diversions to the left-side of Serio River helped this area in coping with the dry spell.

By comparing the results of $WS\text{-}TDI10$ for year 2009 and 2014, it can be inferred that the areas more prone to water scarcity are those characterized by loamy soils and low water availability ($0.50\ m^3 \cdot s^{-1} \cdot ha^{-1}$ with respect to an average supply over the pilot area of $1.10\,m^3 \cdot s^{-1} \cdot ha^{-1}$), in the southern and western part of the area, that show for both years the lowest values of the considered index.

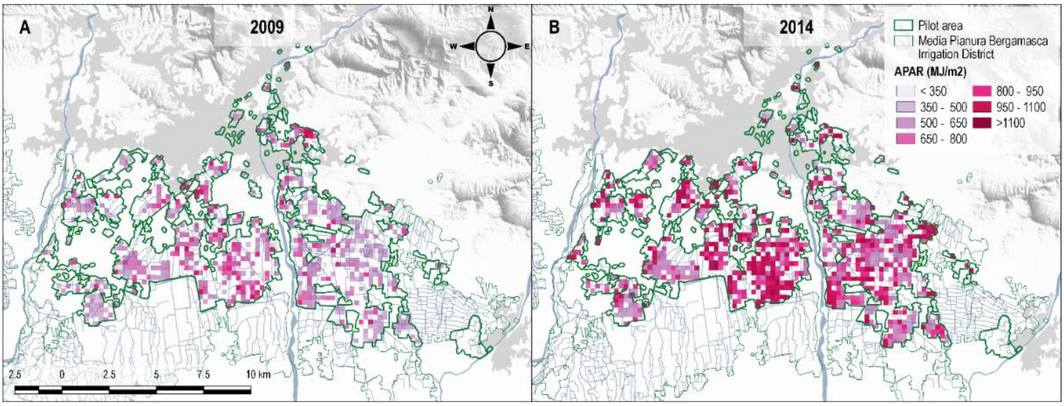

Figure 5-11: $APAR_y$ over the pilot study area within Media Pianura Bergamasca Irrigation District produced from Landsat fAPAR data analysis. Only maize pixels are represented, for the years (a) 2009 and (b) 2014. In these maps, $APAR_y$ results deriving from the processing of Landsat data are not resampled to match IdrAgra output pixels.

5.4.3 $APAR_y$ RESPONSE TO DROUGHT IN SELECTED YEARS

Figure 5-12 illustrates $APAR_y$ maps for the maize pixels respectively in 2009 and in 2014. As expected from the meteorological drought index, 2009 showed a lower productivity ($685 \pm 147\ MJ \cdot m^2$) than 2014 ($926 \pm 238\ MJ \cdot m^2$). By a visual comparison with Figures 5-9 and 5-10, the areas less water scarcity-prone on the right-side of the Serio River showed to be the more productive in both years, while areas characterized by higher values of WS-DTI generally showed lower $APAR_y$, both in 2009 and in 2014. Unfortunately, due to $fAPAR$ yearly maxima lower than the threshold set in § 4.3.1, the areas prone to water scarcity in the south-eastern part of the pilot study could not be represented in the maps – thus indirectly confirming the very low productivity of the area.

5.4.4 CORRELATION ANALYSIS BETWEEN $WS\text{-}TDI10$ AND PRODUCTIVITY DATA

As a first step, an auto-correlation analysis of the $WS\text{-}TDI10$ along the 10-day periods was computed with the objective of verifying whether the terms of each $WS\text{-}TDI10$ series could be considered not correlated, thus the ensemble correlation analysis could be performed.

Table 5-2: Auto-correlation for lag 1:5 of the 10-day period 11th to 27th .

Lag	Auto-correlation
1	0.0850
2	-0.1194
3	-0.1378
4	-0.3541
5	-0.0438
6	0.0165

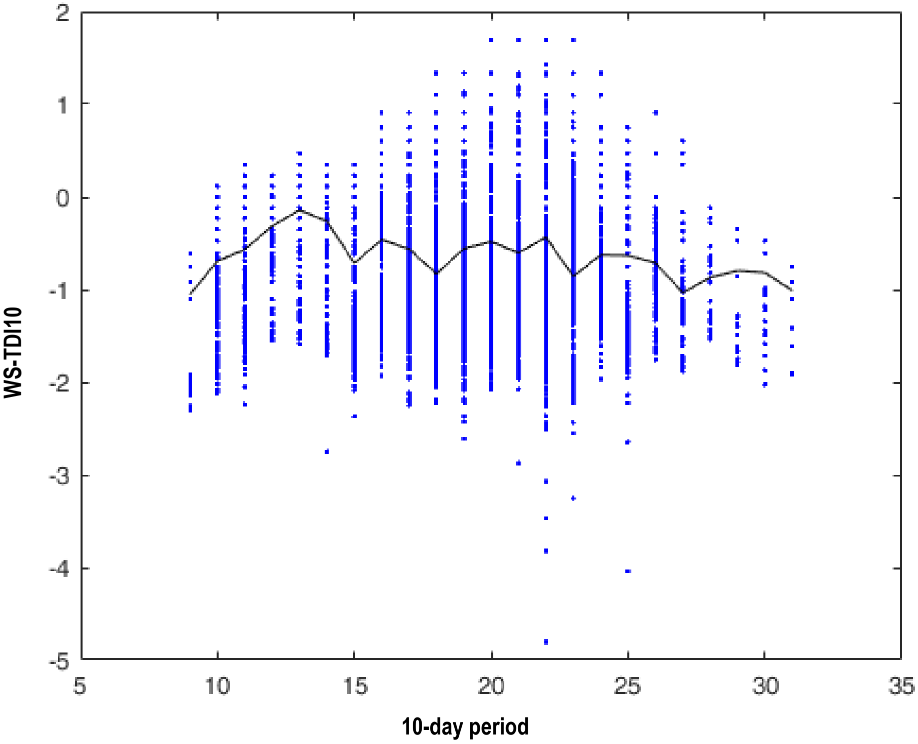

Figure 5-12: $WS\text{-}TDI10$ values in the time series considered (2009-2014), for each cell and year. The black line represents the mean.

Results show that the auto-correlation is usually negative as confirmed by the AC (lag 1 to 6, as reported in Table 5-2) computed for each maize cell and year and averaged over both. Moreover, the higher positive autocorrelation (AC1) is quite low compared to the negative ones, and the overall behaviour of all the series is quite noisy as a consequence of the irrigation process (i.e. if the soil in the root zone of the cell is wet, the model does not irrigate, and this takes to some stress in the next time steps; on the contrary, if the cell is dry, the model irrigate, leading to wet conditions in the next time steps). Figure 5-12 also shows a flat average behaviour of the indicator along the season, due to the standardization procedure bringing from TD to TDI (§§ 3.3.2 and 5.3.2). The negative average of the indicator is probably due to the fact that the indicator is more sensitive to water scarcity than to water abundant periods; in fact, if the transpirative deficit for a cell is zero in a specific 10-day period along all the time series, that pixel is not represented in the plot, because no statistic is available to compute the fitting distribution parameters.

A regression analysis was then performed between $APAR_y$ and the $WS\text{-}TDI10$ time series for the maize growing period (i.e. 10-days periods from the emergence to the harvest) of the corresponding year (y). In particular, the analysis was performed between $WS\text{-}TDI10(i,j)$ and $APAR_y(j)$, where i is the 10-day period counted from January 1st and j is the year. One regression for each 10-day period (10-day periods 11th-27th) and year (2009-2014) were set, leading to a total of 102 regressions. Regressions for 10-day periods after the EOS and before the SOS were removed, leading to 89 meaningful comparisons.

Results showed that the relation between the $WS\text{-}TDI10$ and $APAR_y$ is dominated by noise and characterized by p-values always higher than 0.90. Regression coefficients in Table 5-3 are calculated as the average between the coefficients calculated in each of the maize cells. As the regression coefficients are either positive or negative in each 10-day period along the years, as well as their significativity is always very low, no period that significatively affects $APAR_y$ can be identified.

Table 5-3: Correlation coefficients of $\boldsymbol{WS\text{-}TDI10(i,j)}$ vs $\boldsymbol{APAR_y(j)}$. For each year, correlation regression are calculated only for the 10-day periods from the emergence to the harvest.

10-day period	Year 2009	Year 2010	Year 2011	Year 2012	Year 2013	Year 2014	Average
11	0.20		−0.16		0.04	−0.21	−0.03
12	0.03	−0.27	−0.48	0.35	0.23	0.35	0.04
13	0.14	0.14	−0.16	0.32	0.28	0.25	0.16
14	0.05	0.05	−0.49	0.13	0.16	0.23	0.02
15	−0.19	−0.12	−0.41	0.16	0.19	−0.11	−0.08
16	0.02	−0.27	0.42	0.32	0.09	0.00	0.09
17	0.16	−0.34	0.40	0.40	0.04	0.32	0.16
18	−0.05	0.16	−0.17	0.02	−0.18	0.25	0.00
19	0.02	−0.10	−0.14	−0.03	0.04	0.31	0.02
20	0.17	−0.13	0.39	0.05	−0.13	0.26	0.10
21	0.01	0.22	0.09	−0.11	0.14	0.27	0.10
22	−0.08	0.35	0.06	0.22	0.14	0.20	0.15
23	−0.04	0.26	0.32	0.16	0.10	0.22	0.17
24	−0.11	0.16	0.15	−0.18	0.22	0.23	0.08
25		−0.03	−0.45	−0.24	0.18	0.11	−0.09
26						−0.13	−0.13
27						−0.36	−0.36
Average	0.02	0.01	−0.04	0.11	0.10	0.13	

Finally, an ensemble correlation analysis was conducted to verify the presence of an ensemble correlation, i.e. that it can be hypothesized a causality relationship between $WS\text{-}TDI10$ and $APAR_y$. In equation 5.8, $N = 89$ as represents the meaningful comparisons (i.e 10-day periods accounted for in the analysis, since valid $WS\text{-}TDI10$ values are present). Thus the equation can be written as:

$$n \quad \sim binomial(89, 0.5) \tag{5.9}$$

Negative correlation coefficients in the sample are 31, and the probability of obtaining 31 negative values within a sample of 89 values is very low (0.0028). Thus, the null hypothesis of the absence of an ensemble correlation can be rejected, as the probability that the ensemble correlation would be positive is higher than 0.5, and there is a deterministic component that rises the probability of positive regressions (58) in comparison to negative regressions (31). The result of the analysis thus highlights that there is a positive correlation between $WS\text{-}TDI10(i,j)$ and $APAR(j)$ (i.e. a high value of $WS\text{-}TDI10$, consequence of a higher water availability, is correlated with an increment in biomass accumulation), although the noise in both series masks each single regression response. However, more in-depth statistical analysis of the spatial distributions of $WS\text{-}TDI10$ and $APAR_y$ must be conducted as a further research step, in order to provide more accurate information on their correlation.

5.5 DISCUSSION AND CONCLUSIONS

This chapter assesses the use of TDI both as an agricultural drought ($D\text{-}TDI$) and a water scarcity ($WS\text{-}TDI$) index.

The suitability of $D\text{-}TDI$ for the monitoring of agricultural drought over a territory is demonstrated in this study, since the index shows to respond not only to long-term droughts, like the one in the summer of 2009, but also to shorter phenomena, such, for instance, the dry spell in the summer of 2014. $D\text{-}TDI$ shows to be a helpful tool for the identification of drought prone zones, which in the specific case of the pilot study are characterized by loamy soils.

$WS\text{-}TDI$ can be helpfully used in the monitoring of water shortage and scarcity in irrigated areas. For instance, its application to the pilot study area highlights that water diversions reaching the sub-districts located in the right-side of the Serio River are generally not sufficient to satisfy the crop water requirements during the summer months. $WS\text{-}TDI$ could therefore be used as an operational indicator, periodical producing maps that could support farmers and irrigation district managers to cope with water scarcity and shortages. In particular, if real time data (agro-meteorological and water discharges at the main surface water diversions data series) could be used to feed IdrAgra, $WS\text{-}TDI$ maps could be adopted by competent authorities responsible for the monitoring of the state of agriculture, to set up an early warning system with respect to drought and water scarcity phenomena. Additionally, the indicator may be also adopted in climate change studies, allowing to visualize the evolution of water scarcity phenomena over the territory, as a consequence of changes in meteorological forcing and in the availability of water by irrigation sources. Finally, $WS\text{-}TDI$ could be used as a useful tool to support planning decisions on water resources allocation, or action plans to reduce water consumptions in specific portions of the territory (e.g. conversion of irrigation methods, introduction of different crop species, etc.), also in the view of an adaptation to the climate change. Future developments of the index could include the use of phenological information derived from remote sensing data, in order to better simulate the growing period of the different crops.

When compared to annual crop productivity data, the single $WS\text{-}TDI$ calculated over a 10-day period within a specific year does not show a significant correlation with this variable. This is mainly due to short accumulation period selected for the $WS\text{-}TDI$ in this study, and to the noisy behaviour of the $WS\text{-}TDI10$ series highly influenced by the irrigation process which takes to negative autocorrelation at lags > 1 (i.e. if the soil in the root zone of the cell is wet the hydrological model does not irrigate, and this takes to some stress in the next time steps; on the contrary, if the cell is dry the model do irrigate, leading to wet conditions in the next time steps). However, the results of an ensemble correlation analysis taking into account contemporaneously all the $WS\text{-}TDI10$ over simulated years demonstrates that a positive correlation exists with the corresponding annual productivity data. Nevertheless, a more in-depth statistical analysis of spatial distributions of $WS\text{-}TDI$ with respect to annual productivities shall be conducted as a further step in the research, in order to provide more accurate information on their correlation.

6 CONCLUSIONS AND FUTURE RESEARCH

In recent decades, frequent and severe droughts have occurred in several countries of the world under nearly all climatic regimes (European Environment Agency 2010; International Panel on Climate Change 2012; Mishra & Singh 2010; Rossi & Cancelliere 2013). Since the middle 20th century, drought areas have globally increased, and, more specifically, in southern and central Europe (Dai 2011; Sheffield & Wood 2008). Drought risk is expected to increase in the near future as a result of the climate change, leading to a decline in precipitation and an increase in air temperatures, and consequently in evapotranspiration rates in several regions, including southern Europe and the Mediterranean region (Dai 2011; Giorgi & Lionello 2008; International Panel on Climate Change 2012).

Droughts can significantly affect the agricultural sector since they provoke losses in crop yields and livestock production, increased insect infestations, plant diseases and wind erosion. Moreover, low rainfall during the growing season may affect irrigated agriculture over subsequent years, as a result of low levels of water in reservoirs and groundwater aquifers (European Environment Agency 2010).

In Europe, the monitoring and assessment of drought is entrusted to the European Drought Observatory (EDO), that applies a multi-indicator approach (de Jager & Vogt 2015), based on earth observations (EOs) and hydrological modelling data. EDO indicators are computed considering rainfed agriculture, predominant in middle and northern Europe, and are produced on a $5\ km$ grid. In southern Europe, however, the implementation of drought-coping measures (irrigation) can partially or completely alleviate the impacts of potentially severe droughts. Therefore, for these conditions, specific water scarcity indicators explicitly considering irrigation among the water inputs to agro-ecosystems need to be developed and adopted to inform and support stakeholders and decision makers of irrigated regions.

In this context, the main objective of the Ph.D. thesis is the presentation of the Transpirative Deficit Index (TDI), a newly developed indicator for the monitoring and the management of Water Scarcity and Drought phenomena based on the use of hydrological modelling, applied at a spatial scale of interest for end-users ($250\ m$ grid) and suited for the assessment of water scarcity and drought in Italy as well as in other southern European countries. In particular, TDI was developed as a new module integrated into the spatially distributed hydrological model IdrAgra, and in the Ph.D. research it was tested over the Irrigation District of Media Pianura Bergamasca (IDMPB), considering a simulation period of 22 years (1993-2014) and subdividing the territory by means of a grid with cells of $250\ m \times 250\ m$.

As a first step in the thesis, $D\text{-}TDI$ was described as an agricultural drought index focusing on overcoming the limitation of other approaches, not taking into account with sufficient detail land cover and soil properties. The $D\text{-}TDI$ is based on the calculation of the spatially distributed actual transpiration deficit, to determine the level of drought experienced by crops within the single model cells; thus, it can provide a much more accurate measure of agricultural drought at the irrigation district scale than the one that could be achieved through meteorological drought indices such as SPI or $SPEI$. Statistical analysis were conducted to: (1) compare SPI and $SPEI$ at different time steps, in order to assess whether the use of SPI could be sufficient to describe meteorological drought patterns within the study area, (2) study the characteristics and the memory of $D\text{-}TDI$ as a function of soil and crop variability, and (3) assess the response of $D\text{-}TDI$ to SPI variations over diverse temporal steps. The auto-correlation analysis of $D\text{-}TDI$ showed to be positive with a persistence of 30 days for the two more widespread crops in the study area, maize and permanent grass. The analysis demonstrated also that soils characterized by a high available water content can more easily compensate dry spells. Finally, a positive significant correlation between $D\text{-}TDI$ and SPI was observed for maize, with a persistence of 40 days, while no correlation was observed for permanent grass, probably related to cutting cycles, that could mask the relation between storage capacity and short-time variability of the meteorological conditions.

Successively, a methodology to compute crop yield using moderate spatial and temporal resolution Earth Observation (Landsat) data was set. In particular, the developed procedure, based on the integration of the Available Photosynthetically Active Radiation over the growing season, showed that statistical inventories and satellite data can be integrated to produce annual spatially distributed estimates of cropland productivity, while site-specific observational field data can be used to validate the relationship between $APAR$ and productivity for specific crops (i.e. maize in this Ph.D. research). A phenological parameter extraction algorithm was developed to derive key phenology stages for the maize crop. However, the results presented in the study showed two main weaknesses: (1) cloud cover and noise in the original Landsat dataset were not appropriately removed by the Whittaker algorithm, and (2) SOS (Start of Season) and EOS (End of Season) extracted from satellite data were underestimated for a discrete numbers of fields with respect to observed ground-truths, probably as a consequence of the method adopted for setting the thresholds. A crop specific light use efficiency (ε_b^*) was estimated as the ratio between the average maize yield over the study period taken from Regional Statistic Inventory (Regional Authority and ISTAT), and the average $APAR$ value calculated for the maize pixels over the same spatial extension and time period. The ε_b^* estimated value fell within the range of the coefficients calibrated with other satellite-based algorithms.

Finally, TDI was applied as a water scarcity index ($WS\text{-}TDI$), thus including water availability for irrigation within the inputs of the IdrAgra model. The behaviour of $D\text{-}TDI$ and $WS\text{-}TDI$ was compared over the same area, analysing their spatialized trend in response to varying meteorological conditions, and in particular considering drought events and dry spells. The two indices proved to be suitable to monitor agricultural drought and water scarcity over a territory, and helped in identifying drought and/or water scarcity prone sub-districts, as a function of crop, soil type and water availability. Both $D\text{-}TDI$ and $WS\text{-}TDI$ could therefore be used as operational indicators to produce periodic maps that could help farmers and irrigation district managers in coping with agricultural drought and water scarcity and, eventually, in setting up proper adaptation measures. In particular, in case of availability of real time meteorological data and water discharges at the main surface water diversions, the indicators may be adopted by an authority responsible for the monitoring of the state of agriculture (ERSAF or ARPA in the Lombardy region) to promptly inform (through newsletters or a web site) stakeholders on the agricultural drought/dry spells and water scarcity/shortages phenomena evolution. Additionally, the indicators may be adopted in climate change studies, allowing to visualize the evolution of drought and water scarcity phenomena over the territory, as a consequence of changes in meteorological forcing and in the availability of water by irrigation sources. Finally, they could be used as useful tools to support planning decisions on water resources allocation or action plans to reduce water consumptions in specific portions of the territory (e.g. conversion of irrigation methods, introduction of different crop species, etc.), also in view of an adaptation to the climate change. $WS\text{-}TDI$ maps over a pilot study area were statistically compared with the maize yield maps derived from EO data (Landsat dataset): an ensemble correlation analysis proved a positive correlation between the two variables.

Despite the results presented in this thesis, further research is still needed before proposing the TDI as an operational tool to the competent authorities. The main suggested future research directions are the following:

1. Verifying if an accumulation period of 10 days, adopted in this study for $D\text{-}TDI$ and $WS\text{-}DTI$ ($D\text{-}TDI10$ and $WD\text{-}TDI10$), can be adequate to assess water scarcity over the whole Lombardy region, with respect to the irrigation turns adopted in different part of the territory, or if longer accumulation periods would be better suited. Moreover, It could also be interesting to check with stakeholders their propensity to have the indicator response at the single cell scale, or rather aggregated at the sub-district scale.
2. Collecting observational phenological and yield data through extended field monitoring campaigns, to better calibrate and validate the growth stage extraction and the gross primary production algorithms. At this way, EO dataset could be used to produce useful information to input (growth stages information) and validate (yield maps) TDI indices. Moreover, the developed procedures for extracting information from Landsat satellite images can be applied to the recent Sentinel data.
3. Investigating and applying a better method for the assessment of the correlation between the spatial distributions of $WS - TDI$ and crop production maps.
4. Verifying the possibility of obtaining real-time data of water discharges at the main surface water diversion points with Irrigation Consortia, Lake Regulation Consortia and Lombardy Regional Authority. On the contrary, the availability of real-time and provisional (few days) agro-meteorological data has already been verified with ARPA-Lombardia.

7 BIBLIOGRAPHY

Abramowitz, M. & Stegun, I.A., 1964. *Handbook of Mathematical Functions with Formulas, Graphs, and Mathematical Tables* 10th ed., Available at: http://people.math.sfu.ca/~cbm/aands/toc.htm.

Allen, R.G. et al., 1998. Crop evapotranspiration - Guidelines for computing crop water requirements. *FAO Irrigation and drainage paper*, 56, p.174. Available at: https://www.kimberly.uidaho.edu/water/fao56/fao56.pdf.

Alley, W.M., 1984. The Palmer Drought Severity Index: Limitations and Assumptions. *Journal of Climate and Applied Meteorology*, 23(7), pp.1100–1109. Available at: http://www.engr.colostate.edu/~jsalas/classes/ce624/Handouts/Palmer Index-alley 1984.pdf [Accessed March 24, 2014].

American Meteorological Society, 2004. Statement on meteorological drought. *Bulletin of the American Meteorological Society*, 85, pp.771–773. Available at: https://www.ametsoc.org/ams/index.cfm/about-ams/ams-statements/archive-statements-of-the-ams/meteorological-drought/.

Asadi Zarch, M.A., Sivakumar, B. & Sharma, A., 2015. Droughts in a warming climate: A global assessment of Standardized precipitation index (SPI) and Reconnaissance drought index (RDI). *Journal of Hydrology*, 526, pp.183–195. Available at: http://dx.doi.org/10.1016/j.jhydrol.2014.09.071.

Atzberger, C., 2013. Advances in Remote Sensing of Agriculture: Context Description, Existing Operational Monitoring Systems and Major Information Needs. *Remote Sensing*, 5(2), pp.949–981. Available at: http://www.mdpi.com/2072-4292/5/2/949/.

Atzberger, C. et al., 2013. Phenological Metrics Derived over the European Continent from NDVI3g Data and MODIS Time Series. *Remote Sensing*, 6(1), pp.257–284. Available at: http://www.mdpi.com/2072-4292/6/1/257/.

Atzberger, C. & Eilers, P.H.C., 2011. A time series for monitoring vegetation activity and phenology at 10-daily time steps covering large parts of South America. *International Journal of Digital Earth*, 4(5), pp.365–386. Available at: http://www.tandfonline.com/doi/abs/10.1080/17538947.2010.505664.

Atzberger, C. & Eilers, P.H.C., 2011. Evaluating the effectiveness of smoothing algorithms in the absence of ground reference measurements. *International Journal of Remote Sensing*, 32(13), pp.3689–3709. Available at: http://www.tandfonline.com/doi/abs/10.1080/01431161003762405.

Bandaru, V. et al., 2013. Estimating crop net primary production using national inventory data and MODIS-derived parameters. *ISPRS Journal of Photogrammetry and Remote Sensing*, 80, pp.61–71. Available at: http://dx.doi.org/10.1016/j.isprsjprs.2013.03.005.

Bartier, P.M. & Keller, C.P., 1996. Multivariate interpolation to incorporate thematic surface data using inverse distance weighting (IDW). *Computers & Geosciences*, 22(7), pp.795–799. Available at: http://linkinghub.elsevier.com/retrieve/pii/0098300496000210.

Beguería, S. et al., 2014. Standardized precipitation evapotranspiration index (SPEI) revisited: parameter fitting, evapotranspiration models, tools, datasets and drought monitoring. *International Journal of Climatology*, 34(10), pp.3001–3023. Available at: http://doi.wiley.com/10.1002/joc.3887 [Accessed August 2, 2014].

Blinda, M. et al., 2007. *Mediterranean Water Scarcity and drought report*, European Commission. Available at: http://www.emwis.net/topics/WaterScarcity.

Boschetti, M. et al., 2009. Multi-year monitoring of rice crop phenology through time series analysis of MODIS images. *International Journal of Remote Sensing*, 30(18), pp.4643–4662. Available at: http://www.tandfonline.com/doi/abs/10.1080/01431160802632249.

Bouraoui, F. & Aloe, A., 2007. *European Agrochemicals Geospatial Loss Estimator: Model Development and Applications*, Italy: Institute for Environmental Sustainability, European Communities.

Braden, H., 1985. Ein Energiehaushalts- und Verdunstungsmodell für Wasser- und Stoffhaushaltsuntersuchungen landwirtschaftlich genutzter Einzugsgebiete [An energy balance and evaporation model for water and nutrient budget studies of agricultural catchments]. *Mitteilungen Deutsche Bodenkundliche Gesselschaft*, 42, pp.294–299. Available at: https://www.dbges.de/wb/media/mitteilungen_dbg/Mitteilungen der DBG 1985_42.pdf.

Bradford, J.B., Hicke, J.A. & Lauenroth, W.K., 2005. The relative importance of light-use efficiency modifications from environmental conditions and cultivation for estimation of large-scale net primary productivity. *Remote Sensing of Environment*, 96(2), pp.246–255. Available at: http://linkinghub.elsevier.com/retrieve/pii/S003442570500088X.

Brooks, R. & Corey, A., 1964. Hydraulic properties of porous media. *Hydrology Papers, Colorado State University*, 3(March), p.37. Available at: https://dspace.library.colostate.edu/bitstream/handle/10217/61288/HydrologyPapers_n3.pdf?sequence=1.

Chen, T. et al., 2011. Evaluation of cropland maximum light use efficiency using eddy flux measurements in North America and Europe. *Geophysical Research Letters*, 38(14), p.L14707:1-5. Available at: http://doi.wiley.com/10.1029/2011GL047533.

Choi, M. et al., 2013. Evaluation of drought indices via remotely sensed data with hydrological variables. *Journal of Hydrology*, 476, pp.265–273. Available at: http://www.sciencedirect.com/science/article/pii/S0022169412009420 [Accessed February 2, 2014].

Choudhury, B.J., 2000. Carbon use efficiency, and net primary productivity of terrestrial vegetation. *Advances in Space Research*, 26(7), pp.1105–1108. Available at: http://linkinghub.elsevier.com/retrieve/pii/S0273117799011266.

Ciais, P. et al., 2005. Europe-wide reduction in primary productivity caused by the heat and drought in 2003. *Nature*, 437(7058), pp.529–533. Available at: http://www.nature.com/doifinder/10.1038/nature03972.

Collins, R., Kristensen, P. & Thyssen, N., 2009. *Water resources across Europe — confronting water scarcity and drought*, Copenhagen: European Environment Agency. Available at: http://www.eea.europa.eu/publications/water-resources-across-europe.

Copernicus, 2016. Copernicus Global Land service. Available at: http://land.copernicus.eu/global/ [Accessed November 3, 2016].

Dai, A., 2011. Drought under global warming: a review. *Wiley Interdisciplinary Reviews: Climate Change*, 2(1), pp.45–65. Available at: http://doi.wiley.com/10.1002/wcc.81 [Accessed July 14, 2014].

Dankers, R. & Feyen, L., 2008. Climate change impact on flood hazard in Europe: An assessment based on high-resolution climate simulations. *Journal of Geophysical Research*, 113(D19), p.D19105:1-17. Available at: http://doi.wiley.com/10.1029/2007JD009719.

Döll, P. & Siebert, S., 2002. Global modeling of irrigation water requirements. *Water Resources Research*, 38(4), pp.8-1-8–10. Available at: https://web.uni-frankfurt.de/fb/fb11/ipg/ag/dl/f_publikationen/2002/doell_WRR2002_irrigation.pdf.

Edwards, D.C. & McKee, T.B., 1997. Characteristics of 20th Century drought in the United States at multiple time scales. *Atmospheric Science Paper*, 634(May 1-30), p.174. Available at: http://oai.dtic.mil/oai/oai?verb=getRecord&metadataPrefix=html&identifier=ADA325595 [Accessed March 27, 2014].

ERSAF, 2008. Carta dei suoli in scala 1:50 000 della pianura e collina lombarda [1:50 000 Soil map of Lombardy plain and hills]. Available at: www.ersaf.lombardia.it [Accessed November 8, 2016].

ERSAF, 2012. Carta dell'utilizzo agricolo annuale [Yearly map of agricultural land use].

European Commission, 2007. Addressing the challenge of water scarcity and droughts in the European Union. Available at: http://www.eea.europa.eu/policy-documents/addressing-the-challenge-of-water [Accessed March 28, 2014].

European Drought Observatory, 2016. European Drought Observatory. Available at: http://edo.jrc.ec.europa.eu/ [Accessed November 3, 2016].

European Environment Agency, 2008. *Impacts of Europe's changing climate – An indicator–based assessment*, Copenhagen: European Environment Agency; European Communities. Available at: http://reports.eea.eu.int/climate_report_2_2004/en/impacts_of_europes_changing_climate.pdf Pr?sentation (60 Folien) unter URL: http://reports.eea.eu.int/climate_report_2_2004/en/impacts_of_europes_changing_climate.pdf.

European Environment Agency, 2010. *Mapping the impacts of natural hazards and technological accidents in Europe. An overview of the last decade*, Copenhagen: European Environment Agency. Available at: http://www.eea.europa.eu/publications/mapping-the-impacts-of-natural.

Facchi, A. et al., 2004. Coupled SVAT–groundwater model for water resources simulation in irrigated alluvial plains. *Environmental Modelling & Software*, 19(11), pp.1053–1063. Available at: http://linkinghub.elsevier.com/retrieve/pii/S1364815203002603.

Field, C.B., Randerson, J.T. & Malmström, C.M., 1995. Global net primary production: Combining ecology and remote sensing. *Remote Sensing of Environment*, 51(1), pp.74–88. Available at: http://www.sciencedirect.com/science/article/pii/003442579400066V.

Forzieri, G. et al., 2014. Ensemble projections of future streamflow droughts in Europe. *Hydrology and Earth System Sciences*, 18(1), pp.85–108. Available at: http://www.hydrol-earth-syst-sci.net/18/85/2014/.

Galelli, S. et al., 2010. Building a metamodel of an irrigation district distributed-parameter model. *Agricultural Water Management*, 97(2), pp.187–200. Available at: http://linkinghub.elsevier.com/retrieve/pii/S0378377409002741.

Gandolfi, C. et al., 2014. Integrated modelling for agricultural policies and water resources planning coordination. *Biosystems Engineering*, 128, pp.100–112. Available at: http://dx.doi.org/10.1016/j.biosystemseng.2014.06.006.

Gandolfi, C. et al., 2006. *Twole : un sistema per la pianificazione e la gestione delle risorse idriche. Applicazione pilota ai bacini del Ticino e dell'Adda*, Milano, Italy.

Gao, B., 1996. NDWI—A normalized difference water index for remote sensing of vegetation liquid water from space. *Remote Sensing of Environment*, 58(3), pp.257–266. Available at: http://www.sciencedirect.com/science/article/pii/S0034425796000673 [Accessed February 20, 2014].

Garbulsky, M.F. et al., 2010. Patterns and controls of the variability of radiation use efficiency and primary productivity across terrestrial ecosystems. *Global Ecology and Biogeography*, 19(2), pp.253–267. Available at: http://doi.wiley.com/10.1111/j.1466-8238.2009.00504.x.

Gilabert, M.A. et al., 2015. Daily GPP estimates in Mediterranean ecosystems by combining remote sensing and meteorological data. *ISPRS Journal of Photogrammetry and Remote Sensing*, 102, pp.184–197. Available at: http://dx.doi.org/10.1016/j.isprsjprs.2015.01.017.

Giorgi, F. & Lionello, P., 2008. Climate change projections for the Mediterranean region. *Global and Planetary Change*, 63(2–3), pp.90–104. Available at: http://linkinghub.elsevier.com/retrieve/pii/S0921818107001750.

Gobron, N. et al., 2004a. *Envisat's Medium Resolution Imaging Spectrometer (MERIS) - Algorithm Theoretical Basis Document: FAPAR and Rectified Channels over Terrestrial Surfaces*, Italy: European Union.

Gobron, N. et al., 2004b. *Medium Resolution Imaging Spectrometer (MERIS) - Level 2 Land Surface Products Theoretical Basis Document*, Ispra, Italy.

Guttman, N.B., 1999. Accepting the Standardized Precipitation Index: a calculation algorithm. *JAWRA Journal of the American Water Resources Association*, 35(2), pp.311–322. Available at: http://doi.wiley.com/10.1111/j.1752-1688.1999.tb03592.x.

Guttman, N.B., 1998. Comparing the Palmer Drought Index and the Standardized Precipitation Index. *Journal of the American Water Resources Association*, 34(1), pp.113–121. Available at: http://onlinelibrary.wiley.com/doi/10.1111/j.1752-1688.1998.tb05964.x/full.

Hayes, M.J. et al., 1999. Monitoring the 1996 Drought Using the Standardized Precipitation Index. *Bulletin of the American Meteorological Society*, 80(3), pp.429–438. Available at: http://journals.ametsoc.org/doi/abs/10.1175/1520-0477(1999)080%3C0429:MTDUTS%3E2.0.CO;2.

Heddinghaus, T.R. & Sabol, P., 1991. A Review of the Palmer Drought Severity Index and Where Do We Go from Here? In *Seventh Conference on Applied Climatology*. Salt Lake City, UT: American Meteorological Society, pp. 242–246. Available at: http://www.ncdc.noaa.gov/temp-and-precip/drought/docs/heddinghaus-sabol-pmdi-article.pdf.

Heim, R.R.J., 2002. A Review of Twentieth-Century Drought Indices Used in the United States. *Bulletin of the American Meteorological Society*, 83(8), pp.1149–1165. Available at: http://journals.ametsoc.org/doi/abs/10.1175/1520-0477(2002)083%3C1149:AROTDI%3E2.3.CO;2.

Heinsch, F.A. et al., 2006. Evaluation of remote sensing based terrestrial productivity from MODIS using regional tower eddy flux network observations. *IEEE Transactions on Geoscience and Remote Sensing*, 44(7), pp.1908–1925. Available at: http://ieeexplore.ieee.org/document/1645290/.

Hicke, J.A., Lobell, D.B. & Asner, G.P., 2004. Cropland Area and Net Primary Production Computed from 30 Years of USDA Agricultural Harvest Data. *Earth Interactions*, 8(10), pp.1–20. Available at: http://journals.ametsoc.org/doi/abs/10.1175/1087-3562%282004%29008%3C0001%3ACAANPP%3E2.0.CO%3B2.

Hoekema, D.J. & Ryu, J.H., 2016. Characterizing Drought in Irrigated Agricultural Systems: The Surface Water Delivery Index (SWDI). *JAWRA Journal of the American Water Resources Association*, 52(3), pp.737–755. Available at: http://doi.wiley.com/10.1111/1752-1688.12426.

Hoerling, M. et al., 2012. On the Increased Frequency of Mediterranean Drought. *Journal of Climate*, 25(6), pp.2146–2161. Available at: http://journals.ametsoc.org/doi/abs/10.1175/JCLI-D-11-00296.1.

Horion, S. et al., 2012. *JRC experience on the development of Drought Information Systems. Europe, Africa and Latin America*, Luxembourg. Available at: https://ec.europa.eu/jrc/sites/jrcsh/files/lbna25235enn_0.pdf.

Hosking, J.R.M., 1990. L-Moments: Analysis and Estimation of Distributions Using Linear Combinations of Order Statistics. *Journal of the Royal Statistical Society. Series B (Methodological)*, 52(1), pp.105–124. Available at: https://www.jstor.org/stable/pdf/2345653.pdf.

Hov, Ø. et al., 2013. *Extreme Weather Events in Europe: preparing for climate change adaptation.*, Available at: http://www.easac.eu/fileadmin/PDF_s/reports_statements/Extreme_Weather/Extreme_Weather_full_version_EASAC-EWWG_final_low_resolution_Oct_2013f.pdf.

Von Hoyningen-Hüne, J., 1983. Die Interception des Niederschlags in landwirtschaftlichen Beständen. In *Einfluss der Landnutzung auf den Gebietswasserhaushait. (Schriftenreihe des Deutschen Verbandes für Wasserwirtschaft und Kulturbau e.V., DVWK; H. 57)*. Hamburg und Berlin: Paul Parey, pp. 1–53. Available at: http://wiki.bluemodel.org/images/9/9e/DVWK_57_I.pdf.

Hu, Q. & Willson, G.D., 2000. Effects of temperature anomalies on the Palmer Drought Severity Index in the central United States. *International Journal of Climatology*, 20(15), pp.1899–1911. Available at: http://doi.wiley.com/10.1002/1097-0088%28200012%2920%3A15%3C1899%3A%3AAID-JOC588%3E3.0.CO%3B2-M.

Hunt, E.D. et al., 2014. Monitoring the effects of rapid onset of drought on non-irrigated maize with agronomic data and climate-based drought indices. *Agricultural and Forest Meteorology*, 191, pp.1–11. Available at: http://linkinghub.elsevier.com/retrieve/pii/S0168192314000409 [Accessed September 15, 2014].

International Panel on Climate Change, 2014. *Climate Change 2014: Impacts, Adaptation, and Vulnerability. Part A: Global and Sectoral Aspects. Contribution of Working Group II to the Fifth Assessment Report of the Intergovernmental Panel on Climate Change* C. B. Field et al., eds., Cambridge, United Kingdom and New York, NY, USA: Cambridge University Press. Available at: http://www.ipcc.ch/report/ar5/wg2/.

International Panel on Climate Change, 2012. *Managing the Risks of Extreme Events and Disasters to Advance Climate Change Adaptation* C. B. Field et al., eds., Cambridge: Cambridge University Press. Available at: http://www.ipcc.ch/pdf/special-reports/srex/SREX_Full_Report.pdf.

International Panel on Climate Change, 2000. *Special Report on Emission Scenarios: a special report of Working Group III of the Intergovernmental Panel on Climate Change* N. Nakicenovic & R. Swart, eds., Intergovernmental Panel on Climate Change. Available at: http://www.ipcc.ch/ipccreports/sres/emission/emissions_scenarios.pdf.

Isoard, S. & Henrichs, T., 2005. *European Environment Outlook*, Copenhagen: European Environment Agency. Available at: http://www.eea.europa.eu/publications/eea_report_2005_4/at_download/file [Accessed November 21, 2014].

Istituto Nazionale di Statistica, 2010. 6th Agricultural Census. Available at: http://dati-censimentoagricoltura.istat.it/Index.aspx?lang=en [Accessed October 4, 2016].

Istituto Nazionale di Statistica, 2014. *Utilizzo della risorsa idrica a fini irrigui in agricoltura [Use of irrigation water in agriculture].*, Roma: Istituto Nazionale di Statistica. Available at: http://www.istat.it/it/files/2014/11/Utilizzo_risorsa_idrica.pdf?title=Utilizzo+della+risorsa+idrica+in+agricoltura+-+17%2Fnov%2F2014+-+Volume.pdf.

de Jager, A.L. & Vogt, J. V., 2015. Analyzing the Combined Drought Indicator (CDI): Demonstration and Analysis of its Evolution during Spring and Summer 2013- 2014. *Agriculture and Agricultural Science Procedia*, 4(Cdi), pp.222–231. Available at: http://www.sciencedirect.com/science/article/pii/S2210784315000893.

Jamali, S. et al., 2015. Detecting changes in vegetation trends using time series segmentation. *Remote Sensing of Environment*, 156, pp.182–195. Available at: http://dx.doi.org/10.1016/j.rse.2014.09.010.

Kalfas, J.L. et al., 2011. Modeling gross primary production of irrigated and rain-fed maize using MODIS imagery and CO2 flux tower data. *Agricultural and Forest Meteorology*, 151(12), pp.1514–1528. Available at: http://dx.doi.org/10.1016/j.agrformet.2011.06.007.

Kingston, D.G. et al., 2015. European-Scale Drought: Understanding Connections between Atmospheric Circulation and Meteorological Drought Indices. *Journal of Climate*, 28(2), pp.505–516. Available at: http://journals.ametsoc.org/doi/abs/10.1175/JCLI-D-14-00001.1.

Van der Knijff, J.M. & De Roo, A.P.J., 2008. *LISFLOOD Distributed Water Balance and Flood Simulation Model*, Ispra, Italy: JRC Scientific and Technical report.

Van Der Knijff, J.M., Younis, J. & De Roo, A.P.J., 2010. LISFLOOD: a GIS-based distributed model for river basin scale water balance and flood simulation. *International Journal of Geographical Information Science*, 24(2), pp.189–212. Available at: http://www.tandfonline.com/doi/abs/10.1080/13658810802549154.

Kogan, F.N., 1995. Application of vegetation index and brightness temperature for drought detection. *Advances* *in Space Research*, 15(11), pp.91–100. Available at: http://www.sciencedirect.com/science/article/pii/027311779500079T [Accessed March 14, 2014].

Kogan, F.N., 1995. Droughts of the Late 1980s in the United States as Derived from NOAA Polar-Orbiting Satellite Data. *Bulletin of the American Meteorological Society*, 76(5), pp.655–668. Available at: http://journals.ametsoc.org/doi/abs/10.1175/1520-0477%281995%29076%3C0655%3ADOTLIT%3E2.0.CO%3B2.

Kogan, F.N., 1997. Global Drought Watch from Space. *Bulletin of the American Meteorological Society*, 78(4), pp.621–636. Available at: http://journals.ametsoc.org/doi/abs/10.1175/1520-0477%281997%29078%3C0621%3AGDWFS%3E2.0.CO%3B2.

Laguardia, G. & Niemeyer, S., 2008. On the comparison between the LISFLOOD modelled and the ERS/SCAT derived soil moisture estimates. *Hydrology and Earth System Sciences Discussions*, 5(3), pp.1227–1265. Available at: http://www.hydrol-earth-syst-sci-discuss.net/5/1227/2008/.

Li, L. et al., 2014. Mapping Crop Cycles in China Using MODIS-EVI Time Series. *Remote Sensing*, 6(3), pp.2473–2493. Available at: http://www.mdpi.com/2072-4292/6/3/2473/.

Liu, Y., Pereira, L.S. & Fernando, R.M., 2006. Fluxes through the bottom boundary of the root zone in silty soils: Parametric approaches to estimate groundwater contribution and percolation. *Agricultural Water Management*, 84(1–2), pp.27–40. Available at: http://www.sciencedirect.com/science/article/pii/S0378377406000321 [Accessed April 18, 2014].

Lloyd-Hughes, B. & Saunders, M. a., 2002. A drought climatology for Europe. *International Journal of Climatology*, 22(13), pp.1571–1592. Available at: http://doi.wiley.com/10.1002/joc.846 [Accessed January 28, 2014].

Lobell, D.B. et al., 2002. Satellite estimates of productivity and light use efficiency in United States agriculture, 1982-98. *Global Change Biology*, 8(8), pp.722–735. Available at: http://doi.wiley.com/10.1046/j.1365-2486.2002.00503.x.

Lombardy Regional Authority, 2016. Geographic information portal. Available at: http://www.geoportale.regione.lombardia.it/ [Accessed October 13, 2016].

Lombardy Regional Authority & Istituto Nazionale di Statistica, 2016. Annuario statistico provinciale [Province year statistics]. Available at: http://www.asr-lombardia.it/ASR/ [Accessed November 8, 2016].

Van Loon, A.F. & Van Lanen, H.A.J., 2013. Making the distinction between water scarcity and drought using an observation-modeling framework. *Water Resources Research*, 49(3), pp.1483–1502. Available at: http://doi.wiley.com/10.1002/wrcr.20147.

Marletto, V. et al., 2005. Studio dei fenomeni siccitosi in Emilia-Romagna con il modello di bilancio idrico CRITERIA. In *Rivista Agrometeorologia*. Vasto, Caramanico Terme, pp. 32–33. Available at: http://www.agrometeorologia.it/documenti/Aiam2005/32.pdf [Accessed April 3, 2014].

Marletto, V. & Zinoni, F., 2004. *Un indicatore di siccità agricola: applicazione alla siccità estiva del 2003 in Emilia-Romagna*, Bologna. Available at: https://www.arpae.it/cms3/documenti/_cerca_doc/siccita_desertificazione/DTX_articolo.pdf.

Martínez-Fernández, J. et al., 2015. A soil water based index as a suitable agricultural drought indicator. *Journal of Hydrology*, 522, pp.265–273. Available at: http://linkinghub.elsevier.com/retrieve/pii/S0022169414010622.

Martínez-Fernández, J. et al., 2016. Satellite soil moisture for agricultural drought monitoring: Assessment of the SMOS derived Soil Water Deficit Index. *Remote Sensing of Environment*, 177, pp.277–286. Available at: http://linkinghub.elsevier.com/retrieve/pii/S0034425716300931.

McKee, T.B., Doesken, N.J. & Kleist, J., 1993. The relationship of drought frequency and duration to time scales. In *Proceedings of Eighth Conference on Applied Climatology, Anaheim, CA. American*

Meteorological Society, Boston, MA. pp. 179–184. Available at: http://ccc.atmos.colostate.edu/relationshipofdroughtfrequency.pdf.

McMaster, G.S. & Wilhelm, W.W., 1997. Growing degree-days: one equation, two interpretations. *Agricultural and Forest Meteorology*, 87(4), pp.291–300. Available at: http://linkinghub.elsevier.com/retrieve/pii/S0168192397000270.

Meek, D.. et al., 1999. A note on recognizing autocorrelation and using autoregression. *Agricultural and Forest Meteorology*, 96(1–3), pp.9–17. Available at: http://www.sciencedirect.com/science/article/pii/S0168192399000258.

Meroni, M. et al., 2013. Remote Sensing Based Yield Estimation in a Stochastic Framework — Case Study of Durum Wheat in Tunisia. *Remote Sensing*, 5(2), pp.539–557. Available at: http://www.mdpi.com/2072-4292/5/2/539/.

Milly, P.C.D., Dunne, K.A. & Vecchia, A.V., 2005. Global pattern of trends in streamflow and water availability in a changing climate. *Nature*, 438(7066), pp.347–350. Available at: http://www.nature.com/doifinder/10.1038/nature04312.

Mishra, A.K. et al., 2015. Anatomy of a local-scale drought: Application of assimilated remote sensing products, crop model, and statistical methods to an agricultural drought study. *Journal of Hydrology*, 526, pp.15–29. Available at: http://linkinghub.elsevier.com/retrieve/pii/S0022169414008336.

Mishra, A.K. & Singh, V.P., 2010. A review of drought concepts. *Journal of Hydrology*, 391(1–2), pp.202–216. Available at: http://www.sciencedirect.com/science/article/pii/S0022169410004257 [Accessed March 20, 2014].

Monteith, J.L., 1972. Solar radition and productivity in tropical ecosystems. *Journal Of Applied Ecology*, 9(3), pp.747–766. Available at: http://www.britishecologicalsociety.org/100papers/100_Ecological_Papers/100_Influential_Papers_045.pdf.

Narasimhan, B. & Srinivasan, R., 2005. Development and evaluation of Soil Moisture Deficit Index (SMDI) and Evapotranspiration Deficit Index (ETDI) for agricultural drought monitoring. *Agricultural and Forest Meteorology*, 133(1–4), pp.69–88. Available at: http://www.sciencedirect.com/science/article/pii/S0168192305001565 [Accessed April 3, 2014].

National Aeronautics and Space & Administration, 2016. MODIS Land. Available at: https://modis-land.gsfc.nasa.gov/index.html [Accessed November 3, 2016].

Niemeyer, S., 2008. New drought indices. In A. López-Francos, ed. *Drought management: scientific and technological innovations*. Zaragoza, pp. 267–274. Available at: http://ressources.ciheam.org/om/pdf/a80/00800451.pdf [Accessed April 2, 2014].

Ochsner, T.E. et al., 2013. State of the Art in Large-Scale Soil Moisture Monitoring. *Soil Science Society of America Journal*, 77(6), p.1888. Available at: https://www.soils.org/publications/sssaj/articles/77/6/1888.

Organisation for Econonomic Cooperation and Development, 2016. *Mitigating Droughts and Floods in Agriculture*, Paris: OECD Studies on Water, OECD Publishing. Available at: http://www.keepeek.com/Digital-Asset-Management/oecd/agriculture-and-food/mitigating-droughts-and-floods-in-agriculture_9789264246744-en#.WBmysPTWH7s.

Palmer, W.C., 1965. *Meteorological Drought*, Department of Commerce, United States of America. Available at: https://www.ncdc.noaa.gov/temp-and-precip/drought/docs/palmer.pdf.

Panu, U.S. & Sharma, T.C., 2002. Challenges in drought research: some perspectives and future directions. *Hydrological Sciences Journal*, 47(S), pp.S19–S30. Available at: http://www.tandfonline.com/doi/abs/10.1080/02626660209493019 [Accessed September 23, 2014].

Patel, J.H. & Oza, M.P., 2014. Deriving crop calendar using NDVI time-series. In *ISPRS - International Archives* *of the Photogrammetry, Remote Sensing and Spatial Information Sciences*. pp. 869–873. Available at: http://www.int-arch-photogramm-remote-sens-spatial-inf-sci.net/XL-8/869/2014/.

Peters, A.J. et al., 2002. Drought monitoring with NDVI-based standardized vegetation index. *Photogrammetric engineering and remote sensing*, 68(1), pp.71–75. Available at: http://info.asprs.org/publications/pers/2002journal/january/2002_jan_71-75.pdf [Accessed April 4, 2014].

Pettorelli, N. et al., 2005. Using the satellite-derived NDVI to assess ecological responses to environmental change. *Trends in Ecology & Evolution*, 20(9), pp.503–510. Available at: http://linkinghub.elsevier.com/retrieve/pii/S016953470500162X.

Rawls, W.J. & Brakensiek, D.L., 1989. Estimation of Soil Water Retention and Hydraulic Properties. In H. J. Morel-Seytou, ed. *Unsaturated flow in hydrological modeling*. Springer, pp. 275–300.

Rembold, F. et al., 2013. Using Low Resolution Satellite Imagery for Yield Prediction and Yield Anomaly Detection. *Remote Sensing*, 5(4), pp.1704–1733. Available at: http://www.mdpi.com/2072-4292/5/4/1704/.

Rienzner, M., 2009. *Analisi, trattamento e imputazione dei dati meteorologici necessari alla modellistica agronomico-idrologica.* Università degli Studi di Milano, Facoltà di Agraria.

Rienzner, M. & Gandolfi, C., 2013. A procedure for the detection of undocumented multiple abrupt changes in the mean value of daily temperature time series of a regional network. *International Journal of Climatology*, 33(5), pp.1107–1120. Available at: http://doi.wiley.com/10.1002/joc.3496.

Rohli, R. V. et al., 2016. Drought indices as drought predictors in the south-central USA. *Natural Hazards*, 83(3), pp.1567–1582. Available at: http://link.springer.com/10.1007/s11069-016-2376-z.

Rossi, G. & Cancelliere, A., 2013. Managing drought risk in water supply systems in Europe: a review. *International Journal of Water Resources Development*, 29(2), pp.272–289. Available at: http://www.tandfonline.com/doi/abs/10.1080/07900627.2012.713848 [Accessed September 10, 2014].

Running, S.W. et al., 2000. Global Terrestrial Gross and Net Primary Productivity from the Earth Observing System. In *Methods in Ecosystem Science*. New York, NY: Springer New York, pp. 44–57. Available at: http://link.springer.com/10.1007/978-1-4612-1224-9_4.

Running, S.W. & Nemani, R.R., 1988. Relating seasonal patterns of the AVHRR vegetation index to simulated photosynthesis and transpiration of forests in different climates. *Remote Sensing of Environment*, 24(2), pp.347–367. Available at: http://linkinghub.elsevier.com/retrieve/pii/003442578890034X.

Running, S.W. & Zhao, M., 2015. User's Guide, Daily GPP and Annual NPP (MOD17A2/A3) Products NASA Earth Observing System MODIS Land Algorithm. , p.28. Available at: http://www.ntsg.umt.edu/sites/ntsg.umt.edu/files/modis/MOD17UsersGuide2015_v3.pdf.

Ryu, J.H., Sohrabi, M. & Acharya, A., 2014. Toward Mapping Gridded Drought Indices to Evaluate Local Drought in a Rapidly Changing Global Environment. *Water Resources Management*, 28(11), pp.3859–3869. Available at: http://link.springer.com/10.1007/s11269-014-0714-z.

Sakamoto, T. et al., 2005. A crop phenology detection method using time-series MODIS data. *Remote Sensing of Environment*, 96(3–4), pp.366–374. Available at: http://linkinghub.elsevier.com/retrieve/pii/S0034425705001057.

Sanchez, N. et al., 2012. A simulation of soil water content based on remote sensing in a semi-arid Mediterranean agricultural landscape. *Spanish Journal of Agricultural Research*, 10(2), p.521. Available at: http://revistas.inia.es/index.php/sjar/article/view/2413.

Scaini, A. et al., 2015. SMOS-derived soil moisture anomalies and drought indices: a comparative analysis using in situ measurements. *Hydrological Processes*, 29(3), pp.373–383. Available at: http://doi.wiley.com/10.1002/hyp.10150 [Accessed September 23, 2014].

Schmidt, G., Benítez, J.J. & Benítez, C., 2012. *Working definitions of Water scarcity and Drought*,

Sepulcre-Canto, G. et al., 2012. Development of a Combined Drought Indicator to detect agricultural drought in Europe. *Natural Hazards and Earth System Science*, 12(11), pp.3519–3531. Available at: http://www.nat-hazards-earth-syst-sci.net/12/3519/2012/ [Accessed April 10, 2014].

Shao, Y. et al., 2016. An evaluation of time-series smoothing algorithms for land-cover classifications using MODIS-NDVI multi-temporal data. *Remote Sensing of Environment*, 174, pp.258–265. Available at: http://dx.doi.org/10.1016/j.rse.2015.12.023.

Sheffield, J. & Wood, E.F., 2008. Projected changes in drought occurrence under future global warming from multi-model, multi-scenario, IPCC AR4 simulations. *Climate Dynamics*, 31(1), pp.79–105. Available at: http://link.springer.com/10.1007/s00382-007-0340-z.

Shokoohi, A. & Morovati, R., 2015. Basinwide Comparison of RDI and SPI Within an IWRM Framework. *Water Resources Management*, 29(6), pp.2011–2026. Available at: http://link.springer.com/10.1007/s11269-015-0925-y.

Siebert, S. et al., 2013. Global Map of Irrigation Areas version 5. *Rheinische Friedrich-Wilhelms-University, Bonn, Germany / Food and Agriculture Organization of the United Nations, Rome, Italy*. Available at: http://www.fao.org/nr/water/aquastat/irrigationmap/index10.stm [Accessed October 4, 2016].

Sillmann, J. & Roeckner, E., 2008. Indices for extreme events in projections of anthropogenic climate change. *Climatic Change*, 86(1–2), pp.83–104. Available at: http://link.springer.com/10.1007/s10584-007-9308-6.

Singer, J.W. et al., 2011. Variability of light interception and radiation use efficiency in maize and soybean. *Field Crops Research*, 121(1), pp.147–152. Available at: http://linkinghub.elsevier.com/retrieve/pii/S0378429010003217.

Singh, V.P., Guo, H. & Yu, F.X., 1993. Parameter estimation for 3-parameter log-logistic distribution (LLD3) by Pome. *Stochastic Hydrology and Hydraulics*, 7(3), pp.163–177. Available at: http://link.springer.com/10.1007/BF01585596.

Singleton, A., 2012. *Forecasting Drought in Europe with the Standardized Precipitation Index*, Luxembourg. Available at: https://ec.europa.eu/jrc/sites/jrcsh/files/lbna25254enn_0.pdf.

Sivakumar, M.V.K. et al., 2011. Agricultural Drought Indices. In M. V. K. Sivakumar et al., eds. *Proceedings of the WMO/UNISDR Expert Group Meeting on Agricultural Drought Indices, 2-4 June 2010, Murcia, Spain*. Murcia, Spain: World Meteorological Organization, p. 205. Available at: http://www.droughtmanagement.info/literature/WMO_agricultural_drought_indices_proceedings_2010.pdf.

Sjöström, M. et al., 2013. Evaluation of MODIS gross primary productivity for Africa using eddy covariance data. *Remote Sensing of Environment*, 131, pp.275–286. Available at: http://dx.doi.org/10.1016/j.rse.2012.12.023.

Smakhtin, V.U. & Schipper, E.L.F., 2008. Droughts: The impact of semantics and perceptions. *Water Policy*, 10(2), p.131. Available at: http://wp.iwaponline.com/cgi/doi/10.2166/wp.2008.036.

Spinoni, J. et al., 2015. European drought climatologies and trends based on a multi-indicator approach. *Global and Planetary Change*, 127, pp.50–57. Available at: http://dx.doi.org/10.1016/j.gloplacha.2015.01.012.

Spinoni, J. et al., 2016. *Meteorological Droughts in Europe: Events and Impacts – Past Trends and Future Projections*, Luxembourg.

Spinoni, J. et al., 2014. World drought frequency, duration, and severity for 1951-2010. *International Journal of Climatology*, 34(8), pp.2792–2804. Available at: http://doi.wiley.com/10.1002/joc.3875.

Stahl, K., 2001. *Hydrological Drought - a Study across Europe. PhD Thesis*. Universität Freiburg. Available at:

http://www.freidok.uni-freiburg.de/volltexte/2001/202/ [Accessed September 23, 2014].

Steduto, P. et al., 2012. *Crop yield response to water*, Rome: Food and Agriculture Organization of the United Nations. Available at: https://lirias.kuleuven.be/handle/123456789/356847 [Accessed September 19, 2014].

Stöckle, C.O., Donatelli, M. & Nelson, R., 2003. CropSyst, a cropping systems simulation model. *European Journal of Agronomy*, 18(3–4), pp.289–307. Available at: http://linkinghub.elsevier.com/retrieve/pii/S1161030102001090.

Strosser, P. et al., 2012. *Final Report Gap Analysis of the Water Scarcity and Droughts Policy in the EU European Commission*, Available at: http://ec.europa.eu/environment/water/quantity/pdf/WSDGapAnalysis.pdf.

Thom, H.C.S., 1996. *Some Methods of Climatological Analysis* Secretariat of the World Meteorological Organization, ed., Geneva: WMO N. 199. Technical Note N. 81. Secretariat of the World Meteorological Organization.

Törnros, T. & Menzel, L., 2014. Addressing drought conditions under current and future climates in the Jordan River region. *Hydrology and Earth System Sciences*, 18(1), pp.305–318. Available at: http://www.hydrol-earth-syst-sci.net/18/305/2014/ [Accessed March 28, 2014].

Trenberth, K.E. et al., 2013. Global warming and changes in drought. *Nature Climate Change*, 4(1), pp.17–22. Available at: http://dx.doi.org/10.1038/nclimate2067%255Cn10.1038/nclimate2067.

Tsakiris, G., Loukas, A., et al., 2007. Drought characterization [Part 1. Components of drought planning. 1.3. Methodological component]. In A. Iglesias, M. Moneo, & A. López-Francos, eds. *Drought management guidelines technical annex*. Zaragoza, pp. 85–102. Available at: http://om.ciheam.org/article.php?IDPDF=800535.

Tsakiris, G., Pangalou, D. & Vangelis, H., 2007. Regional Drought Assessment Based on the Reconnaissance Drought Index (RDI). *Water Resources Management*, 21(5), pp.821–833. Available at: http://link.springer.com/10.1007/s11269-006-9105-4 [Accessed March 24, 2014].

Tsakiris, G. & Vangelis, H., 2005. Establishing a drought index incorporating evapotranspiration. *European Water*, 9(10), pp.3–11. Available at: http://www.ewra.net/ew/pdf/EW_2005_9-10_01.pdf.

Tucker, C.J., 1979. Red and photographic infrared linear combinations for monitoring vegetation. *Remote Sensing of Environment*, 8(2), pp.127–150. Available at: http://www.sciencedirect.com/science/article/pii/0034425779900130 [Accessed April 3, 2014].

Tucker, C.J. & Choudhury, B.J., 1987. Satellite remote sensing of drought conditions. *Remote Sensing of Environment*, 23(2), pp.243–251. Available at: http://linkinghub.elsevier.com/retrieve/pii/003442578790040X.

Tucker, C.J. & Sellers, P.J., 1986. Satellite remote sensing of primary production. *International Journal of Remote Sensing*, 7(11), pp.1395–1416. Available at: http://www.tandfonline.com/doi/abs/10.1080/01431168608948944.

United Nations Environment Programme, 1992. *World Atlas of Desertification* N. Middleton & D. S. G. Thomas, eds., London: Edward Arnold.

United States Geological Survey, 2016. Landsat Missions. Available at: http://landsat.usgs.gov/ [Accessed November 3, 2016].

USDA Soil Conservation Service, 1972. Section 4: Hydrology. Estimation of Direct Runoff From Storm Rainfall. In *National Engineering Handbook*.

Vangelis, H., Spiliotis, M. & Tsakiris, G., 2011. Drought Severity Assessment Based on Bivariate Probability Analysis. *Water Resources Management*, 25(1), pp.357–371. Available at:

http://link.springer.com/10.1007/s11269-010-9704-y.

Vanneuville, W. et al., 2012. *Water resources in Europe in the context of vulnerability: EEA 2012 state of water assessment*, Copenhagen. Available at: http://www.eea.europa.eu/publications/water-resources-and-vulnerability/at_download/file.

Vassena, C. et al., 2012. Modeling water resources of a highly irrigated alluvial plain (Italy): calibrating soil and groundwater models. *Hydrogeology Journal*, 20(3), pp.449–467. Available at: http://link.springer.com/10.1007/s10040-011-0822-2.

Vicente-Serrano, S.M. et al., 2015. Contribution of precipitation and reference evapotranspiration to drought indices under different climates. *Journal of Hydrology*, 526, pp.42–54. Available at: http://dx.doi.org/10.1016/j.jhydrol.2014.11.025.

Vicente-Serrano, S.M. et al., 2014. Evidence of increasing drought severity caused by temperature rise in southern Europe. *Environmental Research Letters*, 9(4), p.44001. Available at: http://stacks.iop.org/1748-9326/9/i=4/a=044001?key=crossref.a4db08a1ad24a00be1d79dd69814b0e5 [Accessed September 23, 2014].

Vicente-Serrano, S.M., Beguería, S. & López-Moreno, J.I., 2010. A Multiscalar Drought Index Sensitive to Global Warming: The Standardized Precipitation Evapotranspiration Index. *Journal of Climate*, 23(7), pp.1696–1718. Available at: http://journals.ametsoc.org/doi/abs/10.1175/2009JCLI2909.1 [Accessed February 20, 2014].

Warren Liao, T., 2005. Clustering of time series data—a survey. *Pattern Recognition*, 38(11), pp.1857–1874. Available at: http://www.sciencedirect.com/science/article/pii/S0031320305001305.

Wells, N., Goddard, S. & Hayes, M.J., 2004. A Self-Calibrating Palmer Drought Severity Index. *Journal of Climate*, 17(12), pp.2335–2351. Available at: http://journals.ametsoc.org/doi/abs/10.1175/1520-0442%282004%29017%3C2335%3AASPDSI%3E2.0.CO%3B2.

West, T.O. et al., 2010. Cropland carbon fluxes in the United States: increasing geospatial resolution of inventory-based carbon accounting. *Ecological Applications*, 20(4), pp.1074–1086. Available at: http://doi.wiley.com/10.1890/08-2352.1.

White, M.A. et al., 2009. Intercomparison, interpretation, and assessment of spring phenology in North America estimated from remote sensing for 1982-2006. *Global Change Biology*, 15(10), pp.2335–2359. Available at: http://doi.wiley.com/10.1111/j.1365-2486.2009.01910.x.

Williams, J.R., 1995. The EPIC model. In V. P. Singh, ed. *Computer models of watershed hydrology.* Highland Ranch, Co, USA: Water Resources Publications, pp. 909–1000.

Woli, P. et al., 2014. Predicting Crop Yields with the Agricultural Reference Index for Drought. *Journal of Agronomy and Crop Science*, 200(3), pp.163–171. Available at: http://doi.wiley.com/10.1111/jac.12055 [Accessed September 4, 2014].

World Meteorological Organization, 2006. *Drought monitoring and early warning : concepts , progress and future challenges*, Geneva, Switzerland. Available at: http://www.wamis.org/agm/pubs/brochures/WMO1006e.pdf.

World Meteorological Organization, 2012. *Standardized Precipitation Index User Guide*, Geneva, Switzerland. Available at: http://www.wamis.org/agm/pubs/SPI/WMO_1090_EN.pdf.

World Meteorological Organization & Global Water Partnership, 2016. *Handbook of drought indicators and indices* M. D. Svoboda & B. A. Fuchs, eds., Geneva: World Meteorological Organization and Global Water Partnership.

Wriedt, G., van der Velde, M., et al., 2009. A European irrigation map for spatially distributed agricultural modelling. *Agricultural Water Management*, 96(5), pp.771–789. Available at: http://linkinghub.elsevier.com/retrieve/pii/S0378377408002837 [Accessed October 9, 2014].

Wriedt, G., Van der Velde, M., et al., 2009. Estimating irrigation water requirements in Europe. *Journal of Hydrology*, 373(3–4), pp.527–544. Available at: http://linkinghub.elsevier.com/retrieve/pii/S0022169409003175 [Accessed September 16, 2014].

Wu, H. et al., 2007. Appropriate application of the standardized precipitation index in arid locations and dry seasons. *International Journal of Climatology*, 27(1), pp.65–79. Available at: http://doi.wiley.com/10.1002/joc.1371.

Xin, Q. et al., 2013. A Production Efficiency Model-Based Method for Satellite Estimates of Corn and Soybean Yields in the Midwestern US. *Remote Sensing*, 5(11), pp.5926–5943. Available at: http://www.mdpi.com/2072-4292/5/11/5926/.

Xin, Q. et al., 2015. Multi-scale evaluation of light use efficiency in MODIS gross primary productivity for croplands in the Midwestern United States. *Agricultural and Forest Meteorology*, 201, pp.111–119. Available at: http://linkinghub.elsevier.com/retrieve/pii/S016819231400272X.

Zeng, L. et al., 2016. A hybrid approach for detecting corn and soybean phenology with time-series MODIS data. *Remote Sensing of Environment*, 181, pp.237–250. Available at: http://linkinghub.elsevier.com/retrieve/pii/S0034425716301432.

LIST OF TABLES

LIST OF FIGURES

ANNEX

I IDRAGRA MANUAL

I-1. List of principal symbols

Symbol	Meaning [unit]
a_I	empirical coefficient to compute interception [mm]
$a_{irr\ met}$	parameter that accounts for irrigation method [-]
$a_{irr\ met}^{inf}$	minimum value of $a_{irr\ met}$ for the considered irrigation method [-]
$a_{irr\ met}^{sup}$	maximum value of $a_{irr\ met}$ for the considered irrigation method [-]
$a_{rc,1}$	$a_{rc,1} = W_{FC}$,soil water storage to 1.0 m depth at field capacity [mm]
$a_{rc,2}$	$a_{rc,2} = 1.1\frac{w_{fc}-W_{wp}}{2}$, storage above the average between those at field capacity and the wilting point [mm]
$a_{rc,3}$	empirical parameter to estimate critical groundwater depth that depends on soil type [-]
$a_{rc,4}$	empirical parameter to estimate potential capillary flux that depends on soil type [-]
b_I	soil cover fraction to compute interception, estimated by $b_I = \min\left(\frac{LAI}{3}, 1\right)$ [-]
$b_{rc,1}$	empirical parameter to estimate critical soil water storage that depends on soil type [-]
$b_{rc,2}$	empirical parameter to estimate steady soil water storage that depends on soil type [-]
$b_{rc,3}$	empirical parameter to estimate critical groundwater depth that depends on soil type [-]
$b_{rc,4}$	empirical parameter to estimate potential capillary flux that depends on soil type [-]
CGD_t	accumulated thermal time since planting for the day t [°C d]
CN	Curve Number [-]
CN_x	curve number adjusted for moisture condition and slope [-]
CN_1	moisture condition I curve number [-]
CN_2	moisture condition II curve number [-]
CN_{2s}	moisture condition II curve number adjusted for slope [-]
CN_3	moisture condition III curve number [-]
CN_4	moisture condition at saturation, equal to 95 [-]
$(CN_x)_{crop}$	curve number adjusted for moisture condition and slope, for crop [-]
$(CN_x)_{fallow}$	curve number adjusted for moisture condition and slope, for fallow land use, crop residue cover treatment [-]
c_p	specific heat at constant pressure, $1.013 \cdot 10^{-3}\ MJ\ kg^{-1}C^{-1}$
$D_{e,i-1}$	cumulative depth of evaporation from the soil surface layer the end of the previous day [mm]
$D_{i,k}^2$	squared distance from the n data points to the point estimated (i,j) [m^2]
d_r	inverse relative distance Earth-Sun [-]
d_s	maximum number of days for the translation of crop parameters series [-]
D_w	groundwater depth [m]
D_{WC}	critical groundwater depth [mm]
dlh	daylight hours of the day t [d]
dlh_{if}	daylight hours to inhibit flowering, day length threshold below (for long-day crops) or above (for short-day crops) which no accumulation of physiological time occurs [d]
dlh_{ins}	daylight hours for insensitivity, day length threshold above (for long-day crops) or below (for short-day crops) which maximum physiological time accumulation occurs [d]
E	evaporation rate [mm d^{-1}]
e_a	actual vapour pressure [kPa]
$e^0(T_{air})$	saturation vapour pressure at the air temperature T_{air} [kPa]
$e^0(T_{max})$	saturation vapour pressure at the air temperature T_{max} [kPa]
$e^0(T_{min})$	saturation vapour pressure at the air temperature T_{min} [kPa]
e_s	saturation vapour pressure [kPa]
ET_0	reference evapotranspiration [mm d^{-1}]

ET_c	crop evapotranspiration under standard conditions [mm d^{-1}]
$ET_{c\ adj}$	crop adjusted evapotranspiration [mm d^{-1}]
f_c	average fraction of soil surface covered by vegetation $[0-0.99]$ [-]
f_{ew}	soil surface from which most evaporation occurs [-]
f_w	average fraction of soil surface wetted by irrigation or precipitation $[0.01-1]$ [-]
$f_{w,1}, f_{w,2}, f_{w,3}$	well flow shares [-] [0-1]
G	soil heat flux density [MJ m^{-2} d^{-1}]
g	days elapsed since last irrigation [d]
GD_t	thermal time of the day t [°C d]
G_{max}	potential capillary flux rate [mm d^{-1}]
G_{sc}	solar constant, equal to $0.0820\ MJ\ m^{-2}\ min^{-1}$
h	crop height [m]
h_{irr}	fixed irrigation amount to the field [mm]
h_{max}	maximum crop height [m]
i	day number within the growing season [1 … length of the growing season] [-]
I	canopy rainfall interception [mm d^{-1}]
I_a	initial abstractions which includes surface storage, interception and infiltration prior to runoff [mm d^{-1}]
J	Julian day: number of the day in the year between 1 (January 1st) and 365 or 366 (December 31st) [-]
K_c	crop coefficient [-]
$K_{c\ max}$	maximum value of K_c following rain or irrigation [-]
$K_{c\ min}$	minimum $K_{cb}$for dry bare soil with no ground cover $[\approx 0.15-0.20]$
K_{cb}	basal crop coefficient [-]
$K_{cb\ i}$	crop coefficient on day i [-]
$K_{cb\ ini}$	basal crop coefficient for the initial stage [-]
$K_{cb\ mid}$	basal crop coefficient for the mid-season stage [-]
$K_{cb\ end}$	basal crop coefficient at the of the late season stage [-]
K_e	soil water evaporation coefficient [-]
K_E	unsaturated hydraulic conductivity of the evaporative layer [cm h^{-1}]
K_r	evaporation reduction coefficient dependent on the cumulative depth of water depleted from the topsoil [-]
$K_{s,E}$	saturated hydraulic conductivity of the evaporative layer [cm h^{-1}]
$K_{s,E}^{10th}$	10th percentile of saturated hydraulic conductivity distribution for the evaporative layer [cm h^{-1}]
$K_{s,E}^{90th}$	90th percentile of saturated hydraulic conductivity distribution for the evaporative layer [cm h^{-1}]
$K_{s,T}$	saturated hydraulic conductivity of the transpirative layer [cm h^{-1}]
$K_{s,T}^{10th}$	10th percentile of saturated hydraulic conductivity distribution for the transpirative layer [cm h^{-1}]
$K_{s,T}^{90th}$	90th percentile of saturated hydraulic conductivity distribution for the transpirative layer [cm h^{-1}]
K_T	unsaturated hydraulic conductivity of the transpirative layer [cm h^{-1}]
LAI	Leaf Area Index [-]
M_i	meteorological value estimated for the i-th cell
M_k	known meteorological value for the k-th data point
n	number of interpolating points [-]
n_E	Brooks-Corey exponent for the evaporative layer [-]
n_T	Brooks-Corey exponent for the transpirative layer [-]
P	rainfall rate [mm d^{-1}]
p	average fraction of Total Available Soil Water that can be depleted from the root zone before moisture stress occurs $[0-1]$ [-]
p_{tab}	tabulated values of average fraction of Total Available Soil Water that can be depleted from the root zone before moisture stress occurs [-]
P_{atm}	atmospheric pressure [kPa]
P_{eff}	effective rainfall[mm d^{-1}]
PF	photoperiod factor [0-1] [-]
$P_{i,k}$	normalized weight of the k-th data point on the point estimated (i,j) [-]
Q_e	outflow from the evaporative to the transpirative layer, accounting for irrigation management [mm d^{-1}]
$Q_{e,nc}$	outflow from the evaporative to the transpirative layer, not accounting for irrigation management [mm]
Q_g	inflow from the deeper subsoil to the root zone [mm d^{-1}]
Q_i	irrigation supply [mm d^{-1}]

Q_i^{gross}	gross irrigation supply [mm]
$Q_{i,w}$	irrigation supply from well [mm d^{-1}]
Q_{inf}	infiltration [mm d^{-1}]
Q_p	ponding [mm d^{-1}]
Q_w	maximum well flow rate [mm]
q_{pond}	ponded water ratio [-]
$q_{pond\ max}$	maximum ratio for ponding water, that occurs at minimum slope slp_{min} [-]
$q_{pond\ min}$	maximum ratio for ponding water, that occurs at minimum slope slp_{max} [-]
Q_s	outflow from the root zone to the deeper subsoil, accounting for irrigation management, ($Q_s > 0$) or capillary rise rate ($Q_s < 0$) [mm d^{-1}]
$Q_{s,nc}$	outflow from the root zone to the deeper subsoil, not accounting for irrigation management [mm]
Q_u	net runoff from the cell [mm d^{-1}]
R_a	extraterrestrial radiation [MJ m^{-2} d^{-1}]
RAW	readily available soil water in the root zone [mm]
REW	cumulative depth of evaporation at the end of first stage (readily evaporable water) [mm]
RH_{max}	maximum relative humidity [%]
RH_{min}	minimum relative humidity [%]
R_n	net radiation at the crop surface [MJ m^{-2} d^{-1}]
R_{nl}	net outgoing longwave radiation [MJ m^{-2} d^{-1}]
R_{ns}	net solar or shortwave radiation [MJ m^{-2} d^{-1}]
R_s	incoming solar radiation [MJ m^{-2} d^{-1}]
R_{so}	clear-sky solar radiation [MJ m^{-2} d^{-1}]
S	retention parameter [mm d^{-1}]
slp	average fraction slope of the cell [%]
t	daily time step [d]
T	transpiration rate [mm d^{-1}]
T_{air}	air temperature at $2\ m$ height [°C]
TAW	total available soil water in the root zone [mm]
T_c	potential crop transpiration rate [mm d^{-1}]
T_{cutoff}	maximum temperature for viable crop development [°C]
$T_{daybase}$	minimum temperature for viable crop development [°C]
TEW	total evaporable water, equal to the maximum depth of water that can be evaporated from the soil when the topsoil has been initially completely wetted [mm]
t_h	hourly time step [h]
T_{max}	daily maximum temperature at $2\ m$ height [°C]
$T_{max,K}$	maximum daily absolute temperature $T_{max,K} = T_{max} + 273.16$ [K]
T_{mean}	mean daily air temperature at $2\ m$ height [°C]
T_{min}	daily minimum temperature at $2\ m$ height [°C]
$T_{min,K}$	minimum daily absolute temperature $T_{min,K} = T_{min} + 273.16$ [K]
TV_A	parameter for not optimum vernalization [°C]
TV_{max}	high end temperature threshold for optimum vernalization [°C]
TV_{min}	low end temperature threshold for optimum vernalization [°C]
T_{sow}	sowing temperature threshold [°C]
u_2	wind speed at $2\ m$ height [m s^{-1}]
$\overline{U_i}$	effective readily available soil water in the root zone for the i-th cell [mm]
$\overline{U_i^{MAX}}$	maximum effective readily available soil water in the root zone for the i-th cell [mm]
VD_{end}	required sum to complete vernalization (at which VF reaches a value of 1.0) [d]
VD_{start}	accumulated vernalization days at which VF is set equal to VF_{min} [d]
VD_{sum}	sum of the currently accumulated vernalization days, equal to $\sum_{j=i}^{d} V_{eff}$ [d]
V_{E}	water content of the evaporative layer per unit surface area of the cell [mm]
V_{eff}	vernalization contribution of day d [d]
VF	vernalization factor [0-1] [-]
VF_{min}	minimum vernalization factor value at the beginning of the vernalization process [0-1] [-]
V_{T}	water content of the transpirative layer per unit surface area of the cell [mm]

$V_{T-r,i,t}$	water content minus the residual water content of the transpirative layer for the i-th cell and the day t [mm]
W	actual soil water storage in the root zone [mm]
W_c	critical soil water storage [mm]
W_s	steady soil water storage [mm]
(X_i, Y_i)	i-th cell center coordinates [m]
(X_k, Y_k)	k-th data point coordinates [m]
z	elevation above sea level [m]
Z_e	depth of the surface soil layer that is subject to drying by way of evaporation [0.10-0.15] [m]
Z_r	depth of the transpirative layer [m]
α	albedo, which is 0.23 for the hypothetical grass reference crop [-]
α_i	coefficient for the activation of irrigation[-]
α_w	coefficient for well activation [-] [0-1]
$\alpha_{w,1}, \alpha_{w,2}$	well activation thresholds [-] [0-1]
γ	psychrometric constant [kPa °C^{-1}]
δ	solar declination [rad]
$\varDelta$	slope vapour pressure curve [kPa °C^{-1}]
ε	ratio molecular weight of water vapour/dry air 0.622
θ	soil water content of the entire profile [m^3 m^{-3}]
θ_E	volumetric water content of the evaporative layer [m^3 m^{-3}]
θ_{fc}	field capacity soil profile water content [m^3 m^{-3}]
$\theta_{fc,E}$	soil water content of the evaporating layer at field capacity [m^3 m^{-3}]
$\theta_{fc,T}$	soil water content of the transpirative layer at field capacity [m^3 m^{-3}]
$\theta_{fc,wp}$	Antecedent Moisture Condition II soil profile water content, equal to $\theta_{fc,wp} = \theta_{wp} + \frac{2}{3}(\theta_{fc} - \theta_{wp})$ [m^3 m^{-3}]
$\theta_{r,E}$	residual water content of the evaporative layer [m^3 m^{-3}]
$\theta_{r,T}$	residual water content of the transpirative layer [m^3 m^{-3}]
$\theta_{RAW,T}$	water content corresponding to RAW for the transpirative layer, equal to $\theta_{FC,T} - \ p \cdot (\theta_{FC,T} - \theta_{WP,T})$ [m^3 m^{-3}]
θ_s	saturation soil profile water content [m^3 m^{-3}]
$\theta_{s,E}$	saturated water content of the evaporative layer [m^3 m^{-3}]
$\theta_{s,T}$	saturated water content of the transpirative layer [m^3 m^{-3}]
θ_T	volumetric water content of the transpirative layer [m^3 m^{-3}]
θ_{wp}	wilting point soil profile water content [m^3 m^{-3}]
$\theta_{wp,E}$	soil water content of the evaporating layer at wilting point [m^3 m^{-3}]
$\theta_{wp,T}$	soil water content of the transpirative layer at wilting point [m^3 m^{-3}]
σ	Stefan-Boltzmann constant, equal to $4.903 \cdot 10^{-9}$ MJ K^{-4} m^{-2} d^{-1}
φ	latitude [rad]
$\varphi_{degrees}$	latitude [decimal degrees]
ξ_{conv}	conveyance efficiency [0.01-0.99] [-]
ξ_{field}	field application efficiency [0.01-0.99] [-]
λ	latent heat of vaporization, $2.45\ MJ\ \ kg^{-1}$
ω_s	sunset hour angle [rad]

I-2. IdrAgra

IdrAgra is a distributed-parameter conceptual model, which allows the simulation of the irrigation water distribution in agricultural areas and the estimation of the hydrological balance on a daily basis. IdrAgra includes four main modules devoted to specific tasks (Figure i-1): irrigation water sources, conveyance and distribution over the territory, crop phenological stages and soil-crop water balance.

The soil-crop water balance module simulates soil water content dynamics, computing crop water need and consumptions, and the downward fluxes to the groundwater, accounting for the space variability of soils, crops, meteorological and irrigation inputs. The irrigation water sources, conveyance and distribution modules acquire as input surface water and springs diverted discharges, and estimate irrigation water from wells on the basis of their parameters. It also takes into account conveyance and irrigation efficiency maps to estimate crop water supply and distribution. On the basis of meteorological inputs, the crop phonological stages module simulates crop sowing dates and calculates phenological phases length.

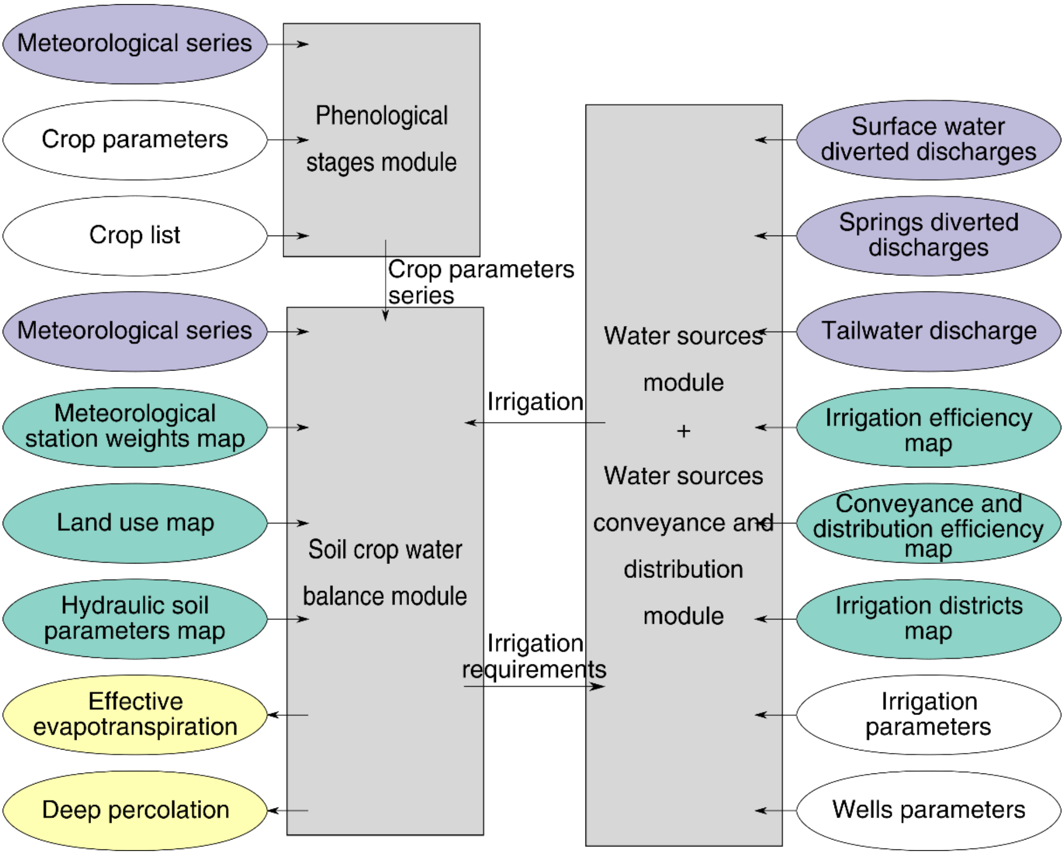

Figure i-1: Flowchart of the IdrAgra simulation model: modules are reported in grey, parameters in whilte, punctual inputs in violet, spatial inputs in light blue, and outputs in yellow.

I-3. Soil-crop water balance

The model core is the soil-crop water balance module, which accounts for the space variability of soils, crops, meteorological and irrigation inputs by dividing the irrigation district with a regular mesh. Soil and crop characteristics, meteorological inputs, and irrigation supply are homogeneous in each cell of the mesh but may vary from cell to cell. Each cell identifies a soil volume which extends from the soil surface to the lower limit of the root zone. The representation of hydrological processes is one-dimensional.

The soil volume of each is subdivided into two layers (Figure i-2): the top one (evaporative layer) represents the upper few centimetres of the soil, while the bottom one (transpirative layer) represents the root zone and has a time-varying depth. The two layers are modelled as two non-linear reservoirs in cascade.

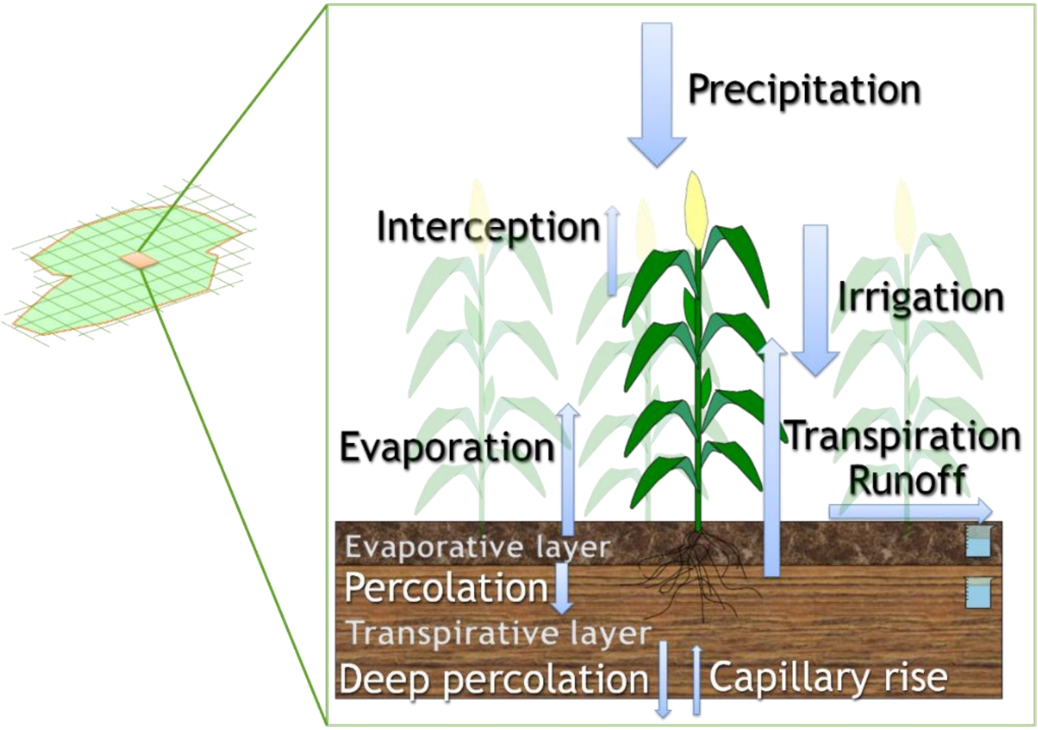

Figure i-2: Scheme of the IdrAgra soil crop water balance module.

The dynamics of the water content in the evaporative (top) layer of the cell is governed by the following balance equation:

$$\left[P - I + Q_i - Q_u - E + Q_g - Q_e \pm Q_p\right]_t = \frac{\Delta V_E}{\Delta t} \qquad \text{(i-1)}$$

where P $(mm \cdot d^{-1})$ is the rainfall rate, I $(mm \cdot d^{-1})$ is the canopy interception, Q_i $(mm \cdot d^{-1})$ is the net inflow to the cell (irrigation supply), Q_u $(mm \cdot d^{-1})$ is the net runoff from the cell, E $(mm \cdot d^{-1})$ is the evaporation rate, Q_g $(mm \cdot d^{-1})$ is the inflow from the deeper subsoil to the root zone, Q_e $(mm \cdot d^{-1})$ is the outflow to the transpirative layer, Q_p $(mm \cdot d^{-1})$ is the ponding,

V_E (mm) is the water content of the evaporative layer per unit surface area of the cell and t (d) is the daily time step.

A similar equation holds for the dynamics of the water content in the transpirative (bottom) layer:

$$[Q_e - T \pm Q_s]_t = \frac{\Delta V_T}{\Delta t} \tag{i-2}$$

where T $(mm \cdot d^{-1})$ is the transpiration rate, Q_e $(mm \cdot d^{-1})$ is the outflow from the evaporative layer, Q_s $(mm \cdot d^{-1})$ is the outflow from the root zone to the deeper subsoil $(Q_s > 0)$ or the capillary rise rate $(Q_s < 0)$, V_T (mm) is the water content of the transpirative layer per unit surface area of the cell and t (d) is the daily time step.

If we assume that the net outflow Q_u from each cell is collected by the drainage network, the net inflow Q_i into each cell of equation i-1 is equal to the irrigation amount that infiltrate into the soil. That hypothesis is acceptable due to the characteristics of the irrigation districts of the Po River Plain. It is also acceptable to neglect the term Q_g, that includes essentially capillary rise fluxes. The last term can be relevant only in clay soils with very shallow groundwater.

I-3.1. Crop reference evapotranspiration

Evapotranspiration terms are calculated using Allen et al. (1998) approach, whereby the effect of the climate on crop water requirements is given by the reference evapotranspiration ET_0 and the effect of the crop by the crop coefficient, splitted into two factors that separately describe the evaporation and transpiration components.

Reference crop evapotranspiration or reference evapotranspiration, denoted as ET_0, is the evapotranspiration calculated from a hypothetical grass reference crop with an assumed crop height of 0.12 m, a fixed surface resistance of 70 $s \cdot m^{-1}$ and an albedo of 0.23 (Figure i-3). The reference surface closely resembles an extensive surface of green, well-watered grass of uniform height, actively growing and completely shading the ground.

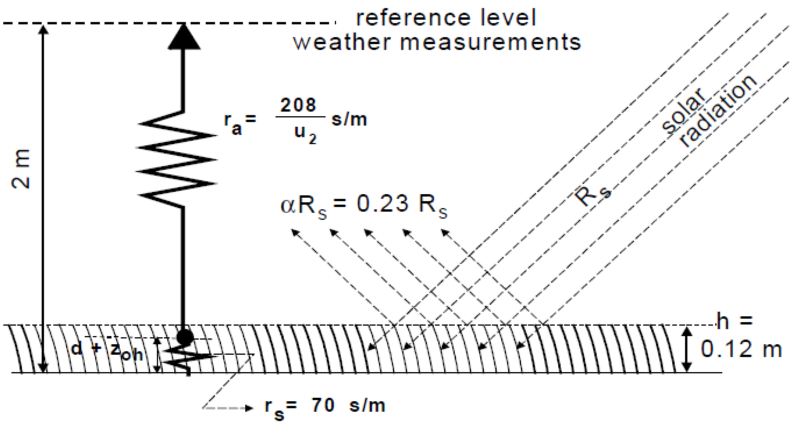

Figure i-3: Characteristics of the hypothetical reference crop. Source: Allen *et al.*, 1998.

ET_0 is computed from meteorological data using the FAO Penman-Monteith method that requires radiation, air temperature, air humidity and wind speed data:

$$ET_0 = \frac{0.408\Delta(R_n - G) + \gamma \frac{900}{T_{mean}+273} u_2 (e_s - e_a)}{\Delta + \gamma(1 + 0.34 u_2)} \tag{i-3}$$

where ET_0 $(mm \cdot d^{-1})$ is the reference evapotranspiration, R_n $(MJ \cdot m^{-2} \cdot d^{-1})$ is the net radiation at the crop surface, G $(MJ \cdot m^{-2} \cdot d^{-1})$ is the soil heat flux density, T_{mean} $(°C)$ and u_2 $(m \cdot s^{-1})$ are respectively the mean daily air temperature and the wind speed at $2 \ m$ height, e_s (kPa) and e_a (kPa) are respectively the saturation and the actual vapour pressure, $\mathit{\Delta}$ $(kPa \cdot °C^{-1})$ is the slope vapour pressure curve and γ $(kPa \cdot °C^{-1})$ is the psychrometric constant.

The approach used to estimate equation i-3 terms is described in Allen et al. (1998), transcribed in the sequel for completeness.

I-3.1.1. Atmospheric parameters

The atmospheric pressure is calculated employing a simplification of the ideal gas law, assuming $20°C$ for a standard atmosphere, as:

$$P_{atm} = 101.3 \left(\frac{293 - 0.0065z}{293}\right)^{5.26} \tag{i-4}$$

where P_{atm} (kPa) is the atmospheric pressure and z (m) is the elevation above sea level.

The latent heat of vaporization, λ, expresses the energy required to change a unit mass of water from liquid to water vapour in a constant pressure and constant temperature process. As it varies only slightly over normal temperature range, a single value of $2.45 \ MJ \ kg^{-1}$ can be taken to calculate the psychometric constant:

$$\gamma = \frac{c_p P_{atm}}{\varepsilon \lambda} = 0.665 \cdot 10^{-3} P_{atm} \tag{i-5}$$

where γ $(kPa \cdot °C^{-1})$ is the psychrometric constant, P_{atm} (kPa) is the atmospheric pressure, λ is the latent heat of vaporization, equal to $2.45 \ MJ \ kg^{-1}, c_p$, specific heat at constant pressure, equal to $1.013 \cdot 10^{-3} \ MJ \ kg^{-1}C^{-1}, \text{and}$ ε (adimensional) is the ratio molecular weight of water vapour/dry air, equal to 0.622.

The mean daily air temperature, employed in the FAO Penman-Monteith equation to calculate the slope of the saturation vapour pressure curves, is defined as the mean of the daily maximum and minimum temperatures:

$$T_{mean} = \frac{T_{max} + T_{min}}{2} \tag{i-6}$$

where T_{mean} $(°C)$, T_{max} $(°C)$ and T_{min} $(°C)$ are the daily mean, maximum and minimum temperatures, respectively, at $2 \ m$ height.

As the saturation vapour pressure is related to air temperature, it can be calculated from the air temperature, as:

$$e^0(T_{air}) = 0.6108e^{\frac{17.27T_{air}}{T_{air}+237.3}} \tag{i-7}$$

where $e^0(T_{air})$ (kPa) is the saturation vapour pressure at the air temperature T_{air} $(°C)$, measured at $2\ m$ height.

Due to the non-linearity of equation i-7, the mean saturation vapour pressure is computed as the mean between the saturation vapour pressure at the mean daily maximum and minimum air temperatures for that period:

$$e_s = \frac{e^0(T_{max})+e^0(T_{min})}{2} \tag{i-8}$$

where e_s (kPa) is the mean saturation vapour pressure and T_{max} $(°C)$ and T_{min} $(°C)$ are respectively the daily maximum and minimum temperatures at $2\ m$ height.

The slope of the relationship between saturation vapour pressure and temperature, Δ, at a temperature T_{air}, is given by:

$$\Delta = \frac{4098\left(0.6108e^{\frac{17.27T_{air}}{T_{air}+237.3}}\right)}{(T_{air}+237.3)^2} \tag{i-9}$$

where Δ (kPa) is the slope of saturation vapour pressure curve at air temperature T_{air} $(°C)$.

The actual vapour pressure is calculated form the relative humidity by:

$$e_a = \frac{e^0(T_{min})\frac{RH_{max}}{100}+e^0(T_{max})\frac{RH_{min}}{100}}{2} \tag{i-10}$$

where e_a (kPa) is the actual vapour pressure, $e^0(T_{min})$ (kPa) and $e^0(T_{max})$ (kPa) are respectively the saturation vapour pressures at daily minimum (T_{min}) and maximum temperature (T_{max}), and RH_{max} (%) and RH_{min} (%) are respectively the maximum and minimum relative humidities.

I-3.1.2. Radiation

The extraterrestrial radiation, for each day of the year and for different latitudes, is estimated from the solar constant, the solar declination and the time of the year by:

$$R_a = \frac{24\cdot 60}{\pi} G_{sc} d_r[\omega_s \sin(\varphi)\sin(\delta) + \cos(\varphi)\cos(\delta)\sin(\omega_s)] \tag{i-11}$$

where R_a $(MJ \cdot m^{-2} \cdot d^{-1})$ is the extraterrestrial radiation, G_{sc} is the solar constant, equal to $0.0820\ MJ\ m^{-2}\ min^{-1}, d_r$ (adimensional) is the inverse relative distance between Earth and Sun, ω_s (rad) is the sunset hour angle, φ (rad) is the latitude and δ (rad) is the solar declination.

The latitude, expressed in radians in equation i-11, can be converted from decimal degrees by:

$$\varphi = \frac{\pi}{180} \cdot \varphi_{degrees} \tag{i-12}$$

where φ (rad) and $\varphi_{degrees}$ (°) are respectively the latitude expressed in radians and in decimal degrees.

The inverse relative distance between Earth and Sun, d_r, and the solar declination, δ, are given by:

$$d_r = 1 + 0.033\cos\left(\frac{2\pi}{365}day\right) \tag{i-13}$$

$$\delta = 0.409\sin\left(\frac{2\pi}{365}J - 1.39\right) \tag{i-14}$$

where d_r (adimensional) is the inverse relative distance between Earth and Sun, δ (rad) is the solar declination and J (adimensional) is the Julian day (i.e. the number of the day in the year between 1, January 1st and 365 or 366, December 31st).

The sunset hour angle is given by:

$$\omega_s = \arccos[-\tan(\varphi)\tan(\delta)] \tag{i-15}$$

where ω_s (rad) is the sunset hour angle, φ (rad) is the latitude and δ (rad) is the solar declination.

The calculation of the clear-sky radiation, R_{so}, can be calculated with the Ångström formula, which relates solar radiation to extraterrestrial radiation and relative sunshine duration:

$$R_{so} = (0.75 + 2\cdot 10^{-5}z)R_a \tag{i-16}$$

where R_{so} $(MJ\cdot m^{-2}\cdot d^{-1})$ is the clear-sky solar radiation, z (m) is the elevation above sea level and R_a $(MJ\cdot m^{-2}\cdot d^{-1})$ is the extraterrestrial radiation.

The net shortwave radiation resulting from the balance between incoming and reflected solar radiation is given by:

$$R_{ns} = (1-\alpha)R_s \tag{i-17}$$

where R_{ns} $(MJ\cdot m^{-2}\cdot d^{-1})$ is the net solar (or shortwave) radiation, α (adimensional) is the albedo, which is 0.23 for the hypothetical grass reference crop, and R_s $(MJ\cdot m^{-2}\cdot d^{-1})$ is the incoming solar radiation.

To express the rate of longwave energy emission, the Stefan-Boltzmann law is corrected by humidity and cloudiness, which play an important role in absorbing and emitting longwave radiation. The rate of longwave energy emission is therefore given by:

$$R_{nl} = \sigma\left(\frac{T_{max,K}^4 + T_{min,K}^4}{2}\right)\left(0.34 - 0.14\sqrt{e_a}\right)\left(1.35\frac{R_s}{R_{so}} - 0.35\right) \tag{i-18}$$

where R_{nl} $(MJ\cdot m^{-2}\cdot d^{-1})$ is the net outgoing longwave radiation, σ is the Stefan-Boltzmann constant, equal to $4.903\cdot 10^{-9}$ $MJ\cdot K^{-4}\cdot m^{-2}\cdot d^{-1}$, $T_{max,K}$ (K) and $T_{min,K}$ (K) are respectively the maximum ($T_{max,K} = T_{max} + 273.16$) and minimum ($T_{min,K} = T_{min} + 273.16$) daily absolute temperatures, e_a (kPa) is the actual vapour pressure, and R_s $(MJ\cdot m^{-2}\cdot d^{-1})$ and

R_{so} $(MJ \cdot m^{-2} \cdot d^{-1})$ are respectively the incoming solar radiation and the clear-sky radiation. The relative shortwave radiation is limited so that $\frac{R_s}{R_{so}} \leq 1.0$.

The net radiation is the difference between the incoming net shortwave radiation and the outgoing net longwave radiation:

$$R_n = R_{ns} - R_{nl} \tag{i-19}$$

where R_n $(MJ \cdot m^{-2} \cdot d^{-1})$ is the net radiation, and R_{nl} $(MJ \cdot m^{-2} \cdot d^{-1})$ and R_{ns} $(MJ \cdot m^{-2} \cdot d^{-1})$ are respectively the net outgoing longwave radiation and the net solar (or shortwave) radiation.

The soil heat flux, G, beneath the grass reference surface may be ignored at the magnitude of the day, thus $G \approx 0$.

I-3.2. Crop evapotranspiration

The crop evapotranspiration under standard conditions (ET_c), is calculated, according to Allen *et al.* (1998), referring to crops grown in large fields under excellent agronomic and soil water conditions. The crop evapotranspiration differs distinctly from the reference evapotranspiration (ET_0) as the ground cover, canopy properties and aerodynamic resistance of the crop are different from grass. The effects of characteristics that distinguish field crops from grass are integrated into the crop coefficient (K_c). In the crop coefficient approach, crop evapotranspiration is calculated by:

$$ET_c = K_c ET_0 \tag{i-20}$$

where ET_c $(mm \cdot d^{-1})$ is the crop evapotranspiration under standard conditions, K_c (adimensional) is the crop coefficient and ET_0 $(mm \cdot d^{-1})$ is the reference evapotranspiration.

In the dual crop coefficient approach, the effects of crop transpiration and soil evaporation are determined separately. Two coefficient are used: the basal crop coefficient (K_{cb}) to describe plant transpiration, and the soil water evaporation coefficient (K_e) to describe evaporation from the soil surface. The single K_c coefficient is replaced by:

$$K_c = K_{cb} + K_e \tag{i-21}$$

where K_c (adimensional) is the crop coefficient, K_{cb} (adimensional) is the basal crop coefficient and K_e (adimensional) is the soil water evaporation coefficient.

I-3.2.1. Transpiration component

The basal crop coefficient (K_{cb}) is defined as the ratio of the crop evapotranspiration over the reference transpiration (ET_c/ET_0) when the soil surface is dry but transpiration is occurring at a potential rate (i.e. water is not limiting transpiration).

Changes in vegetation and ground cover mean that the crop coefficient K_{cb} varies during the growing period (Figure i-4). The trends in K_{cb} during the growing period are represented in the crop coefficient curve. Only three values for K_{cb} are required to describe and construct the crop coefficient curve: those during the initial stage ($K_{cb\ \ ini}$), the mid-season stage ($K_{cb\ \ mid}$) and at the end of the late season stage ($K_{cb\ \ end}$).

Recommended basal crop coefficients, K_{cb}, for non stressed, well-managed crops are listed in Allen *et al.* (1998); the values implemented in IdrAgra are listed in Table i-1.

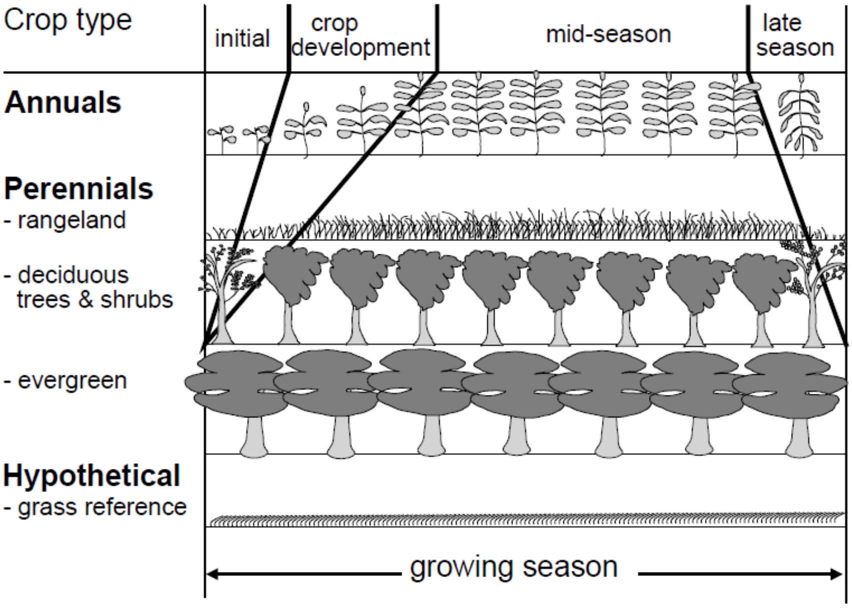

Figure i-4: Crop growth stages for different types of crops. Surce: Allen *et al.*, 1998.

Table i-1: Basal crop coefficients, K_{cb}, mean maximum plant heights, h_{max}, maximum effective rooting depth ($Z_r + Z_e$) and soil water depletion fraction (p) for non stressed, well-managed crops, implemented in IdrAgra.

Crop	$K_{cb\ \ ini}$ (adimensional)	$K_{cb\ \ mid}$ (adimensional)	$K_{cb\ \ end}$ (adimensional)	h_{max} (m)	$(Z_r + Z_e)$ (m)	p (adimensional)
Tomato	0.30	1.10	0.70	0.7	1.0	0.40
Sweet melons	0.40	1.00	0.75	0.4	0.8	0.40
Sugar beet	0.15	0.95	0.50	0.6	1.0	0.50
Soybeans	0.15	1.066	0.318	0.8	1.0	0.50
Cereals	0.15	1.067	0.212	0.6	1.0	0.50
Maize – field (grain) harvest after complete field drying of the grain	0.15	0.95	0.15^{a}	3.0	0.85	0.50
Maize – field (grain) harvest at high grain moisture	0.15	1.107	0.50^{b}	2.0	1.0	0.50
Rice	0.80	1.10	0.90	$0.7 - 0.8^{d}$	0.40	0.20^{e}
Alfalfa Hay – individual cutting periods	0.30^{c}	1.09^{c}	1.04^{c}	0.7	1.0	0.50
Clover Hay, Berseem – individual cutting periods	0.30^{c}	1.12^{c}	1.07^{c}	0.6	0.75	0.50

[a] The $K_{cb\ \ end}$ value is for harvest after complete field drying of the grain (to about 18% soil moisture, wet mass basis).
[b] The $K_{cb\ \ end}$ value is for harvest at high grain moisture.
[c] These K_{cb} coefficients for hay crops represent immediately following cutting; at full cover; and immediately before cutting, respectively. The growing season is described as a series of individual cutting periods.
[d] The high value for h_{max} is for paddyfield rice
[e] The value for p for rice is 0.20 of saturation.

The K_{cb} curve is constructed for annual crops by connecting straight lines segments through each of the four growth stages (Figure i-5). Horizontal lines are drawn through $K_{cb\ ini}$ in the initial stage and through $K_{cb\ mid}$ in the mid-season stage. Diagonal lines are drawn from $K_{cb\ ini}$ to $K_{cb\ mid}$ within the course of the crop development stage and from $K_{cb\ mid}$ to $K_{cb\ end}$ within the course of the late season stage. For forage crops harvested several times during the growing season, each harvest essentially terminates a 'sub' growing season and associated K_{cb} curve and initiates a new 'sub' growing season and associated K_{cb} curve.

The numerical determination of the K_{cb} for any period of the growing season can be derived by:

$$K_{cb\ i} = K_{cb\ prev} + \left[\frac{i - \Sigma(L_{prev})}{L_{stage}}\right] (K_{cb\ next} - K_{cb\ prev}) \qquad \text{(i-22)}$$

where i (adimensional) is the day number within the growing season, $K_{cb\ i}$ (adimensional) is the crop coefficient on day i, L_{stage} (d) is the length of the stage under consideration, $\sum(L_{prev})$ (d) is the sum of the lengths of all previous stages, and $K_{cb\ prev}$ (adimensional) and $K_{cb\ next}$ (adimensional) are the crop coefficients of the previous and the next stage respectively.

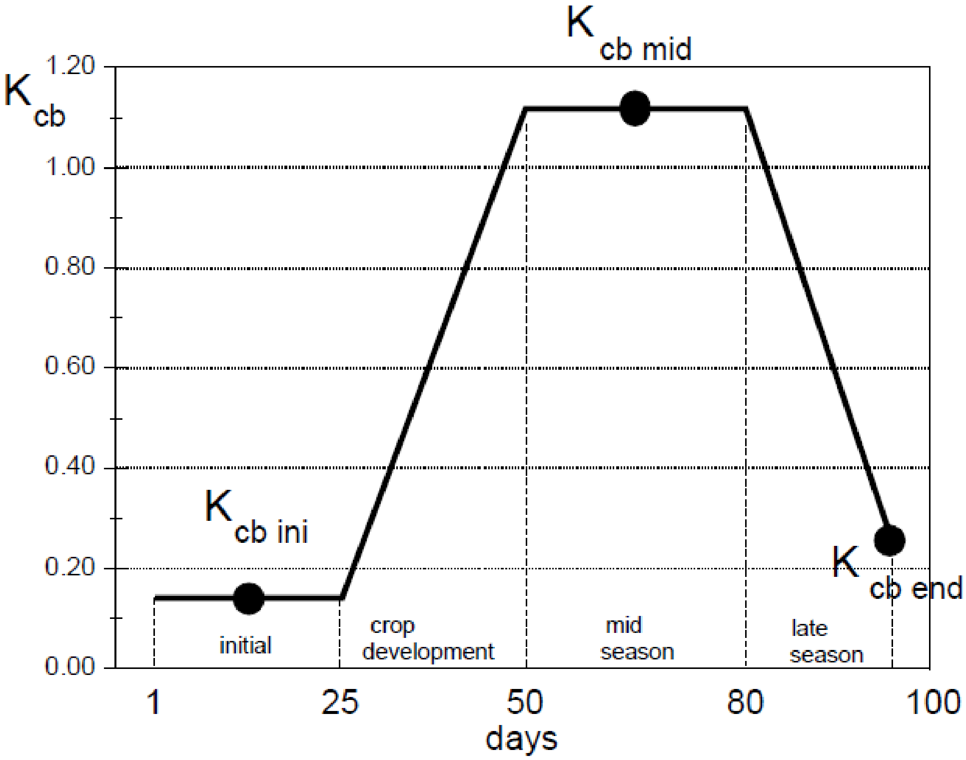

Figure i-5: Crop coefficient curve for annual crops. Source: Allen *et al.*, 1998.

I-3.2.2. Evaporation component

The soil evaporation coefficient K_e describes the evaporation component of ET_c. Where the topsoil is wet, following rain or irrigation, K_e is maximal. Where the soil surface is dry, K_e is small and even zero when no water remains near the soil surface for evaporation.

The crop coefficient ($K_c = K_{cb} + K_e$) can never exceed a maximum value, $K_{c\ max}$. This value is determined by the energy available for evapotranspiration at the soil surface: $K_{cb} + K_e \leq K_{c\ max}$.

When the topsoil dries out, less water is available for evaporation and a reduction in evaporation begins to occur in proportion to the amount of water remaining in the surface soil layer, or $K_e = K_r(K_{c\ max}K_{cb}) \leq f_{ew}K_{c\ max}$. The equation can be expressed as:

$$K_e = \min(K_r(K_{c\ max} - K_{cb}), f_{ew}K_{c\ max}) \tag{i-23}$$

where K_e (adimensional) is the soil evaporation coefficient, K_{cb} (adimensional) is the basal crop coefficient, $K_{c\ max}$ (adimensional) is the maximum value of K_c following rain or irrigation, K_r (adimensional) is the evaporation reduction coefficient dependent on the cumulative depth of water depleted from the topsoil and f_{ew} (adimensional) is the soil surface from which most evaporation occurs.

$K_{c\ max}$ represents an upper limit on the evaporation and transpiration from any cropped surfaced and is imposed to reflect the natural constraints placed on available energy represented by the energy balance difference $R_n - G - H$:

$$K_{c\ max} = \max\left(\begin{matrix}\left\{1.2 + [0.04(u_2 - 2) - 0.004(RH_{min} - 45)]\left(\frac{h}{3}\right)^{0.3}\right\}, \\ \{K_{cb} + 0.05\}\end{matrix}\right) \tag{i-24}$$

where u_2 $(m \cdot s^{-1})$ is the daily wind speed at $2\ m$ height, RH_{min} (%) is the daily minimum relative humidity, h (m) is the daily plant height and K_{cb} (adimensional) is the basal crop coefficient. Equation i-24 ensures that $K_{c\ max}$ is always greater or equal to the sum $K_{cb} + 0.05$.

Soil evaporation from the exposed soil can be assumed to take place in two stages: an energy limiting stage, and a falling rate stage. When the soil surface is wet, $K_r = 1$. When the water content in the upper soil becomes limiting, K_r decreases and becomes zero when the total amount of water that can be evaporated from the topsoil is depleted (Figure i-6).

It is assumed that the water content of the evaporating layer of the soil is at field capacity, $\theta_{FC,E}$, shortly following rain or irrigation and that the soil can dry to a soil water content level that is halfway between oven dry and wilting point, $\theta_{WP,E}$. The amount of water that can be depleted by evaporation during a complete drying cycle can hence be estimated as:

$$TEW = 1000(\theta_{fc,E} - 0.5\theta_{wp,E})Z_e \tag{i-25}$$

where TEW (mm) is the total evaporable water (i.e. the maximum depth of water that can be evaporated from the soil when the topsoil has been initially completely wetted), $\theta_{fc,E}$ $(m^3 \cdot m^{-3})$ and $\theta_{wp,E}$ $(m^3 \cdot m^{-3})$ are respectively the soil water contents of the evaporating layer at field capacity and at wilting point, and Z_e (m) is the depth of the surface soil layer that is subject to drying by way of evaporation $[0.10 - 0.15]$.

At the start of a drying cycle, following rain or irrigation, the soil water content in the topsoil is at field capacity and the amount of water depleted by evaporation, D_e, is zero. During the first stage of the drying process, the soil surface remains wet and it is assumed that evaporation from soil exposed to the atmosphere will occur at the maximum rate limited only by energy availability at the soil surface. This stage holds until the cumulative depth of evaporation, D_e, is such that the hydraulic properties of the upper soil become limiting and water cannot be transported to the soil surface at a rate that can supply the potential demand. During first stage drying, $K_r = 1$. The cumulative depth of evaporation, D_e, at the end of first stage drying is the Ready Evaporable Water (REW, i.e. the maximum depth of water that can be evaporated from the topsoil layer without restriction).

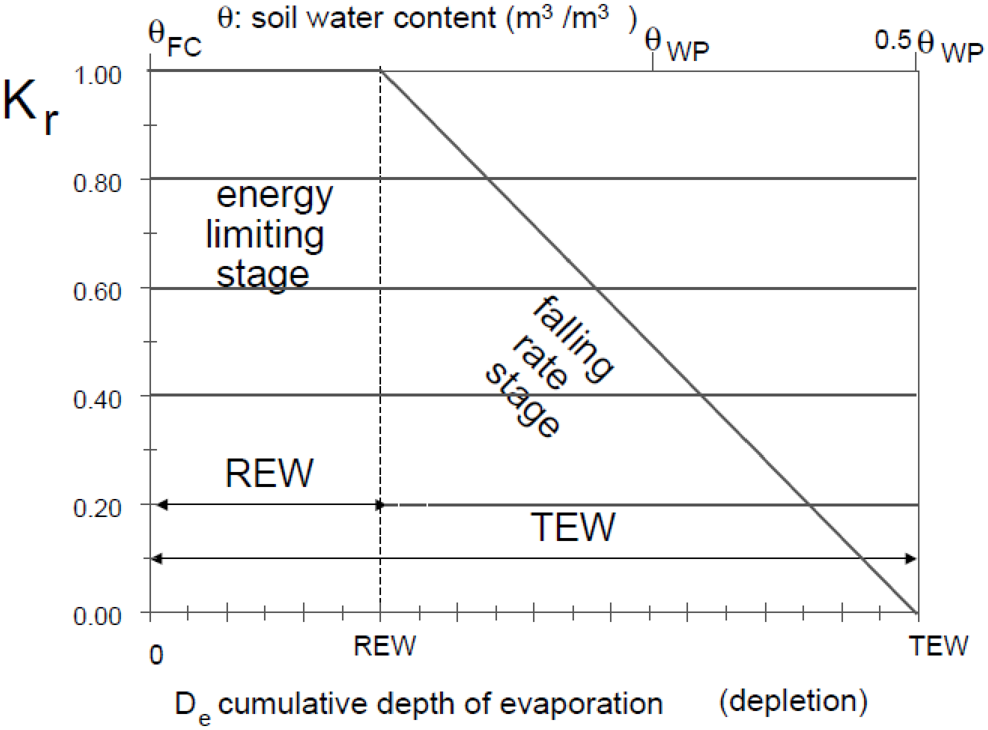

Figure i-6: Soil evaporation reduction coefficient, K_r. Source: Allen *et al.*, 1998.

The second stage, where the evaporation rate is reducing, starts when D_e exceeds REW. At this point, the soil surface is visibly dry, and the evaporation from the exposed soil decreases in proportion to the amount of water remaining in the surface soil layer:

$$K_r = \frac{TEW - D_{e,i-1}}{TEW - REW} \quad \text{for} \quad D_{e,i-1} > REW \tag{i-26}$$

where K_r (adimensional) is the evaporation reduction coefficient dependent on the soil water depletion from the topsoil layer, $D_{e,i-1}$ (mm) is the cumulative depth of evaporation from the soil surface layer the end of the previous day, TEW (mm) is the total evaporable water (i.e. the maximum cumulative depth of evaporation from the soil surface layer when $K_r = 0$) and REW (mm) is the readily evaporable water (i.e. the cumulative depth of evaporation at the end of first stage).

I-3.2.3. Exposed and wetted soil fraction

Where the complete soil surface is wetted, as by precipitation or by surface irrigation, then the fraction of soil surface from which most evaporation occurs, f_{ew}, is essentially defined as $(1 - f_c)$, where f_c is the average fraction of soil surface covered by vegetation. However, for irrigation systems where only a fraction of the ground surface is wetted, f_{ew} is limited to the fraction of the soil surface wetted by irrigation:

$$f_{ew} = \min(1 - f_c, f_w) \tag{i-27}$$

where f_{ew} (adimensional) is the exposed and wetted soil fraction, f_c (adimensional) is the average fraction of soil surface covered by vegetation $[0 - 0.99]$ and f_w (adimensional) is the average fraction of soil surface wetted by irrigation or precipitation $[0.01 - 1]$.

The fraction of the soil surface that is covered by vegetation is estimated using the relationship:

$$f_c = \left(\frac{K_{cb} - K_{c\ min}}{K_{c\ max} - K_{c\ min}}\right)^{(1+0.5h)} \tag{i-28}$$

where f_c (adimensional) is the effective fraction of soil surface covered by vegetation $[0 - 0.99]$, K_{cb} (adimensional) is the basal crop coefficient for the particular day, $K_{c\ min}$ (adimensional) is the minimum K_{cb} for dry bare soil with no ground cover $[\approx 0.15 - 0.20]$, $K_{c\ max}$ (adimensional) is the maximum K_{cb} immediately following wetting (equation i-24) and h (m) is the mean plant height. The difference $K_{cb} - K_{c\ min} \geq 0.01$ for numerical stability.

Considering the irrigation systems applied to the area, the value of the average fraction of soil surface wetted by irrigation, f_w, is supposed equal to 1 for each wetting event.

I-3.2.4. Crop evapotranspiration under non-standard conditions

Where the conditions encountered in the field differ from the standard conditions, a correction on ET_c is required. When the potential energy of the soil water drops below a threshold value, the crop is water stressed. The effects of soil water stress are described by multiplying the basal crop coefficient by the water stress coefficient K_s:

$$ET_{c\ adj} = (K_s K_c + K_e) ET_0 \tag{i-29}$$

where $ET_{c\ adj}$ ($mm \cdot d^{-1}$) is the crop adjusted evapotranspiration, K_s (adimensional) is the transpiration reduction factor dependent of available soil water $[0 - 1]$, K_{cb} (adimensional) is the basal crop coefficient, K_e (adimensional) is the soil evaporation coefficient and ET_0 ($mm \cdot d^{-1}$) is the reference evapotranspiration.

Soil water availability refers to the capacity of a soil to retain water available to plants. After rainfall or irrigation, the soil will drain until field capacity is reached. In the absence of water supply, the water content in the root zone decreases as a result of water uptake by the crop. As water uptake progresses, the remaining water is held to the soil particles with greater force, lowering its potential energy and making it more difficult for the plant to extract it. Eventually, the water uptake becomes zero when wilting point is reached and plants will permanently wilt.

As the water content above field capacity cannot be held against the forces of gravity and will drain and as the water content below wilting point cannot be extracted by plant roots, the total available water in the root zone is given by:

$$TAW = 1000(\theta_{fc,T} - \theta_{wp,T})Z_r \qquad \text{(i-30)}$$

where TAW (mm) is the total available soil water in the root zone, $\theta_{fc,T}$ $(m^3 \cdot m^{-3})$ and $\theta_{wp,T}$ $(m^3 \cdot m^{-3})$ are respectively the soil water contents of the transpirative layer at field capacity and at wilting point, and Z_r (m) is the depth of the transpirative layer.

Although water is theoretically available until wilting point, crop water uptake is reduced well before wilting point is reached. Where the soil is sufficiently wet, the soil supplies water fast enough to meet the atmospheric demand of the crop, and water uptake equals ET_c. As the soil water content decreases, water becomes more strongly bound to the soil matrix and is more difficult to extract. When the soil water content drops below a threshold water, soil water can no longer be transported quickly enough towards the roots to respond to the transpiration demand and the crop begins to experience stress. The fraction of TAW that a crop from the root zone without suffering water stress is:

$$RAW = pTAW \qquad \text{(i-31)}$$

where RAW (mm) is the readily available soil water in the root zone, p (adimensional) is the average fraction of total available soil water that can be depleted from the root zone before moisture stress occurs $[0-1\ ]$ and TAW (mm) is the total available soil water in the root zone.

The fraction p is a function of the evaporation power of the atmosphere. A numerical approximation for adjusting p for ET_c rate is:

$$p = p_{tab} + 0.04(5 - ET_c) \qquad \text{(i-32)}$$

where p (adimensional) is the adjusted mean fraction of TAW that can be depleted from the root zone before moisture stress occurs $[0.1 - 0.8], p_{tab}$ (adimensional) is the the tabulated value of average fraction of total available soil water that can be depleted from the root zone before moisture stress occurs and ET_c (mm) is the crop evapotranspiration.

The effects of soil water stress on crop evapotranspiration are described by reducing the value for the crop coefficient. This is accomplished by multiplying the crop coefficient by the water stress coefficient, K_s.

Water content in the root zone can by expressed by root zone depletion, D_r (i.e. the water shortage relative to field capacity). At field capacity, the root zone depletion is zero ($D_r = 0$). When soil water is extracted by evapotranspiration, the depletion increases and stress will be induced when D_r

becomes equal to RAW. After the root zone depletion is high enough to limit evapotranspiration to less than potential values and the crop evapotranspiration begins to decrease in proportion to the amount of water remaining in the root zone (Figure i-7).

For $D_r > RAW$, K_s is given by:

$$K_s = \frac{TAW - D_r}{TAW - RAW} = \frac{TAW - D_r}{(1-p)TAW} \qquad \text{(i-33)}$$

where K_s (adimensional) is the transpiration reduction factor dependent on available soil water, D_r (mm) is the root zone depletion, TAW (mm) is the total available soil water in the root zone and p (adimensional) is the fraction of TAW that a crop can extract from the root zone without suffering water stress.

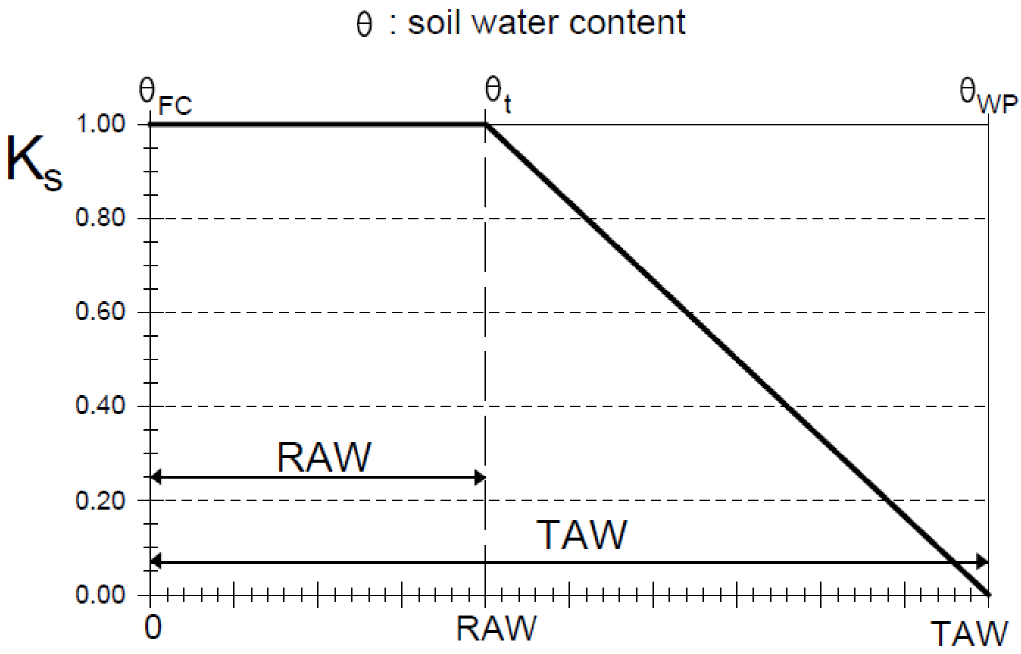

Figure i-7: Water stress coefficient, K_s. Source: Allen *et al.*, 1998.

I-3.3. Surface runoff

Surface runoff occurs whenever the rate of water application, either from rainfall or from surface irrigation, to the ground surface exceeds the infiltration rate. When water is initially applied to a dry soil, the infiltration rate is usually very high. However, it will decrease as the soil becomes wetter. When the application rate is higher than the infiltration rate, surface depressions begin to fill. If the application rate continues to be higher than the infiltration rate once all surface depressions have filled, surface runoff will start.

IdrAgra computes surface runoff volume using a modification of the Soil Conservation Service curve number method (SCS, 1972). The method, run on a daily basis, is applied after interception and infiltration are calculated, but before taking into account surface storage.

The SCS runoff equation is an empirical model that came into common use in the 1950s to estimate direct runoff from storm rainfall. The model was developed to provide a consistent basis for estimating the amounts of runoff under varying land use and soil types (Rallison and Miller, 1981) and is also used in SWAT model (Neitsch et al., 2011).

The SCS curve number equation is:

$$Q_u = \frac{(P - I_a)^2}{P - I_a + S} \tag{i-34}$$

where Q_u $(mm \cdot d^{-1})$ is the accumulated runoff or superficial rainfall excess, P $(mm \cdot d^{-1})$ is the rainfall rate for the day, I_a $(mm \cdot d^{-1})$ are the initial abstractions which includes surface storage, interception and infiltration prior to runoff, and S $(mm \cdot d^{-1})$ is the retention parameter.

The retention parameter represents the potential maximum water volume after runoff begins, and varies spatially due to changes in soils, land use, management and slope, and temporally due to changes in soil water content. It is defined as:

$$S = 25.4\left(\frac{1000}{CN} - 10\right) \tag{i-35}$$

where S $(mm \cdot d^{-1})$ is the retention parameter and CN (adimensional) is the Curve Number. In equation i-35, the number 25.4 is a conversion factor from inches to millimetres.

The initial abstractions, I_a, is commonly approximated as $I_a = 0.2S$, and equation i-34 becomes:

$$Q_u = \frac{(P - 0.2S)^2}{P + 0.8S} \tag{i-36}$$

Runoff will only occur when $P > I_a$, or, substituting I_a by $0.2S$, when $P > 0.2S$.

In the SCS method, the change in S (actually in CN) is based on an antecedent moisture condition (AMC). Typical curve numbers for moisture condition II are listed in Table i-2 for agricultural land covers and soil types of the study area (SCS Engineering Division, 1986); the correspondences between land uses and crops are listed in Table i-3. Tabled values are appropriate for a 5% slope.

Treatment is a cover type modifier to describe the management of cultivate agricultural lands. It includes mechanical practices, such as contouring and terracing, and management practices, such as crop rotations and reduced or no tillage.

Hydrologic condition indicates the effects of cover type and treatment on infiltration and runoff. Good hydrologic condition indicates that the soil usually has a low runoff potential for that specific hydrologic soil group, cover type, and treatment. Affecting factors are canopy or density of lawns, crops, or other vegetative areas, amount of year-round cover, amount of grass or close-seeded legumes in rotations, percent of residue cover and degree of surface roughness.

Table i-2: Runoff curve numbers for antecedent moisture condition II for agricultural lands; values for a 5% slope. Selection for study area. Source: SCS Engineering Division, 1986.

Cover			Hydrologic Soil Group			
Land use	**Treatment or practice**	**Hydrologic condition**	**A**	**B**	**C**	**D**
Fallow	Bare soil	---	77	89	91	94
	Crop residue cover[1]	Poor	76	85	90	93
		Good	74	83	88	90
Row crops	Straight row	Poor	72	81	88	91
		Good	67	78	85	89
Small grains	Straight row	Poor	65	76	84	88
		Good	63	75	83	87
Close-seeded or broadcast legumes or rotation	Straight row	Poor	66	77	85	89
		Good	58	72	81	85
Meadow – continuous grass, protected from grazing and generally mowed for hay	---	---	30	58	71	78
Woods – grass combination (orchard or tree farm)	---	Poor	57	73	82	86
		Fair	43	65	76	82
		Good	32	58	72	79

[1] Crop residue cover applies only if residue is on at least 5% of the surface.

Table i-3: : Correspondence between land uses and crops.

Land use	Crops
Row crops	Maize Soybean Vegetables
Small grains	Winter cereals
Close-seeded or broadcast legumes or rotation	Forages, cutting cycles
Meadow	Permanent grasslands
Woods – grass combination (orchard or tree farm)	Vines

I-3.3.1. Antecedent soil moisture condition

For this method, soils are classified into four hydrologic groups based on infiltration characteristics. A hydrologic group is a group of soils having similar runoff potential under similar storm and cover conditions (NRCS Soil Survey Staff, 1996). Soil properties that influence runoff potential are those that impact the minimum rate of infiltration for a bare soil after prolonged wetting and when not frozen. These properties are depth to seasonally high water table, saturated hydraulic conductivity, and depth to a very slowly permeable layer. Soil may be placed in one of four classes:

A. (Low runoff potential). The soils have a high infiltration rate even thoroughly wetted. They chiefly consist of deep, well drained to excessively drained sands or gravels. They have a high rate of water transmission.
B. (Moderately low runoff potential). The soils have a moderate infiltration rate when thoroughly wetted. They chiefly are moderately deep to deep, moderately well-drained to well-drained soils that have moderately fine to moderately coarse textures. They have a moderate rate of water transmission.
C. (Moderately high runoff potential). The soils have a slow infiltration rate when thoroughly wetted. They chiefly have a layer that impedes downward movement of water or have moderately fine to fine texture. They have a slow rate of water transmission.

D. (High runoff potential). The soils have a very slow infiltration rate when thoroughly wetted. They chiefly consist of clay soils that have a high swelling potential, soils that have a permanent water table, soils that have a claypan or clay layer at or near the surface, and shallow soils over nearly impervious material. They have a very slow rate of water transmission.

Hydrologic group classification is derived for the study area from soil type derived map.

SCS defines three antecedent moisture conditions:

I. (Dry). The moisture condition I curve number is the lowest value the daily curve number can assume in dry conditions (at wilting point).
II. (Average moisture). The moisture condition II for which the values listed in Table i-2 are designed.
III. (Wet). The moisture condition III curve number is the higher value the daily curve number can assume in wet conditions (at field capacity).

The curve numbers for moisture conditions I and III are calculated with the equations (Neitsch et al., 2011):

$$CN_1 = CN_2 - \frac{20\cdot(100-CN_2)}{100-CN_2+e^{2.533-0.0636\cdot\ (100-CN_2)}} \tag{i-37}$$

$$CN_3 = CN_2 \cdot e^{0.0673\cdot(100-CN_2)} \tag{i-38}$$

where CN_1 (adimensional), CN_2 (adimensional) and CN_3 (adimensional) are the moisture condition I, II and III curve numbers respectively.

The curve number varies with soil water profile content by linear interpolation:

$$CN_x = \begin{cases} CN_1 & \theta \geq \ \theta_{wp} \\ \frac{CN_2-\ CN_1}{\theta_{fc,wp}-\theta_{wp}}\left(\theta-\theta_{wp}\right)+CN_1 & \theta_{wp} < \theta < \theta_{fc,wp} \\ CN_2 & \theta = \theta_{fc,wp} \\ \frac{CN_3-\ CN_2}{\theta_{fc}-\theta_{fc,wp}}\left(\theta-\theta_{fc,wp}\right)+CN_2 & \theta_{fc,wp} < \theta < \theta_{fc} \\ CN_3 & \theta = \theta_{fc} \\ \frac{CN_4-\ CN_3}{\theta_s-\theta_{fc}}\left(\theta-\theta_{fc}\right)+CN_3 & \theta_{fc} < \theta < \theta_s \\ CN_4 & \theta \geq \theta_s \end{cases} \tag{i-39}$$

where CN_1 (adimensional), CN_2 (adimensional) and CN_3 (adimensional) are the moisture condition I, II and III curve numbers respectively, CN_4 (adimensional) is the moisture condition at saturation, equal to 95, θ $(m^3 \cdot m^{-3})$ is the soil water content of the entire profile, θ_{wp} $(m^3 \cdot m^{-3})$, θ_{fc} $(m^3 \cdot m^{-3})$ and θ_s $(m^3 \cdot m^{-3})$ are the soil water contents at wilting point, at field capacity and at saturation respectively, and $\theta_{fc,wp}$ $(m^3 \cdot m^{-3})$ is the soil water content at Antecedent Moisture Condition II, equal to $\theta_{fc,wp} = \theta_{wp} + \frac{2}{3}(\theta_{fc} - \theta_{wp})$.

I-3.3.2. *Slope adjustments*

The moisture condition II curve numbers provided in Table i-2 are assumed appropriate for 5% slopes. Williams (1995) developed an equation to adjust the curve number to a different slope:

$$\begin{aligned}\mathrm{CN}_{2s} &= \frac{\mathrm{CN}_3-\mathrm{CN}_2}{3}\cdot\left(1-2\cdot\mathrm{e}^{-13.86\cdot slp}\right)+\mathrm{CN}_2 = \\ &= \frac{\mathrm{CN}_2\cdot\left(e^{0.0673\cdot(100-CN_2)}-1\right)}{3}\cdot\left(1-2\cdot\mathrm{e}^{-13.86\cdot slp}\right)+\mathrm{CN}_2 \qquad \text{(i-40)}\end{aligned}$$

where CN_{2s} (adimensional) is the moisture condition II curve number adjusted for slope, CN_2 (adimensional) and CN_3 (adimensional) are the moisture condition II and III curve numbers, respectively, for the default 5% slope, and slp (%) is the average fraction slope of the cell.

I-3.3.3. *Seasonal variations*

The average CN in Table i-2 apply to average crop conditions for a growing season. To account for seasonal variations of the CN, IdrAgra consider the stages of growth of crops (USDA, 1985):

$$CN_x = \begin{cases} (CN)_{fallow} & before\ \ plowing \\ (CN)_{crop} & between\ \ plowing\ \ and\ \ normal\ \ peak\ \ height \\ 2(CN)_{crop}-(CN)_{fallow} & between\ \ normal\ \ peak\ \ height\ \ and\ \ harvest\ \ time \\ (CN)_{suolonudo} & after\ \ harvesting \end{cases} \qquad \text{(i-41)}$$

where CN_x (adimensional) is the curve number adjusted for moisture condition and slope, $(CN_x)_{fallow}$ (adimensional) is the curve number adjusted for moisture condition and slope, for fallow land use, crop residue cover treatment, and $(CN_x)_{crop}$ (adimensional) is the curve number adjusted for moisture condition and slope, for the considered crop.

I-3.3.4. *Specifications for paddy fields*

Paddy fields are treated as completely pervious from emergence to harvest; in this case surface runoff is considered equal to 0. Elsewhere, before emergence and after harvest, surface runoff is calculated as described in the precedent paragraphs.

I-3.4. Ponding

Ponding can occur if there is an excess of water on top of the soil surface, caused by micro relief that retains water that otherwise would runoff, or if the top soil is over saturated.

In the first case, to account for the micro relief at soil surface, it is assumed that surface runoff is reduced by a ratio q_{pond} that is function of mean slope of the cell:

$$Q_p = q_{pond}Q_u \qquad \text{(i-42)}$$

where Q_p $(mm\cdot d^{-1})$ is the ponding, q_{pond} (adimensional) is the ponded water ratio and Q_u $(mm\cdot d^{-1})$ is the accumulated runoff or superficial rainfall excess.

The ratio q_{pond} is calculated as:

$$q_{pond} = \begin{cases} q_{pond\ \ max} & slp \leq slp_{min} \\ q_{min} + \ \frac{slp - slp_{max}}{slp_{min} - slp_{max}} \left(q_{pond\ \ max} - q_{pond\ \ min}\right) & slp_{min} < slp < slp_{max} \\ q_{pond\ \ min} & slp \geq slp_{max} \end{cases} \qquad \text{(i-43)}$$

where q_{pond} (adimensional) is the ponded water ratio, slp (%) is the average fraction slope of the cell, $q_{pond\ \ max}$ (adimensional) and $q_{pond\ \ min}$ (adimensional) are the maximum and minimum ratios for ponding water, that occur respectively at minimum slope slp_{min} and at maximum slope slp_{max}.

The ponding water amount is subtracted from the calculated runoff of the each day and summed to the next day water availability.

In the second case, it is assumed that the excess of water at hourly time step is available to infiltrate in the next time step.

I-3.5. Interception

IdrAgra computes the interception following Von Hoyningen-Hüne (1983) e Braden (1985). They proposed the following general formula for canopy interception:

$$I = a_I \cdot LAI \ \left(1 - \ \frac{1}{1 + \frac{b_I \cdot P}{a_I \cdot LAI}}\right) \qquad \text{(i-44)}$$

where I $(mm \cdot d^{-1})$ is the canopy rainfall interception, LAI (adimensional) is the Leaf Area Index, a_I (mm) is an empirical coefficient, that in case of ordinary agricultural crops in the Padana Plain can be assumed as $0.6\ mm$ for all the crops, b_I (adimensional) is the soil cover fraction, estimated by $b_I = \min\left(\frac{LAI}{3}, 1\right)$, and P $(mm \cdot d^{-1})$ is the rainfall rate.

I-3.6. Infiltration

The amount of water that is available for infiltration, Q_{inf}, equals:

$$Q_{inf} = P + Q_i - Q_u - I \qquad \text{(i-45)}$$

where Q_{inf} $(mm \cdot d^{-1})$ is the infiltration rate, Q_i $(mm \cdot d^{-1})$ is the irrigation supply, P $(mm \cdot d^{-1})$ is the rainfall rate, I $(mm \cdot d^{-1})$ is the canopy rainfall interception and Q_u $(mm \cdot d^{-1})$ is the net runoff.

Different approaches are used to estimate infiltration in case of precipitation or of irrigation supply.

I-3.6.1. Rainfall event

In this situation, runoff is calculated with equation i-34. This value is then compared to initial abstractions, I_a, estimated by the Curve Number method, and to infiltration rate, calculated with equation i-45. Effective rainfall value is then the maximum value of net rainfall:

$$P_{eff} = \max(P - I, P - I_a) \qquad \text{(i-46)}$$

where P_{eff} $(mm \cdot d^{-1})$ is the effective rainfall, P $(mm \cdot d^{-1})$ is the rainfall rate, I $(mm \cdot d^{-1})$ is the interception and I_a $(mm \cdot d^{-1})$ are the initial abstractions.

The infiltration thus equals to:

$$Q_{inf} = P_{eff} - Q_u \tag{i-47}$$

where Q_{inf} $(mm \cdot d^{-1})$ is the infiltration, P_{eff} $(mm \cdot d^{-1})$ is the effective rainfall and Q_u $(mm \cdot d^{-1})$ is the runoff.

I-3.6.2. Irrigation

In this case, $Q_u = 0$, thus:

$$Q_{inf} = Q_i - I \tag{i-48}$$

where Q_{inf} $(mm \cdot d^{-1})$ is the infiltration, Q_i $(mm \cdot d^{-1})$ is the irrigation supply and I $(mm \cdot d^{-1})$ is the interception.

I-3.7. Percolation

Percolation includes both the downward flux from the evaporative layer to the transpirative layer (Q_e) and the deep percolation flux from the transpirative layer to groundwater (Q_s). These balance terms also depend upon the water table depth, that can produce an upward flux (capillary rise), that is described in the next section.

Assuming that the vertical flux is only driven by gravitational forces, the vertical flux owing to gravity is:

$$Q_{e,nc} = K_E t_h \cdot 10 \tag{i-49}$$

$$Q_{s,nc} = K_T t_h \cdot 10 \tag{i-50}$$

where $Q_{e,nc}$ $(mm \cdot h^{-1})$ and $Q_{s,nc}$ $(mm \cdot h^{-1})$ are respectively the outflows from the evaporative to the transpirative layer and from the root zone to the deeper subsoil, both not accounting for irrigation management, K_E $(cm \cdot h^{-1})$ and K_T $(cm \cdot h^{-1})$ are the unsaturated hydraulic conductivities, function of water content, of the evaporative and the transpirative layer respectively and t_h (h) is the hourly time step. In both equations, the number 10 is a conversion factor to homogenize hydraulic conductivities to the outflows.

The Brooks-Corey (1964) unsaturated hydraulic conductivity function is used to evaluate unsaturated hydraulic conductivity:

$$K_E = K_{s,E} \left(\frac{\theta_E - \theta_{r,E}}{\theta_{s,E} - \theta_{r,E}}\right)^{\mathrm{n_E}} \tag{i-51}$$

$$K_T = K_{s,T} \left(\frac{\theta_T - \theta_{r,T}}{\theta_{s,T} - \theta_{r,T}}\right)^{n_T} \tag{i-52}$$

where K_E $(cm \cdot h^{-1})$ and K_T $(cm \cdot h^{-1})$ are the unsaturated hydraulic conductivities of the evaporative and the transpirative layers, $K_{s,E}$ $(cm \cdot h^{-1})$ and $K_{s,T}$ $(cm \cdot h^{-1})$ are the saturated hydraulic conductivities of the evaporative and the transpirative layers, θ_E $(m^3 \cdot m^{-3})$ and θ_T $(m^3 \cdot m^{-3})$ are the volumetric water contents of the evaporative and the transpirative layers, $\theta_{r,E}$ $(m^3 \cdot m^{-3})$ and $\theta_{r,T}$ $(m^3 \cdot m^{-3})$ are the residual water contents of the evaporative and the transpirative layers, $\theta_{s,E}$ $(m^3 \cdot m^{-3})$ and $\theta_{s,T}$ $(m^3 \cdot m^{-3})$ are the saturated water contents of the evaporative and the transpirative layers, and n_E (adimensional) and n_T (adimensional) are the Brooks-Corey exponents of the evaporative and the transpirative layers respectively.

I-3.7.1. Percolation following irrigation

The percolation model expressed by the equations i-49 and i-50 has been modified to account for greater fluxes following irrigation and for the spatial distribution of hydraulic conductivity, using the following equations:

$$Q_e = (1 + a_{irr\ \ met,e} e^{-g}) Q_{e,nc} \tag{i-53}$$

$$Q_s = (1 + a_{irr\ \ met,s} e^{-g}) Q_{s,nc} \tag{i-54}$$

where Q_e (mm) and Q_s (mm) are the outflows from the evaporative to the transpirative layer and from the root zone to the deeper subsoil, accounting for irrigation management, $Q_{e,nc}$ (mm) and $Q_{s,nc}$ (mm) are the outflows from the evaporative to the transpirative layer and from the root zone to the deeper subsoil, not accounting for irrigation management, $a_{irr\ \ met,e}$ (adimensional) and $a_{irr\ \ met,s}$ (adimensional) are parameters that account for irrigation method, for the evaporative and the transpirative layers respectively, and g (d) are the days elapsed since last irrigation.

The parameters $a_{irr\ \ met,e}$ and $a_{irr\ \ met,s}$ depend upon the irrigation method and the hydraulic conductivity distribution, according to the following equations:

$$a_{irr\ \ met,e} = \begin{cases} a_{irr\ \ met}^{sup} & K_{s,E} \leq K_{s,E}^{10th} \\ \frac{a_{irr\ \ met}^{sup} - a_{irr\ \ met}^{inf}}{K_{s,E}^{10th} - K_{s,E}^{90th}} \left(K_{s,E} - K_{s,E}^{90th}\right) + a^{inf} & K_{s,E}^{10th} < K_{s,E} < K_{s,E}^{90th} \\ a_{irr\ \ met}^{inf} & K_{s,E}^{90th} \leq K_{s,E} \end{cases} \tag{i-55}$$

$$a_{irr\ \ met,s} = \begin{cases} a_{irr\ \ met}^{sup} & K_{s,T} \leq K_{s,\mathrm{T}}^{10th} \\ \frac{a_{irr\ \ met}^{sup} - a_{irr\ \ met}^{inf}}{K_{s,\mathrm{T}}^{10th} - K_{s,\mathrm{T}}^{90th}} \left(K_{s,T} - K_{s,\mathrm{T}}^{90th}\right) + a^{inf} & K_{s,\mathrm{T}}^{10th} < K_{s,T} < K_{s,\mathrm{T}}^{90th} \\ a_{irr\ \ met}^{inf} & K_{s,T}^{90th} \leq K_{s,\mathrm{T}} \end{cases} \tag{i-56}$$

where $a_{irr\ \ met}^{sup}$ (adimensional) and $a_{irr\ \ met}^{inf}$ (adimensional) are the maximum and the minimum values of both $a_{irr\ \ met,e}$ and $a_{irr\ \ met,s}$ for the considered irrigation method, $K_{s,T}$ $(cm \cdot h^{-1})$ and $K_{s,E}$ $(cm \cdot h^{-1})$ are respectively the saturated hydraulic conductivities of the transpirative and the evaporative layers, and $K_{s,E}^{10th}$ $(cm \cdot h^{-1})$, $K_{s,E}^{90th}$ $(cm \cdot h^{-1})$, $K_{s,T}^{10th}$ $(cm \cdot h^{-1})$ and $K_{s,T}^{90th}$ $(cm \cdot h^{-1})$ are the 10th and the 90th percentiles of saturated hydraulic conductivity distribution for the evaporative and the transpirative layers respectively. Maxima and minima $a_{irr\ \ met,e}$ and $a_{irr\ \ met,s}$ values are reported in Table i- 4.

Table i- 4: Maxima and minima $a_{irr\ \ met,e}$ and $a_{irr\ \ met,s}$ values.

Irrigation method	$a_{irr\ \ met}^{sup}$	$a_{irr\ \ met}^{inf}$
Surface irrigation	15	5
Sprinkler irrigation	30	10

I-3.8. Capillary rise

The estimation of capillary rise is required for computing the soil water balance in presence of high water tables that favour upward fluxes into the root zone. This process depends upon the soil characteristics, the actual water storage in the root zone and the actual evapotranspiration.

The methodology proposed by Liu et al. (2006) to estimate the groundwater contribution assumes that the root zone depth is equal to $1.0\ \ m$. The potential groundwater contribution, G_{max}, greatly depends upon the groundwater depth and the evapotranspiration demand. Above a critical groundwater depth, D_{wc}, the groundwater contribution approaches the potential crop transpiration, T.

The actual capillary rise, G_c, depends upon the actual soil water storage. The upward fluxes initiate for the critical soil water storage, W_c, that mainly depends upon the groundwater depth but is influenced by higher evapotranspiration rates. The actual capillary rise is higher and closer to its potential value as much as groundwater depth is close to the critical groundwater depth, and the soil water storage is smaller, near the steady soil water storage, W_s, that mainly depends upon the groundwater depth.

The critical soil water storage is estimated by:

$$W_c = a_{rc,1} D_w^{b_{rc,1}} \tag{i-57}$$

where W_c (mm) is the critical soil water storage, $a_{rc,1}$ (mm) is the soil water storage to $1.0\ \ m$ depth at field capacity, equal to $a_{rc,1} = W_{FC}$, $b_{rc,1}$ (adimensional) is an empirical parameter that depends on soil type and D_w (m) is the groundwater depth.

The steady soil water storage is approximated by:

$$W_s = a_{rc,2} D_w^{b_{rc,2}} \tag{i-58}$$

where W_s (mm) is the steady soil water storage, $a_{rc,2}$ (mm) is the steady soil water storage to $1.0\ \ m$ depth, equal to $a_{rc,2} = 1.1 \frac{W_{fc} - W_{wp}}{2}$, $b_{rc,2}$ (adimensional) is an empirical parameter that depends on soil type and D_w (mm) is the groundwater depth.

The critical groundwater depth, which is the threshold value for groundwater depth above which the potential capillary flux do not increase anymore, is estimated by:

$$D_{WC} = \begin{cases} a_{rc,3}(E + T_c) + b_{rc,3} & (E + T_c) \leq 4 \ \ mm \cdot d^{-1} \\ Z_r + 0.4 & (E + T_c) > 4 \ \ mm \cdot d^{-1} \end{cases} \tag{i-59}$$

where D_{WC} (mm) is the critical groundwater depth, $a_{rc,3}$ (adimensional) and $b_{rc,3}$ (adimensional) are empirical parameters that depend on soil type, E $(mm \cdot d^{-1})$ is the evaporation rate, T_c $(mm \cdot d^{-1})$ is the potential crop transpiration rate and Z_r (mm) is the depth of the transpirative layer.

The potential capillary flux is estimated by:

$$G_{max} = \begin{cases} T_C & D_W \leq D_{WC} \\ a_{rc,4} D_W^{b_{rc,4}} & D_W > D_{WC} \end{cases} \tag{i-60}$$

where G_{max} $(mm \cdot d^{-1})$ is the potential capillary flux rate, T_c $(mm \cdot d^{-1})$ is the potential crop transpiration rate, D_W (m) is the groundwater depth, D_{WC} (m) is the critical groundwater depth, $a_{rc,4}$ (adimensional) and $b_{rc,4}$ (adimensional) are empirical parameters that depend on soil type.

The fluxes are then approximated by the following parametric equations:

$$Q_s = \begin{cases} G_{max} \ \ (D_W, ET_c) & W < W_s(D_W) \\ G_{max}(D_W, ET_c)\left(\frac{W_c(D_W) - W}{W_c(D_W) - W_s(D_W)}\right) & W_s(D_W) \leq W \leq W_c(D_W) \\ 0 & W > W_c(D_W) \end{cases} \tag{i-61}$$

where Q_s $(mm \cdot d^{-1})$ is the capillary rise, W (mm) is the actual soil water storage in the root zone, G_{max} $(mm \cdot d^{-1})$ is the potential ground water contribution, W_c (mm) and W_s (mm) are the critical and the steady state soil water storages respectively.

The parameters for the equations are reported in Table i 5.

Table i 5: Parameters of the groundwater contribution semi-empirical equations for different soil types. Source: Liu *et al.,* 2006.

Parameter	Silt loam soil	Sandy loam soil	Clay loam soil
$b_{rc,1}$	-0.17	-0.16	-0.32
$b_{rc,2}$	-0.27	-0.54	-0.16
$a_{rc,3}$	-1.3	-0.15	-1.4
$b_{rc,3}$	6.6	2.1	6.8
$a_{rc,4}$	4.6	7.55	1.11
$b_{rc,4}$	-0.65	-2.03	-0.98

I-3.9. Spatial interpolation of meteorogical and crop datasets

As IdrAgra needs complete datasets for each cell of the domain, spatial interpolation algorithm allows the creation of a continuous field of variable from sparse observations, such as meteorological and crop parameters datasets, that are only available for the meteorological stations. In particular, crop parameters are derived from the temperature series recorded at the meteorological stations using the separate module CropCoeff.

I-3.9.1. Spatial interpolation of meteorological data

The spatial interpolation of the agro-meteorological data is based upon the inverse-square distance weighting (IDW). It is based on the assumption that in any given location (x, y) the value of a generic meteorological variable z is best approximated by a combination of the n station measures weighted by a function of the inverse-squared of the distance between the point (x, y) and the meteorological station:

$$z_{x,y} = \frac{\sum_{i=1}^{n} z_i d_{x,j,i}^{-2}}{\sum_{i=1}^{n} d_{x,j,i}^{-2}} \tag{7.1}$$

where $z_{x,y}$ is the value of the variable at the point to be estimated (x, y), z_i is the value of the observed variable at the meteorological station i, and $d_{x,j,i}$ is the distance between (x, y) and i (Bartier & Keller, 1996). The model requires as input the number of interpolating points n and the normalized weight of the n^{th} data points for each cell.

I-3.9.2. Spatial interpolation of crop parameters

Each cell of the modeled domain is assigned to a cluster (region of influence), according to the nearest meteorological stasions. To assure the spatial variability of the parameters inside the same cluster, the series computed for each cell is shifted for a maxium of $\pm d_s$ days, with d_s defined in the simulation parameters (e.g. 10 days).

For each cell, the series are computed taking into account the emergence dates and the total crop growing cycle length computed on the n nearest meteorological stations, as the inverse weighting average of these vales.

Thus, if tab is the series of a phenological parameter of a crop, on a day d its value is:

$$tab_d = tab[g_{x,y}^e + (d - g_{x,y}^e)d_{x,y} - iran_{x,y}] \tag{i-62}$$

where $g_{x,y}^e$ (adimensional) is the emergence date in the (x, y) cell, d (adimensional) is the day of the simulation, $d_{x,y}$ (adimensional) is the weighting length factor in the (x, y) cell, $iran_{x,y}$ (adimensional) is the random shifting of the emergence date, equal to

$$iran_{x,y} = \delta_{x,y}^s + \delta_{x,y}^e \tag{i-63}$$

where $\delta_{x,y}^s$ (adimensional) is the random shift $[-d_s, d_s]$ and $d_{x,y}^e$ (adimensional) is the difference between the emergence date $g_{x,y}^e$ in the (x, y) cel and the emergence date g_1^e at the nearest meteorological station.

I-4. Irrigation

Irrigation is calculated as a function of different factors related to water availability, distribution and conveyance. In particular, IdrAgra runs on three different modes:

- **No irrigation**: no irrigation is applicated to the domain;

- **Water supplies**: derivation time series and information about conveyance and distribution are fed into the model, that simulates the behaviour of the irrigation system, from sources to cell distribution, accounting for consumptions and crop water deficit;
- **Water needs**: the model estimates the irrigation on the basins of the meteorological inputs, and calculates the water abstraction needs.

I-4.1. Water supplies simulation

In this type of siulation, irrigation inputs depend on the diverted discharges, from surface waters, springs, and weels, their conveyances and distributions into the irrigation districts, and the irrigation efficiencies.

I-4.1.1. Irrigation scheme

IdrAgra takes into account different types of irrigation inputs: surface water diversions, springs diversions, tailwaters and wells. Surface water, springs and tailwater diverted discharges are read from a daily input file, while irrigation from wells is estimated with an internal algorithm.

I-4.1.2. Conveyance

Each irrigation district is irrigated from different sources (i.e. surface water, springs, wells and tailwaters), each one allocated in a different way, in dependence to its maximum licensed quantity, water diversions and irrigation efficiency.

Gross available water on a day t is therefore calculated as:

$$q_{j,t} = \sum_{i=1}^{N_f} \varepsilon_{ij} \eta_{ij} Q_{i,t} \tag{i-64}$$

where $q_{j,t}$ $(mm \cdot d^{-1})$ is the water available for the jth irrigation district in the day t, ε_{ij} (adimensional) is the ratio of water diverted from the ith source to the jth irrigation district, η_{ij} (adimensional) is the conveyance efficiency of the ith source to the jth irrigation district (equal to the ratio between water conveyed to the irrigation district and water diverted from the source) and $Q_{i,t}$ $(mm \cdot d^{-1})$ is the water diverted from the ith source on the day t.

I-4.1.3. Distribution

The description of the water conveyance and distribution reflects the typical structure of the irrigation network in most districts of the Po River plain. The district is subdivided into a number of subdistricts, i.e. each single unit of the territory that receives continuous (non-turned) irrigation supply from one or more sources. During the irrigation season, water derived from the sources is conveyed to the subdistricts and each of them receives a fixed share of the flow that is diverted from the sources supplying that specific subdistrict through the irrigation network. In practice, an incidence matrix is used to represent the links between the sources and the subdistricts, and two numerical values are associated with each active link: the fraction of the diverted discharge which is conveyed to the subdistrict and the conveyance efficiency.

Distribution within each subdistrict takes place with a mechanism that simulates the timetable of water allocation to the farms (Figure i- 8). In each day, (i) a fixed number of cells is explored to check if irrigation is required and (ii) a cell is actually irrigated only if the soil water content in the root zoned, provided by the soil volume balance model, is at risk of limiting crop growth:

$$V_{Tr} - (TAW - RAW) < \alpha_i RAW \tag{i-65}$$

where V_{Tr} $(mm \cdot d^{-1})$ is the water content, minus the residual water content, of the transpirative layer, TAW $(mm \cdot d^{-1})$ is the total available water in the root zone, RAW $(mm \cdot d^{-1})$ is the readily available water in the root zone, and α_i (adimensional) is the threshold coefficient for the activation of irrigation.

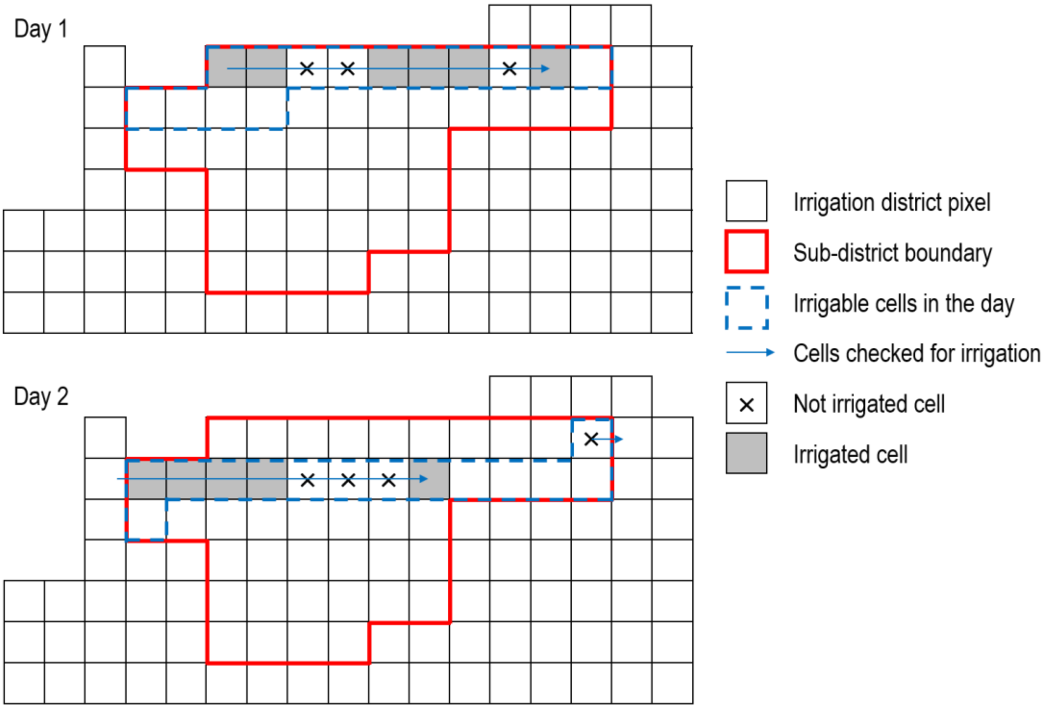

Figure i- 8: IdrAgra simulation of irrigation water distribution in a subdistrict in two consecutive days.

I-4.1.4. Irrigation from wells

The model distinguish between two different types of wells:

- Public (irrigation district) wells: wells (or groups of wells), typically managed by irrigation district authorities, of which the specific features are known;
- Private (farm) wells: wells groups that are located in a specified area (i.e. an irrigation district) and for which it is not possible to know specific features.

In both cases, it is supposed that water can be unlimitedly pumped, thus satisfying the irrigation need of the cell or cells subdued by the well.

In the case of **public wells**, the water pumped by the well is estimated on the basis of soil moisture conditions of the grid cells subdued by the well. For a day t of irrigation season, the weighted mean of available water is calculated as:

$$\overline{U_i} = \frac{\sum_{i=1}^{n}\{V_{T,i} - [\theta_{fc,T,i} - (\theta_{fc,T,i} - \theta_{wp,T,i})p_i]Z_{r,i}\cdot 1000\}\cdot T_{c,i}}{\sum_{i=1}^{n} T_{c,i}} \qquad \text{(i-66)}$$

where $\overline{U_i}$ (mm) is the effective readily available soil water in the root zone for the ith cell, $V_{T,i}$ (mm) is the water content of the transpirative layer per unit surface area of the ith cell, $\theta_{fc,T,i}$ $(m^3 \cdot m^{-3})$ and $\theta_{wp,T,i}$ $(m^3 \cdot m^{-3})$ are respectively the soil water contents of the transpirative layer of the ith cell respectively at field capacity and at wilting point, p_i (adimensional) is the average fraction of TAW that can be depleted from the root zone before moisture stress occurs $[0-1]$, $Z_{r,i}$ (m) is the depth of the transpirative layer of the ith cell and $T_{c,i}$ $(mm \cdot d^{-1})$ is the potential crop transpiration rate for the ith cell.

The well (or the wells group) is activated only if the $\overline{U_i}$ drops below a share, α_w, of its maximum value $\overline{U_i^{MAX}}$

$$\overline{U_i^{MAX}} = \frac{\sum_{i=1}^{n}(\theta_{fc,T,i} - \theta_{wp,T,i})p_i Z_{r,i}\cdot 1000\cdot T_{c,i}}{\sum_{i=1}^{n} T_{c,i}} \qquad \text{(i-67)}$$

where $\overline{U_i^{MAX}}$ (mm) is the maximum effective readily available soil water in the root zone for the ith cell, $\theta_{fc,T,i}$ $(m^3 \cdot m^{-3})$ and $\theta_{wp,T,i}$ $(m^3 \cdot m^{-3})$ are respectively the soil water contents of the transpirative layer of the ith cell respectively at field capacity and at wilting point, p_i (adimensional) is the average fraction of TAW that can be depleted from the root zone before moisture stress occurs $[0-1]$, $Z_{r,i}$ (m) is the depth of the transpirative layer of the ith cell and $T_{c,i}$ $(mm \cdot d^{-1})$ is the potential crop transpiration rate for the ith cell.

Every well can be activated partially or totally, in function of the ratio between $\overline{U_i}$ and $\overline{U_i^{MAX}}$:

$$Q_{i,w} = \begin{cases} f_{w,1}Q_w & \overline{U_i} \le \alpha_{w,1}\overline{U_i^{MAX}} \\ f_{w,2}Q_w & \alpha_{w,1}\overline{U_i^{MAX}} < \overline{U_i} \le \alpha_{w,2}\overline{U_i^{MAX}} \\ f_{w,3}Q_w & \alpha_{w,2}\overline{U_i^{MAX}} < \overline{U_i} < \alpha_w\overline{U_i^{MAX}} \end{cases} \qquad \text{(i-68)}$$

where $Q_{i,w}$ $(mm \cdot d^{-1})$ is the irrigation supply from well, Q_w (mm) is th maximum well flow rate, $f_{w,1}$, $f_{w,2}$ and $f_{w,3}$ are incremental well flow shares $[0-1]$, $\alpha_{w,1}$ (adimensional) and $\alpha_{w,2}$ (adimensional) are the respective well activation thresholds $[0-1]$; α_w (adimensional) is the coefficient for well activation $[0-1]$, $\overline{U_i^{MAX}}$ (mm) is the maximum effective readily available soil water in the root zone for the ith cell and $\overline{U_i}$ (mm) is the effective readily available soil water in the root zone for the ith cell.

Water pumped from **private wells** is estimated by identifying the cells where private wells are probably located. The well is activated if two conditions are satisfied: (1) that the cell would not be irrigated from superficial sources in a short time period (i.e. it does not fall into the cells potentially irrigated in the next days, defined for each sub-district; Figure i- 9), and (2) the water content of the transpirative layer of the cell satisfies the equation:

$$V_{T,i} - \left[\theta_{fc,T,i} - \left(\theta_{fc,T,i} - \theta_{wp,T,i}\right)p_i\right]Z_{r,i} \cdot 1000 < \alpha_a\left(\theta_{fc,T,i} - \theta_{wp,T,i}\right)p_i Z_{r,i} \cdot 1000 \quad \text{(i-69)}$$

where $V_{T,i}$ (mm) is the water content of the transpirative layer per unit surface area of the i^{th} cell, $\theta_{fc,T,i}$ $(m^3 \cdot m^{-3})$ and $\theta_{wp,T,i}$ $(m^3 \cdot m^{-3})$ are respectively the soil water contents of the transpirative layer of the i^{th} cell respectively at field capacity and at wilting point, p_i (adimensional) is the average fraction of TAW that can be depleted from the root zone before moisture stress occurs $[0-1]$, $Z_{r,i}$ (m) is the depth of the transpirative layer of the i^{th} cell and α_a (adimensional) is the coefficient for private well activation $[0-1]$.

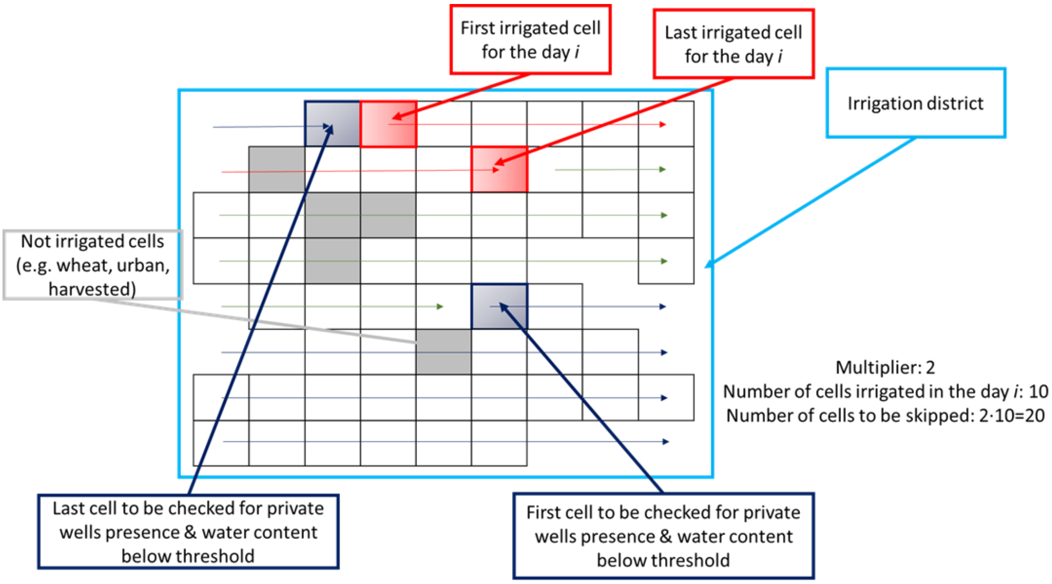

Figure i- 9: Irrigation from private wells: check for irrigation from superficial sources.

I-4.2. Irrigation water needs simulations

In these types of simulation, irrigation is estimated assuming the availability of unlimited amount of water.

The water need for a day t is determined calculating the irrigation deficit for the transpirative layer at the end of the previous day $(t-1)$. The criterion to estabilish which cells are irrigated on a day t is:

$$V_{T-r,i,t} - \left(TAW_{i,t} - RAW_{i,t}\right) < \alpha_i RAW_{i,t} \quad \text{(i-70)}$$

where $V_{T-r,i,t}$ (mm) is the water content minus the residual water content of the transpirative layer for the i^{th} cell and the day t, $TAW_{i,t}$ (mm) and $RAW_{i,t}$ (mm) are the total available soil water and the readily available soil water in the root zone for the i^{th} cell and the day t and α_i (adimensional) is the coefficient for the activation of irrigation.

For each cell, the irrigation amount Q_{irr} is calculated differently according to the chosen type of simulation: fixed irrigation supply or crop needs supply.

I-4.2.1. Fixed irrigation supply

In this case, the net irrigation supply at field Q_i is equal to a fixed irrigation amount h_{irr}.

The gross irrigation supply, that takes into account water conveyance and distribution efficiencies, is equal to:

$$Q_i^{gross} = \frac{Q_{irr}}{\xi_{field} \cdot \xi_{conv}} = \frac{h_{irr}}{\xi_{field} \cdot \xi_{conv}} \tag{i-71}$$

where Q_i^{gross} (mm) is the gross irrigation supply, Q_i (mm) is the net irrigation supply at field, h_{irr} (mm) is the fixed irrigation amount to the field, ξ_{field} (adimensional) is the field application efficiency $[0.01 - 0.99]$ and ξ_{conv} (adimensional) is the conveyance efficiency.

Specifications for paddy fields

In paddy fields, irrigation is supplied only if effective rainfall is zero and from emergence to mid-season; the irrigation amount is at least equal to the unsaturated hydraulic conductivity of the transpirative layer:

$$\{P_{eff} = 0 \quad \wedge K_{cb\ \ i-1} \leq K_{cb\ \ i}\} \Rightarrow Q_{i,min} \quad = 10 \cdot 24 \cdot K_T \tag{i-72}$$

where P_{eff} $(mm \cdot d^{-1})$ is the effective rainfall, $K_{cb\ \ i}$ (adimensional) is the crop coefficient on day i, $Q_{i,min}$ $(mm \cdot d^{-1})$ is the minimum irrigation supply, K_T is the unsaturated hydraulic conductivity of the transpirative layer, equal for rice to $0.04 \quad cm \cdot h^{-1}$.

The effective gross irrigation is therefore calculated as:

$$Q_{i,i} = \max\left\{\frac{E_{i-1}+T_{c,i-1}}{\xi_{field} \cdot \xi_{conv}}, Q_{i,min}\right\} \tag{i-73}$$

where $Q_{i,j}$ (mm) is the net irrigation supply at field on day i, E_{i-1} $(mm \cdot d^{-1})$ is the evaporation rate of day $i - 1$, $T_{c,i-1}$ $(mm \cdot d^{-1})$ is the potential crop transpiration rate of day $t - 1$, ξ_{field} (adimensional) is the field application efficiency $[0.01 - 0.99]$, ξ_{conv} (adimensional) is the conveyance efficiency $[0.01 - 0.99]$ and $Q_{i,min}$ $(mm \cdot d^{-1})$ is the minimum irrigation supply.

I-4.2.2. Crop needs irrigation supply

In this case, the irrigation supply at field Q_i is equal to the water needed to bring the soil back to field capacity, thus:

$$Q_i = \begin{cases} 1000 \cdot [(\theta_{fc,E} - \theta_E)Z_e + (\theta_{fc,T} - \theta_T)Z_T] & \theta_E \leq \theta_{fc,E} \\ 1000 \cdot (\theta_{fc,T} - \theta_T)Z_r & \theta_E > \theta_{fc,E} \end{cases} \tag{i-74}$$

where Q_i (mm) is the net irrigation supply at field, $\theta_{fc,E}$ $(m^3 \cdot m^{-3})$ and $\theta_{fc,T}$ $(m^3 \cdot m^{-3})$ are the soil water content of the evaporative and the transpirative layers at field capacity, θ_E $(m^3 \cdot m^{-3})$

and θ_T $(m^3 \cdot m^{-3})$ are the volumetric water contents of the evaporative and the transpirative layers, Z_e (m) is the depth of the surface soil layer that is subject to drying by way of evaporation $[0.10 - 0.15]$ and Z_r (m) is the depth of the transpirative layer.

The gross irrigation supply, that takes into account water conveyance and distribution efficiencies, is equal to:

$$Q_i^{gross} = \frac{Q_i}{\xi_{field} \cdot \xi_{conv}} \tag{i-75}$$

where Q_i^{gross} (mm) is the gross irrigation supply, Q_i (mm) is the net irrigation supply at field, ξ_{field} (adimensional) is the field application efficiency $[0.01 - 0.99]$ and ξ_{conv} (adimensional) is the conveyance efficiency $[0.01 - 0.99]$.

Specifications for paddy fields

In paddy fields, irrigation is supplied only if effective rainfall is zero and from emergence to mid-season; the irrigation amount is at least equal to the unsaturated hydraulic conductivity of the transpirative layer:

$$\{P_{eff} = 0 \quad \wedge K_{cb\ \ i-1} \leq K_{cb\ \ i}\} \Rightarrow Q_{i,min} \quad = 10 \cdot 24 \cdot K_T \tag{i-76}$$

where P_{eff} $(mm \cdot d^{-1})$ is the effective rainfall, $K_{cb\ \ i}$ (adimensional) is the crop coefficient on day i, $Q_{i,min}$ $(mm \cdot d^{-1})$ is the minimum irrigation supply, K_T is the unsaturated hydraulic conductivity of the transpirative layer, equal for rice to $0.04 \quad cm \cdot h^{-1}$.

The effective gross irrigation is therefore calculated as:

$$Q_{i,i} = \max\left\{\frac{E_{i-1}+T_{c,i-1}}{\xi_{field} \cdot \xi_{conv}}, Q_{i,min}\right\} \tag{i-77}$$

where $Q_{i,j}$ (mm) is the net irrigation supply at field on day i, E_{i-1} $(mm \cdot d^{-1})$ is the evaporation rate of day $i-1$, $T_{c,i-1}$ $(mm \cdot d^{-1})$ is the potential crop transpiration rate of day $t-1$, ξ_{field} (adimensional) is the field application efficiency $[0.01 - 0.99]$, ξ_{conv} (adimensional) is the conveyance efficiency $[0.01 - 0.99]$ and $Q_{i,min}$ $(mm \cdot d^{-1})$ is the minimum irrigation supply.

I-5. Phenological stages module

The phenological stages module, CropCoeff, allows to simulate crop parameters at a daily time step, as a function of weather conditions, specifically of temperatures. Modelized parameters are crop height (h_c), leaf area index (LAI), crop coefficient K_c and root depth (Z_r).

I-5.1. Sowing date

Crops are sowed based on the temperature for a 5-day window, that is compared with a crop specific sowing temperature threshold, and the time when farmers actually plant their crops. The model will search for suitable planting conditions from the date specified in theinput data, until it is satisfied:

$$\frac{\sum_{i=t}^{t+4} T_{mean}}{5} \geq T_{sow} \qquad \text{(i-78)}$$

where t (d) is the daily time step, T_{mean} $(°C)$ is the mean daily temperature at $2\ \ m$ height and T_{sow} $(°C)$ is the sowing temperature threshold.

Under certain conditions, particularly with rotations and perennial crops, a crop might not achieve thermal time to reach full maturity which triggers harvest. A latest date to harvest is set to force the crop to be harvested on this date if not already done.

I-5.2. Computation of thermal time

Crop parameters are based on thermal time (Growing degree-days, Stöckle & Nelson, 2003), accumulated throughout the growing season. For perennial crops, such as hays and trees, the growing season is assumed starting January 1st and ending December 31st; for annual crops computation of thermal time starts with planting and ends with harvesting. A crop enters the next stage of development when the thermal time reaches the thermal time requirement for the respective stage.

Thermal time is computed with the following equation:

$$GD_t = \begin{cases} 0 & T_{mean} < T_{daybase} \\ T_{mean} \quad - T_{daybase} & T_{daybase} \leq T_{mean} \leq T_{cutoff} \\ T_{cutoff} - T_{daybase} & T_{cutoff} < T_{mean} \end{cases} \qquad \text{(i-79)}$$

where t (d) is the daily time step, GD_t $(°C \cdot d)$ is the thermal time of the day t, T_{mean} $(°C)$ is the mean daily temperature at $2\ \ m$ height, and $T_{daybase}$ $(°C)$ and T_{cutoff} $(°C)$ are the minimum and maximum temperatures for viable crop development.

I-5.3. Vernalization and photo-period effects on thermal time

I-5.3.1. Vernalization

Some crops such as winter cereals undergo the process of vernalization. It can be defined as the low temperature promotion of flowering. Winter crops requires a period of exposure to low temperatures (between approximaltey 0 to $12°C$) for a significant period of time (from 10 to 60 days) from germination to proceed into the reproductive phase.

Vernalization is simulated by defining a vernalization factor, which fluctuates from 0 to 1 depending on the accumulation of vernalization days:

$$VF = VF_{min} + \frac{(1-VF_{min})[VD_{sum}-VD_{start}]}{VD_{end}-VD_{start}} \qquad \text{(i-80)}$$

where VF (adimensional) is the vernalization factor $[0-1]$, VF_{min} (adimensional) is the minimum vernalization factor value at the beginning of the vernalization process $[0-1]$, VD_{sum} (d) is the sum of the currently accumulated vernalization days, equal to $\sum_{j=i}^{t} V_{eff}$, VD_{start} (d) is the accumulated vernalization days at which VF is set equal to VF_{min}, VD_{end} (d) is the required sum to complete vernalization (at which VF reaches a value of 1.0), t (d) is the daily time step, i

(adimensional) is the day number within the growing season and V_{eff} (d) is the vernalization contribution of day t.

V_{eff} is calculated from average air temperature as:

$$V_{eff} = \begin{cases} 0 & T_{mean} < TV_{min} - TV_A \\ 1 - \frac{TV_{min} - T_{mean}}{TV_A} & TV_{min} - TV_A \le T_{mean} < TV_{min} \\ 1 & TV_{min} \le T_{mean} < TV_{max} \\ 1 - \frac{T_{mean} - TV_{max}}{TV_A} & TV_{max} \le T_{mean} < TV_{max} + TV_A \\ 0 & T_{mean} \ge TV_{max} + TV_A \end{cases} \quad \text{(i-81)}$$

where V_{eff} (d) is the vernalization contribution of day t, TV_{min} $(°C)$ and TV_{max} $(°C)$ are respectively the low end and high end temperature thresholds for optimum vernalization, TV_A $(°C)$ is a parameter for not optimum vernalization and T_{mean} $(°C)$ is the mean daily air temperature at $2\ m$ height.

I-5.3.2. Photo-period

Plant develpoment may respond to the relative lengths of days and nights. Some crops (long-day plants) accumulate physiological time towards flowering when the daylight hours exceeds some minimum threshold (i.e. oats, sugarbeet, winter barley, winter wheat). Some crops (short-day plants) accumulate physiological time towards flowering when the daylight hours is shorter than some maximum (i.e. soybeans, maize, rice, etc.). Other crops are insensitive to day length.

The response to photo-period is approximated with a simple linear relation.

For long-day crops, the relation is:

$$PF = \begin{cases} 0 & dlh < dlh_{if} \\ \frac{dlh - dlh_{if}}{dlh_{ins} - dlh_{if}} & dlh_{if} \le dlh \le dlh_{ins} \\ 1 & dlh > dlh_{ins} \end{cases} \quad \text{(i-82)}$$

where PF (adimensional) is the photoperiod factor $[0-1]$, dlh (h) is the number of daylight hours of the day t, dlh_{ins} (h) is the number of daylight hours for insensitivity (i.e. the day length threshold above which maximum physiological time accumulation occurs) and dlh_{if} (h) is the number of daylight hours to inhibit flowering (i.e. the day length threshold below which no accumulation of physiological time occurs).

For short-day crops, the relation is:

$$PF = \begin{cases} 1 & dlh < dlh_{ins} \\ \frac{dlh - dlh_{if}}{dlh_{ins} - dlh_{if}} & dlh_{ins} \le dlh \le dlh_{if} \\ 0 & dlh > dlh_{if} \end{cases} \quad \text{(i-83)}$$

where PF (adimensional) is the photoperiod factor $[0-1]$, dlh (h) is the number of daylight hours of the day t, dlh_{ins} (h) is the number of daylight hours for insensitivity (i.e. the day length threshold below which maximum physiological time accumulation occurs) and dlh_{if} (h) is the number of daylight hours to inhibit flowering (i.e. the day length threshold above which no accumulation of physiological time occurs).

The daylight hours, dlh, are given by:

$$dlh = \frac{24}{\pi}\omega_s \qquad \text{(i-84)}$$

where dlh (h) is the number of daylight hours and ω_s (rad) is the sunset hour angle.

I-5.4. Computation of cumulated thermal time

Each day, the thermal time calculated from temperature is multiplied by the minimum of vernalization and photoperiod factors to determine the actual amount of degree-days accumulated for the day.

The cumulated thermal time for a day t is given by:

$$CGD_t = \sum_{j=i}^{t} GD_j \min(PF_j, VF_j) \qquad \text{(i-85)}$$

where CGD_t $(°C)$ is accumulated thermal time since planting for the day t, i (adimensional) is the day number within the growing season, GD_j $(°C \cdot d)$ is the thermal time computed for the day j, PF_j (adimensional) is the photoperiod factor for the day j $[0-1]$ and VF_j (adimensional) is the vernalization factor for the day j $[0-1]$.

I-6. Model setup: input files

All model input is provided as either maps (grid files in ASCII raster format) or tables (in text format, with tabs or spaces). This chapter describes all the data that are required to run the model.

I-6.1. Input maps

All maps that are needed to run the model are listed in Table i-6. An example of their structure is reported in Table i-7.

Table i-6: IdrAgra input maps.

General	
Default name	Description
dominio.asc	Mask map that defines model boundaries. Mask cells are defined with the code 1 [integer]
Topography	
pendenza.asc	Slope gradient [real] $(m \cdot m^{-1})$
Land	
usosuolo.asc	Map with land use classes [integer]
usosuolo*yyyy*.asc	Yearly maps with land use classes [integer]. It should be provided one map for each year *yyyy* of simulation (e.g. usosuolo2014.asc for year 2014)
dren.asc	Hydrologic condition to apply CN method, that indicates the effects of cover type and treatment on infiltration and runoff. Generally can be assumed equal to 1 for cropland [integer] (adimensional)

Soil	
Ksat_I.asc	Saturated hydraulic conductivity of the evaporative layer ($K_{s,E}$)[real] ($cm \cdot h^{-1}$)
Ksat_II.asc	Saturated hydraulic conductivity of the transpirative layer ($K_{s,T}$) [real] ($cm \cdot h^{-1}$)
N_I.asc	Brooks-Corey exponent for the evaporative layer (n_E)[real] (adimensional)
N_II.asc	Brooks-Corey exponent for the transpirative layer (n_T)[real] (adimensional)
ParRisCap_a3.asc	Capillary rise parameter a_3[real] (adimensional)
ParRisCap_a4.asc	Capillary rise parameter a_4[real] (adimensional)
ParRisCap_b1.asc	Capillary rise parameter b_1[real] (adimensional)
ParRisCap_b2.asc	Capillary rise parameter b_2[real] (adimensional)
ParRisCap_b3.asc	Capillary rise parameter b_3[real] (adimensional)
ParRisCap_b4.asc	Capillary rise parameter b_4[real] (adimensional)
tetaI_r.asc	Residual soil water content of the evaporative layer ($\theta_{r,E}$) [real] ($m^3 \cdot m^{-3}$)
tetaI_wp.asc	Soil water content of the evaporative layer at wilting point ($\theta_{wp,E}$) [real] ($m^3 \cdot m^{-3}$)
tetaI_fc.asc	Soil water content of the evaporative layer at field capacity ($\theta_{fc,E}$) [real] ($m^3 \cdot m^{-3}$)
tetaI_sat.asc	Saturated soil water content of the evaporative layer ($\theta_{s,T}$) [real] ($m^3 \cdot m^{-3}$)
tetaII_r.asc	Residual soil water content of the transpirative layer ($\theta_{r,T}$) [real] ($m^3 \cdot m^{-3}$)
tetaII_wp.asc	Soil water content of the transpirative layer at wilting point ($\theta_{wp,T}$) [real] ($m^3 \cdot m^{-3}$)
tetaII_fc.asc	Soil water content of the transpirative layer at field capacity ($\theta_{fc,T}$) [real] ($m^3 \cdot m^{-3}$)
tetaII_sat.asc	Saturated soil water content of the transpirative layer ($\theta_{s,T}$) [real] ($m^3 \cdot m^{-3}$)
tetaI_0.asc	Initial soil water content of the evaporative layer (θ_E) [real] ($m^3 \cdot m^{-3}$)
tetaII_0.asc	Initial soil water content of the transpirative layer (θ_T) [real] ($m^3 \cdot m^{-3}$)
gr_idr.asc	Hydrologic soil group classification to apply CN method. The correspondence is A=1, B=2, C=3 and D=4 [integer] (adimensional)
soggiacenza.asc	groundwater table level [real] (m)
Meteorological spatialization	
Meteo_*n*.asc	Weighting meteorological data parameters [real] (adimensional)
Irrigation districts information	
birrigui.asc	Sub-irrigation districts identification codes [integer]
codice_metodo.asc	Irrigation methods codes [integer]
codice_metodo *yyyy*.asc	Yearly maps with irrigation method codes [integer]. It should be provided one map for each year *yyyy* of simulation (e.g. codice_metodo2014.asc for year 2014)
eff_metodo.asc	Field application irrigation efficiency [real] $[0-1]$ (adimensional)
eff_metodo *yyyy*.asc	Yearly maps with field application irrigation efficiency [real] $[0-1]$. It should be provided one map for each year *yyyy* of simulation (e.g. eff_metodo2014.asc for year 2014)
eff_rete.asc	Conveyance and distribution efficiency [real] $[0-1]$ (adimensional)

Table i-7: Map (*.asc) structure. Ncols: number of columns, nrows: number of rows, xllcorner: longitude of the low left corner [m], yllcorner: latitude of the low left corner [m], cellsize: cell size [m], NODATA_value: no data value

ncols	97				
nrows	62				
xllcorner	1544355.766				
yllcorner	5049010.424				
cellsize	250				
NODATA_value	-9999				
-9999.000000	0.308809	0.114233	0.114233	0.256496	…
0.308809	0.308809	0.114233	0.114233	0.256496	…
0.308809	0.143943	0.114233	0.256496	0.256496	…
0.143943	0.114233	0.256496	0.256496	0.256496	…
-9999.000000	0.114233	0.256496	-9999.000000	-9999.000000	…
0.143943	0.114233	0.256496	-9999.000000	-9999.000000	…
0.143943	0.114233	0.114233	-9999.000000	-9999.000000	…
…	…	…	…	…	…

All maps must have identical location attributes (number of rows, columns, and so on). IdrAgra needs to know the size properties of each grid cell (length, area) in order to calculate water volumes from meteorological forcing variables that are all defined as water depths. IdrAgra obtains this information from the input parameters file. This will only work if all maps area in an equiareal projection, and the map coordinates and cell size are defined in meters.

I-6.1.1. Role of mask map

The mask map (i.e. “dominio.asc”) defines the model domain. In order to avoid unexpected results, it is vital that all maps that are related to topography, land use, soil, irrigation methods and meteorological distribution are defined (i.e. do not contain a missing value) for each pixel that is “true” (has a value equal to 1) on the mask map. Undefined pixels can lead to unexpected behavior of the model, i.e. output that is full of missing values.

I-6.1.2. Optional map stacks

Land use and irrigation method can be defined either as static maps (i.e. using the same land use and irrigation method for each year of simulation) or as a map stacks. A map stack is a series of maps, where each map represents the value of a variable at an individual time step (i.e. using different land use and irrigation maps for each year of simulation). The name of each map is made up combining the default name with the year of simulation (i.e. usosuolo2014.asc).

All map stacks that are needed to run the model are listed in the Table i- 8.

Table i- 8: IdrAgra map stacks.

Map stacks	
Land	
usosuolo*yyyy*.asc	Yearly maps with land use classes [integer]. It should be provided one map for each year *yyyy* of simulation (e.g. usosuolo2014.asc for year 2014).
Irrigation methods	
codice_metodo*yyyy*.asc	Yearly maps of irrigation methods [integer]. It should be provided one map for each year yyyy of simulation (e.g. codice_metodo2014.asc for year 2014).
eff_metodo*yyyy*.asc	Yearly maps with field application irrigation efficiency [real] $[0-1]$. It should be provided one map for each year yyyy of simulation (e.g. eff_metodo2014.asc for year 2014).

I-6.2. Organisation of input data

The following input structure is used (Figure i-10):

- all base maps are in “input_bilancio” directory
- all crop growth tables are in “fenofasi” directory
- all meteorological input maps are in “input_meteo” directory
- all irrigation methods tables are in “input_metodi” directory
- derivation information are in “dotazioni” directory
- output goes to one directory, whose name is customable (e.g. “output”).

In the root directory, a part of the code executables, some text files with simulation parameters are stored.

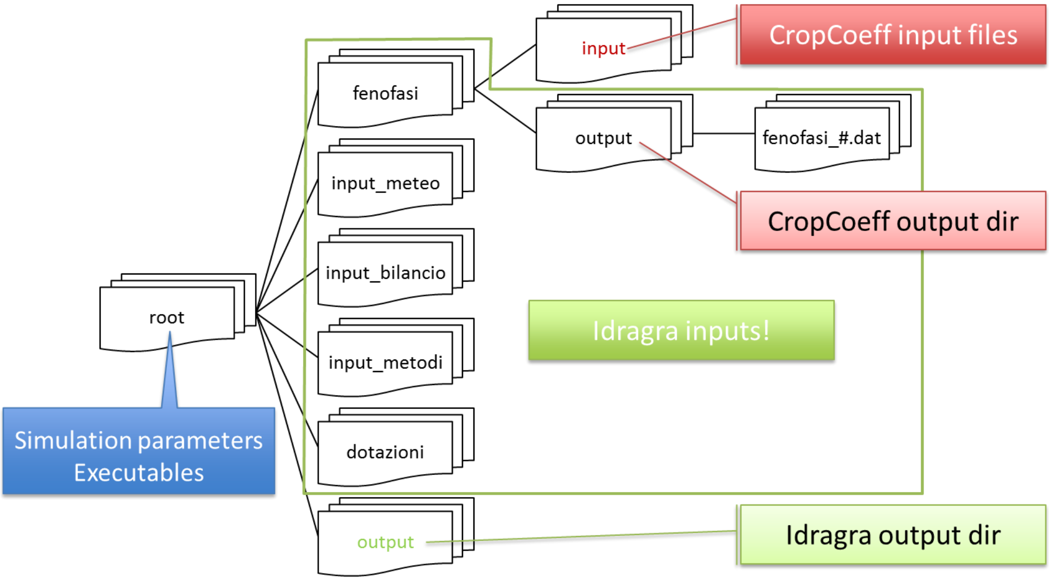

Figure i-10: Dataset structure for IdrAgra.

I-6.2.1. Meteorological inputs

Daily meteorological datasets are stored in the default directory .\input_meteo\. Their complete list is stored in the simulation parameters file File_meteo.dat, stored in the root directory. An example of its structure is reported in Table i- 9

Table i- 9: Meteorological list (File_meteo.dat) structure. 2nd line: number of meteorological stations. 4th – nth lines: meteorological station names, completed with their extension, their longitude (x_utm), (m) and latitude (y_utm), (m). Meteorological station list must contain the stated number of stations.

```
Number of meteorological stations:
12
SAR code        x_utm           y_utm
1.dat           1551000         5056000
3.dat           1506000         5056000
…
43.dat          1550000         5033000
```

One meteorological dataset for each considered station has to be provided, containing daily measures and technical details of the station. For practical reasons, due to the structure of meteorological network of Lombardy Region, the code number of the station (namely, SAR[1] code) is used as its file name: <*SAR_code*>.dat (i.e. the meteorological dataset of the Stezzano (BG) station, which SAR code is 132, is stored in 132.dat). An example of their stucture is reported in Table i-10.

To avoid unexpected results, all the meteorological datasets must have the same starting date and the same length.

Table i-10: Meteorological data (<*SAR_code*>.dat) structure. 1st line: Station ID: meteorological station code, Located in: localization. 2nd line: latitude (m), altitude (m). 3rd line: starting date (dd mm yyyy). 5th – nth lines: meteorological daily datasets: maximum temperature (T_max), $(^{\circ}C)$, minimum temperature (T_min), $(^{\circ}C)$, precipitation (P_tot), (mm), maximum relative humidity (U_max), (%), minimum relative humidity (U_min), (%), wind speed (V_med), $(m \cdot s^{-1})$, solar radiation (RG_CORR), $(MJ \cdot m^{-2} \cdot d^{-1})$.

```
Station ID: 132, Located in: Stezzano
45.64       266
1 1 1993
T_max       T_min       P_tot       U_max       U_min       V_med       RG_CORR
2.14        -5.29       0           88.77       54.96       1.38        5.15
-1.06       -9.03       0           85.9        67.96       1.37        1.53
…           …           …           …           …           …           …
7.24        2.28        0           95.47       67.96       1.41        2.21
```

---

[1] The acronym SAR stays for Servizio Agrometeorologico Regionale (Regional Agrometeorological Service). For this service, every meteorological station is coded with a number, that is also used in IdrAgra.

I-6.2.2. Phenological inputs

Crop and soil uses tables

All crop phenology data are simulated with the program Crop_Coeff_*yyyymmdd*.exe[2]. This model allows to elaborate the phenological series datasets, given the meteorological series. CropCoeff outputs are formatted to be used without any modification as IdrAgra inputs.

These datasets are stored in the directory .\fenofasi\input\. This path should not be modified, because currently CropCoeff cannot manage different paths. This directory contains two subdirectories, .\fenofasi\input\db_colture, which contains the soil uses list, and .\fenofasi\input\param_colture, which contains each crop parameters.

Table i-11: Crop database file (DB_cult.txt) structure. 2nd line: number of soil uses in the database. 4th – nth lines: crop id, crop parameters files, completed with their extension, and notes on the soil use. Crop parameters files list must contain the stated number of soil uses. The crop parameter file name can be repeated, i.e. in case of soil uses not simulated, as residential landuse, or in case of a crop that can be either alterned or not (e.g. maize and vernine cereals).

```
# Number of crops in database:
23
# Crop_id                  file_name                % notes
1                          altro.tab                % aree antropizzate
…
6                          cereali_AV.tab           % altri cereali (comprende grano tenero e orzo)
…
13                         mais600.tab              % mais 600
…
22                         mais300.tab              % mais 300
23                         prato_avvicendato        % foraggere
```

Table i-12: Soil uses database file (soil_uses.txt) structure. 2th – nth lines: soil uses, expressed as crop id (with the same ID of Table i- 9), with alternate crop. Soil uses list must contain the same number of soil uses as in crop database file. If there is no alternate crop, the second number is 0.

```
# DB-ID code (with alternate crop, otherwise it has to be set equal to 0)
1                          0
…
6                          0
…
13                         0
…
22                         6
23                         0
```

Soil uses list is structured in two files, DB_cult.txt, that lists crop files and associates a soil use number to each crop, and soil_uses.txt, that partially modifies soil uses database, describing which soil uses are actually composed by two alternate crops. Currently, IdrAgra code do not allow to simulate properly vernine or alternate crops if soil use changes every year, because of the partial overlapping of the vernine crops between two years. Examples of DB_cult.txt and soil_uses.txt

---

[2] Each program release is defined by a version date, that is reported in the executable as a 8-digits string, in the form *yyyymmdd* (year, month and day).

structure are reported in Table i-11 and Table i-12. An example of crop parameters files, named by default as <*crop_name*>.tab, is reported in Table i-7.

Table i-13: Crop parameters file (<*crop_name*>.dat) structure. 1st line: crop name, 2th – 5th lines: parameters for growing degree days calculation, 6th – 12th lines: vernalization parameters, 13th – 15th lines: daylength response parameters; 16th line: p_{tab} coefficient to compute RAW, 17th line: a_I coefficient used to compute interception, 18th line: landuse code to apply Curve Number method Table i-3), 19th line: irrigation flag, 20th line: number of breakpoints of Kcb, Leaf Area Index, crop height and root depth curves, 21st – nth lines: correspondence between cumulated growing degree days and breakpoint values. Cross-check is made to assure that each curve of a crop starts and ends with the same GDD value.

```
mais classe 600
98          # SowingDate_min: minimum sowing date (1-366)
10          # Treq: sowing temperature threshold [°C]
10          # Tdaybase: minimum temperature for viable crop development [°C]
30          # Tcutoff: maximum temperature for viable crop development [°C]
.false.     # V: vernalization sensitivity (.true. or .false.)
0           # Tv_min: low end temperature threshold for optimum vernalization [°C]
0           # Tv_max: high end temperature threshold for optimum vernalization [°C]
0           # VFmin: minimum vernalization factor value at the beginning of the vernalization process [-]
0           # Vstart: accumulated vernalization days at vernalization start
0           # Vend: required sum to complete vernalization
0           # A: parameter for not optimum vernalization
0           # ph_r: daylength response: 0: insensitivity; 1: long-day crop; 2: short-day crop
0           # daylenght_if: daylight hours to inhibit flowering, day length threshold below (above) which no
            accumulation of physiological time occurs   for long-day (short-day) crops
0           # daylenght_ins: daylight hours for insensitivity, day length threshold above (below) which maximum
            physiological time accumulation occurs for long-day (short-day) crops
0.5         # p: crop parameter "p"
0.6         # a: crop parameter "a"
2           # cl_CN: CN cover code
1           # irrigated (1) or not (0)
6             6             6             6                   # Breakpoints of Kcb, LAI, Hc, Sr curves
# GDD         Kcb
29            0
…             …
1675          0.15
# GDD         LAI
29            0
...           …
1675          3.7
# GDD         Hc
29            0
…             …
1675          2.5
# GDD         Sr
29            0
…             …
1675          0.85
```

Soil uses daily series

CropCoeff module stores its outputs into the directory .\fenofasi\output\, creating a subdirectory, named fenofasi_<*SAR_code*>.dat for each meterological (*SAR_code*) station. In each subdirectory are stored some *.dat files, that are used for IdrAgra simulation, and some *.xls files, useful for data analysis. The *.dat files, each containing daily crop parameter series for each soil use, are listed in

Table i-14. An example of their structure is reported in Table i-15. Examples of param_colturali.dat and classi_CN.dat are reported in Table i-16 and Table i-17.

Table i-14: Daily crop parameter series files for each meteorological station.

Crop parameter series files	
Kcb.dat	Basal crop coefficient [real]
LAI.dat	Leaf Area Index [real]
H.dat	Crop height [real]
Sr.dat	Root depth [real]
param_colturali.dat	Crop parameters p_{tab} and a_I [real]
classi_CN.dat	Land use and stage of growth codes to apply Curve Number method [integer]
uso_irriguo.dat	Irrigation flag [integer]

Table i-15: Daily crop parameter series structure, for Kcb.dat, LAI.dat, H.dat, Sr.dat and uso_irriguo.dat. 1st line: number of soil uses (equal to the number of columns), 3rd – nth lines: daily values.

```
23
coltura_1            coltura_2            …          coltura_23
0.0000000000000000   0.0000000000000000   …          0.0000000000000000
…                    …                    …          …
1.0590476190476190   0.0000000000000000   …          0.26470588235294118
…                    …                    …          …
```

Table i-16: Daily crop parameter series structure for param_colturali.dat. 1st line: number of soil uses (equal to half of the number of columns), 3rd – nth lines: daily values of p_{tab} (first half of the columns) and a_I (second half of the columns).

```
23
coltura_1_p      …   coltura_23_p     coltura_1_a      …   coltura_23_a
0.00000000000    …   0.00000000000    0.00000000000    …   0.00000000000
…                …   …                …                …   …
0.500000000000   …   0.500000000000   0.600000000000   …   0.600000000000
…                …   …                …                …   …
```

Table i-17: Daily crop parameter series structure for classi_CN.dat. 1st line: number of soil uses (equal to half of the number of columns), 3rd – nth lines: daily values of land use code (even columns) and of code to account for seasonal variations (0: before plowing and after harvesting, 1: between plowing and normal peak height, 2: between normal peak height and harvest time).

```
23
coltura_1_class   coltura_1_value   …   …   coltura_23_class   coltura_23_value
2                 0                         5                  1
…                 …                 …   …   …                  …
2                 0                 …   …   5                  2
…                 …                 …   …   …                  …
```

For each crop and parameter, a *.xls file is provided, named <*parameter*>_<*crop*>.tab, that contains the daily series of the calculated parameter, separated in different columns according to the year.

I-6.2.3. Irrigation methods tables

Irrigation methods tables are stored in the default directory .\input_metodi\. Irrigation method list has to be set in metodi.txt, and each method is described in a separate file, which is named

<*method_name*>.txt. Examples of metodi.txt and <*method_name*>.txt structure are reported in Table i-18 and Table i-19.

Table i-18: : Irrigation method list file (metodi.txt) structure. 2nd line: number of irrigation methods. 4th – nth lines: irrigation method files, completed with their extension. Irrigation methods list must contain the stated number of irrigation methods.

```
# Number of irrigation methods:
4
# Irrigation methods list
metodo_irriguo_aspersione.txt
…
metodo_irriguo_sommersione.txt
```

Table i-19: Irrigation method file (<*method_name*>.txt) structure. 1st line: irrigation method code, 2nd line: irrigation method water height, 3rd line: stress threshold coefficient for surface water irrigation, 4th line: stress threshold coefficient for private wells irrigation, 6th line: minimum $a_{irr\ met}$ value of percolation model, 7th line: maximum $a_{irr\ met}$ value of percolation model, 9th – 33th lines: hourly distribution of irrigation.

```
2              # Id: Irrigation method code
40             # Qadaq: irrigation water height [mm]
0.5            # k_stress: stress threshold coefficient for surface water irrigation
0.8            # k_stresspozzi: stress threshold coefficient for private wells irrigation
# «a» values of percolation model
10             # min: minimum «a» value
30             # max: maximum «a» value
# Hourly distribution
0.0417         # Irrigation between 0:00 and 0:59
…
0.0416         # Irrigation between 23:00 and 23:59
```

I-6.2.4. *Diversions tables*

Diversions tables are stored in the default directory .\dotazioni\, that contains water sources flow series and their distribution in each subdomain.

The file dotazioni.txt contains the distribution of each source to each irrigation district; currently, water cannot be allocated dynamically but each source will provide a fixed ratio of daily flow to each subdomain. An example of dotazioni.txt structure is reported in Table i-20.

Table i-20: Irrigation water distribution file (dotazioni.txt) structure. 1st column: subdomain code (that identify each irrigation district, as read in birrigui.asc), 2nd column: source code (that relates the irrigation district with a source listed in derivazioni.txt), 3rd column: source type (1. Surface water, 2. Springs, 3. Public wells, 4. Tailwater), 4th column: flow ratio from source to subdistrict.

```
60001              POZ1N              3          0.088105727
…
60007              F_HSL              2          0.004369475
60007              POZ1S              3          0.057016611
…
```

Daily flow series have to be provided for each source water. The files derivazioni.txt, that describes surface water sources flows, and coli.txt, concerning tailwater, have an identical format, as reported in Table i-21. The file fontanili.txt, that lists springs flow series, have a slightly different format, as reported in Table i-22.

Table i-21: Surface water sources (derivazioni.txt) and tailwater (coli.txt) daily flow series structure. 1st line: sources code, 2nd line: nominal flow ($m^3 \cdot s^{-1}$) for the source, 3rd – nth lines: daily flow series ($m^3 \cdot s^{-1}$).

```
C_ADS                   R_VAI
6.400                   9.500
0                       0
…
4.85                    9.7
…
```

Table i-22: Springs daily flow series (fontanili.txt) structure. 1st line: sources code, 2nd line: area code, 3rd line: nominal flow ($m \cdot s^{-1}$) for the source, 4th – nth lines: daily flow series ($m^3 \cdot s^{-1}$).

```
F_HSL                   F_AS2
6                       2
15.43                   3.83
5.64                    1.09
…
7.16                    1.09
```

Public wells have to be listed in pozzi_consortili.txt, and each well is parameterized in a separate file, which is named <*well_name*>.txt. Examples of pozzi_consortili.txt and <*well_name*>.txt structure are reported in Table i-23 and Table i-24.

Table i-23: Public wells list file (pozzi_consortili.txt) structure. 2nd line: number of public wells. 4th – nth lines: wells parameters files, completed with their extension. Public wells list must contain the stated number of public wells.

```
Number of public wells:
13
Wells parameters files
a_alt.txt
…
s_mar.txt
```

Table i-24: Public well parameters file (<*well_name*>.txt) structure. 1st line: public well name, 2nd line: public well code, 3rd line: maximum flow ($m^3 \cdot s^{-1}$), 4th line: nominal flow ($m^3 \cdot s^{-1}$), 5th line: activation threshold, 7th line: first activation threshold, 8th line: first nominal flow ratio if activated, 10th line: secobd activation threshold, 11th line: second nominal flow ratio if activated, 13th line: third activation threshold, 14th line: third nominal flow ratio if activated.

```
A_ALT
8                # Well code
3.300            # Maximum Q
0.913            # Nominal Q
0.9              # Activation threshold
1
0.9              # Activation threshold
0.5              # Flow threshold ratio
2
0.8              # Activation threshold
0.7              # Flow threshold ratio
3
0.5              # Activation threshold
0.9              # Flow threshold ratio
```

I-6.2.5. Simulation parameters file

A simulation parameters file, whose name is customable (e.g. “IdrAgra_parameters_yyyymmdd”.txt) has to be provided in the root directory to run the program. An example of its structure is reported in Table i-25. Comment lines are provided to help the user setting the simulation parameters.

Table i-25: Simulation parameters file structure: grey lines are comments, that help the user setting the parameters.

```
# Input file for Idragra
# Note: lines starting with <#> are comments
### 1. General section ###
# 1.1. Input and output folders and files
# 1.1.1. Output folder
# OutputPath: path to output folder [name_outputpath\\]
OutputPath = cellcheck_2003mais\\
# 1.1.2. Input folders
# MeteoPath: path to meteorological stations folder
MeteoPath = input_meteo\\
# MeteoFileName: file, located in root folder, in which meteorological filenames are stored
MeteoFileName = file_meteo.dat
# PhenoPath: path to phenological parameters folder
PhenoPath = fenofasi\\output\\
# PhenoFileRoot: first part of the name of phenological parameters subfolders (labelled as
PhenoFileRoot_MeteoNum.dat)
PhenoFileRoot = fenofasi_
# IrrMethPath: path to irrigation methods folder
IrrMethPath = input_metodi\\
# IrrMethFileName: file, located in irrigation methods folder, in which irrigation methods filenames are stored
IrrMethFileName = metodi.txt
# 1.2. Simulation settings
# 1.2.1. Type of simulation
# Mode: type of simulation [0...4]
# Mode = 0 # simulation without irrigation
# Mode = 1 # simulation with irrigation, mode consumptions
# Mode = 2 # simulation with irrigation, field capacity needs satisfaction
# Mode = 3 # simulation with irrigation, fixed volumes
# Mode = 4 # fixed irrigation applications, data and volumes are specified in a file
Mode = 0
# 1.2.2. Simulation conditions
# InitialThetaFlag: switch, external setting of initial soil moisture condition [T F] (T=true, F= false)
# InitialThetaFlag = T # initial moisture condition read from external file
# InitialThetaFlag = F # internally generated initial moisture condition by running the first year and using its output as
initial moisture for the simulation
InitialThetaFlag = T
# CapillaryFlag: switch, simulation of capillary rise [T F] (T=true, F= false)
# CapillaryFlag = T # capillary rise simulated
# CapillaryFlag = F # capillary rise not simulated
CapillaryFlag = T
# SoilUseVarFlag: switch, simulation uses yearly soil uses [T F] (T=true, F= false)
# SoilUseVarFlag = T # soil uses changes every year
# SoilUseVarFlag = F # soil uses does not change
SoilUseVarFlag = F
# 1.2.3. Meteorological inputs
# MeteoStatTotNum: number of meteorological stations
MeteoStatTotNum = 9
# MeteoStatWeightNum: number of nearest meteorological stations used to weight crop phenology
```

```
MeteoStatWeightNum = 3
# 1.2.4. Soil uses inputs
# SoilUsesNum: number of considered soil uses in each of phenological series
SoilUsesNum = 23
# RandSowDaysWind: number of days of window for sowing date randomization
RandSowDaysWind = 0
# 1.2.5. Periodical output setting
# MonthlyFlag: output interval (monthly or specific interval) [T F] (T=true, F= false)
# MonthlyFlag = T # switch, output each month
# MonthlyFlag = F # switch, periodical output
MonthlyFlag = F
# if MonthlyFlag = F, choose output interval - output will be recorded from StartDate to EndDate every DeltaDate days
# StartDate: start Julian day [1...366] for periodic output
StartDate = 1
# EndDate: end Julian day [1...366] for periodic output
EndDate = 365
# DeltaDate: output interval, Julian days [1... 366]
DeltaDate = 365
### 2. Simulation specifications   ###
# 2.1. Ponding parameters
# PondSlopeMin: slope below which (or equal to) maximum ponding (q_max) occurs
PondSlopeMin = 0.00
# PondFracMax : maximum ponding ratio between ponded water and theorical runoff
PondFracMax = 0.90
# PondSlopeMax: slope over which minimum ponding (q_min) occurs
PondSlopeMax = 0.05
# PondFracMin: minimum ponding ratio between ponded water and theorical runoff
PondFracMin = 0.10
# 2.2. Irrigation inputs
# StartIrrSeason: Julian day [1...366] in which irrigation season starts
StartIrrSeason = 91
# EndIrrSeason: Julian day [1...366] in which irrigation season starts
EndIrrSeason = 304
# if Mode = 1 (consumptions), define irrigation sources
# BasinsTotNum: total number of irrigation districts
BasinsTotNum = 45
# BasinsXSourceTotNum: number of combinations of irrigation districts and diversions
BasinsXSourceTotNum = 44
# SourceSpringTotNum: total number of springs
SourceSpringTotNum = 0
# SourceSurfDerivTotNum: total number of surface derivations
SourceSurfDerivTotNum = 3
# SourceWellTotNum: total number of public wells
SourceWellTotNum = 0
# SourceTailwaterTotNum: total number of tailwater sources
SourceTailwaterTotNum = 0
# 2.3. Layers depth [m]
# zEvap: evaporative layer depth [m]
zEvap = 0.15
# zRoot: transpirative layer depth [m]
zRoot = 0.85
### 3. DTx specifications ###
# DTxMode: DTx calculation off [none], DTx statistical analysis [analysis] or DTx application [application]
# DTxMode = none
# DTxMode = analysis
# DTxMode = application
DTxMode = analysis
```

```
# DTxNumXs: number of calculated indices (one for each integration period), i.e. elements of DTx_x
DTxNumXs = 3
# DTx_x: integration period   (DT10 sums transpirative deficit of 10 days)
DTx_x = 10 20 30
# DTxDeltaDate: DTx calculation interval
DTxDeltaDate = 10 #
# DTxDelayDays: delay from the first day of year to start calculation
DTxDelayDays = 1
# if DTxMode = analysis, choose minimum cardinality (i.e. number of elements for a valid estimate)
# DTxMinCard: minimum cardinality for statistical analysis
DTxMinCard = 3
```

I-6.3. Output maps

All maps that are generated by the model are listed in Table i-26. Their structure, analogous to the one of input maps, is reported in Table i-7.

Table i-26: IdrAgra output maps.

Default name	Description
Yearly maps	
anno*y*_eva_cum.asc	Yearly maps of cumulated evaporation [real]. A map for each year *y* of simulation (e.g. anno1_eva_cum.asc for the 1st year of the simulation) is generated.
anno*y*_irr_cum.asc	Yearly maps of cumulated irrigation [real]. A map for each year *y* of simulation is generated.
anno*y*_pioggia_cum.asc	Yearly maps of cumulated precipitation [real]. A map for each year *y* of simulation is generated.
anno*y*_trasp_cum.asc	Yearly maps of cumulated transpiration [real]. A map for each year *y* of simulation is generated.
anno*y*_uso_pioggia.asc	Yearly maps of cumulated precipitation use efficiency (i.e. the ratio between evapotranspiration and precipitation) [real]. A map for each year *y* of simulation is generated.
anno*y*_uso_pioggia_irr.asc	Yearly maps of cumulated precipitation and irrigation use efficiency (i.e. the ratio between evapotranspiration and the sum of precipitation and irrigation) [real]. A map for each year *y* of simulation is generated.
Periodic maps	
anno*y*_step*n*_capflux.asc	Periodic maps of cumulated capillary rise [real]. A map for each output interval – set in # 1.2.5 of simulation parameters file – *n* of each year *y* of simulation (e.g. anno1_step1_capflux.asc for the 1st output interval of the 1st year of the simulation) is generated.
anno*y*_step*n*_eva.asc	Periodic maps of cumulated evaporation [real]. A map for each output interval *n* of each year *y* of simulation is generated.
anno*y*_step*n*_flux.asc	Periodic maps of cumulated fluxes (i.e. percolation minus capillary rise) between the transpirative layer and the deeper subsoil [real]. A map for each output interval *n* of each year *y* of simulation is generated.
anno*y*_step*n*_irr.asc	Periodic maps of cumulated irrigation [real]. A map for each output interval *n* of each year *y* of simulation is generated.
anno*y*_step*n*_irr_az.asc	Periodic maps of cumulated irrigation from private wells [real]. A map for each output interval *n* of each year *y* of simulation is generated.

anno*y*_step*n*_irr_com.asc	Periodic maps of cumulated irrigation from public wells [real]. A map for each output interval *n* of each year *y* of simulation is generated.
anno*y*_step*n*_peff.asc	Periodic maps of cumulated effective rainfall [real]. A map for each output interval *n* of each year *y* of simulation is generated.
anno*y*_step*n*_perc1.asc	Periodic maps of cumulated percolation from the evaporative to the transpirative layer [real]. A map for each output interval *n* of each year *y* of simulation is generated.
anno*y*_step*n*_perc2.asc	Periodic maps of cumulated percolation from the transpirative layer to the deeper subsoil [real]. A map for each output interval *n* of each year *y* of simulation is generated.
anno*y*_step*n*_pioggia.asc	Periodic maps of cumulated precipiation [real]. A map for each output interval *n* of each year *y* of simulation is generated.
anno*y*_step*n*_trasp.asc	Periodic maps of cumulated actual transpiration [real]. A map for each output interval *n* of each year *y* of simulation is generated.
anno*y*_step*n*_trasp_c.asc	Periodic maps of cumulated potential transpiration [real]. A map for each output interval *n* of each year *y* of simulation is generated.
TD distribution	
dt*x*_alpha_*d*.asc	α parameter of TD distribution for the integration period *x*, calculated for the d^{th} x-day period of the year
dt*x*_beta_*d*.asc	β parameter of TD distribution for the integration period *x*, calculated for the d^{th} x-day period of the year
dt*x*_zero_prob_*d*.asc	Probability of zero of TD distribution for the integration period *x*, calculated for the d^{th} x-day period of the year

I-7. References

Allen, R.G. et al., 1998. Crop evapotranspiration - Guidelines for computing crop water requirements. *FAO Irrigation and drainage paper*, 56, p.174. Available at: https://www.kimberly.uidaho.edu/water/fao56/fao56.pdf.

Bartier, P.M. & Keller, C.P., 1996. Multivariate interpolation to incorporate thematic surface data using inverse distance weighting (IDW). *Computers & Geosciences*, 22(7), pp.795–799. Available at: http://linkinghub.elsevier.com/retrieve/pii/0098300496000210.

Braden, H., 1985. Ein Energiehaushalts- und Verdunstungsmodell für Wasser- und Stoffhaushaltsuntersuchungen landwirtschaftlich genutzter Einzugsgebiete [An energy balance and evaporation model for water and nutrient budget studies of agricultural catchments]. *Mitteilungen Deutsche Bodenkundliche Gesselschaft*, 42, pp.294–299. Available at: https://www.dbges.de/wb/media/mitteilungen_dbg/Mitteilungen der DBG 1985_42.pdf.

Brooks, R. & Corey, A., 1964. Hydraulic properties of porous media. *Hydrology Papers, Colorado State University*, 3(March), p.37. Available at: https://dspace.library.colostate.edu/bitstream/handle/10217/61288/HydrologyPapers_n3.pdf?sequence=1.

Von Hoyningen-Hüne, J., 1983. Die Interception des Niederschlags in landwirtschaftlichen Beständen. In *Einfluss der Landnutzung auf den Gebietswasserhaushait. (Schriftenreihe des Deutschen Verbandes für Wasserwirtschaft und Kulturbau e.V., DVWK; H. 57)*. Hamburg und Berlin: Paul Parey, pp. 1–53. Available at: http://wiki.bluemodel.org/images/9/9e/DVWK_57_I.pdf.

Liu, Y., Pereira, L.S. & Fernando, R.M., 2006. Fluxes through the bottom boundary of the root zone in silty soils: Parametric approaches to estimate groundwater contribution and percolation. *Agricultural Water Management*, 84(1–2), pp.27–40. Available at:

http://www.sciencedirect.com/science/article/pii/S0378377406000321 [Accessed April 18, 2014].

Natural Resources Conservation Service Soil Survey Staff, 1996. National soil survey handbook, title 430-VI. U.S. Government Printing Office, Washington, D.C.

Neitsch, S.K., Arnold, J.G., Kiniry, J.R. Williams, J.R., 2011. Soil and Water Assessment Tool. Theoretical Documentation Version 2009. Texas Water Resources Institute Technical Report No. 406. September 2011

Rallison, R.E. and Miller, N., 1981. Past, present and future SCS runoff procedure. In Singh, V.P. (ed.). Rainfall-runoff relationship. Water Resources Publication, Littleton, CO., USA, pp. 353-364.

Soil Conservation Service, 1972. National engineering handbook, Section 4, Hydrology. Chapter 10. Soil Conserv. Serv., Washington, D. C.

Soil Conservation Service Engineering Division, 1986. Urban hydrology for small watersheds. U.S. Department of Agriculture, Washington, D.C., Technical Release 55.

Stöckle, C.O., Nelson, R.L., 2000. Cropsyst User's manual (Version 3.0). Biological Systems Engineering Dept., Washington State University, Pullman, WA.

U S Department of Agriculture, U. S., 1985. National Engineering Handbook, Section 4 - Hydrology. Washington, DC, U.S. Printing Office.

Williams, J.R., 1995. The EPIC model. In V. P. Singh, ed. *Computer models of watershed hydrology.* Highland Ranch, Co, USA: Water Resources Publications, pp. 909–1000.